Detecting and Mapping Seasonal Variations in Water Turbidity and Mouth Bar Geometry along an Asymmetrical Delta using Normalized Different Turbidity Index (NDTI) with Sentinel 2 Satellite Imagery

By

Ly, Chanveasna

Thesis
Submitted to Flinders University
for the degree of

Masters of Geospatial Information Science

College of Science and Engineering
31/10/2021

TABLE OF CONTENTS

LIST OF ABBREVIATIONS

ANNs	Artificial Neural Networks
BNs	Bayesian Networks
CDOM	Coloured Dissolved Organic Matter
CVA	Change Vector Analysis
DEA	Digital Earth Australia
E	East
EC	Element Complex
ENE	East North East
ENVISAT	Environmental Satellite
ESA	European Space Agency
ESE	East South East
ETM+	Enhanced Thematic Mapper Plus
F-Mouth Bar	Fluvial Mouth Bar
GEE	Google Earth Engine
GIS	Geographical Information System
GoC	Gulf of Carpentaria
ka BP	Kilo Annum (thousand years) Before Present
km	Kilometre
km/h	Kilometre per Hour
km^2	Square Kilometre
m	Metre
MERIS	Medium Resolution Imaging Spectrometer
MNDWI	Modified Normalised Different Water Index
MODIS	Moderate Resolution Imaging Spectroradiometer
MODIS-A	MODIS Aqua
MODIS-T	MODIS Terra
MSG	Meteosat Second Generation
MSI	Multispectral Instrument
m^3/s	Cubic Metre per Second
NE	North East
NDTI	Normalised Different Turbidity Index
NDWI	Normalised Different Water Index
NIR	Near Infra-Red
nm	Nanometre
NNE	North North East
NW	North West

OBIA	Object-Based Image Analysis
OLCI	Ocean and Land Colour Instrument
OLI	Operational Land Imager
RS	Remote Sensing
SE	South East
SEVIRIS	Spinning Enhanced Visible and Infrared Imager
SLC	Scan Line Corrector
SMA	Spectral Mixture Analysis
SPM	Suspended particulate matter
SPOT	Satellite Pour l'Observation de la Terre
SVM	Support Vector Machine
SSC	Suspended Sediment Concentration
SWIR	Short Wave Infra-Red
yr BP	Year Before Present
3D	Three-dimensional

ABSTRACT

Remote sensing studies for ocean monitoring first appeared in the 1960s and have subsequently increased in popularity (Potes et al. 2018). Satellite remote sensing compliments traditional in-situ data specimen and laboratorial examination of water quality variables, which is laborious and expensive and typically has a limited spatial and temporal range. In contrast to traditional field measurement techniques, satellite-based remote sensing methodologies are inexpensive and can cover relatively large spatiotemporal ranges. Satellite-based remote sensing techniques are effective for investigations that monitor river discharge into the coastal waters and subsequent reworking by near-shore basinal processes. This investigation focuses on suspended particulate matter (SPM) concentrations in rivers, their associated plumes, and the near-offshore. Monitoring of SPM concentrations is crucial for sediment transport and ecosystem modelling, and for understanding the morphology and evolution of marginal marine systems. Furthermore, the relative concentration of SPM has been treated as a proxy for turbidity and is used to investigate plume geometry and understand erosion and/or progradation of the coastline.

This research aims to implement remote sensing to detect the relative suspended sediment concentration (SSC) for as a proxy for turbidity and erosional processes mapping the plume and mouth bar geometry for investigating two specific purposes: 1) to determine how fluvial discharge and basinal processes (waves, tides and longshore currents) influence mouth bar and sediment plume formation, and 2) determine how the interplay of sea level, sediment supply vs erosional activities influence the rates of localized progradation or erosion in the asymmetric, shallow basin, Mitchell River, Gulf of Carpentaria (GoC). The Mitchell River delta is complex delta system, which is an asymmetrical (sediment acquired from longshore drift trapping on the updrift delta as the mouth bar performs as a groyne), tide-dominated, wave-influenced, fluvial-affected (Twf) system (Nanson et al. 2013), with incredibly limited research where mostly about the lower delta plain and no research about near offshore system leading this research to be an understudied geographical regime that contribute to the understanding about the depositional sediment both onshore and offshore and enhance the understanding of delta morpho-dynamic. These understanding will become beneficial for delta ecosystem investigations in Australia, essentially in the GoC. Moreover, the most significant outcome of this research is to theoretically enhance understanding of processes affecting localized shoreline changes (either side of the asymmetrical delta).

To detect and map the plume and mouth bar geometry, the Sentinel 2 L2A (atmospheric and geometric corrections) products were collected from January 2020 to August 2021 using automation process in Google Earth Engine (GEE) for analysis along the meteorological and hydrological statistics for the interpretation. The pilot process is performed to verify the best method in selecting sensitive bands included: (1) Red+Green+NIR, 2) Red+Green (NDTI), 3) Red+NIR+SWIR to get optimal result, which the NDTI is the most suitable, before the semi-automatically method is applied

for this study including automation process: 1) water area extraction (image pre-processing) using band ratioing method of MNDWI (Modified Normalized Different Index), 2) turbidity detection using band ratioing method of NDTI; manual process: 3) plume pattern corrections, and 4) digitizing mouth bar geometry. This method is performed in the ArcGIS Pro version 2.8.2 for both the pilot and semi-automatically methods, yet the Erdas Imagine was assisted for visualizing the sensitivity of band combinations and spectral reflectance to enhance the confidence of choosing suitable bands in the pilot stage. Three significant inaccuracies of the algorithm revealed: 1) errors of MNDWI in masking out clouds where thin cloud and cloud shadow could be less masked out leading to confuse classified as plume and over masked out resulting in missing plume areas, 2) error of NDTI in differentiating pixels due to undistinguished between low concentration plume reflectance with water pixel leading to miss classified plume area, and 3) error of pixel-based classification in classifying plume boundary leading to assisting of the manual correction of plume pattern.

The results revealed that the large-scale sediment plume orientated to southward (analogue to palaeo-flow orientation) in the wet season while it shifted its orientation in the dry season to northerly directed (analogue to longshore drift current) and parallel to the palaeo-channels orientation within the Mithcell River delta. Another discovery in this study showed that the high and very high turbidity constantly dominate in the vicinity of the north nearshore zone in both wet and dry seasons where severe coastline erosion has occurred. At the same time, the south nearshore zone of the Mitchell mouth bar, where the progradation coastline has prograded, experienced low turbidity in the dry season and moderate turbidity in the wet season.

DECLARATION

I certify that this thesis does not incorporate without acknowledgment any material previously submitted for a degree or diploma in any university; and that to the best of my knowledge and belief it does not contain any material previously published or written by another person except where due reference is made in the text.

Signed.....

Date: 31/10/2020

ACKNOWLEDGEMENTS

I would like to express my special appreciation and thanks to my supervisor **Dr. Tessa Lane,** Lecturer in Geospatial Information Systems who has been taught, encouraged and supervised me to complete this thesis. Her guidance helped me in all the time of writing to achieve this final report. Thanks for providing me the interesting topic that I can expand my knowledge in geomorphology field. Words cannot express how grateful I am to her for all she has done for me. Also, I would like to express my gratitude to my co-supervisor **David Bruce**, Associate Professor in remote sensing, for his kind support and helpfulness in teaching, guiding and challenging me to perform a variety of remote sensing and GIS processing. This thesis could not be accomplished without their help and supports.

Special thanks to **Dr. Rachel Nanson**, Geomorphologist at Geoscience Australia, for her value times in consulting on some geomorphological complications of this thesis. Thanks, her advice and suggestion.

Additional thanks to **Robert Keane** for his help and support in some difficulties of software and license. I am also grateful to all my lecturers in the Geospatial Sciences Department at Flinders University, for their sacrifices to transfer precious knowledge to me as well as other students.

Last but not the least, I am thankful to my parents, siblings and friends who emotionally supported and encouraged me to continue my study and accomplish this thesis, especially in my depressed time during this COVID-19 outbreak.

LIST OF FIGURES

LIST OF TABLES

LIST OF EQUATIONS

CHAPTER 1. INTRODUCTION

1.1. Background

Deltas form where rivers and streams debouch into a standing body (Seybold, Andrade & Herrmann 2007). The place where fluvial sediments commence to accumulate into the delta is called a mouth bar. The Mouth bar is formed when an overload sediment is spread out from the river into a persistent water body (Bates 1953). As a river emerges into a standing body of water, there is an interaction of the river plume with the receiving standing body of water (Wright 1978). In estuarine and coastal water, the coastal river plume is the primary transport mechanism for fresh water, suspended sediment, dissolved carbon, nutrients, and pollutants (Guo et al. 2017). Deltaic systems are important from many perspectives; they provide habitats for many different species' assemblages, including human populations and are important for many natural resources including water, agriculture, and fisheries. Morphology of deltaic system varies widely among deltas and is a function of many drivers including fluvial processes including discharge and sediment supply and basinal processes including waves, tides and longshore currents (Galloway 1975). The iconic delta called the Mississippi delta (known as the bird-foot delta since its appearance is more probable equivalent to the natural appearance of a bird's foot) in Louisiana, USA is considered as a delta affected by the fluvial flow (Coleman 1976). Many deltas, however, exhibit complex morphologies, particularly if they are influenced by a variety of factors. For instance, the Ganges delta (Sundarbans Delta or Bengal Delta), located in Bengel region of South Asia, represents a complex morphology along the bat of Bengel due to the variation influences of the fluvial flow, waves and tides (Ainsworth, Vakarelov & Nanson 2011). This delta is characterised as wave-dominated, tide-influenced, fluvial-affected (Wtf).

During the last three decades, numerous investigations have targeted on monitoring water quality parameters not only in coastal waters but also in inland using satellite imagery (Sebastiá-Frasquet et al. 2019). The product of satellite imagery delivers synoptic and recurrent indications of coastal water and could possibly be the only method on synoptic scales to monitor the dispersal of river plumes (Hopkins et al. 2013). By using the visual characteristics of coastal surface waters, it is possible to identify turbid plume water from ambient water masses (Lahet & Stramski 2010). Additionally, the surface reflectance characteristics derived from the satellite imagery were recognised as a consistence property in evaluating the variability of the plume geometry including its shape and area (Ahn et al. 2008; Hu et al. 2004; Palacios, Peterson & Kudela 2009). Therefore, the satellite sensors of ocean colouring are effective instruments to investigate and monitor the dynamic variables discharged by streams and rivers into the coastal water such as coastal water plume (Ody et al. 2016).The majority of the coastal river plume studies using satellite remote sensing technique have been caried out at inter-annual and seasonal scale when few studies have examined the plume variation in short-term period (inter-day or intra-day) to understand the drastic transformation for a short-term event (Guo et al. 2017).

The Mitchell River Delta in the Gulf of Carpentaria provides a unique opportunity to study a modern, minimally disturbed, mixed influenced delta in a shallow basin setting. Detailed sedimentary and stratigraphic analysis of the preserved Holocene delta has been provided by Lane et al. (2017); Massey et al. (2014); Nanson et al. (2013); Rhodes (1980). However, very constrained research is known about the near-offshore mouth bar and sediment plume processes, which are fundamental for understanding delta construction, and the effects of recent anthropogenic changes (for example, gully erosion triggered by grazing and sea-level rise).

As such, this study aims to investigate the architecture and morphological processes of the mouth bars and sediment plumes of the modern delta in recent history, linking these findings to fluvial (rainfall and river discharge), and basinal processes (wave, wind, tide, longshore currents). Given the remote location of the study site and the high spatial and temporal advantages provided by satellite imagery, this thesis will employ remote sensing methods integrated with government field data in the analysis.

1.2. Thesis Structure

Chapter 1 aims to introduce the study site and articulate the research questions and objectives of the thesis. A detailed literature review on deltaic systems, remote sensing methods in detecting turbidity, and GIS applications in mapping delta geometry is presented in **Chapter 2**. **Chapter 3** provides a detailed description of the pilot process and the employed methodology. The results are presented in **Chapter 4**, with frequent refence to the appendices. **Chapter 5** includes a detailed discussion of the key findings, particularly in relation to intra-seasonal mouth bar and sediment plume variability, and key limitations. **Chapter 6** gives a brief conclusion and summary. It also highlights some limitations and directions for future investigation.

1.3. Study Area

The study area of the research is situated in the Mitchell River Delta, Gulf of Carpentaria (GoC), Queensland, Australia (**Figure 1.1**). This research specifically concentrates on the main Mitchell River mouth although various river outlets are reported on the Mitchell River delta.

1.3.1. Geographical Setting

The Mitchell River delta into is located on the west coast of the Cape York Peninsula in North Queensland, Australia and drains into the Gulf of Carpentaria (in **Figure 1.2**). The delta system is feed by a large megafan, and has a catchment area of 71 757 km^2, draining from the Great Dividing Range highlands, 250 km to the east. The upper delta plain comprises a complex network of fluvial channels characterised by frequent avulsions (Lane et al. 2017). The lower delta plain expands approximately 17 km from the shoreline inland and approximately 50 alongshore (Rhodes 1980). The lower delta plain has built over the last 6500 years under a ~2m sea-level fall (Sloss et al. 2018),

as a series of lobes, the position of which is largely driven by avulsions on the upper delta plain and megafan (Lane et al. 2017; Nanson et al. 2013). The lobes display a complex architecture which reflects the relative influence of basinal processes (waves, tides, longshore currents) and sediment supply, which varies laterally and through time (Lane et al. 2017; Nanson et al. 2013). Currently, the delta is feed by three primary tidally affected distributary streams: the South Mitchell, Main Mitchell, and North Arm rivers (**Figure 1.1**).

1.3.2. Holocene sea level

During the Late Pleistocene lowstand in the Gulf of Carpentaria, low onshore and offshore gradients resulted in very minor channel incision (Jones, Martin & Senapati 1993). Low offshore gradients and a minor reduction in relative sea level resulted in widespread progradation of Holocene coastal systems following floods during the post-glacial marine transgression, which reached a sediment thickness of approximately 10 m on the Mitchell River (Lane et al. 2017).

Sloss et al. (2018) used previous studies' results and the modern data from the South Wellesley Archipelago to revise the history of the Holocene sea level change. Based on the revision, the Holocene sea level history was separated into three major phases:

- Phrase 1 from approximately 12,000 to approximately 7000 yr BP (during the post-glacial marine transgression (PMT) of the GoC): there was an increased sea level in approximately 11,700 yr BP breaching the Arafura Sill. The increase of sea level continued to reach approximately -30 m in 10,000 yr BP resulting in the full marine condition.
- Phrase 2 from approximately 7000 to approximately 4000 yr BP (Mid-Holocene sea-level highstand): the sea level was equivalent to the present mean sea level (PMSL) in 7,700 yr BP and continued to increase between +1.5 m and +2 m of PMSL.
- Phrase 3 from approximately 4000 yr BP to present (Regression from mid-Holocene sea-level highstand to PMSL): the sea level remained approximately 1.5 m above PMSL during 7,000 yr BP and 4,000 yr BP until a rapid decline to within ± 0.5 m of PMSL in approximately 3500 yr BP.

However, a recent sea level is reported to increase approximately 0.5 m in this modern shoreline period (between 2014 to 2020) according to the sea level projection tool from NASA (https://sealevel.nasa.gov/ipcc-ar6-sea-level-projection-tool).

1.3.3. Holocene climate

The Mitchell basin is characterised by a hot and dry semi-arid to sub-humid climate that is highly seasonal with a long-dry season and a short-wet season. The rainfall is approximately 996 mm per year on average, with 97% falling during the rainy season. In the Mitchell catchment, over 90% of total runoff occurs during the three-month period (from January to March), which is extremely high when compared to rivers in southern Australia (Charles et al. 2016).

Shulmeister (1999) identified three variations of climatic periods in the northern Australian Holocene climate:

- from the early Holocene until 5 ka BP, the temperature and effective precipitation (EP) were increased
- from 5 to 3.7 ka BP, the EP was increased
- from 3.7 ka BP to the present, the EP was sharply declined, and there was an increase of variability in climate.

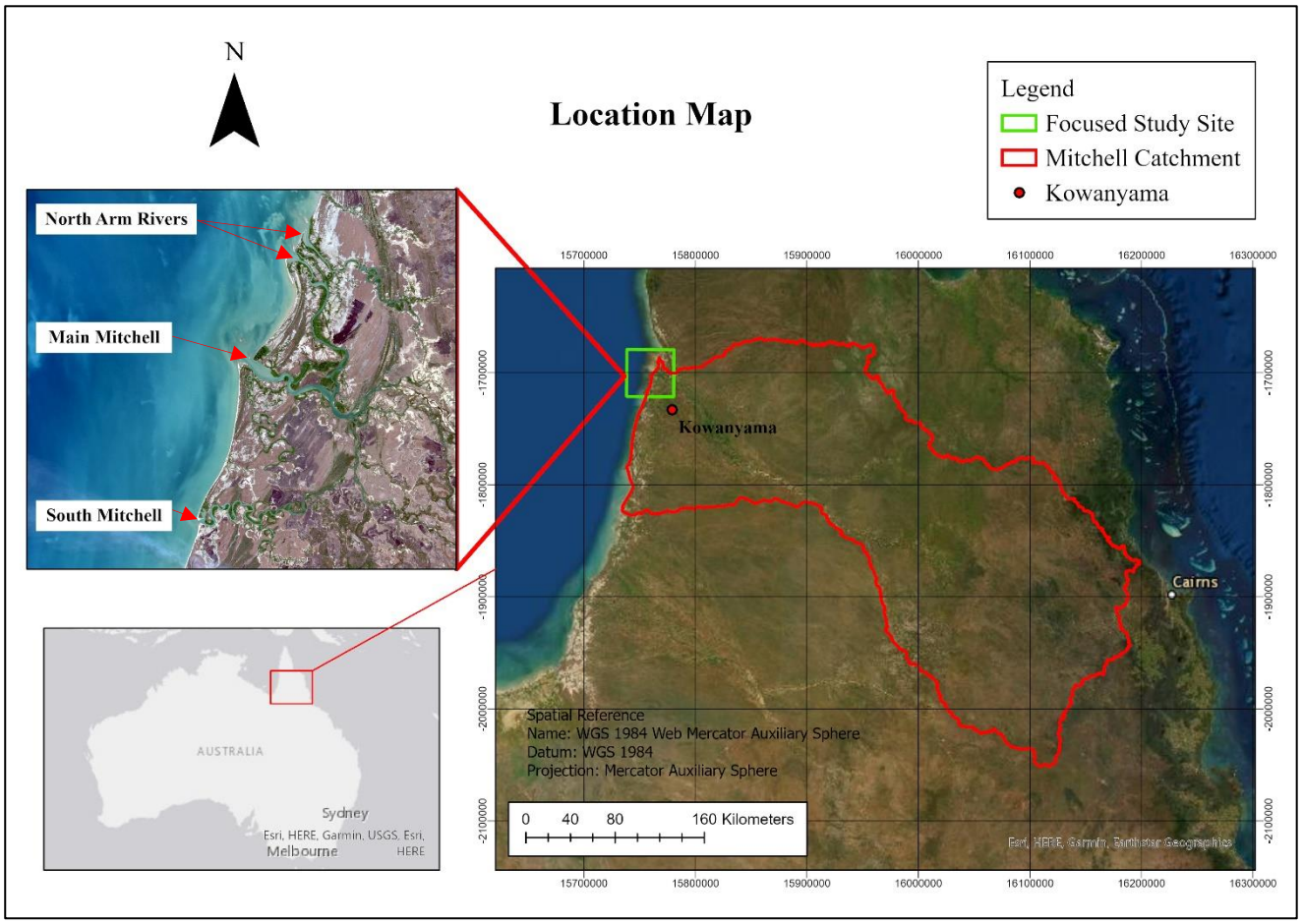

Figure 1.1 Location Map of the Mitchell River Delta.

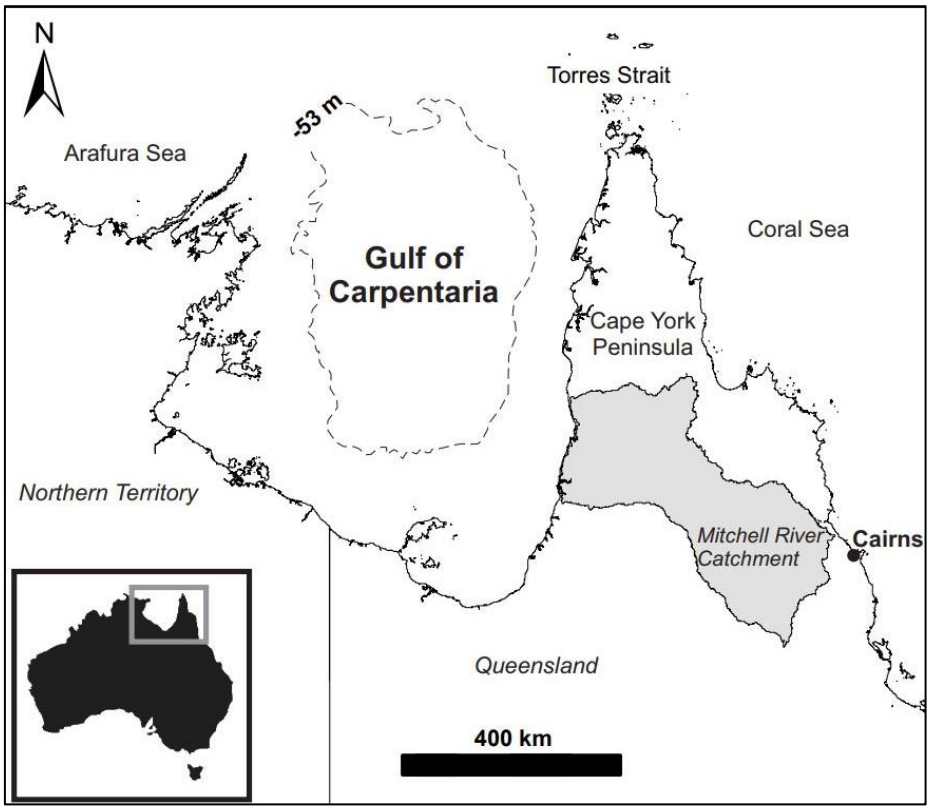

Figure 1.2 Location Map of the GoC focusing on the Mitchell Catchment Area.

1.1. Research Questions

Two research question raised in this research are:

1. How do fluvial discharge and basinal processes (waves, tides and longshore currents) influence mouth bar and sediment plume structures in the asymmetric, shallow basin, Mitchell River Delta, Gulf of Carpentaria?
2. How does the interplay of sea level, and sediment supply vs erosional activities influence the rates of localised progradation or erosion in the asymmetric, shallow basin, Mitchell River, Gulf of Carpentaria?

1.2. Objectives

These objectives responding to the raised questions in this research are:

- Map changes in mouth bar geometry at various stages through two-year period and relate this to changes in rainfall, fluvial discharge, wind speed and direction and tide.
- Map changes in sediment plume dimension and orientation using turbidity indices at various stages through two-year period and relate to changes in rainfall, fluvial discharge, wind speed and direction and tide.
- Relate turbidity indices (as proxy for erosion), sediment supply and sea level changes to recent shoreline erosion and progradation rates on the Mitchell River Delta, Gulf of Carpentaria.

1.3. Significance

The Mitchell River Delta provides a well-preserved, understudied area to investigate mixed-influenced asymmetric delta morphodynamics. This study will reveal new insights into the shallow basin, asymmetrical, mixed-influence Mitchell River, Gulf of Carpentaria. Due to the limited research about the Mitchell River delta, which mostly investigate about the lower Mitchell River delta plain, the significance of this research remains in its capability as understudied geographical regime to contribute to the new understandings about context and its inclusion in the study of the water turbidity in the nearshore of shallow basin, Mitchell River, Gulf of Carpentaria. The study, moreover, enhances the understanding of the in the Gulf of Carpentaria associating to the erosion, progradation and sedimentation. Applicable to the sedimentation, it not only enhances the delta morpho-dynamic knowledges but also contributes to the discourse of both onshore and offshore depositional sediment mechanism in that region. The perspective of these analysis and discourse could be potentially beneficial for delta ecosystem investigations in Australia, essentially in the Gulf of Carpentaria. Finally, the most significant outcome of this research is to theoretically enhance understanding of processes affecting localized shoreline changes either side of the asymmetrical Mitchell River delta.

CHAPTER 2. LITERATURE REVIEW

2.1. Review of Deltaic System

2.1.1. Delta Overview

Deltas can be defined as a substantial coastal sedimentary deposit including both subaerial and subaquatic portions at the location of rivers or streams debouch into a standing body of water (Reading 2009; Seybold, Andrade & Herrmann 2007). The point that the standing water enters the ocean or lake is the river mouth, and the place where sediments start to form into the delta is called a mouth bar. The Mouth bar is formed when an overload sediment is spread out from the river into a persistent water body creating a sediment plume (Bates 1953). It could have a scope and width of several kilometres and integrate for developing massive delta lobes (Bhattacharya 2006). The deposits of the mouth bar have an intricate structure although they appear to demonstrate a clinoform geometry progradation and upwards vertical profiles (Bhattacharya 2006). The formation of the deltas consists of the deposition of sediments such as sand or mud at the mouth bar (Seybold, Andrade & Herrmann 2007). Conventionally, worldwide deltas have been categorized principally by dominant forces included fluvial discharge, wave regime and tidal range as summarized in treble classifications (Burpee et al. 2015) such as River(Fluvial)-dominated delta, Wave-dominated delta and Tide-dominated delta according to Galloway (1975) classification scheme (in **Figure 2.1**).

River-dominated delta occurs when the river flow and the resultant transportation of the sediments are exceedingly powerful while the marine influences such wave and tide reworking procedures are remarkably minimal (Seybold, Andrade & Herrmann 2007). It is elongated alongside with digitate shorelines because of the progradation into basin ward of their distributaries (Burpee et al. 2015), and this delta type tends to develop huge delta lobes into the ocean, which could slightly contain beyond distributary channels and appear with levees exposed above sea level, for instance, the Nile River Delta, Egypt (Seybold, Andrade & Herrmann 2007). This delta type is also called as the Bird-foot delta since its appearance is more probable equivalent to the natural appearance of a bird's foot, for example, the giant bird's foot delta in Louisiana known as Mississippi River delta, USA (Coleman 1976). Tide-dominated deltas occur in regions with extensive tidal ranges or greater energy of tidal current. A delta of this kind similarly resembles an estuarine bay filled with various stretched islands parallel to the major tidal flow and perpendicular to the shoreline (Seybold, Andrade & Herrmann 2007), for instance, the Lena River Delta, Siberia and the Fly River delta, Papua New Guinea (Burpee et al. 2015). Wave-dominated deltas are characterised by their smooth shorelines and their planform structures of arcuate to cuspate when larger wave effects typically imply more cuspate shape of deltas (Anthony 2015). Wave dominated deltas typically have one or few distributary channels as waves typically rework mouth bar sediments into strand-plains, preventing river bifurcation (Bhattacharya & Giosan 2003). The Paraíba do Sul in Brazil is considered as a

wave-dominated delta exemplified by an extensive sedimentation of its beach ridge. These examples of delta types were reviewed in a previous study by Lane (2016) (as shown in **Figure 2.2**).

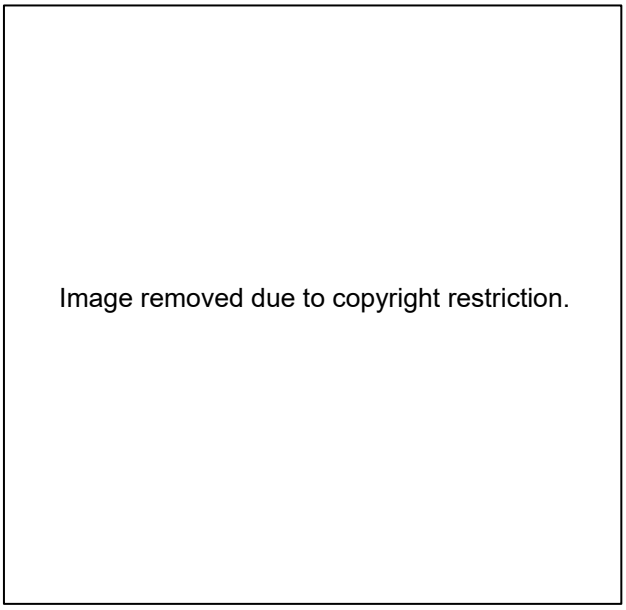

Figure 2.1 Delta types based on Galloway (1975) classification scheme (Seybold, Andrade & Herrmann 2007).

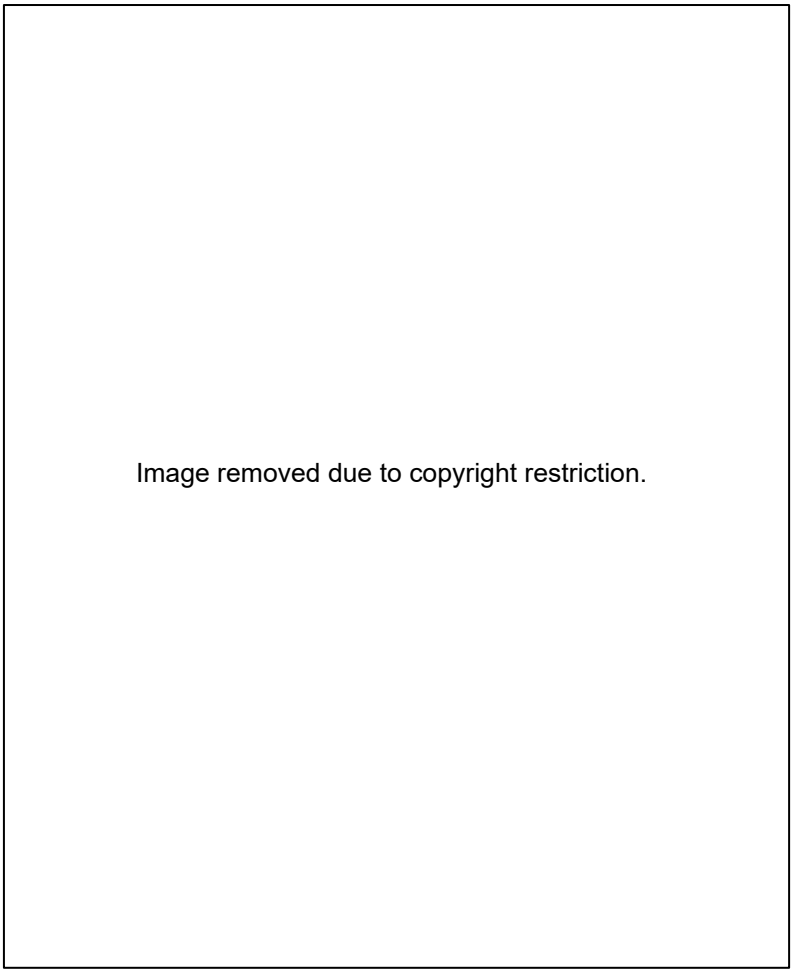

Figure 2.2 Satellite and shuttle photos of various modern deltas (NASA) showing a wide variation in morphology: (A). The Nile River Delta, Egypt; (B). The Mississippi River Delta, USA; (C). The Lena River Delta, Siberia; (D). The Fly River Delta, Papua New Guinea; (E). The Paraíba do Sul, Brazil (Lane 2016).

2.1.2. Morphological Controls of Delta

As mentioned in the **Section 2.1.1**, fluvial, wave, and tide energies are deemed to be responsible for the predominant monitored mechanisms on delta morphology (Ainsworth, Vakarelov & Nanson 2011; Coleman & Wright 1975; Galloway 1975).

All deltas, by definition, inevitably have some level of fluvial influence (Bhattacharya 2006). As a river emerges into a standing body of water, there is an interaction of the river plume with the receiving standing body of water (Wright 1978). The flow from the plume can be hypopycnal that occurs when the sediment plume is less intense than the receiving basin water. This frequently phenomenon occurs in deltas that enter oceans, as freshwater density is less than the density of salt water (Bates 1953). In this situation, sediment becomes disconnected from the bedload and can migrate extensive distances to the offshore (Orton & Reading 1993). Hyperpycnal flow occurs when fluid from a sediment plume is denser than the receiving body of water. They can form during high discharge incidents such as a flood and typically result in a basal coarsening-up unit with a capping of fining up sediment deposited during the waning phases of accumulation. Since they are correlated with high discharge incidents, they generally scour and have erosive contacts. Most of the world's deltas could possibly contain sporadic hyperpycnal sediment plumes (Mulder et al. 2003). At the seaward section of the delta, there is an autogenic procedure of mouth bar accumulation and terminal distributary channel development which affects the morphology of river-dominated delta plains. This mechanism which arises due to the spatial deceleration of the river plume turn into as it leaves the restrained setting of a channel (Wright 1977). The distance between the coastline and the basinward limit of the mouth bar is monitored by the degree of jet momentum flux, so for each sequential bifurcation, as flow is apportioned through distributaries, the jet moment flux declines, and so too does the terminal distributary channel extent (Edmonds & Slingerland 2007).

Waves rework deltaic sediments into a coast-parallel alignment (Coleman & Wright 1975; Galloway 1975). If wave energy relative to fluvial energy is adequate, the mouth bar sediments would eventually be reworked up the shoreline into strand plain deposits (Bhattacharya 2006). Due to this, wave-dominated deltas typically have constrained amounts of distributary channels with numerous waves affected deltas being consume by a single delta. The role of waves in shaping the delta shoreline and in modifying the expansion of large-scale delta have effectively concentrated on the scale to which waves, reaching shorelines of the delta, can generate currents that reallocate fluvial and coastal sediments. The destruction role of waves on the mouth bar evolution could be thoroughly related to longshore current because the latter produces a relocation approach of deposited sediment from river mouths (mouth bar) that could possibly turn out to be choked consequently impacting not only the main channel width but also backwater length (Anthony 2015). Dominguez (1996) illustrates how rivers could play a role as groynes on wave-dominated deltas causing sediment travelling alongshore to be preserved on the updrift side of the delta mouth. This phenomenon leads to asymmetric delta development, which has intense implications for the quality

of reservoirs on the downdrift and updrift sections of the delta as displayed in **Figure2.3** (Bhattacharya & Giosan 2003). Delta asymmetry has been examined on countless modern deltas around the world including the Mitchell River Delta (Nanson et al. 2013).

Tide-affected deltas are altered by bidirectional currents and are characterised by distinctive features such as funnel shaped distributary channels, and elongate mouth bars and extensive tidal flats (Galloway 1975). Wide shelves and embayed environment can have amplifying impacts on tides, and as such, tide-dominated deltas are frequent in these environments (Ainsworth, Vakarelov & Nanson 2011). Tidal currents can eliminate fluvially sourced sediment from mouths of distributary channel (Bhattacharya 2006). Consequently, mouths of tide-dominated distributary channels could be secured for thousands of years (Ta et al., 2005).

While major endmember influences of wave, tide and fluvial systems spontaneously occur, the majority of deltas reveal mixed-process morphologies (Ainsworth, Vakarelov & Nanson 2011). During the evolution of the delta, there could be severe fluctuations in process dominance. In this contemporary period, the alterations in process influence are being noticed within single deltaic mechanisms (Nanson et al. 2013; Vakarelov & Ainsworth 2013).

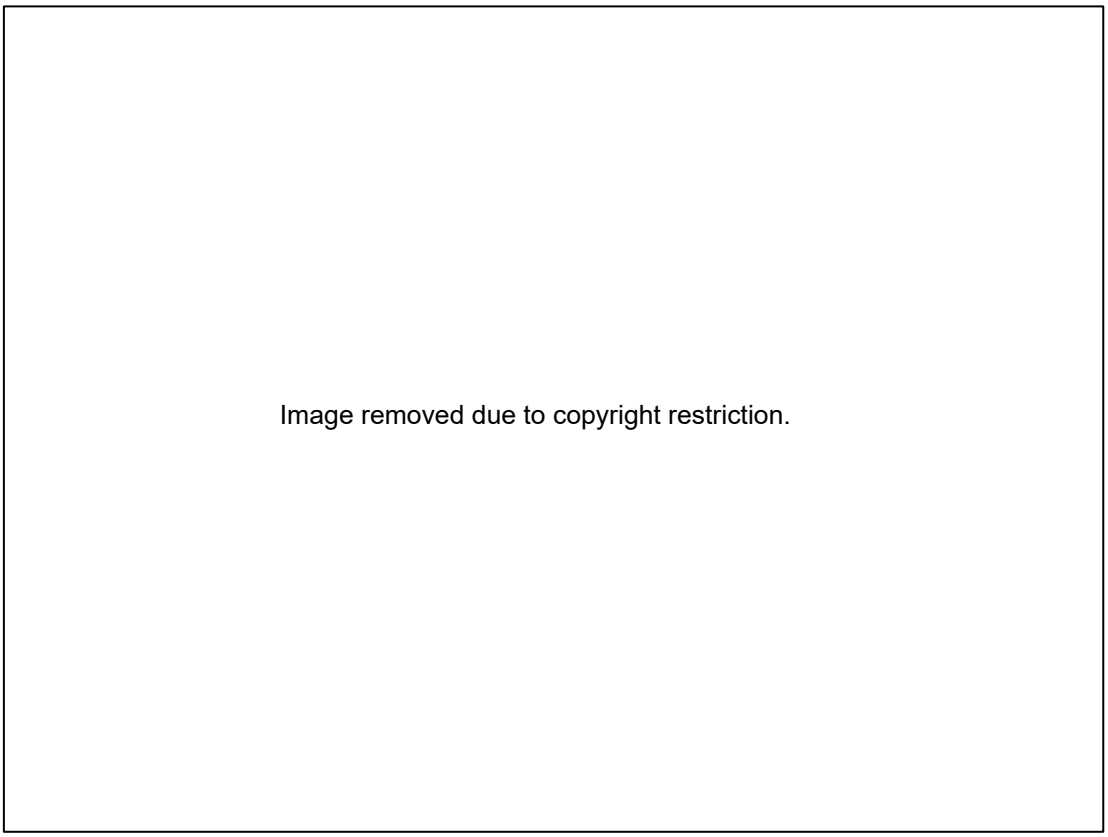

Figure 2.3 A diagram illustrating three dissimilarities of wave dominated deltas. (A) a symmetric delta, net sediment transport from longshore drift is minimal. (B) an asymmetric delta; sediment resulting from longshore drift is confined on the updrift delta as the mouth bar behaves as a groyne. (C) A deflected delta; longshore drift is so intense relative to fluvial flow and the feeder channel is deflected in the direction of the longshore drift (Bhattacharya & Giosan 2003).

2.1.3. Deltaic Depositional Facies

The delta is subdivided into three major depositional zones: (1) delta plain (upper and lower), (2) delta-front and (3) pro-delta (see in **Figure 2.4**), and the resulting deposits display a consistency in texture, structure and associated elements indicating the consequences of those disparate mechanisms (Nichols 2009). The delta plain is typically characterised by distributary channels and non-marine to brackish environments including swamps, tidal flats and lagoons (Bhattacharya 2006). The delta plain could be further separated into the upper delta plain and the lower delta plain. The extent of the upper delta plain would be the backwater limited, which for most deltas is the apex (driven by backwater mediated avulsions). For instance, on the Mitchell River delta, the apex is of the megafan and the upper delta plain is characterised by many avulsions. The lower delta plain is the zone between the shoreline and the upper tidal reach. Posamentier, Jervey and Vail (1988) explained the division of delta plain can be marked by the tidal limit, which also divides the fluvial dominated from the paralic portion of the delta. The delta front can be identified as the steeply sloping section of the delta where deposits slope of delta downward from sea level to the sea floor level. The pro-delta forms the foundation for the delta and has been historically interpreted to be constructed from suspension settling (Galloway & Hobday 2012). The pro-delta is the distal part of the delta characterised by mud deposition. the rapidly deposited fluid mud from hyperpycnal might be contributed to this pro-delta deposition (Bhattacharya & MacEachern 2009).

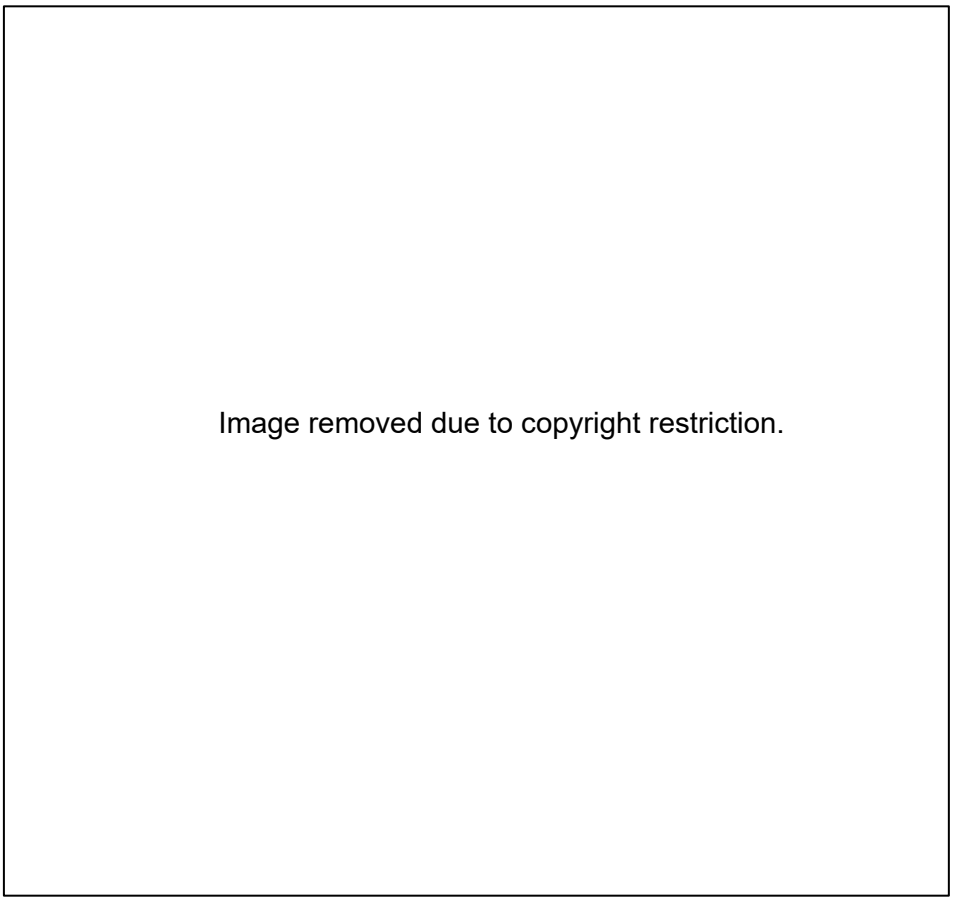

Figure 2.4 Delta subdivision zones (Bhattacharya 2006).

2.2. Review of Mitchell River Delta

2.2.1. Evolution of Mitchell River Delta

The Mitchell River delta is partitioned into three depocentres; as the Main Mitchell depocentre, the Central Mitchell depocentre and the Nassau depocentre. Heap et al. (2001) indicated that the combination of these deltas represents the largest delta in Australia when considering the total mangrove area (more than 112 km^2) and second largest considering to the total main channel length (more than 61 km). The Mitchell River delta morphologies are not only influenced by the interaction between tides, waves and fluvial energies (Ainsworth, Vakarelov & Nanson 2011), but also strongly related with the avulsion history of the megafan evolution throughout the Holocene (Nanson et al. 2013). While end-member examples of fluvial, wave and tide processes naturally occur, the majority of deltas exhibit mixed morphological systems as stated by Ainsworth, Vakarelov and Nanson (2011). During the evolution of delta, the drastic changes in procedure dominance may occur. The alterations in process influence are being noticed inside single deltaic structures (Ainsworth, Vakarelov & Nanson 2011; Nanson et al. 2013). The complexity systems of mixed influences deltas classification are thoroughly demonstrated in the **Figure 2.5**.

According to a study, the Mitchell River delta is categorized as tide dominated with fluvial influenced and wave affected (Massey et al. 2014). However, another research about the revolution of the Mitchell River delta by Nanson et al. (2013), which has later been expanded by Lane et al. (2017), explained that this delta has developed through three geometrically separated pulses of delta progradation such as a symmetrical, wave-dominated, fluvial-influenced, tide-affected (Wft) system at the early Holocene, to a rapidly prograding asymmetrical, tide-dominated, fluvial-influenced, wave-affected (Tfw) system at the mid-Holocene, and lastly to an asymmetrical, tide-dominated, wave-influenced, fluvial-affected (Twf) system at the modern shoreline (see in **Figure 2.6**).

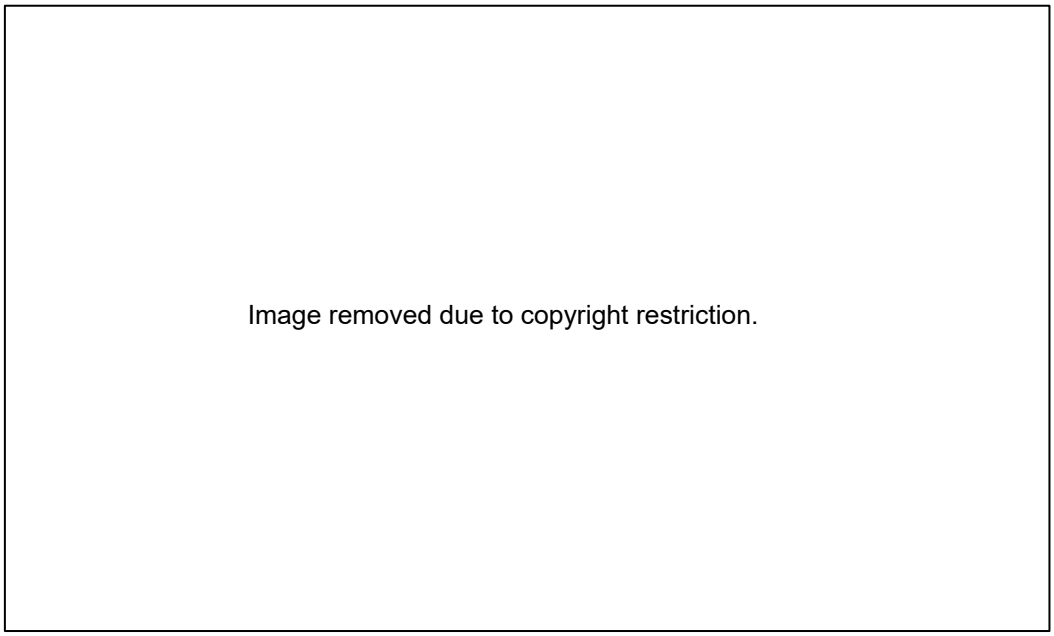

Figure 2.5 Complex delta system classification (Ainsworth, Vakarelov & Nanson 2011).

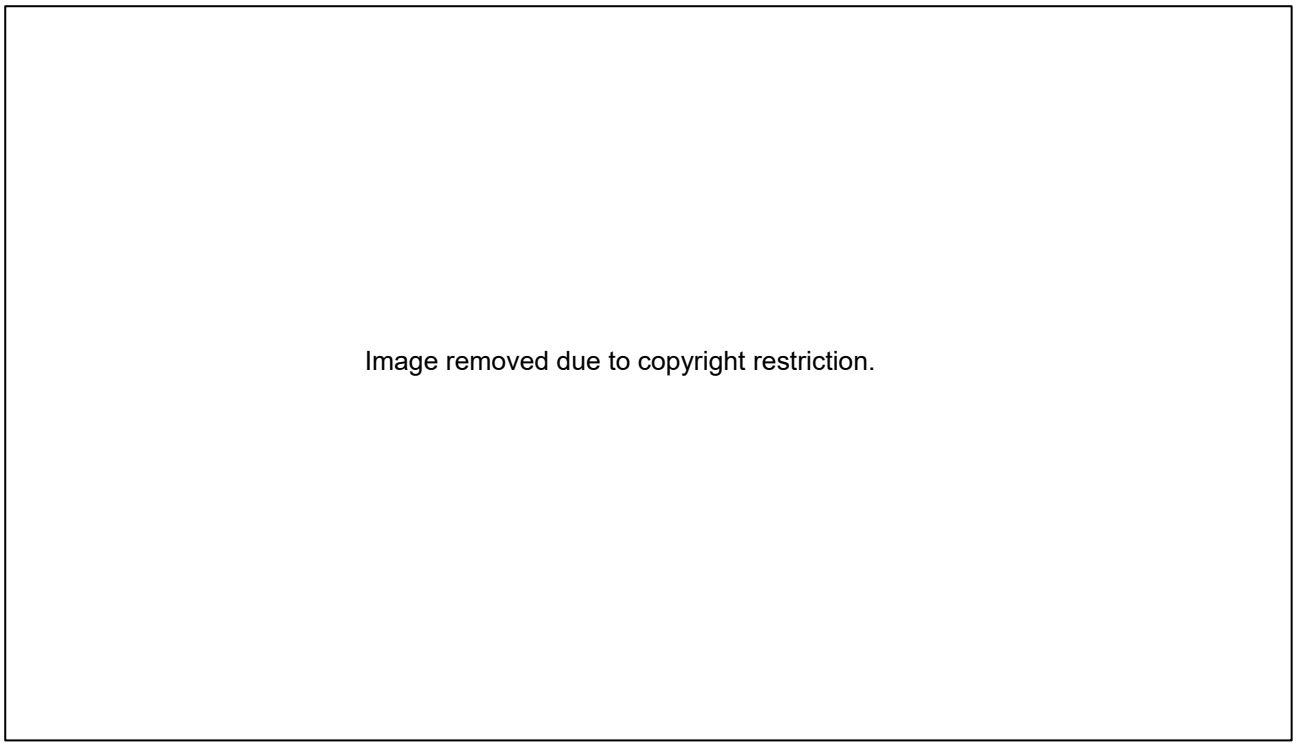

Figure 2.6 The Evolution of the Mitchell River Delta devided into 4 phases (Lane 2016).

Albatross Bay, Weipa, 300 km north of the Mitchell River mouth, is the closest wave height gauge station to the Mitchell River delta. CSIRO Marine and Atmosphere Research modelling experiments indicate a reduction in wave height from a nearest recording station of the Mitchell River delta, stationed in Albatross Bay, Weipa approximately 300 kilometres north of the Mitchell River mouth, to the shoreline of this delta. The record from December to March, during the rainy season, reveals that the average wave height is 0.5 metre whereas it decreases to 0.35 metre during the dry season from April to November (Mouhoupt et al. 2004). In addition, the wave height could raise up to 3.5 metres in the wet season due to the frequency phenomena of storms and cyclones (Mouhoupt et al. 2004).

Tides are periodically diurnal in the Southeast GoC while a semi-diurnal frequency is noticeable during neap tides (Munro 1984). According to the tidal range recorded at Karumba, the nearest recording station located approximately 250 kilometres south of the Mitchell River delta, it indicates that the tidal range could be 0.3 metres as low and 4 metres as high during the neap tide and spring tides, respectively. The average spring tidal range could be 3.3 metres, but it could technically raise to above the mean spring range during rainy season and decline to below the mean spring range during dry season due to seasonal amplitude variations of spring tide (Munro 1984). In the south-east part of the GoC, the wind generated during the wet season by a summer monsoon increases the sea level to about 0.5 metres (Wolanski 1993), this occurrence causes the inundation of the enormous coastal plain described by supratidal mud flats (Ridd, Sandstrom & Wolanski 1988). Mainly throughout the year in GoC, a weak anticlockwise circulation form occurs with the association to the south-easterly trade winds monitoring months of the dry season (Forbes & Church 1983;

Wolanski 1993). However, the cyclone stimulated currents during the wet season generate a water circulation in clockwise direction at the GoC that has a stronger influence on sediment redistribution (Preda & Cox 2005).

Catchment flow data is constrained on the Mitchell River. The data discovered by Rustomji (2010) is constrained as numerous stations are positioned on either river terraces or bed rock valleys and not illustrative of the current flow system to model consistent bank full discharges. Flood flows with a recurrence interval (or repeat interval) between 2 to 4 years separation into distributary channels, and the flow inside the main channel does not affect downstream increases (Rustomji 2010). Mitchell River discharge is extremely seasonal, and the summer monsoon from December until March correlates to excessive fluvial activity. In this contemporary period, the Mitchell River delta has been prograding into GoC for approximately 17 km (Nanson et al. 2013).

2.2.2. Previous Studies about Mitchell River Delta

There are limited number of previous studies about the Mitchell River delta in the Gulf of Carpentaria. A research applied remote sensing technics by using Landsat satellite imagery to identify approximately 130 km^2 area of the active alluvial gullies within the Mitchell megafan and to determine the estimation of minimum river channel bed turnover (Brooks et al. 2008). By evaluating the spatial patterns of various erosion procedures within the megafan and utilizing the fan evolutionary framework to provide the awareness into the erosion mechanisms, this study initially concentrates on two main erosion factors included alluvial gully erosion and channel erosion (Brooks et al. 2008). Another study of the Mitchell River delta is to classify the diverse phases of the mixed-process delta evolution in term of procedure and architecture and to restructure the paleogeographic evolution of the Mitchell River delta by considering the distribution of depositional elements and published records of allogenic forcing mechanisms (Nanson et al. 2013). A similar study on the evolution and architecture of the Mitchell River Delta by Lane et al. (2017) is to connect the palaeogeographical evolution of the Holocene Mitchell River megafan and delta to autogenic and allogenic controls and to characterise the channel belt style and distribution across the Mitchell River megafan and delta using detailed mapping, vibracoring, trenching and topographic surveying. Massey et al. (2014) applied satellite imagery, field measurements data and analogues to construct 3D geocellular facies model of a modern mixed-influence delta system, the Mitchell River Delta and generate detailed mapping to identify 16 different facies elements and classify the delta. This 3D model, utilized both static and dynamic metrics to examine various techniques and degrees of basin model detail, was exposed to differing upscaling degrees of the horizontal and vertical dimensions and allowed assessment of volume and connectivity adjustments (Massey et al. 2014).

2.3. Remote Sensing Perspective in Detecting Turbidity

Water remote sensing was initially reported about its employment to monitor ocean colouring since the 1960s and has been an increasing appeal to similarly operate this remote sensing technique for inland water quality (Potes et al. 2018). During the last three decades, numerous investigations have targeted on monitoring water quality parameters not only in coastal waters but also in inland using satellite imagery (Sebastiá-Frasquet et al. 2019). The satellite sensors of ocean colouring are effective instruments to investigate and monitor the dynamic variables discharged by streams and rivers into the coastal water such as suspended particulate matter (SPM) (Ody et al. 2016).

According to a literature, testing the spectral reflectance of SPM concentrations and the capability of each sensor (in terms of spectral, spatial and temporal resolutions) to monitor the changing aspects of SPM in such estuaries and river plume are considerably substantial. Therefore, major components that should be considered and reviewed for water remote sensing perspective included the evaluation of remote sensing technique and traditional field measurement (in-situ method), the relationship of remote sensing with suspended sediments and turbidity, suitable satellite sensors and their products employed, sensitive wavelengths and bands selections from previous literatures are thoroughly demonstrated in sequence sections below.

2.3.1. Remote Sensing Perspective vs In-Situ Method

Satellite remote sensing compliments in-situ data specimen and laboratorial examination of water quality variables that is laborious and expensive with temporally and spatially inadequate. Unless a water reservoir is sufficiently observed with in-situ devices, remote sensing is the only approach to remotely monitor the quality of coastal and inland waters and be able to provide the initial warning systems for the water quality environment (Gholizadeh, Melesse & Reddi 2016). However, there are some difficulties for the satellite remote sensing implementation in water monitoring due to inadequate product accuracy, inexact data continuity and lack of programmatic provision included both software and training (Soomets et al. 2020). Despite the consequences of these technical dilemmas, remote sensing, an efficient technique for monitoring water quality, has shown to be advantageous in both spatial and temporal extends compared with in-situ procedures (Dörnhöfer & Oppelt 2016; Ogashawara, Mishra & Gitelson 2017). According to a study by Soomets et al. (2020), utilising remote sensing data in ocean monitoring has benefits in both spatial and temporal coverage over traditional time consuming and expensive in-situ procedures.

2.3.2. The Relationship of Satellite Spectral Reflectance with SSC and Turbidity

A variety of studies in the last decade focus on the approximation of turbidity, chlorophyll and coloured dissolved organic matter (CDOM) concentration (Chander et al. 2019; Gholizadeh, Melesse & Reddi 2016; Lim & Choi 2015; Luis et al. 2019). Turbidity is a significant optical component of water where suspended sediments disperse the light rather than transmit it in the column of water (Sebastiá-Frasquet et al. 2019). The turbidity increases with an enhancement in the suspended

solids or sediments concentrations in water (Garg et al. 2017), and it improves the water opacity obstructing the aquatic life (Güttler, Niculescu & Gohin 2013; Quang et al. 2017; Sebastiá-Frasquet et al. 2019). Since the turbidity and suspended sediment concentration (SSC) are considered to be intimately related (Garg, Aggarwal & Chauhan 2020; Sebastiá-Frasquet et al. 2019), these two parameters of water quality are commonly considered analogous or equivalent in the perspective of remote sensing field (Ritchie, Zimba & Everitt 2003). In a recent study, for example, the term of turbidity has been treated as a proxy for SSC in the in detection and investigation of plume geometry (Garg, Aggarwal & Chauhan 2020).

Amongst all the parameters of water quality, suspended sediments are the most problematic in both coastal and inland waters including rivers, lakes, and estuaries (Garg, Aggarwal & Chauhan 2020). For a detailed explanation of the relationships between the surface SSC, surface reflectance, plume geometry, and water discharge are extremely intense, the reader is referred to Schild et al. (2017). Conventionally, these sediments concentrations are visually measured or through gravimetric or laboratory assessment (Garg, Aggarwal & Chauhan 2020; Pavelsky & Smith 2009). Currently, sediment concentration is measured optically through Secchi disk depth or directly, using the light turbidimeters in the field (Pavelsky & Smith 2009; Quang et al. 2017). Measurements derived from field and laboratory studies measurements are constrained to the spot location and time, despite the fact that the total suspended particles concentration differs both spatially and temporally (Garg et al. 2017; Gholizadeh, Melesse & Reddi 2016).Moreover, the traditional field measurements are be both labour-intensive and time-consuming for water quality investigation, and for estimating the sediment plume concentration although they could provide more precise results (Garg, Aggarwal & Chauhan 2020; Pavelsky & Smith 2009; Quang et al. 2017). Therefore, SSC and turbidity measurements via remote sensing methods provides a cost-effective way to obtain data that is extensive both in space and time.

Various proposals about satellite remote sensing investigations have been made using a variety of sensors over numerous coastal and inland reservoirs worldwide based on the spectral reflectance (Gholizadeh, Melesse & Reddi 2016). The application of remote sensing to water bodies relies on the diverse natural water colours that correspond to their unique spectral reflectance due to the varying constituents of the water (Potes et al. 2018). Depending on their spectral response, these characteristics are recognized in satellite imagery, and the variations in the feature's spectral properties will be caused even by a minor change in their composition (Garg, Aggarwal & Chauhan 2020). As a result, many factors could impact the spectral reflectance in the water column such as seasonal changes, the concentration of atmospheric components, turbidity, suspended substance, sun-elevation angle, roughness of the water, emergent or submerged vegetation and water depth (Garg, Aggarwal & Chauhan 2020; Moore 1980). The amount of light reflecting off the surface water (water surface reflectance) of a sediment plume is a function of the sediment concentration, shape, size and type of materials consisting of not only minerals but also biological elements (Schild et al.

2017). It is additionally declared in the literature that there is a possible temporal deviation in turbidity intensity due to variability in weather, climate pattern and human anthropogenic along the banks (Garg, Aggarwal & Chauhan 2020; Luis et al. 2019). This composition of water is being detected and mapped utilising remote sensing data as it offers synoptical earth coverage at a conventional temporal time realm whilst it also has been done by examining how SSC transformation modifies the visual the water column composition (Garg, Aggarwal & Chauhan 2020). Other literature has shown that the spectral reflectance alterations in visible spectrum regions are substantial due to the variation in turbidity of the water (Brezonik, Menken & Bauer 2005; Garg, Aggarwal & Chauhan 2020; Liedtke, Roberts & Luternauer 1995).

2.3.3. Various Satellite Sensors for Turbidity

Choosing a proper satellite sensor in turbidity detection is extremely significant. This selection is mainly based on the spatial, spectral and temporal resolutions of the satellite sensor. Ody et al. (2016) stated that the limits and capabilities in terms of spatial, spectral and temporal resolutions of satellite sensors are suggested to be major consideration in monitoring the SPM dynamics. Although the turbidity is the major detecting aspect, different satellite sensors are required in various research circumstances relative to the research budget, spatial extend, temporal scale and the availability of effective spectral bands. Among currently available satellite-borne sensors, a variety of recommended sensors from previous turbidity monitoring studies are SEVIRI (Spinning Enhanced Visible and Infrared Imager) onboard the Meteosat Second Generation (MSG-3) geostationary platforms (Ody et al. 2016), the ocean colour sensor MODIS (Moderate Resolution Imaging Spectroradiometer) on board the polar-orbiting Aqua and Terra satellites, (Sebastiá-Frasquet et al. 2019), the MERIS sensor onboard ENVISAT satellite (Potes et al. 2018), the Operational Land Imager (OLI) on the polar-orbiting Landsat 8 satellite (compared with Landsat 7) (Ody et al. 2016; Sebastiá-Frasquet et al. 2019), the SPOT 6 and 7 (Satellite Pour l'Observation de la Terre) (Ody et al. 2016) and finally the Multispectral Instrument (MSI) on Sentinel 2 (compared with the Ocean and Land Colour Instrument (OLCI) on Sentinel 3) (Garg, Aggarwal & Chauhan 2020; Renosh et al. 2020; Soomets et al. 2020). These satellite sensors are briefly demonstrated in the **table 2.1**.

Table 2.1: Summary table of commonly applied satellites with their sensors, spatial and temporal resoultions for turbidity investigation.

Satellites	Sensors	Spatial Resolution	Temporal Resolution
MGS-3	SEVIRI	3000 m	15 mn
Aqua & Terra	MODIS	250 m	Daily
ENVISAT	MERIS	300 m	3 days
Landsat 8	OLI	30 m	16 Days
Landsat 7	ETM+	30 m	16 Days
SPOT 6/7	NAOMI	6 m	Daily
Sentinel 2	MSI	10m	5 Days
Sentinel 3	OLCI	300 m	27 Days

One of most recommended sensors for turbidity monitoring is SEVIRI, on board MSG-3. The SEVIRI is a meteorological sensor orbiting on the geostationary platform MSG-3 that delivers information at an immensely high temporal resolution with an image captured every 15 minutes yet extremely low spatial resolution of 3 km (Ody et al. 2016). It is reported that two spectral bands out of 12 available bands can be implemented for SPM retrieval where the VIS0.6 spectral band (635 nm) for detecting SPM and the VIS0.8 spectral band (810 nm) for atmospheric corrections in sensing turbidity purpose (Neukermans et al. 2009; Ody et al. 2016). Due to its temporal and spatial resolutions conditions, this type of satellite sensor is inappropriate for small spatial scale but preferable for detecting the high frequency changes in turbidity.

Because of various distinct research purposes, MODIS is considered to be a good candidate for studies where high temporal and medium spatial resolutions are required. MODIS is the ocean colouring sensor onboard the polar-orbiting Aqua (MODIS-A) and Terra (MODIS-T) satellite platforms. Both MODIS-A and MODIS-T sensors deliver a daily temporal resolution, which provide one image captured globally every day. In the term of spatial resolution, it is informed that MODIS sensors carry out 36 spectral bands with different three spatial resolutions of 250 m, 500 m and 1 km (Ody et al. 2016).

Additionally, MERIS sensor on board ENVISAT satellite is another satellite sensor providing similar spatial and temporal resolutions to the MODIS sensors for monitoring the turbidity. This satellite sensor presents a maximum spatial resolution of 300 m with 3 days of revisit time as its temporal resolution (Potes et al. 2018). A study over Portuguese reservoirs was proposed by Potes, Costa and Salgado (2012) utilising the semi-empirical bio-optical models to approximate chlorophyll concentrations and cyanobacteria in 2011 as well as turbidity in 2012 over Alqueva with images from MERIS sensor onboard ENVISAT satellite. Although these two sensors are believed to be a decent compromise of their revisit time (about 1 to 3 days revisit depending on cloud cover), high temporal resolution sensors (MODIS and MERIS) have an inadequate spatial resolution (typically varying from 250 to 3000 m) (Sebastiá-Frasquet et al. 2019).

To resolve this inadequate spatial resolution, an openly satellite series known as Landsat series, in particularly Landsat 8, is considered. The series of Landsat high spatial resolution sensors have proved their competence in detecting SSC in highly turbid waters (Ody et al. 2016; Vanhellemont & Ruddick 2014, 2015). However, OLI sensor on the Landsat-8 polar-orbiting satellite has an advantage over its senior satellite platform, the Landsat 7 carrying the Enhanced Thematic Mapper Plus (ETM+) sensor which is the improved version of the Thematic Mapper instruments onboard Landsat 4 and Landsat 5, due to the product delivery with data gaps caused by the Scan Line Corrector (SLC) failure of Landsat 7. Beside the technical issue of SLC failure in Landsat 7, the Landsat 8 OLI has additionally enhanced its calibration, signal to noise qualities, greater 12-bit radiometric resolution and narrower spectrally wavebands if comparing to the Landsat 7 (Roy et al. 2016). The OLI sensor on Landsat 8 offers products with a spatial resolution of 30 m in 9 spectral bands in the visible, NIR and

shortwave-infrared (SWIR) wavelength regions and a temporal resolution of 16 days (Ody et al. 2016).

According to literature, higher spatial resolution sensors of Landsat series (30 m) were still not good enough for mapping the extremely dynamic turbid waters in coastal regions due to their low temporal resolution (16 days) (Dona et al. 2015; Gernez et al. 2015; Sebastiá-Frasquet et al. 2019). A variety of studies has revealed the capabilities in offering valuable information of SPOT 6 and SPOT 7 satellite sensors in sensing SSC in the extremely dynamic turbid waters (Vanhellemont & Ruddick 2014, 2015). The ocean colouring sensors of SPOT 6/7 (Satellite Pour l'Observation de la Terre) onboard geostationary satellite platforms contain not only a high spatial resolution of 6 m but also a high temporal resolution of a daily images captured with four multi-spectral bands included blue (450 to 525 nm), green (530 to 590 nm), red (625 to 695 nm) and NIR (760 to 890 nm) (Ody et al. 2016; Vanhellemont, Neukermans & Ruddick 2014). However, the expensive charge of SPOT 6/7 products could be a challenge for low budget studies since these satellite products are not publicly; it is recommended in mapping turbidity if the research's budget is not a concern because of its high spatial and temporal resolution.

The innovative capabilities of recent ocean colouring satellite sensors have been mentioned by various studies in representing an efficient way to complement the dilemma in low research's budget with ideal consideration in the term of spatial and temporal resolution for monitoring the transported SPM through river mouths, in river plumes and estuaries (Gholizadeh, Melesse & Reddi 2016; Potes et al. 2018). Since the combination of high temporal and high spatial resolution sensors could technically provide optimal RS observations of surface SPM dynamics in coastal waters, the next generation of ocean colouring sensors such as Multi-Spectral Instrument (MSI) and Ocean and Land Colour Instrument (OLCI) sensors respectively onboard the Sentinel 2 and Sentinel 3 polar-orbit platforms are employed in various turbidity detection studies (Ody et al. 2016). The Copernicus Sentinel 2 mission of the European Space Agency (ESA) consists of a constellation of two polar-orbiting satellites, Sentinel 2A launched in June 2015 and Sentinel 2B launched in March 2017 in order to bring a remarkable potential to investigate both land observation and inland reservoirs (Potes et al. 2018). This mission integrates both high spatial (10 to 60 m) and high temporal resolution (5 days) with 13 spectral bands where four high spatial resolution bands (10 m) such blue (490), green (560), red (665) and NIR (842 nm) are essential to monitor turbid waters (Caballero, Navarro & Ruiz 2018; Gernez et al. 2015; Sebastiá-Frasquet et al. 2019). In contrast, Sentinel 3 contains a medium spatial resolution of 300 m with high temporal resolution of 27 days onboard for marine and land investigation while its sensor, OLCI, was intentionally constructed with well-placed spectral bands for specifically water monitoring purpose (Sebastiá-Frasquet et al. 2019). For instance, a recent study revealed the comparable result from evaluating the performance of Sentinel 2 MSI and Sentinel 3 OLCI sensors with the assistant of state-of-the-art atmospheric correction algorithms to observe from moderately to highly turbid estuarine waters in the Gironde Estuary,

France (Renosh et al. 2020). Soomets et al. (2020) explained that these two ESA satellite sensors are appropriate for turbidity studies, yet the bias of SPM ingredients in the turbid water is addressed where Sentinel 2 MSI sensor performance is greater for sensing SSC in smaller extend of turbid water areas whereas Sentinel 3 OLCI could perform better in sensing turbidity focusing Chlorophyll a (Chl-a) (Soomets et al. 2020). Another literature explained that the capability of Sentinel 2 MSI sensor has advantages over Sentinel 3 OLCI sensor because of the spatial and temporal resolution perspective (Ody et al., 2016). Hence, this MSI sensor is strongly believed to be a proper sensor in investigating turbidity in the term of high spatial and high temporal resolution for low budget studies.

2.3.4. Sensitive Wavelength Regions (Bands) for Turbidity

Defining turbidity in shallow waters necessitates the implementation of sensitive spectral bands to turbidity and contain an inadequate depth penetration to prevent an extensive involvement from the bottom (Caballero, Stumpf & Meredith 2019; Sebastiá-Frasquet et al. 2019). The sensitive spectral band to turbidity could be defined from just a single band to multiple bands combination of two bands or three bands. Literature indicates that even a single band, if properly selected, can offer a vigorous approximation of turbidity (Garg, Aggarwal & Chauhan 2020; Gholizadeh, Melesse & Reddi 2016; Pavelsky & Smith 2009).

2.3.4.1. Single Red Band

It is believed that a single red wavelength has been utilised to approximate the water turbidity (Garg, Aggarwal & Chauhan 2020; Shi & Wang 2009) since the reflectance in visible region, in particularly red wavelength region, increases with enhancement of turbidity or sediments in the water column (Doxaran et al. 2002; Garg, Aggarwal & Chauhan 2020; Garg et al. 2017; Gholizadeh, Melesse & Reddi 2016; Moore 1980; Pavelsky & Smith 2009). Early studies were successfully applied red band (620 – 670 nm) with spatial resolution of 250m from MODIS (Moderate Resolution Imaging Spectroradiometer) sensor to determine SSC even in the less turbidity region (Chu, V et al. 2012; Chu, VW et al. 2009; Schild et al. 2017). Another study revealed the successful in calculating SSC using the red spectral band not only from the MODIS sensors (both AQUA & TERRA) but also from further 2 sensors included of Landsat 8 OLI (Operational Land Imager) sensor and Spinning Enhanced Visible and Infrared Imager (SEVIRI) sensors (Ody et al. 2016). However, as turbidity improves and sediment concentration values achieve more than 80 mg/L, the surface reflectance overwhelms (Chu, VW et al. 2009) and decreases the correctness of defining SSC (Schild et al. 2017).

2.3.4.2. Single NIR Band

Another single sensitive band that is likewise reported to equally respond to turbidity yet less impacted by the bottom reflectance in the shallow water is the NIR wavelength region (Garg, Aggarwal & Chauhan 2020; Sebastiá-Frasquet et al. 2019). According to Caballero, Stumpf and Meredith (2019), the NIR band, 704 nm wavelength, provides the essential reflectance of light to the

satellite sensor at depths between 1 and 2 metres. Nevertheless, the sensitivity to suspended particles is lost in incredibly turbid and shallow waters at longer wavelengths (Sebastiá-Frasquet et al. 2019). A study by Doxaran et al. (2002) demonstrated the reflectance of NIR wavelength region in between 700 and 900 nm range was almost zero for SSC values less than 50 mg/L yet improved as SSC increased (Schild et al. 2017). Consequently, it is believed that the application of the NIR wavelength region is highly applicable in extremely turbid waters with supreme concentrations of sediment (Schild et al. 2017). It is additionally reported in another literature that the atmospheric correction for most satellite imagery is necessitated for not only near-infrared (NIR) wavelength region but also all visible bands in order to achieve a precise outcome (Ody et al. 2016).

2.3.4.3. Red and NIR Bands Combination

Although a single band algorithm is proven to be a sensitive and appropriate in estimating turbidity, it is reported in another literature that depending on a single band algorithm occasionally can result in overestimation or underestimation of SSC (Garg, Aggarwal & Chauhan 2020; Kuhn et al. 2019; Pahlevan et al. 2019). Consequently, implementing bands combination of either two or three sensitive bands algorithms is suggested to achieve improved results (Garg, Aggarwal & Chauhan 2020).

The integration of red and NIR spectral bands in various Satellite-borne sensors primarily constructed for land and/or meteorological purposes is believed to be employed for monitoring SPM in coastal waters (Ody et al. 2016) while a variety of research has strongly agreed about the implementation of red and NIR collaboration could highly deliver a superior turbidity estimation (Doxaran et al. 2002; Toming et al. 2016). Garg, Aggarwal and Chauhan (2020) also explained that the reflectance of these two bands could individually offer a clearly respond to the SSC resulting in providing an improved result if integrated, the reflectance will boost with increment in turbidity. Moreover, Water absorption promptly improves from red (645 – 700 nm wavelength) to red edge NIR (700 – 780 nm wavelength) Vanhellemont and Ruddick (2016) since this absorption constraints the light received from the bottom while it reflects light scattered by suspended particles (Sebastiá-Frasquet et al. 2019). Because of that, these bands combination provides an excellent stability between turbidity detection and bottom detection (Lee 2006). It is additionally confirmed by Numerous studies that these two spectral bands are applicable for successfully monitoring turbidity or suspended particles in optically dynamic zones (Caballero, Stumpf & Meredith 2019; Lee 2006; Toming et al. 2016).

2.3.4.4. Green and Red Bands Combination (NDTI)

Garg, Aggarwal and Chauhan (2020) reported the beneficial influence of sensitive green and red bands combination in detecting the turbid water while it is noticed by a recent deltaic study by Gholizadeh, Melesse and Reddi (2016) that the peak reflectance of in the turbid water zones highly shifts from the wavelength region of green to the red spectrum. Moreover, applying the NDTI

algorithm developed by Lacaux et al. (2007) into these sensitive bands' combination could potentially generate the maximum enhanced outcomes of turbidity concentration with the comprehensive information for approximating temporal turbid waters (Garg, Aggarwal & Chauhan 2020). For instance, a recent study reported the satisfactory result of the application of green and red bands' combination in Sentinel 2 satellite imagery to calculate NDTI compared to the reflectance value of individual visible and NIR bands for investigating the turbidity occurring in the Haihe River Basin (Chen et al. 2021). It is similarly confirmed by another study by Garg et al. (2017) that the NDTI's results from band ratioing procedure (will be thoroughly explained in the Pixel-Based Methods section below) in mapping turbidity is exceptionally positive and recommended as evaluated to single band algorithm. However, these sensitive bands' integration approach typically delivers qualitative rather than quantitative approximations of turbidity (Garg et al. 2017). It is reported in a recent study that this NDTI technique with green and red bands retrieved from Sentinel 2 product was implemented to represent qualitative terms of detected turbidity results in various stretches along the Ganga River since the field measurement data could not be collected due to the lockdown period of COVID-19 (Garg, Aggarwal & Chauhan 2020). Therefore, the NDTI of band ratioing algorithm using the combination of sensitive green and red bands is generally suggested for retrieving the turbidity concentration from spectral reflectance of multispectral satellite imagery in order to preferably obtain qualitative terms of detected turbidity results (Garg et al. 2017).

2.3.4.5. Red, Green and NIR Bands Combination

Another literature mentioned the integration of three spectral bands for turbidity reflectance. The wavelength regions of 560nm (green), 655 to 665 nm (red) and 865 (NIR) has been reported to be a powerful combination to sense the SPM concentrations varying from 1 to 2000 mg/L in clear water to highly turbidity (Renosh et al. 2020). Ody et al. (2016) similarly implemented the combination of green (560 nm), red (655 nm) and NIR (864 nm) spectral bands in detecting SPM concentrations with additionally atmospheric corrections using two spectral bands of SWIR bands (1601 nm and 2380 nm) to enhance the inversion of spectral reflectance into SPM concentration. Following to this approach, another study utilised this collaboration technique of green, red and NIR bands at 555 nm, 645 nm and 859 nm respectively in measuring SPM retrieval while applying the atmospheric correction algorithm using two SWIR bands at 1240 nm and 2130 nm provided by MODIS-A and MODIS-T sensors (Wang & Shi 2007).

2.3.4.6. All Visible Bands (RGB and NIR)

It has been declared that the SSC or turbidity has a great display in the visible wavelength region from blue to NIR (Caballero, Stumpf & Meredith 2019; Garg, Aggarwal & Chauhan 2020; Sebastiá-Frasquet et al. 2019; Toming et al. 2016), and various studies employed all bands of the whole visible wavelength region for investigating turbidity estimation either independently or in integration (Sebastiá-Frasquet et al. 2019). For example, a recent study in India utilised the visible bands

through blue to NIR to analyse the spectral reflectance variations linking to the alteration of turbidity concentrations (Garg, Aggarwal & Chauhan 2020). By employing the density slicing method to slice or classify the reflectance of water pixel over each visible bands, Garg, Aggarwal and Chauhan (2020) explained that the increase of reflectance in visible wavelength regions represents the SSC enhancement leading to the assumption that high reflectance of pixels in all visible bands are considered as high turbid water regions whereas low turbid areas are represented in low reflectance. Another study by Potes et al. (2018) argued that the major purpose of RS measurements utilising principally wavelength in visible and NIR bands is to improve bio-optical models that focus to correlate radiometric (optical) and biological quantities. They additionally signified that the implementation of visible and NIR bands could sense the optically dynamic turbid area containing organic matters, but the uncertainties in the RS retrievals of turbidity were addressed depending on the existence of various ingredients interacted in the turbid water column (Ogashawara, Mishra & Gitelson 2017; Toming et al. 2016).

2.4. GIS Applications in Mapping Delta Geometry

A variety of classification methods integrating with satellite remote sensing technique have been implemented for deltaic research such as land and water line extraction, mouth bar identification and sediment plume detection. Munasinghe, Cohen and Gadiraju (2021) critically reviewed literature on employed classification approaches with satellite imagery in detecting deltaic features and investigating the variations of delta morphology over decades from 146 articles/books. According to this literature, 18 classification methods were identified and categorised into 3 major classes (as shown in the **Figure2.7**); (1) one-step change detection including image differencing and change vector analysis (CVA), (2) two-step change detection including pixel-based approaches (manual digitization, density slicing, unsupervised classification, supervised classification, image segmentation and edge detection, band ratioing, object-based image analysis, transformation method, decision trees and random forest classifier, artificial neural network, Bayesian network, and support vector machines) and sub-pixel-based approaches (Fuzzy logic, spectral mixture analysis, and sub-pixel analysis), and (3) ensemble classifications.

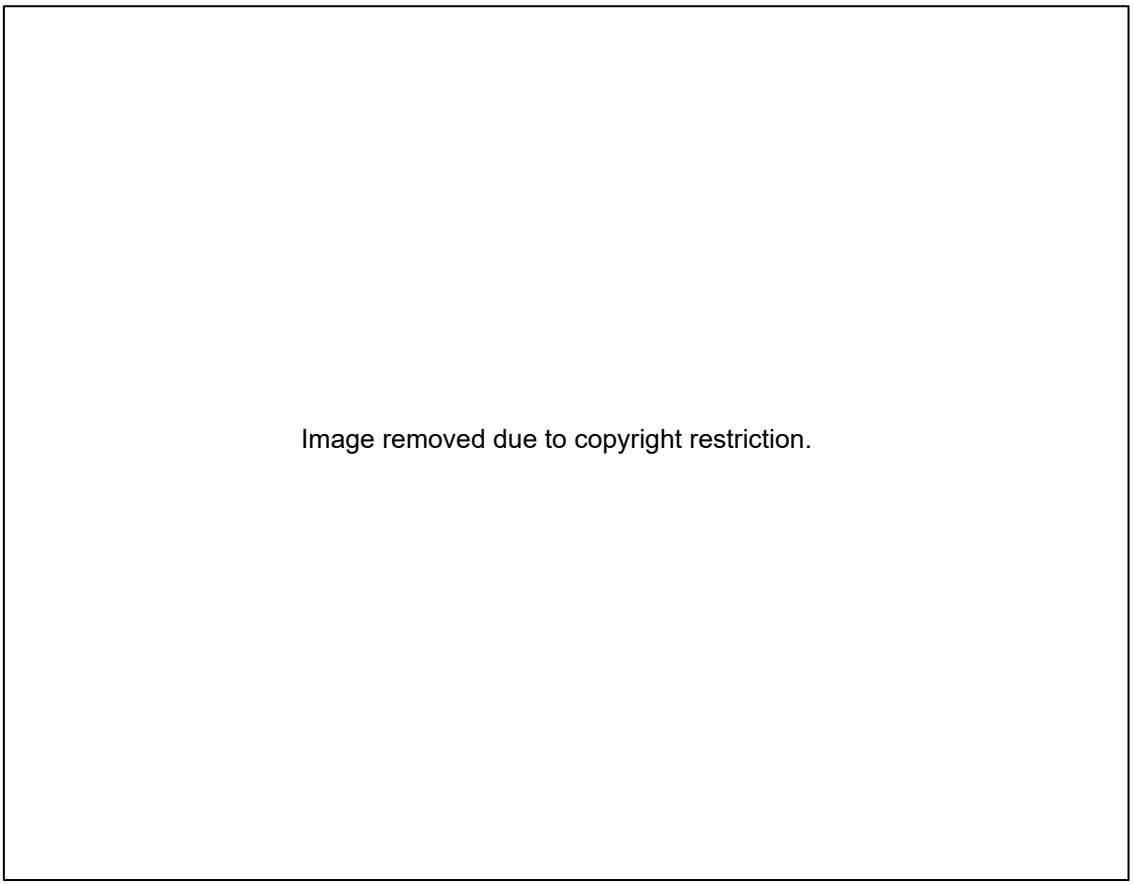

Figure 2.7 Classification of GIS techniques that have been implemented in detecting variation of delta morphology (Munasinghe, Cohen & Gadiraju 2021)

One-step change detection is the application of GIS and RS techniques on multidate satellite imagery to notice a variation in one step such as the technique of layer arithmetic utilising of band mathematics on the reflectance values to differentiate between multidate imagery and the change vector analysis applying of the radiometric properties of multidate imagery to generate both magnitude and orientation of alteration. On the other hand, two-step change detection is the implementation of GIS and RS techniques to define morphology for a specific time step by using the identical or distinct set of approaches to retrieve morphology at a diverse time step for comparing; the ensemble classification is the approach of integrating multiple classification methods (Munasinghe, Cohen & Gadiraju 2021).

This study is intentionally to review only the two-step change detection methods since this research aims to delineate the delta morphology in a specific time and later compare leading the one-step change detection become not suitable. Both pixel-based and sub-pixel-based methods in two-step change detections will be reviewed, but not all their techniques will be included. For sub-pixel-based method, the Fuzzy logic technique will not be explained since this classification method is a probability-based classification that could cause various uncertainties during classification resulting to inaccuracy rather than a hard classification (Xiao-ge 2002). For pixel-based method, unsupervised classification, supervised classification, object-based image analysis (OBIA), transformation method, and machine learning algorithms such as decision trees and random forest classifier, artificial neural

networks (ANNs), Bayesian networks (BNs), and support vector machine (SVM) will be excluded since they are considered inefficient in detecting and mapping deltaic morphological environment. The unsupervised and supervised classification methods are believed to be ineffective methods due to the inaccuracy results (Enderle & Weih Jr 2005; Khatami, Mountrakis & Stehman 2016; Shalaby & Tateishi 2007) whilst the OBIA technique is not suggested for huge boundary or area detection, in this case of turbidity, but recommended for detecting specific objects or feature based on their shapes in grouping adjacent pixels into classes, according to Kamal and Phinn (2011); Yoshino et al. (2014). Moreover, the dynamic in detecting deltaic boundary and turbidity could extremely be a challenge for the machine learning algorithms due to their technical issues such as overfitting, misidentifying turbid waters resulting in seriously inaccurate outcomes and requiring a huge amount of supplementary training data to set up networks in order to receive or enhance the accurate results (Munasinghe, Cohen & Gadiraju 2021). Hence, only effective and consistent classification approaches such as manual digitization, density slicing, image segmentation and edge detection, band ratioing, spectral mixture analysis, and sub-pixel analysis will be thoroughly demonstrated in the subsequence sections below.

2.4.1. Pixel-Based Methods

2.4.1.1. Manual Digitizing

Manual digitizing on deltaic system is a technique to delineate the boundary line manually based on digitizer's awareness and understanding of the morphological features, vegetation, and sediment characteristics of the delta. By applying humans' interpretation and judgment skills in identifying what and where the boundary is, manual digitizing takes advantage over computer assisted classification methods (Kong et al. 2015). However, this method contains several fundamental issues. The first issue is the imprecisions induced through the repetitive digitization. Another concern is the digitization, which mainly based on digitizer's experiences, can be challenging for the human eye to interpret the boundary since colour shades may gradually decay in particularly low-resolution images (Nath & Deb 2010). This method is also extremely time-consuming and monotonous which is expensive for labouring cost and ineffective if analysing numerous images. It is proven that the integration of digitization and automatic boundary detection procedures to map the deltaic boundary lines were favourably successful (Kong et al. 2015).

2.4.1.2. Density Slicing

The principle of density slicing consists of classifying the satellite images into distinct territories such land and water regions by frequently identifying a threshold value of a single spectral band. A performing of histogram analysis is generally implemented in order to define this significant threshold without bias (see in the **Figure 2.8**). It is believed that the overall performance of density slicing is efficient, but this technique has its specific limitations. The accuracy of water line estimation is occasionally minimal due to the complexity of land and water interactions in coastal deltaic areas

even though land and water mostly occur to be spectrally distinguishable. The reason could possibly be due to spectral confusion occurring from conditions such as inconstant depth and turbidity linking with the spatial resolution of the imagery. This circumstance affects the boundary clarity boundaries and sections of mixed pixels that limits the water line mapping accuracy (Malthus & Mumby 2003; Ryu, Won & Min 2002). Additionally, the application of one spectral band typically cannot tolerate every form of alteration to be detected (Munasinghe, Cohen & Gadiraju 2021). It has been recommended that individual density slicing method is not adequate in defining the water line and typically should be applied in combination with other techniques to achieve greater deltaic boundary lines classification accuracies (Marghany, Sabu & Hashim 2010).

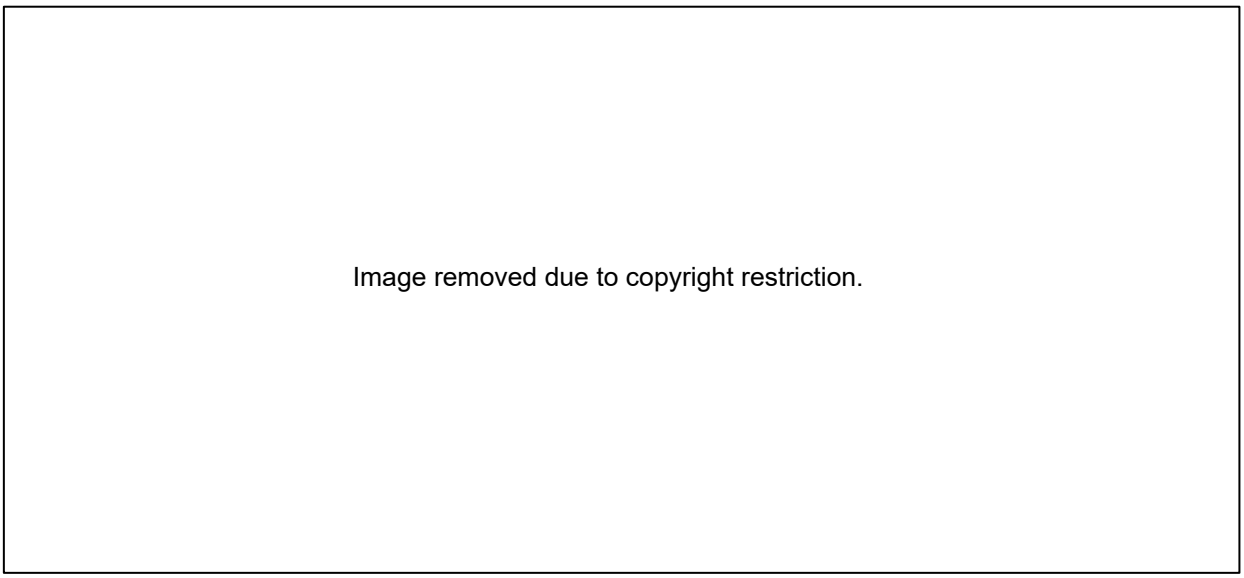

Figure 2.8 Example of Density Slicing to extract water body using Landsat TM band 5 along the Danube delta (Munasinghe, Cohen & Gadiraju 2021)

2.4.1.3. Image Segmentation and Edge Detection

Image segmentation and edge detection approaches follow to the procedure of manual digitization further closely by differentiating an image into distinct sections where sharp intensity variations arise. One of two crucial image segmentation and edge detection methods, the alternative connective approach, is utilised in deltaic studies where consistent regions are intended to be developed by combining pixels or sub-regions on the similarity criterion fundamental (Le Moigne & Tilton 1995). This procedure is based on guiding the software by defining points manually along the boundary line of the original image. The program later analyses the image edges by following these points, and the analyst will verify the modification of identified boundary lines. This examination is noticed to be faster and additionally consistent than entirely automation procedures (Loos & Niemann 2002) because of the gathered information (training samples) by the analyst. Although it is considered as successful, this technique still contains limitations in potential inclusion of distinct feature classes into the same area resulting in difficulty of spectral partition and consequent classification of thematic information categories.

2.4.1.4. Band Ratioing

Band ratioing method is the technique using two sensitive spectral bands combination of detected deltaic features to sense the reflectance level in order to identify detected deltaic areas, in particular land-water regions and turbid waters. In the case of land-water extraction, this technique exploits the green and SWIR bands whose wavelengths are absorbed by water resulting in water region rendered as white whereas land region rendered as black colours in the processed image (Munasinghe, Cohen & Gadiraju 2021). The calculation of these sensitive spectral bands' integration within the MNDWI formular (as explained in the **Figure 2.9**) is applied to diminish the influence of suspended sediment near coastlines (Lohani 1999) and emphasise higher reflectance attributes from soil and strong vegetation offering a perspective for the land-water boundary (Braud & Feng 1998; Guariglia et al. 2006). For turbidity detection, in addition, the method integrates the sensitive bands of green and red bands (as demonstrated in the Sensitive Wavelength Regions (Bands) section above) to calculate NDTI layer that can sense the variation of turbidity concentrations varying from low to high concentrations. By comparing with other approaches, this band ratioing is a comparatively rapid process of distinguishing alteration deltaic areas, yet the specific obstacle of this technique is addressed. For instance, the ratio of band calculation assumes values greater than one as water and less than one as land in large areas of the coastal zone while this ratio can be inaccurate for some deltaic and coastal zones based on their reality characteristics (Alesheikh, Ghorbanali & Nouri 2007). This ratio is believed to perform well in deltaic and coastal zones covered mainly by soil but not in regions with vegetative cover that can lead to erroneously classify other land use classes as water (Alesheikh, Ghorbanali & Nouri 2007). Therefore, this method is the most effective of instantly go-to approach comparing to other procedures in the purpose to rapidly extract the coastline and deltaic boundary lines with satisfactory results but not extremely precise. It is not suggested to implement this method if the research aims to generate extraordinarily accurate results of shoreline extraction (Munasinghe, Cohen & Gadiraju 2021).

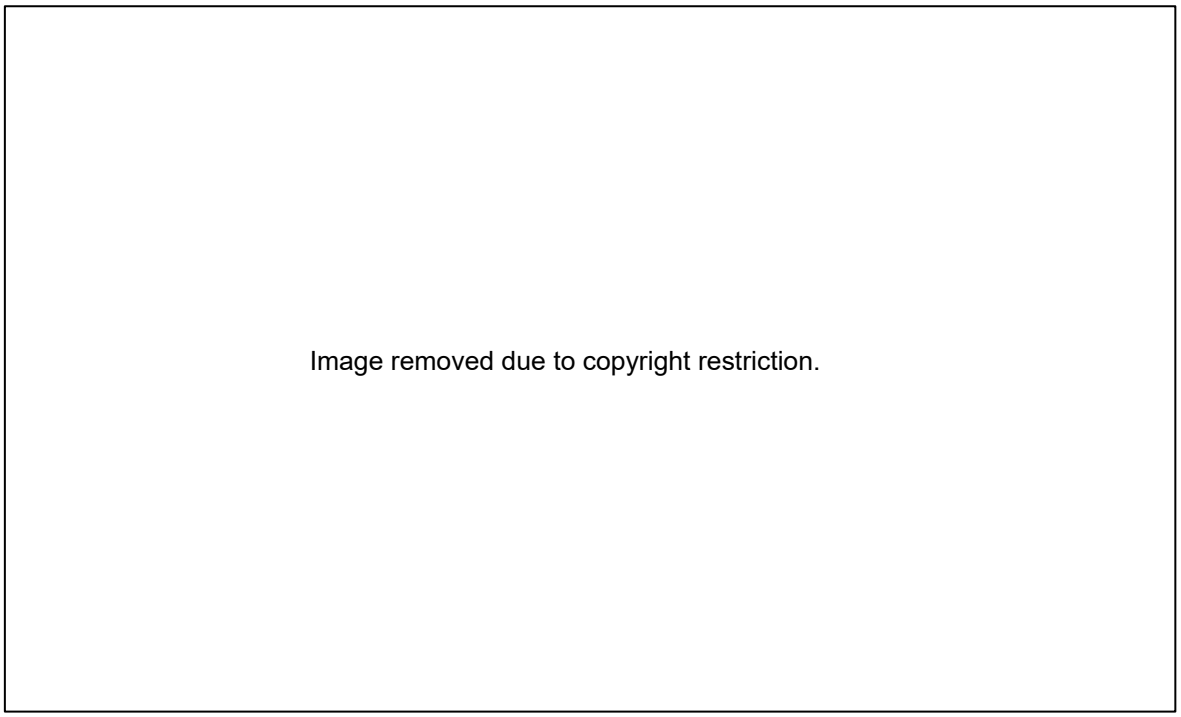

Figure 2.9 Example of Band Ratioing to generate a land-water raster for shoreline extracting using Landsat OLI imagery along the Irrawaddy River delta. The combination and ratio of the Modified Normalized Water Index (MNDWI) is applied to emphasise water body. *Left*: A subtracted difference layer of SWIR and Green bands. *Middle*: An added difference layer of SWIR and Green bands. *Right*: The MNDWI raster (feature-accentuated layer) from the subtracted difference and the added difference layers (Munasinghe, Cohen & Gadiraju 2021)

2.4.2. Sub Pixel-Based Methods

Dissimilarly to discussed classification methods above based on per-pixel information in which every pixel is classified as one class, a comparatively latest discipline in image analysis, sub-pixel procedures, offers the prospect to extract information about the fraction of diverse classes within a mixed pixel (soft classification) as shown in the **Figure 2.10**. It has been reported soft classification methods were generally revealed to enhance the cartographic representations of transitional zones and heterogeneous landscapes (Frohn et al. 2012; Wei et al. 2008; Zhang 2009).

Figure 2.10 The illustration of the mixed pixel in the imagery (Munasinghe, Cohen & Gadiraju 2021)

2.4.2.1. Spectral Mixture Analysis

Spectral mixture analysis (SMA) is the technique to extract information about the surface substances appearing in a pixel that is performed by estimating the least-squares best match for every pixel along mixing boundary lines using spectral endmembers to account for the variation in the mixture composition of each pixel. An endmember ideally exemplifies a pure constituent of the mixtures represent in pixels. The SMA outcome is typically exhibited in the fraction images forms with one image of each endmember spectrum indicating the area dimensions of the endmembers within the pixel, and the selection and identification of endmember is deemed to be one of the most significant aspects in SMA (Small 2004; Theseira et al. 2003). A previous study by Lu, Moran and Batistella (2003) signified that SMA is beneficial in enhancing the accuracy of classification and is specifically critical in enhancing area approximation of deltaic classes based on coarse spatial resolution data. Beside its advantage over other techniques in enhanced accuracy, SMA distresses from two critical limitations. Firstly, it does not have potential endmembers appearing in areas greater than the image resolution, and features could be existed in tinier spots lesser than pixel proportions; this causes the endmember identification impossible for classification and subsequently be classified speciously. Secondly, endmembers are not indeed persistent within an image. Due to the existence reflectance values range for a specific endmember class, the overlap between diverse endmember classes could arise causing the incompatibility between the defined endmember and ground truth leading to misclassification results.

2.4.2.2. Sub-Pixel Analysis

Sub-pixel analysis process is characterized as the technique seeking for certain interested features from within hybrid digital number scale of a multispectral image pixel. This approach has benefits over SMA and fuzzy classifications since the overall constituents of every pixel is not restricted to a mixture of previously specified image classes (endmembers). The phases in sub-pixel approach consist of signature derivation for the interest feature and each pixel classification distinguishing the portion of interest feature represent. Consequently, an individual classification must be performed for each substance when the fraction pixel values differ from 0.0 to 1.0 (Ozesmi & Bauer 2002). However, this specific method of sub-pixel analysis was reported to be the least implemented technique for detecting and mapping deltaic environments although it provides the most accurate result among all 18 reviewed methods according to the reviewed literature (Munasinghe, Cohen & Gadiraju 2021).

CHAPTER 3. METHODOLOGY

3.1. Satellite Images Acquisition

In order to detect the sediment plume in main outlet of Mitchell River Delta, the Sentinel 2 level 2A from Multi Spectral Instrument (MSI) dataset has been utilised. The reason the Sentinel 2 satellite was considered for this research is due to its high spatial and high spatial resolutions which are beneficial in turbidity detection. The high spatial resolution can provide an opportunity to get more accurate result in identify sediment plume and mouth bar geometries while the high temporal resolution can offer a high chance in retrieving cloud free or minor cloud condition images, especially in the wet season. The Sentinel 2A and Sentinel 2B satellites were initiated by the European Space Agency (ESA) Copernicus program on 23 June 2015 and 07 March 2017, respectively, with global coverage every 5 days. The Sentinel 2 mission is to assist Copernicus land monitoring research, which includes the monitoring of vegetation, soil and water cover, along with observation of inland waterways and coastal extents. Its MSI sensor delivers imagery data with 13 spectral bands ranging from visible and near infrared to short wave infrared (central wavelength from 443 to 2190 nm) regions, with 290 kilometres of a wide-swath width and a high spatial resolution of 10 metres (four visible and near infrared bands), 20 metres (six red edge and shortwave infrared bands) and 60 metres (three atmospheric correction bands) (Potes et al., 2018; Garg, Aggarwal & Chauhan, 2020; Soomets et al., 2020).

The Google Earth Engine (GEE) was implemented to automatically collect Sentinel 2 level 2A imagery, which is atmospherically and geometrically corrected (computed by running Sen2cor according to Sentinel 2 level 2A catalogue detail) providing surface reflectance information, with cloud free and low cloud conditions (less than 10 percentages of cloud cover) of specific time periods (January 2020 to August 2021) from scihub. This imagery can be manually downloaded from the Sentinel Scientific Data Hub (https://scihub.copernicus.eu/). This imagery was chosen to analyse the relationship between the sediment plume pattern and stream flow and precipitation. Satellite imagery was acquired based on the minimum and maximum discharge and rainfall events in both wet and dry season. Due to the limitation of revisit time interval (every 5 days) of Sentinel 2 associating to meteorological condition issues in particularly in massive cloud events, the imagery could not be exactly gathered with precise days of minimum and maximum discharge and rainfall. The imagery collection is, however, acquired with as finest circumstances as possible to the requirement of discharge and rainfall perspectives, yet depending on the availability of Sentinel 2 imagery with acceptable cloud condition. The images are subset to the study area that focuses on the main outlet of the Mitchell River Delta (as mentioned above in **Figure 1.1**). The specifications of each band and wavelength regions are presented in **Table 3.1** whilst the specifics of stretch wise satellite data applied and time periods selected are provided in **Table 3.2**.

Table 3.1: Summary table of Sentinel 2 satellite specification included its bands, wavelegth regions, central wavelegth and spatial resolution.

	Bands	Wavelength Region	Central Wavelength (nm)	Resolution (m)
1	Band 1	Coastal Aerosol	443	60
2	Band 2	Blue	490	10
3	Band 3	Green	560	10
4	Band 4	Red	665	10
5	Band 5	Vegetation Red Edge	705	20
6	Band 6	Vegetation Red Edge	740	20
7	Band 7	Vegetation Red Edge	783	20
8	Band 8	Near Infrared (NIR)	842	10
9	Band 8A	Vegetation Red Edge	865	20
10	Band 9	Water Vapor	945	60
11	Band 10	Short Wave Infrared (SWIR) - Cirrus	1375	60
12	Band 11	Short Wave Infrared (SWIR)	1610	20
13	Band 12	Short Wave Infrared (SWIR)	2190	20

Table 3.2: Summary table of specifically selected date with the Sentinel 2 satellite sensor and its products that were implemented in the research. These dates were chosen based on image availability of Sentinel 2 and cloud conditions relative to the low and high discharge and rainfall as possible.

	Dates	Satellite / Sensor	Product	Cloud Condition
1	15 / 01 / 2020	Sentinel 2 / MSI	L2A	Minor cloud
2	14 / 02 / 2020	Sentinel 2 / MSI	L2A	Cloudy (not in critical region)
3	20 / 03 / 2020	Sentinel 2 / MSI	L2A	Cloudy (only thin cloud)
4	09 / 05 / 2020	Sentinel 2 / MSI	L2A	No cloud
5	03 / 06 / 2020	Sentinel 2 / MSI	L2A	No cloud
6	28 / 07 / 2020	Sentinel 2 / MSI	L2A	No cloud
7	11 / 09 / 2020	Sentinel 2 / MSI	L2A	No cloud
8	24 / 01 / 2021	Sentinel 2 / MSI	L2A	Minor cloud
9	10 / 03 / 2021	Sentinel 2 / MSI	L2A	No cloud
10	14 / 04 / 2021	Sentinel 2 / MSI	L2A	Minor cloud
11	14 / 05 / 2021	Sentinel 2 / MSI	L2A	No cloud
12	08 / 06 / 2021	Sentinel 2 / MSI	L2A	No cloud
13	23 / 07 / 2021	Sentinel 2 / MSI	L2A	No cloud
14	12 / 08 / 2021	Sentinel 2 / MSI	L2A	No cloud

3.2. Pilot Procedure

A series of pilots were performed in ArcGIS Pro version 2.8.2 as an initial process in this study to evaluate the best bands combination to detect the turbidity. Although the single band algorithm included both red (665 nm) and NIR (842 nm) has been reported to be one of the most sensitive response of turbidity, it was not being considered in this research due to its issues of overestimated or underestimated in sensing the turbidity (Garg, Aggarwal & Chauhan 2020; Kuhn et al. 2019; Pahlevan et al. 2019). Therefore, three integrations of bands combination algorithm were employed in the pilot to check and compare the sensitivity of turbidity reflectance.

Firstly, the combination of multiple bands included red, NIR and SWIR was selected on a Sentinel 2 imagery on 15 January 2020 (see in **Figure 3.1**). It is believed that the combination of red and NIR can receive a good response of turbidity (Doxaran et al. 2002; Garg, Aggarwal & Chauhan 2020; Toming et al. 2016), and red, NIR and SWIR bands combination could be the enhancement version of red and NIR combination with additional SWIR band to improve the outcome. The reason the SWIR band was included is that the SWIR band can clearly reveal thin cloud regions which is the most problematic for image analysis in this Sentinel 2 imagery (as shown in the **Figure 3.1**). It is believed that both SWIR bands in Sentinel 2 can distinguish clouds from other features in the satellite image, especially when integrating these two SWIR bands with the blue band, and even differentiate between clouds and snows (Bian et al. 2016). Vanhellemont and Ruddick (2015) explained in their research that the implementation of SWIR band can highly benefit in ocean colouring process due to its capability to reveal some clouds that could be misclassified as water. After integrating these three bands into a raster image, the classification called the spectral unmixing method was applied to define the area of plume (low and high plume concentrations) and water by using training samples of multiple classes such as land, cloud, clear water, low plume concentration and high plume concentration classes. The spectral unmixing method is a sub-pixel-based classification method that can separate mixing features in a pixel, for example a pixel contains 2 classes of land and water, using training samples in the form of either spectral signatures or adjacent areas of similar pixel values. The outcome of this first pilot is demonstrated in **Figure3.1** below.

Secondly, another pilot was executed by using three spectral bands of green (560 nm), red (665 nm) and NIR (842 nm) on the identical Sentinel 2 image (in **Figure 3.2**). This band combination technique is reminiscent of the cooperation between theoretical and practical remote sensing perspectives. In theory, the red and NIR combination, as above mentioned, are considered to be the most sensitive bands, both in individual and combination approaches for turbidity approximation. In practise, the green and red bands are the wavelength regions that provide high spectral reflectance value of turbidity collected from multiple spots of sediment plume area. The spectral signature is represented in **Figure 3.3**. Although reviewing previous literature advantageous in providing a variety of principles on how to generally select sensitive bands for turbidity, observing and inspecting spectral signature

of specific investigated images can practically offer the exact reflectance information in sensing turbidity of one specific study location since different research regions can possibly have quite different variables in turbidity depending on the SPM compositions that can produce comparable spectral signature yet not identical. Based on these perspectives, the integration of green, red and NIR bands could hypothetically be a decent choice in sensing turbidity. Renosh et al. (2020) explained in their research about implementing the green, red and NIR bands with similar wavelength regions of 560 nm, 655 to 665 nm and 865, respectively, could sense the SPM concentrations in clear water to highly turbidity varying from 1 to 2000 mg/L. This band combination image was then employed with the identical classification method to the first pilot of the spectral unmixing and the approach on how training samples and classes are trained and identified. The testing result of this second pilot is exhibited in the **Figure 3.2** below.

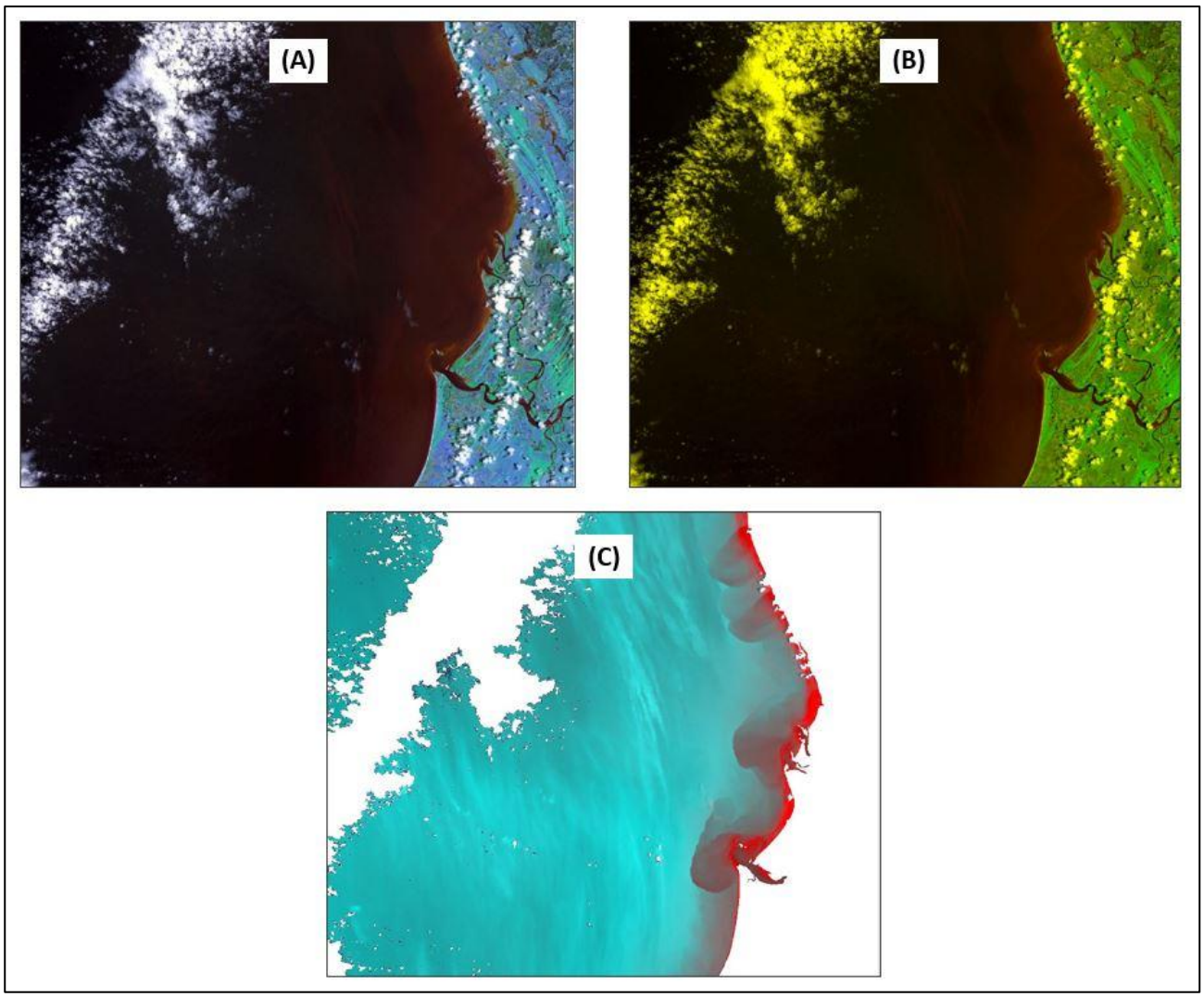

Figure 3.1 (A) The analysed image of Red, NIR and SWIR bands combination (clearly differentiate between cloud, land and turbid water), (B) The analysed image of Red and NIR bands combination (indecisively differentiate between cloud, land and turbid water), (C) The raster layer of turbidity detection using the Red and NIR bands combination with the spectral unmixing method; the turbidity concentration could be identified (bule represents the water area while red represents the detected plume area).

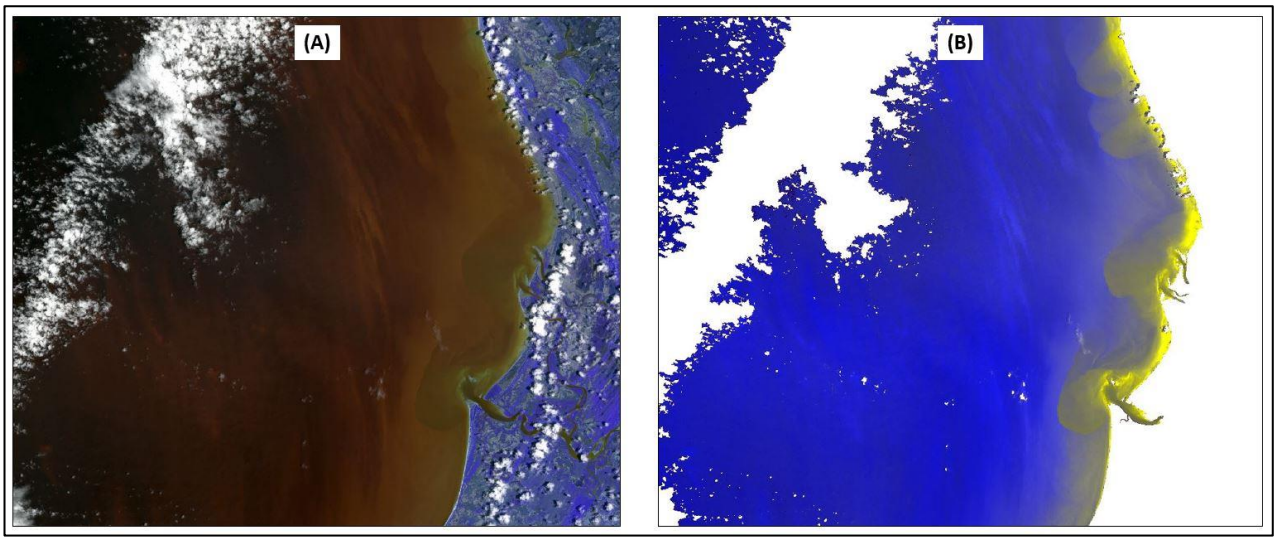

Figure 3.2 (A) The analysed image of Green, Red and NIR bands combination, (B) The raster layer of turbidity detection using the Green, Red and NIR bands combination with the spectral unmixing method; the turbidity concentration could be identified (bule represents the water area while yellow represents the detected plume area).

Finally, the third pilot was performed on the identical testing Sentinel 2 image using band ratioing technique to calculate the NDTI layer, an algorithm developed by Lacaux et al. (2007), from two sensitive band of red (560 nm) and green (665 nm) wavelength regions. The selection of these two sensitive bands' combination is likewise based on both theoretical and practical remote sensing perspectives. Gholizadeh, Melesse and Reddi (2016) showed that the integration of sensitive green and red wavelength regions could offer the most effective spectral reflectance in sensing the turbidity concentrations among other sensitive bands. This indication is verified by not only other research but also the spectral signature observation from various turbidity spots in the Sentinel 2 image (as above mentioned in **Figure 3.3**). A study by Garg, Aggarwal and Chauhan (2020) demonstrated that the peak reflectance of in the turbidity concentration zones highly shifts from the green to the red wavelength region while the graph of spectral signature observation plotted from various turbidity spots likewise reveals the peak turbidity reflectance in the green and red spectrums. Garg, Aggarwal and Chauhan (2020) additionally mentioned that the application of band ratioing method of NDTI using green and red bands' combination could potentially generate superior results of turbidity concentration with the comprehensive information for detecting temporal turbid waters. The output layer of this third pilot is displayed in the **Figure 3.4** below.

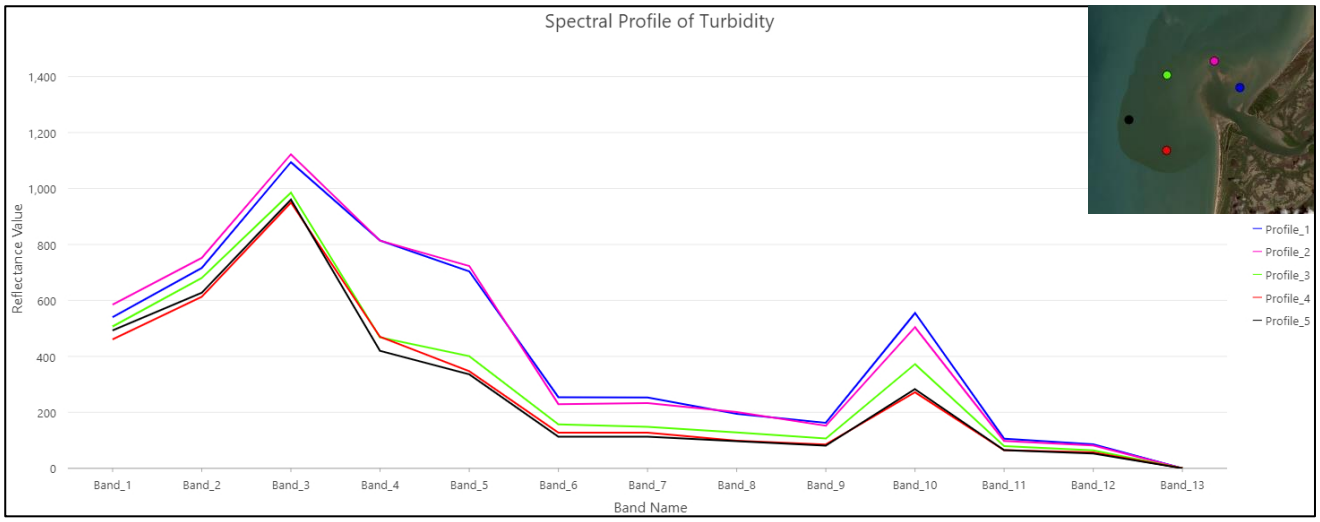

Figure 3.3 Spectral profiles of selected high turbidity spots (see band numbers in Table 3.1).

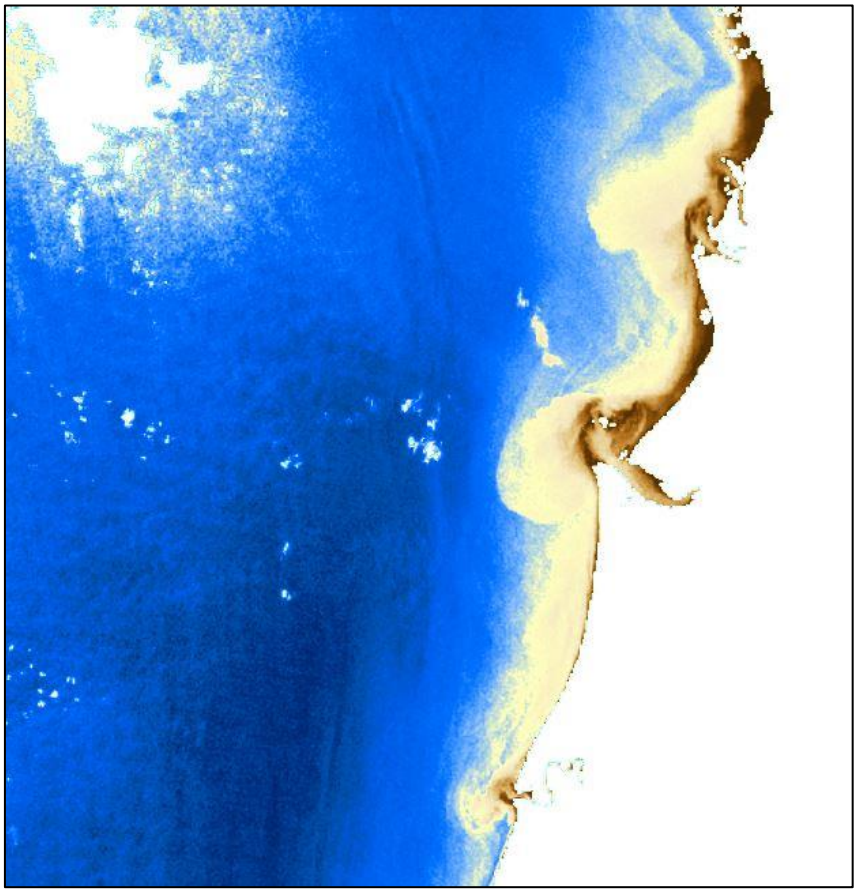

Figure 3.4 Result layer of turbidity detection using NDTI algorithm (bule represents the water area; yellow represents the low and moderate turbidity; brown represents the high and very high turbidity).

By visually comparing these three pilots' output layers, the NDTI layer of the third pilot is believed have the best out output when compared to the of first and second pilots using red, NIR, SWIR bands combination and green, red, NIR bands integration, respectively, with the spectral unmixing algorithm. Therefore, the band ratioing of NDTI algorithm will be chosen as the principal detection technique for analysing seasonal variations of turbidity in this research.

3.3. Automation Procedure

After experimenting with multiple pilots, the automation procedure included two major stage of water extractions using MNDWI and turbidity detection using NDTI, which will be thoroughly exemplified in sections below, was processed for twice excluded the trial runs for testing if the automated algorithm is working. The first run was performed with a single Sentinel 2 image to inspect and evaluate the overall results and errors of the algorithm and to generate standard templates of the MNDWI index ranges for water extractions and NDTI indices values for both turbidity concentration visualising and plume boundaries extraction purposes intentionally for the final run. The second run was performed with the entire Sentinel 2 images (14 images) and generated standard templates of MNDWI and NDTI to receive the detected results utilising for the final mapping. This automated algorithm was executed in the ArcGIS Pro version 2.8.2 using the Model Builders platform (see **Appendix 1**) later converted into the ArcPy script (as presented in **Appendix 2**). However, this conversion produced some gaps causing the errors occurred in ArcPy environment and will be demonstrated in the Discussion section.

3.3.1. Image Pre-Processing (Automated Water Extraction)

Before detecting the turbidity using NDTI algorithm, the land area and clouds were required to be masked out from all Sentinel 2 L2A imagery as an image pre-processing (automated water extraction step). This step is considered as a beneficial step to clean undesirable regions (land area and clouds) from images in order to boost the processing momentum in the further processing (detection stage) since only the water regions are significant in this analysis. A variety of studies demonstrated about the benefit of masking out regions that are not significant for analysis, especially land area for monitoring the turbid water, in the purpose to enhance the processing speed (Munasinghe, Cohen & Gadiraju 2021). Moreover, masking out unnecessary part of images could improve the accuracy of the result since keeping images with all type of features or classes could lead confusion in detecting and classifying due to similar spectral reflectance of two district objects or classes. According to Munasinghe, Cohen and Gadiraju (2021), the accuracy of detection and classification could be diminished when numerous classes are characterized in satellite image analysis, in particularly the unsolicited classes. Various automation and manual methods have been implemented to differentiate between water and land areas while numerous of cloud masking algorithm are available in both online and offline versions. While a significant amount of research implemented the cloud masking algorithm to obtain cloud-free satellite image before applying classification methods to separate between land and water, this image pre-processing, on the other hand, was employed the automatically band rationing algorithm of Modified Normalised Different Water Index (MNDWI) to classify the water area. The reason behind this decision is that the water area is the only significant while other features are considered as insignificant leading to the classification of just water class and not water class. It is believed that the cloud masking algorithm is separately performed due to the possibility of misclassified or confusion in identifying clouds and

the objects with similar spectral reflectance as clouds such as white buildings or vehicles while this concern does not exist in this research. The band ratioing technique is one of effective pixel-based classification method that could promptly extract the two distinct features or classes such as land and water extraction yet inappropriate if the accurate extraction results are strongly required (Munasinghe, Cohen & Gadiraju 2021). Since the purpose of this water area extraction in this pre-processing is primarily to enhance the further detection processing speed and not strongly focus about the accuracy of water area extraction, the MNDWI is the suitable method for this pre-processing. The MNDWI is the combination of two bands (green and SWIR) to create the (Green – SWIR) layer dividing to the (Green + SWIR) layer where the MNDWI formular is explained in the **Equation 3.1**. It is, in addition, the enhancement version of Normalised Different Water Index (NDWI) which is originally introduced as band ratioing method to extract water from land area. The formula of NDWI is indicated in the **Equation 3.2**.

Equation 3.1: The formular of Modified Normalised Different Water Index (MNDWI)

$$\mathbf{MNDWI} = \frac{(\mathbf{Green} - \mathbf{SWIR})}{(\mathbf{Green} + \mathbf{SWIR})}$$

$Where$:
$Green = \ the\ Green\ band\ (band\ 3\ in\ Sentinel\ 2)$
$SWIR = \ the\ Short\ Wave\ InfraRed\ band\ (band\ 11/12\ in\ Sentinel\ 2)$

Equation 3.2: The formular of Normalised Different Water Index (NDWI)

$$\mathbf{NDWI} = \frac{(\mathbf{Green} - \mathbf{NIR})}{(\mathbf{Green} + \mathbf{NIR})}$$

$Where$:
$Green = \ the\ Green\ band\ (band\ 3\ in\ Sentinel\ 2)$
$NIR = \ the\ Near\ InfraRed\ band\ (band\ 8\ in\ Sentinel\ 2)$

After the MNDWI layers were generated from the entire Sentinel 2 images, these MNDWI layers were later applied to extract the water areas by identifying the MNDWI ratio values for three distinct categories using the Jenks Natural Breaks classification method of water and not water (land and clouds) classes while habitually two classes of water and land are categorised in a variety of studies. The Jenks Natural Breaks Classification approach is a statistics classification technique designed to group a set of values into an optimal class range with similar characteristics, known as a “natural” class. The reason of this diversity could be due to the researchers’ perspectives and the conditions

of collected satellite imagery (clouds free) in those studies while low cloud conditions and thin clouds in this research. The ranges of specified MNDWI ratio values using 3 classes provided more precise results of water areas than using 2 classes as shown in the **Figure 3.5**. It is displayed that using 3 identified classes can clearly differentiate between water area (in red colour region), land area (in yellow colour region) and clouds area (in orange colour region), which this clouds area is missing when using 2 defined classes. It is, however, believed that the adjustments of the MNDWI ratio values ranges should be performed to enhance the accuracy of water area extraction if the manual process is employed or before generating these ratio scales into a standard template for the automated algorithm using the Model Builders since the minor inaccuracies of pixel values along water area boundaries were addressed. The ratio values of MNDWI in this study varies from -1 to 1 where assigned ranges of -1 to -0.268, -0.268 to 0.361 and 0.361 to 1 represent land, clouds and water classes, respectively.

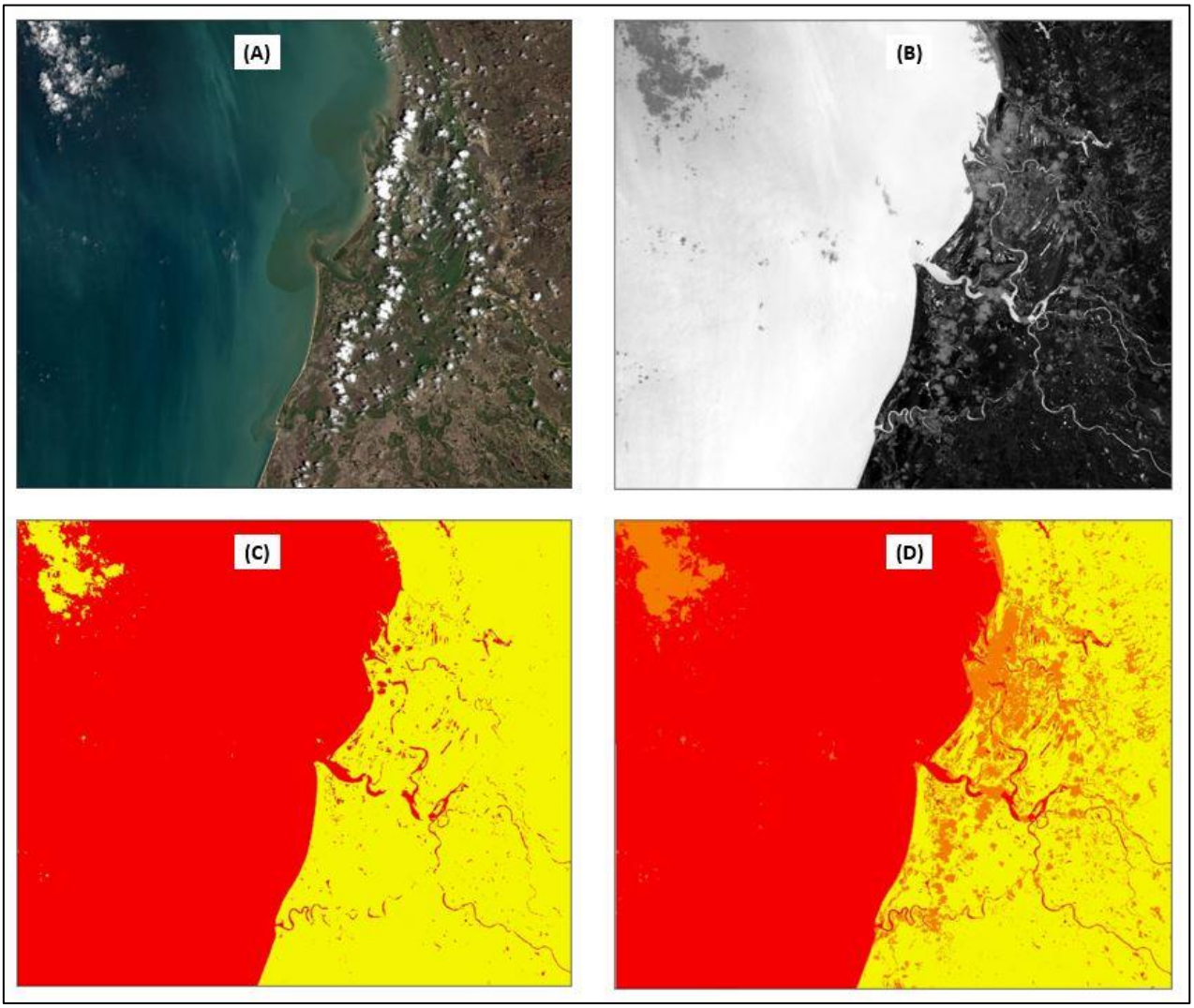

Figure 3.5 (A) The RGB image used for analysis, (B) The raster layer of MNDWI without classification (stretch value), (C) The raster layer of MNDWI with two assigned classes (missing most cloud areas), (D) The raster layer of MNDWI with three assigned classes (most cloud areas revealed).

3.3.2. Turbidity Detection using NDTI

After the water area extraction, the automated turbidity detection stage is processed with the most effective band ratioing method of NDTI using two sensitive wavelength regions of green and red spectrums. Because of 3 significant circumstances, the band ratioing method of NDTI was hypothetically and practically considered as the most sufficient and efficient technique for this deltaic study. Firstly, by visually pilots' comparison, this NDTI algorithm offered a comparable result of accuracy to other two approaches yet advantages in thorough information of turbidity concentration that is beneficial for further processing and analysing. Secondly, according to a literature, this band ratioing of NDTI method is believed to well operate in deltaic and coastal zones covered predominantly by soil, which is the case of this study area environment, but not in regions with vegetative cover that can lead to mistakenly classify other land use classes as water (Alesheikh, Ghorbanali & Nouri 2007; Munasinghe, Cohen & Gadiraju 2021). Finally, the NDTI algorithm using the mixture of sensitive green and red bands typically provides qualitative rather than quantitative estimations of turbidity and is suggested for research intentionally detecting the turbidity concentration from spectral reflectance of multispectral satellite imagery in order to preferably obtain qualitative terms of detected turbidity results (Garg et al. 2017). In this case, this method is extremely appropriate since the intention of this research is not to investigate and estimate the statistics of turbidity concentrations when the field measurement turbidity concentrations are unobtainable. A comparable scenario was also applied in a recent study where Garg, Aggarwal and Chauhan (2020) utilised this NDTI algorithm with the identical satellite sensor (Sentinel 2 MSI) to investigate and represent qualitative terms of detected turbidity results in several stretches along the Ganga River since the field measurement data could not be collected due to the lockdown period of COVID-19.

The NDTI is the band ratioing algorithm that combine green and red wavelength regions to generate the (Green – Red) layer dividing to the (Green + Red) layer as NDTI formular is indicated in the **Equation 3.2**. After this procedure was performed, the results of NDTI layers revealed the detected turbidity concentration in the water that their indices values ranging from -1 to -0.5 represent from clear water to high concentration of sediment plume. However, this turbidity indices values were found challenging to identify and analysis both the turbidity concentrations and geometries. To overcome this difficulty for visualising turbidity concentrations, the comprehensive indices classification was executed by assigning the classes values in every 0.05 (as demonstrated in **Figure 3.6**). This classified NDTI indices was generated as a standard template using manual classification method for the automated algorithm using the Model Builders. Manual classification method is a classifying technique using humans' interpretation to assign the indices ranges.

Equation 3.3: The formular of Normalised Different Turbidity Index (NDTI)

$$\mathbf{NDTI} = \frac{(\mathbf{Green} - \mathbf{Red})}{(\mathbf{Green} + \mathbf{Red})}$$

$Where$:

$Green = \ the\ Green\ band\ (band\ 3\ in\ Sentinel\ 2)$

$Red = \ the\ Red\ band\ (band\ 4\ in\ Sentinel\ 2)$

In contrast to the NDTI indices classification for visualising purpose, another indices classification was implemented to identify clear water and turbid water areas. By evaluating, the appropriate indices ranges were assigned values from -1 to -0.4 for the clear water region while from -0.4 to 0.5 for the plume area. Although the plume boundaries were extracted by from this automated classification approach, the inaccuracies of the boundaries and several confusions in the classification were addressed (the errors and limitations of this automated algorithm will be thoroughly discoursed in the discussion section below) leading to the assistant of manual digitisation method.

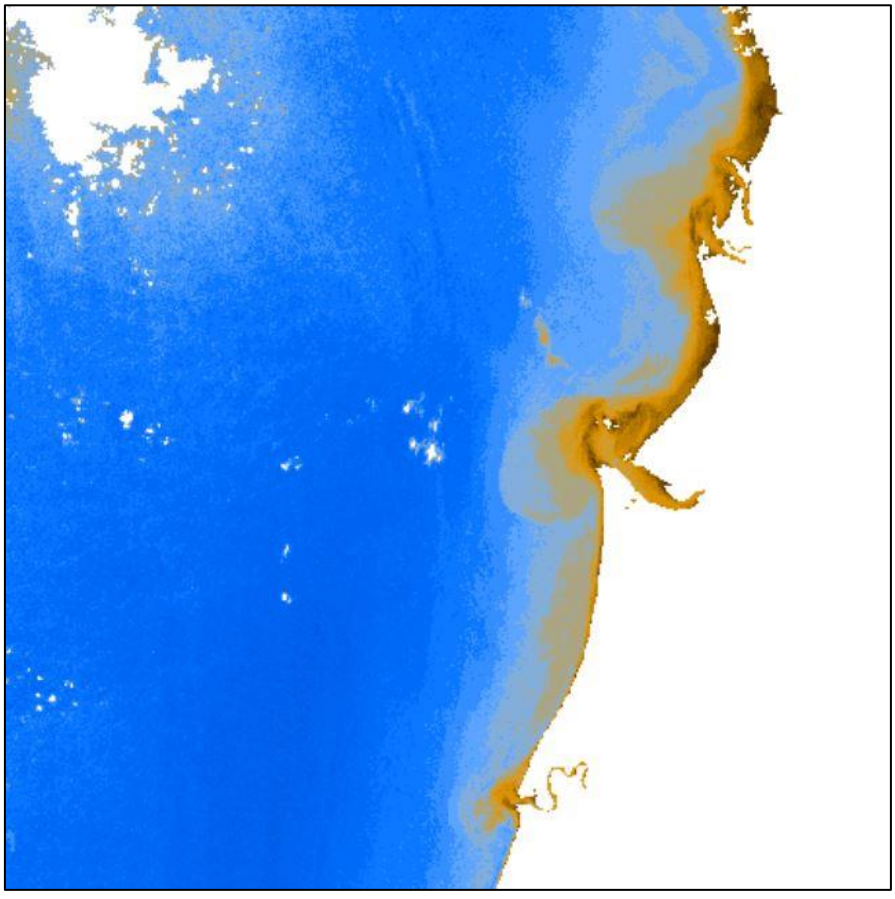

Figure 3.6 NDTI layer after assigning indices (0.05 per class).

3.4. Manual Digitizing Procedure

The manual digitising approach is the final process after the automation process in this study to not only correct the inaccuracy boundaries of the plumes but also to delineate the dynamic mouth bar geometries including mouth bar boundaries and possible distributary channels where the automation approach could not be successful executed. The corrections of plume patterns and the mouth bar geometries digitisation will be thoroughly demonstrated in sections below. This procedure is likewise performed in the ArcGIS Pro version 2.8.2.

3.4.1. Plume Pattern Corrections

In order to enhance the accuracy of the plume boundaries, the manual digitising was executed to correct various errors due to the limitation of the algorithm causing misclassified spots and the confusion in classifying different features as sediment plumes such as thin clouds, cloud shadows, unextracted clouds, and unextracted land regions. It is proven to be a satisfactorily successful in mapping the deltaic boundary lines with the integration of manual digitization and automatic boundary detection algorithm (Kong et al. 2015; Munasinghe, Cohen & Gadiraju 2021). The plume pattern corrections were manually delineating on every analysed NDTI layers using human's interpretation and judgement to identify the edge of plume boundary with the assistant of Sentinel 2 RGB images evaluation. RGB images are believed to be beneficial in assisting this correction since they could provide additional reality information about features and scenarios occurred in the study location on the specific time period. This editing process, furthermore, intends to correct the plume boundaries by removing overestimated areas and fill misclassified regions to obtain superior plume boundaries results.

3.4.2. Digitizing Mouth Bar geometry

Disparate to plume boundaries, the mouth bar geometries were not mapped using automated classification algorithm but the manual digitisation approach. Due to the complexity of geometrical mouth bar structures, the automated band ratioing using NDTI algorithm could not be successfully performed in mapping these dynamic structures resulting in manual digitisation process was implemented. By applying humans' interpretation and judgment skills in identifying what and where the boundary is, manual digitizing is advantageous over computer assisted classification methods (Kong et al. 2015; Munasinghe, Cohen & Gadiraju 2021). Munasinghe, Cohen and Gadiraju (2021) demonstrated that this manual technique is extremely effective in mapping deltaic regions, in particularly mouth bar, where the identification of the deltaic boundary using automatic classification is tremendously problematic due to the shallowness and turbidity of water and dynamically shifting waterline. Another study additionally revealed that this deltaic type provides various obstacles for simple band mathematics techniques, especially band ratioing algorithm, in labelling mouth bar due to complicated physical scene characteristics on the satellite image (Munasinghe, Cohen & Gadiraju 2021).

During this process, two deltaic features included the distributary channels within the mouth bar and the mouth bar boundaries were being delineating. The digitisation of distributary channels within the mouth bar were utilised on occasional time periods optically based on their possible appearances in the NDTI result layers. It is believed that the event of high fluvial discharge with high level of turbidity concentrations are the obstacles in visualising the geometry of distributary channels in some time periods especially in the wet season. On the contrary, the mouth bar boundaries were illustrated in in every time periods although the event of high fluvial discharge with high level of turbidity concentrations occurred. This digitisation of mouth bar boundaries was preferably an approximated drawing where they were supposed as mouth bars based on the patterns of high concentration SSC and exposed mouth bars pattern with the understating, knowledges about morphological deltaic structures and assumptions of the researcher. The exposed mouth bars could provide some principal patterns on the deposited sediments around mouth bars whilst the high turbidity concentration regions are believed to be the most potential deposited sediment areas. Based on these two assumption perspectives, the mouth bar geometries were mapped with uncertainty and biased boundaries since mapping features underneath oceans could be extremely problematic and mainly using imaginative sketching.

3.5. Hydrological and Meteorological data collection

3.5.1. Fluvial Discharge Data

Seasonal wet-dry conditions are known to cause fluctuating river discharge and turbidity patterns. As such, the total daily discharge data (in m^3/s) at Dunbar has been plotted over the study period (15 January 2020 until 25 August 2021) and compared with corresponding imagery. River gauge data is limited in the Mitchell River catchment and Dunbar provides the best proxy for discharge at the river mouth. the daily discharge data from Dunbar station retrieved from Water Monitoring Information Portal about stream flow information at the Mitchell basin published by Queensland Government (https://water-monitoring.information.qld.gov.au/). The location map of stream flow gauge station is represented in **Figure 3.7**.

3.5.2. Precipitation Data

The intense correlation of precipitation and discharge through run off in enhancing or diminishing stream flow can be considered as an altered turbidity factor in this study. Likewise to discharge data, the daily precipitation data (in mm) from every gauge station in the Mitchell Basin are evaluated, yet just the statistic from Dunbar station is acquired due to identical circumstances and significant considered aspects of data availability limitations. Precipitation data was collected for the period January 2020 to August 2021 from Water Monitoring Information Portal about stream flow information at the Mitchell basin published by Queensland Government (https://water-monitoring.information.qld.gov.au/). The location map of precipitation gauge station is shown in **Figure 3.7**.

3.5.3. Tide Data

Tide is one of the three principal influences that affect a delta's morphology (Ainsworth, Vakarelov & Nanson 2011; Galloway 1975). Unlike discharge and precipitation data, tide data is collected in hourly intervals for the specific time period of satellite imagery captured. Hourly tide data is acquired to assist our understanding of its impact for the investigation in between January 2020 and August 2021 from the Karumba gauge station, the closest tidal station to the main outlet of the Mitchell River. The tide data is retrieved from Tide Predictions for Australia, South Pacific and Antarctica published by Bureau of Meteorology (http://www.bom.gov.au/australia/tides/). The location map of tidal station is indicated in **Figure 3.7**.

3.5.4. Wave Data

In addition to fluvial discharge and tide data, wave data is also considered as wave energy is has a substantial influence on delta morphology. Not only is wave height data included (significant wave height and maximum wave height) but also wave direction, which are both considered significant influences. The significant wave height is an average height of the highest third of the waves measured in a record while the maximum wave height is the supreme height of waves occurring in a record period since the wave data is technically recorded in every 30 minutes (exactly 26.6 minutes for recording period) when the nature of the wave can occur multiple times in this recoding period Queensland wave monitoring sites description. Hourly wave data is acquired from the Albatross Bay (Weipa) wave monitoring Station, which is the closest to the study site (there are only six wave monitoring station in the far north Queensland region).This wave data is downloaded from Queensland wave monitoring sites website (https://www.qld.gov.au/environment/coasts-waterways/beach/monitoring/waves-sites) and presented for each of the dates the imagery was collected and analysed for the study period (see **Table 3.2**). The location map of this wave monitoring station is exhibited in the **Figure 3.7**.

3.5.5. Wind Data

The strong correlation of wind direction and speed with the ocean current (longshore current) is considered as the most significant aspect driving the seasonal variations of sediment plume and geometrical mouth bar orientation along the Mithcell River delta. Because of this, understanding the occurred scenarios of wind direction and speed in every specific period of investigation will assist in explaining the alteration of phenomena leading to the gathering of daily (hourly if possible) wind data. The daily wind data is acquired the investigation in between January 2020 and August 2021 from the Kowanyama gauge station, nearby wind station to the main outlet of the Mitchell River. The wind data is retrieved from Kowanyama, Queensland Daily Weather Observations published by Bureau of Meteorology (http://www.bom.gov.au/climate/dwo/IDCJDW4070.latest.shtml). The location map of wind station is specified in the **Figure 3.7**.

3.5.6. Digital Shoreline Data

The relationship between shoreline changes rate and the turbidity is one analysis perspective among the investigation in this research where the turbidity is believed to be a strong proxy for the erosion in the Mitchell River delta. Since the Australian shoreline changes from 1988 to 2019 are detected yearly by using detecting algorithm on the Landsat imagery, the digital shoreline data is acquired from the Digital Earth Australia (DEA) for the specific year of investigation in this research (2020 and 2021). The Derived product of DEA Coastline can be retrieved from DEA website (https://www.dea.ga.gov.au/products/dea-coastlines).

The product of annual DEA coastline from Geoscience Australia integrates the Landsat satellite imagery with the tidal modelling to estimate the median coastline position at annual mean sea level. This rate of shoreline changes included the erosion and progradation rates are estimated at every 30 metres along the entire Australia's coastline (non-rocky coastline). Trends in coastal growth and retreat can be analysed on a local and continental scale each year, and patterns of shoreline change can be traced historically and regularly updated as satellite data is continuously gathered. This permits researchers to compare the present rates of coastal change to those seen in earlier years or decades.

The sub-pixel method is applied by Geoscience Australia in extracting this annual DEA coastline. Comparing to traditional whole-pixel methods, the sub-pixel extraction method demonstrates a high level of accuracy when it comes to reproducing both relative waterline shapes and absolute waterline positions in environments with low contrast between land and water (Bishop-Taylor et al. 2019). The accuracy of this sub-pixel method applied on 30 m resolution of Landsat imagery is approximately 1.5 m to 3.28 m when the optimal water index thresholds are employed (Bishop-Taylor et al. 2019).

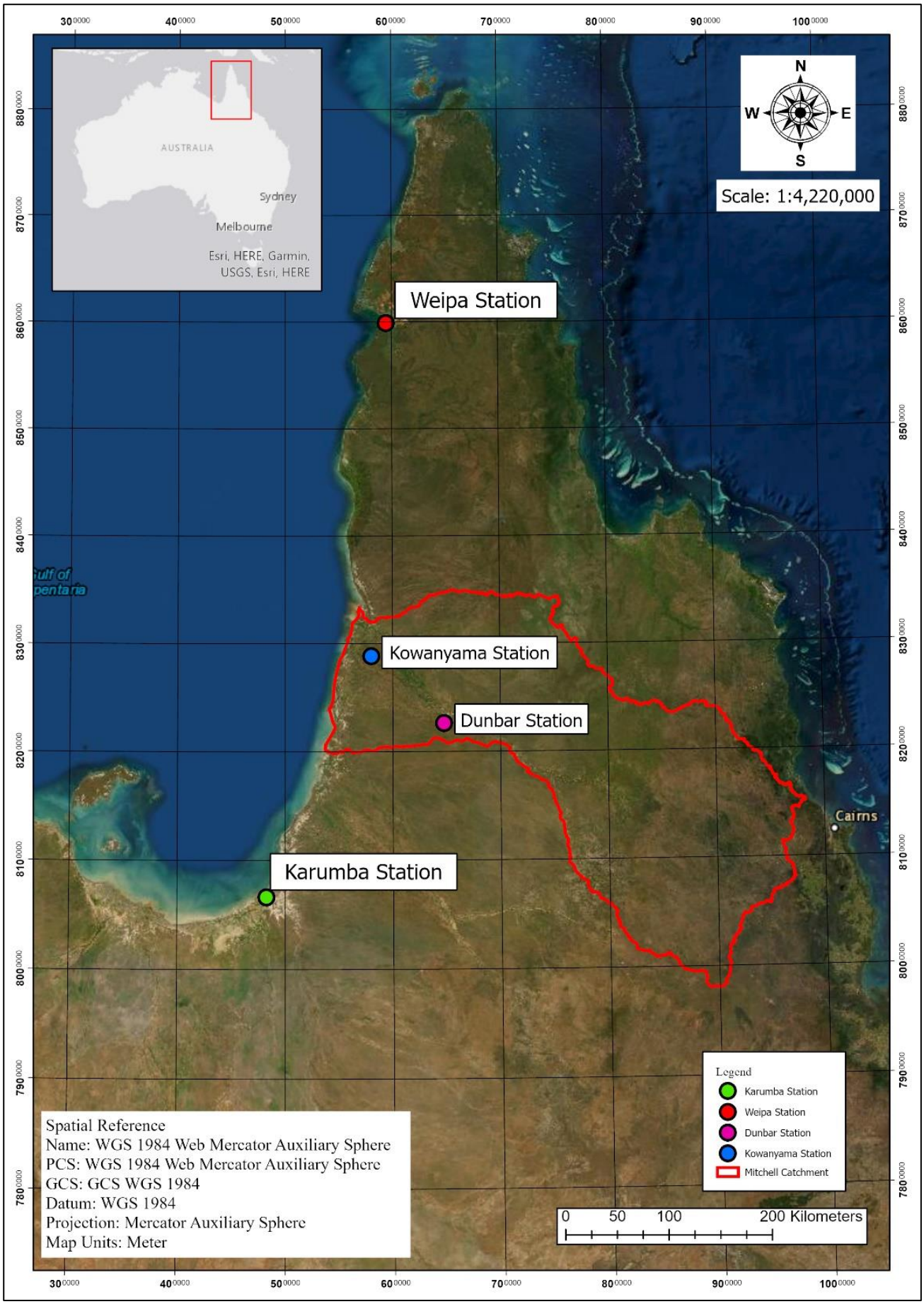

Figure 3.7 Location Map of All Gauge Stations.

CHAPTER 4. RESULTS

Three significant results were discovered for independently investigating the seasonal variations in water turbidity and mouth bar geometry. (1) Firstly, the seasonal variations of sediment plume dimension and orientation were analysed throughout 2020 and 2021 and correlated to precipitation, fluvial discharge, wind conditions and basinal processes including wave, tide and longshore current in the Mitchell River delta. (2) Secondly, the significant variability of mouth bar geometries including mouth bar shape and optically detected distributary channels within the mouth bar were investigated in both wet and dry season. (3) Finally, the concentration of water turbidity was analysed linking to the sea level changes and sediment supply loads as proxy for erosion activities influencing the shoreline erosion and progradation rate along both sides of this asymmetrical delta within these two years period.

4.1. Seasonal Variations of Plume Dimension and Orientation

4.1.1. Seasonal Variations in 2020 (15/01/2020 to 11/09/2020)

The results of seasonal turbidity detection were identified from 7 specific dates in both wet and dry seasons in 2020 (see in **Table 3.2**) demonstrated in **Appendix 3-01**, **Appendix 3-02**, **Appendix 3-03**, **Appendix 3-04**, **Appendix 3-05**, **Appendix 3-06** and **Appendix 3-07**, respectively, with the overall assessment map represented in **Appendix 5-01**. These results predominantly signify the dimensions and orientations of the sediment plumes phenomena in 3 designated months of wet season and 4 designated months in dry season where the direction of the plumes is specifically indicated in **Table 4.1**. This table shows that the sediment plumes in the wet season were predominantly orientated to the south while they, in contrary, shifted to the north direction in the dry season; one unidentified plume direction on 14 February of wet season and one unoriented plume trend on 09 May of dry season are addressed.

Two significant images in the wet season and two in the dry season of sediment plume on 15 January, 14 February, 09 May and 03 June are thoroughly investigated comparing to statistics of daily precipitation, fluvial discharge and wind data as shown in **Table 4.2** and hourly statistics of tide and wave data presented in **Table 4.3**. In addition, the graphs of daily precipitation and fluvial discharge for the entire year of 2020 are exhibited in **Figure 4.1** and **Figure 4.2**, respectively.

In the wet season, **Figure 4.3** reveals a large-scale sediment plume (about 7 km length from shoreline) occurred in the 15 January 2020 image oriented to the south direction with no rainfall condition, and the fluvial discharge coming out from the Mitchell River was 8 m^3/s. The wind direction and speed on that day was 13.1 km/h and oriented to north-east while the significant wave height was 0.217 m a 298-degree angle; the tide was reported to be 0.96 m. On 14 February 2020, the tremendous sediment plume magnitude (approximately 13.1 km into the offshore) is discovered with

undetermined orientation as demonstrated in **Figure 4.4**. Nearby gauge stations indicate that the precipitation rate was 0 mm whilst the fluvial discharge was approximately 411 m^3/s on that day. The wind speed and direction were 27.7 km/h in north-west direction, and the tide level was confirmed as 1.85 m when the significant wave height was 1.149 m with the angle of 282-degree.

In the dry season, a phenomenon arises on 09 May 2020 where the minimal magnitude of sediment plume (roughly 4.8 km into seaward) at the main outlet of the Mitchell River orientates to neither south nor north direction (see in **Figure 4.5**). Accordingly, the pattern of this sediment plume seems to be in the unoriented circumstance relatively to the influences of fluvial discharge, tide, wave and wind conditions. The fluvial discharge of 15 m^3/s and 0 mm of precipitation were reported on that day while 2.59 m of tide level and 0.393 m of significant wave height with 108-degree angle were informed in the hour of this occurrence. The wind direction was reported to be east-north-east oriented with the speed of 13 km/h. **Figure 4.6** shows the variability of the marginal plume extend (approximately 4.5 km from shoreline) shifting to the slightly north direction and corresponding to the direction of the exposed distributary channels within the Mitchell River delta on the 03 June 2020. The reported statistics on the occurrence day were 0 mm for precipitation, 8.4 m^3/s for fluvial discharge, 2.01 m for tide level, 0.699 m for significant wave height and 216-degree for wave direction; the wind speed and direction were 18.4 km/h in east-south-east direction.

Table 4.1: Summary table of the plume orientations and lengths from shoreline into the offshore at the main Mitchell River mouth on specific dates during wet and dry seasons in 2020.

	Dates	Seasons	Plume Directions	Plume Length (km)
1	15 / 01 / 2020	Wet	S	7
2	14 / 02 / 2020	Wet	Unidentified	13.1
3	20 / 03 / 2020	Wet	S	15.3
4	09 / 05 / 2020	Dry	Unoriented	4.8
5	03 / 06 / 2020	Dry	N	4.5
6	28 / 07 / 2020	Dry	N	5.8
7	11 / 09 / 2020	Dry	N	5.9

Table 4.2: Summary table of daily rainfall, discharge, wind direction and wind speed statistics recorded on specific dates during wet and dry seasons in 2020. Daily wind direction and speed data are observed on 9 am at the Kowanyama station by the Bureau of Meteorology.

	Dates	Rainfall (mm)	Discharge (m^3/s)	Wind Direction	Wind Speed (km/h)
1	15 / 01 / 2020	0	8	NE	9.4
2	14 / 02 / 2020	0	411	NW	27.7
3	20 / 03 / 2020	0	210	ESE	9.4
4	09 / 05 / 2020	0	15	ENE	13
5	03 / 06 / 2020	0	8.4	ESE	18.4
6	28 / 07 / 2020	0	1.8	SE	18.2
7	11 / 09 / 2020	0	0.37	ESE	19

Table 4.3: Summary table of hourly tide, wave height and wave direction statistics recorded on specific dates during wet and dry seasons in 2020.

	Dates	Time	Tide (m)	Wave Height (m)	Wave Direction (degree)
1	15 / 01 / 2020	10:50 am	0.96	0.217	298
2	14 / 02 / 2020	10:50 am	1.85	1.149	282
3	20 / 03 / 2020	10:50 am	2.39	0.382	95
4	09 / 05 / 2020	10:50 am	2.59	0.393	108
5	03 / 06 / 2020	10:50 am	2.01	0.699	216
6	28 / 07 / 2020	10:50 am	2.33	0.661	225
7	11 / 09 / 2020	10:50 am	1.33	0.302	99

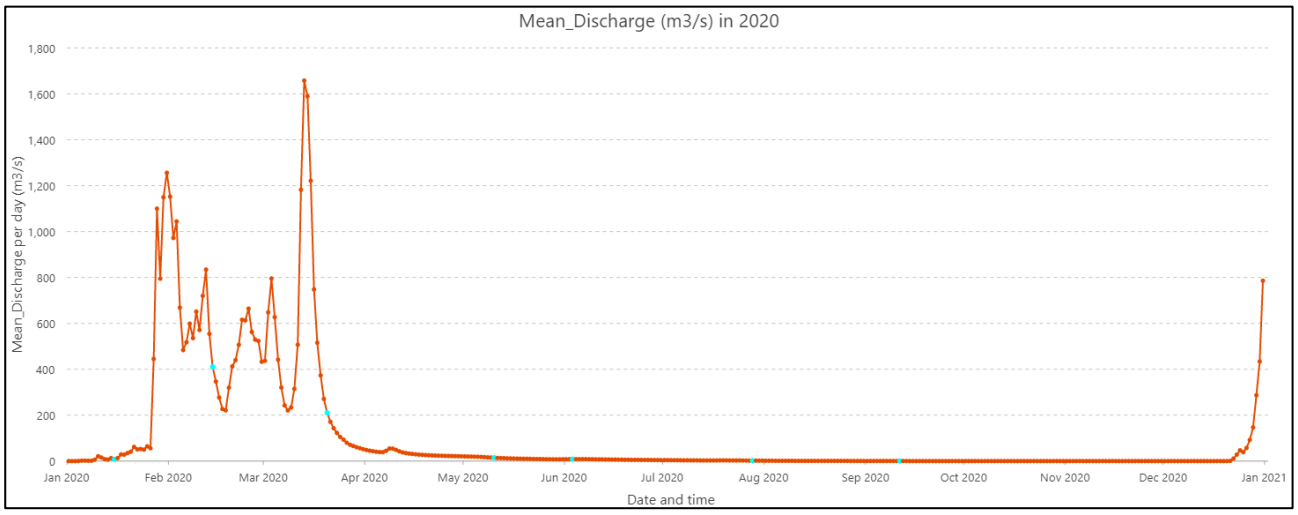

Figure 4.1 Graph of daily discharge per day (in m^3/s) in 2020. Blue highlight spots represent the selected dates for analysis.

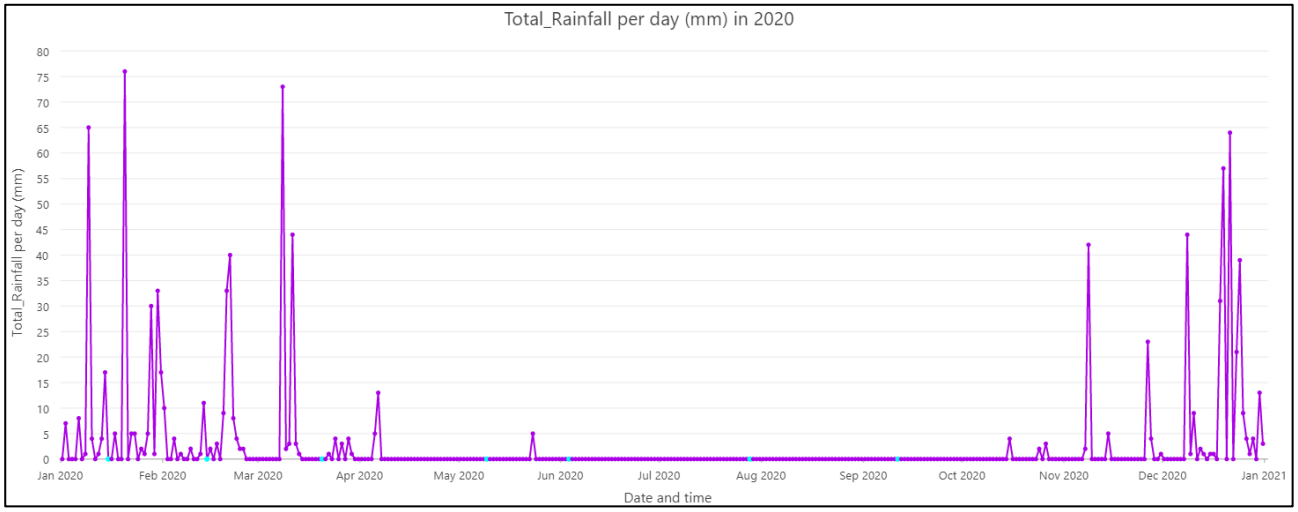

Figure 4.2 Graph of daily rainfall per day (in mm) in 2020. Blue highlight spots represent the selected dates for analysis.

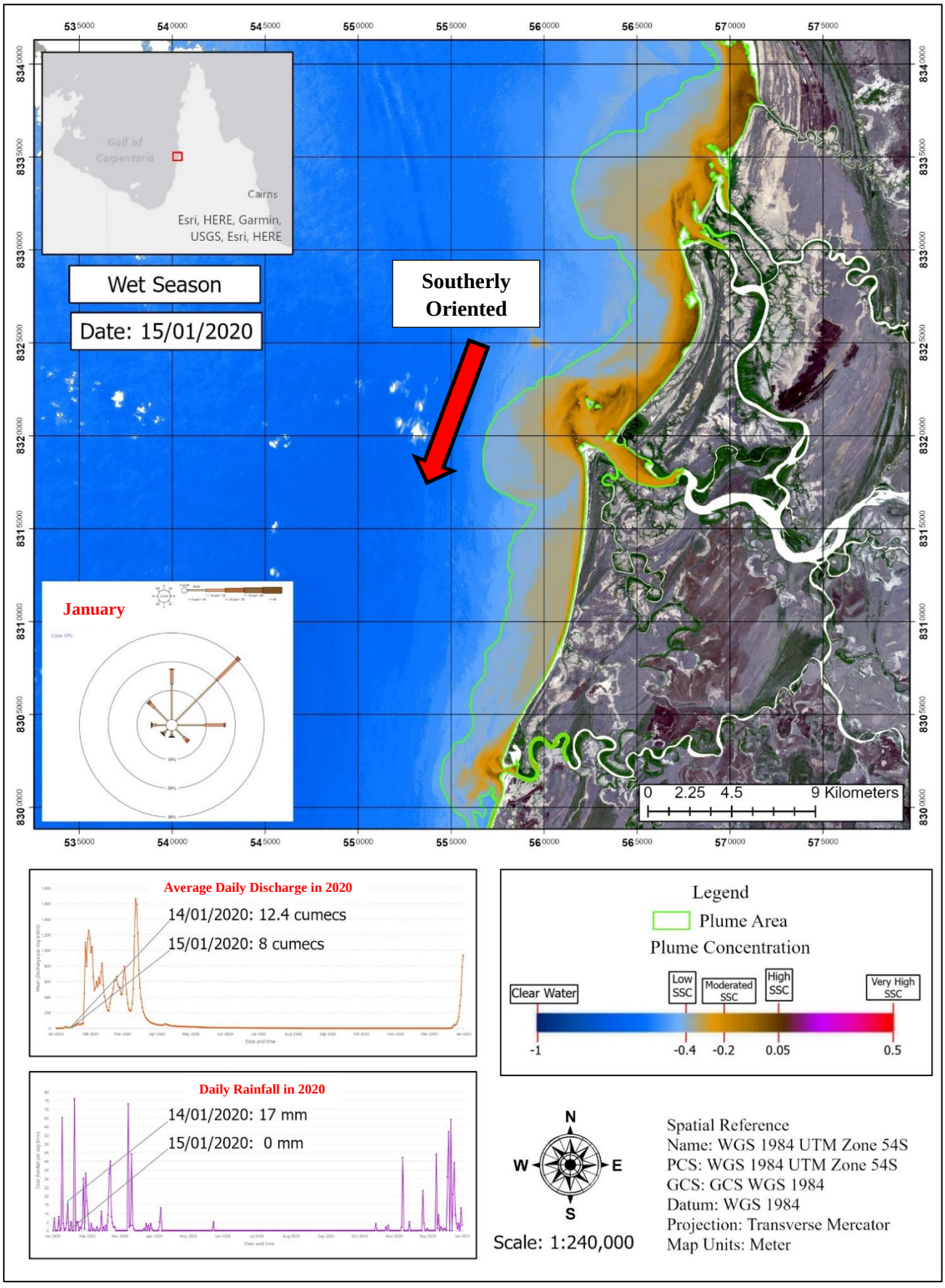

Figure 4.3 Sediment Plume Orientation, Dimension and Concentration in Wet Season on 15 January 2020. Wind roses represented in maps and appendices are aggregated monthly at the Kowanyama station by the Bureau of Meteorology. (Note: cumec = m^3/s for discharge)

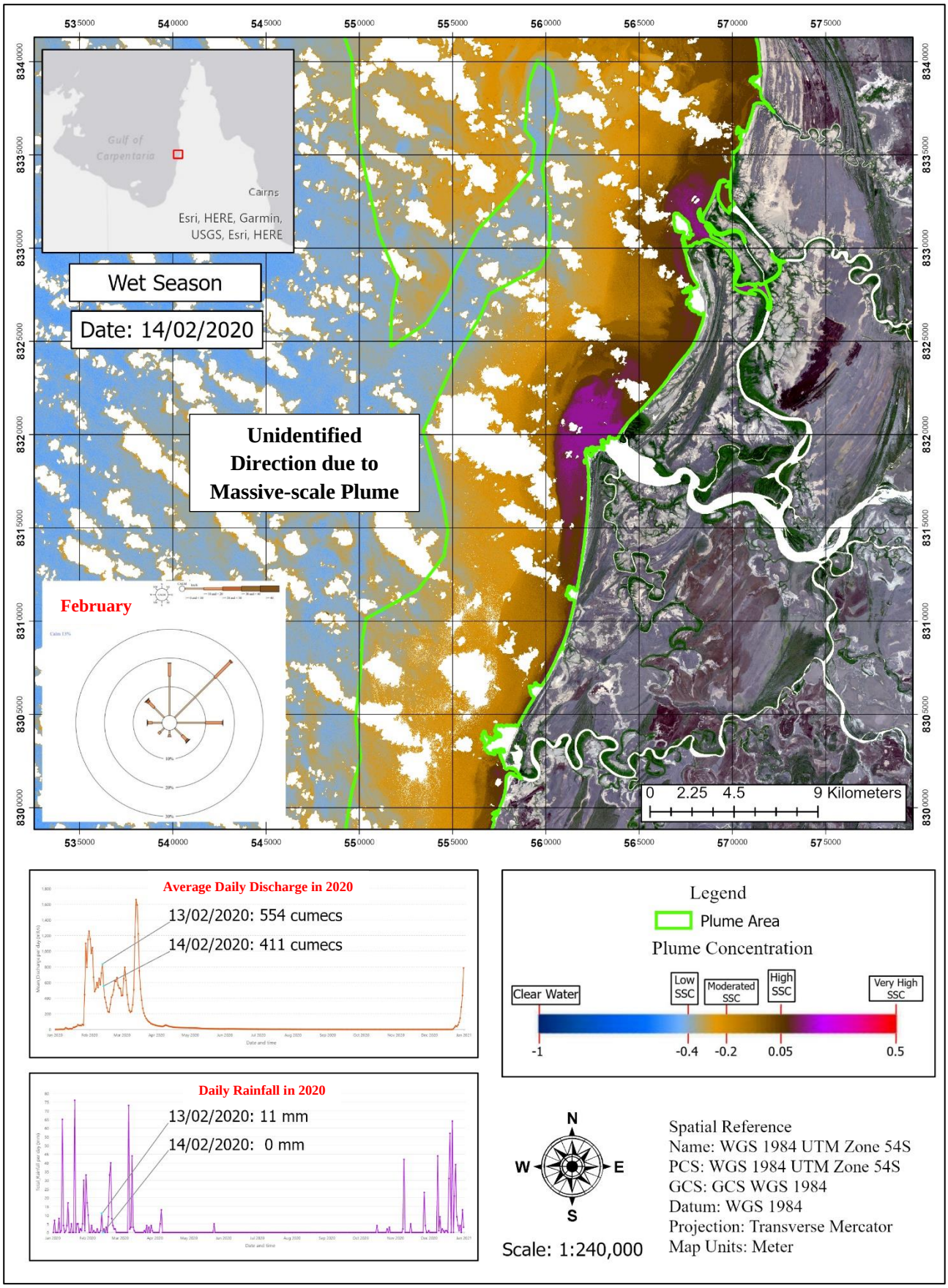

Figure 4.4 Sediment Plume Orientation, Dimension and Concentration in Wet Season on 14 February 2020. Wind roses represented in maps and appendices are aggregated monthly at the Kowanyama station by the Bureau of Meteorology. (Note: cumec = m^3/s for discharge)

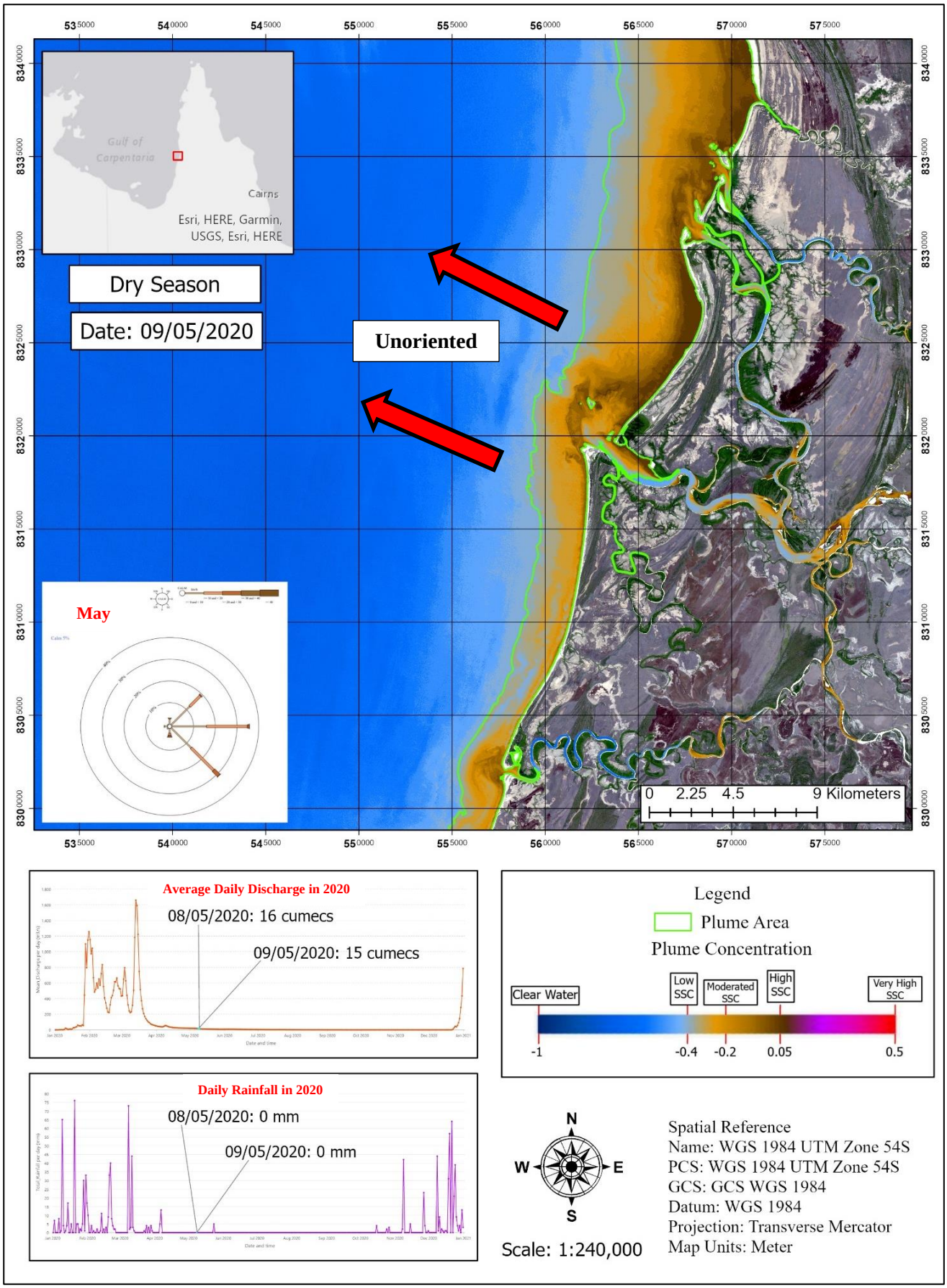

Figure 4.5 Sediment Plume Orientation, Dimension and Concentration in Dry Season on 09 May 2020. Wind roses represented in maps and appendices are aggregated monthly at the Kowanyama station by the Bureau of Meteorology. (Note: cumec = m^3/s for discharge)

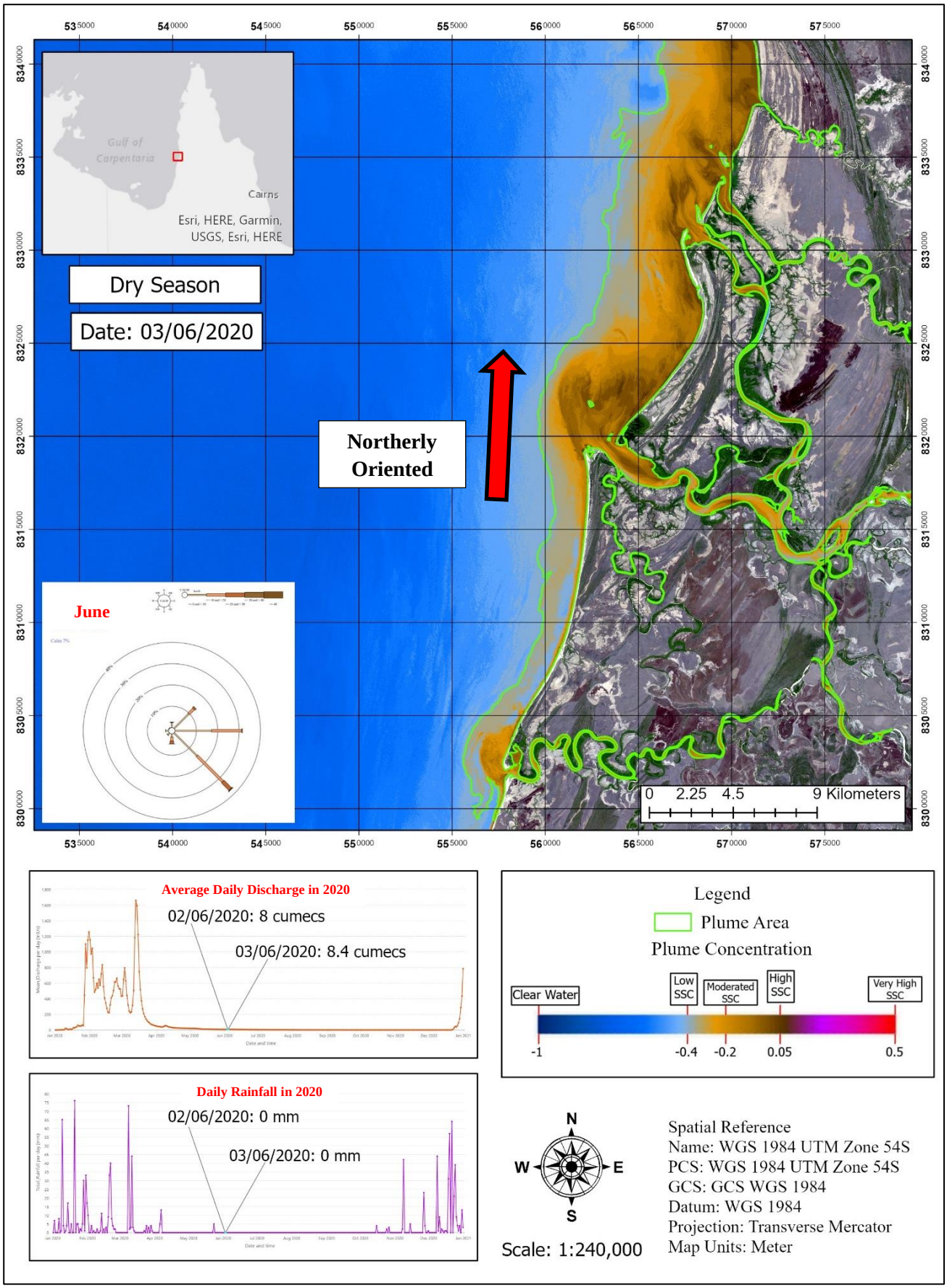

Figure 4.6 Sediment Plume Orientation, Dimension and Concentration in Dry Season on 03 June 2020. Wind roses represented in maps and appendices are aggregated monthly at the Kowanyama station by the Bureau of Meteorology. (Note: cumec = m^3/s for discharge)

4.1.2. Seasonal Variations in 2021 (24/01/2021 to 12/08/2021)

Appendix 3-08, **Appendix 3-09**, **Appendix 3-10**, **Appendix 3-11**, **Appendix 3-12**, **Appendix 3-13** and **Appendix 3-14** show the 7 results of seasonal turbidity identification from specific dates of wet and dry seasons in 2021 (see in **Table 3.2**) while **Appendix 5-02** revealed the overall evaluation map of these scenarios. The dimensions and orientations of the sediment plumes occurrences in 3 specified months of wet season and 4 specified months in dry season are mainly demonstrated in these maps where the plumes orientations are exclusively designated in **Table 4.4**. It is simplified that the orientations of sediment plumes were predominantly to the south direction in the wet season whilst they shifted to the north direction in the dry season. However, a sediment plume phenomenon on 14 May in the dry season is recognised as unoriented pattern.

A crucial plume image on 10 March in the wet season and two significances on 14 May and 23 July in the dry season of sediment are systematically analysed correlating to statistics of daily precipitation, fluvial discharge and wind data as represented in **Table 4.5** and hourly statistics of tide and wave data are indicated in **Table 4.6**. The graphs of daily precipitation and fluvial discharge for the entire year of 2021 are additionally displayed in **Figure 4.7** and **Figure 4.8**, respectively.

In the wet season, the enormous sediment plume dimension (roughly 12.5 km into the offshore) on 10 March 2021 is shown in **Figure 4.9** orientated to the southwest direction with 0 mm of the precipitation rate and 528 m^3/s of the fluvial discharge while the wind speed was 11 km/h, and the wind direction was oriented to the eastward. The tide level was reported to be 2.21 m, yet the significant wave height and direction could not be obtainable on that day.

In the dry season, **Figure 4.10** demonstrates the instinctive trend occurred on 14 May 2021 where the sizable sediment plume extend (6.2 km from the shoreline) at the main outlet of the Mitchell River does not adjusts to either south or north direction. This sediment plume pattern appears to be in an impartial incidence relatively to the effects of fluvial discharge, tide, wave and wind conditions. The statistics on the occurrence day were reported to be 0 mm for precipitation, 51.6 m^3/s for fluvial discharge, 3.02 m for tide level, 13 km/h for wind speed and north-north-east for wind direction while the significant wave height and wave direction were unavailable.

On the 23 July 2021, the inconsistency of the minimal plume magnitude (3.9 km into seaward) switched marginally to the north direction and parallel to the exposed distributary channels orientation within the Mithcell River delta (as displayed in **Figure 4.11**). The fluvial discharge of 25.3 m^3/s and 0 mm of precipitation with 9.4 km/h of wind speed and north-north-east of wind direction are informed on that day while 2.20 m of tide level are likewise notified in the hour of this occurrence, yet the significant wave height and direction were not available.

Table 4.4: Summary table of the plume orientations and lengths from shoreline into the offshore at the main Mitchell River mouth on specific dates during wet and dry seasons in 2021.

	Dates	Seasons	Plume Directions	Plume Length (km)
1	24 / 01 / 2021	Wet	S	7.2
2	10 / 03 / 2021	Wet	S	12.5
3	14 / 04 / 2021	Wet	S	8.4
4	14 / 05 / 2021	Dry	Unoriented	6.2
5	08 / 06 / 2021	Dry	N	3.6
6	23 / 07 / 2021	Dry	N	3.9
7	12 / 08 / 2021	Dry	N	3.7

Table 4.5 Summary table of daily rainfall, discharge, wind direction and wind speed statistics recorded on specific dates during wet and dry seasons in 2021. Daily wind direction and speed data are observed on 9 am at the Kowanyama station by the Bureau of Meteorology.

	Dates	Rainfall (mm)	Discharge (m^3/s)	Wind Direction	Wind Speed (km/h)
1	24 / 01 / 2021	0	1059	ENE	14.8
2	10 / 03 / 2021	0	528	E	11.2
3	14 / 04 / 2021	0	51.7	ESE	18.4
4	14 / 05 / 2021	0	51.6	NNE	13
5	08 / 06 / 2021	0	35.6	ESE	13
6	23 / 07 / 2021	0	25.3	NNE	9.4
7	12 / 08 / 2021	0	18.1	E	14.8

Table 4.6 Summary table of hourly tide, wave height and wave direction statistics recorded on specific dates during wet and dry seasons in 2021.

	Dates	Time	Tide (m)	Wave Height (m)	Wave Direction (degree)
1	24 / 01 / 2021	10:50 am	2.03	N/A	N/A
2	10 / 03 / 2021	10:50 am	2.21	N/A	N/A
3	14 / 04 / 2021	10:50 am	2.61	N/A	N/A
4	14 / 05 / 2021	10:50 am	3.02	N/A	N/A
5	08 / 06 / 2021	10:50 am	2.26	N/A	N/A
6	23 / 07 / 2021	10:50 am	2.20	N/A	N/A
7	12 / 08 / 2021	10:50 am	3.20	N/A	N/A

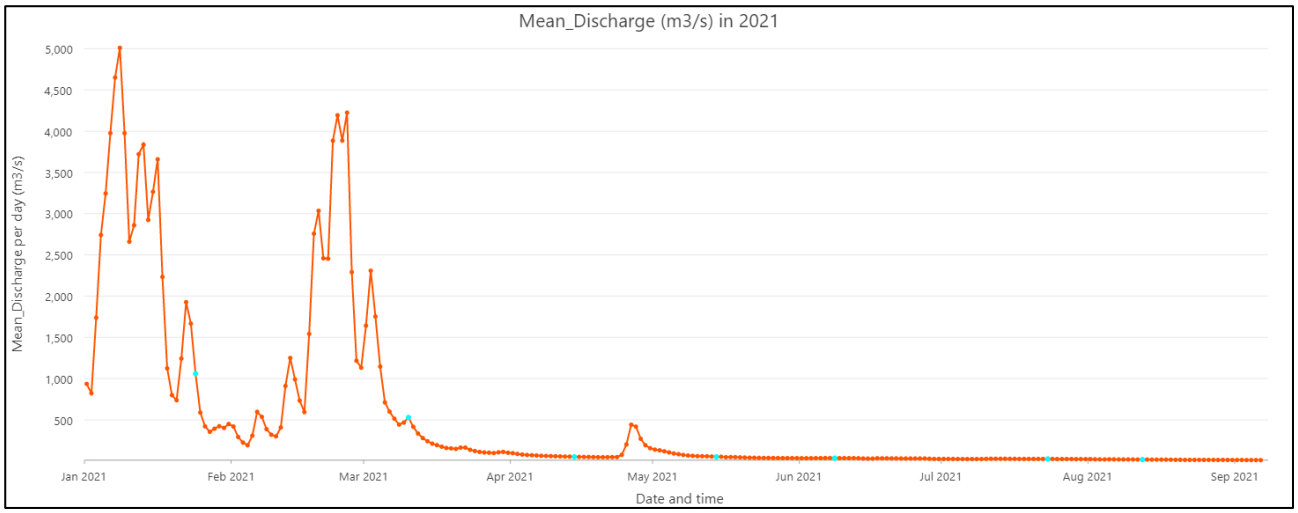

Figure 4.7 Graph of daily discharge per day (in m^3/s) in 2021. Blue highlight spots represent the selected dates for analysis.

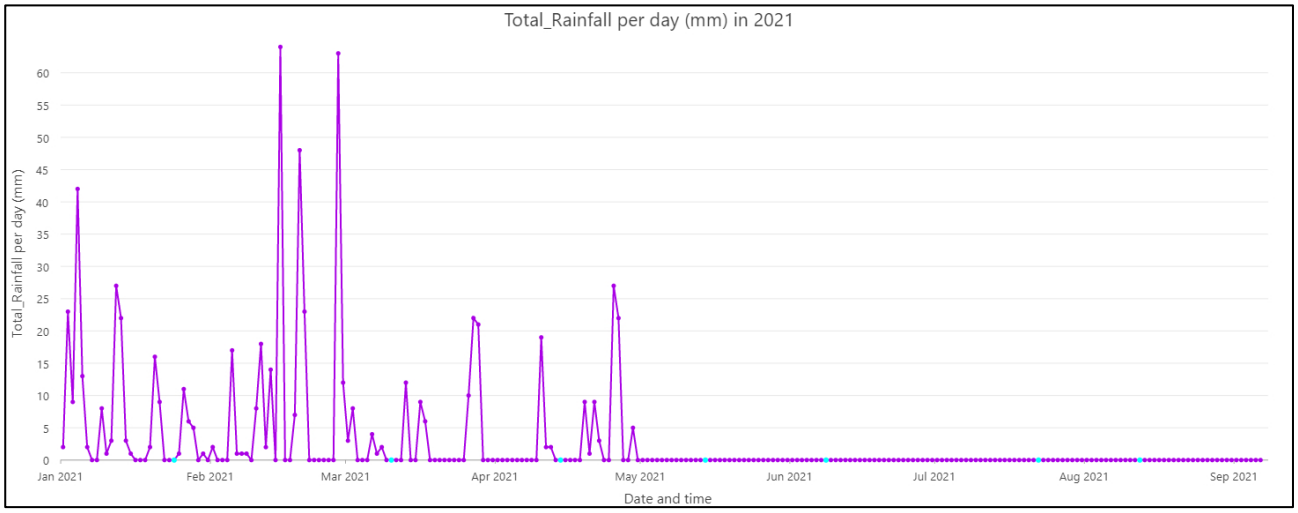

Figure 4.8 Graph of daily rainfall per day (in m^3/s) in 2021. Blue highlight spots represent the selected dates for analysis.

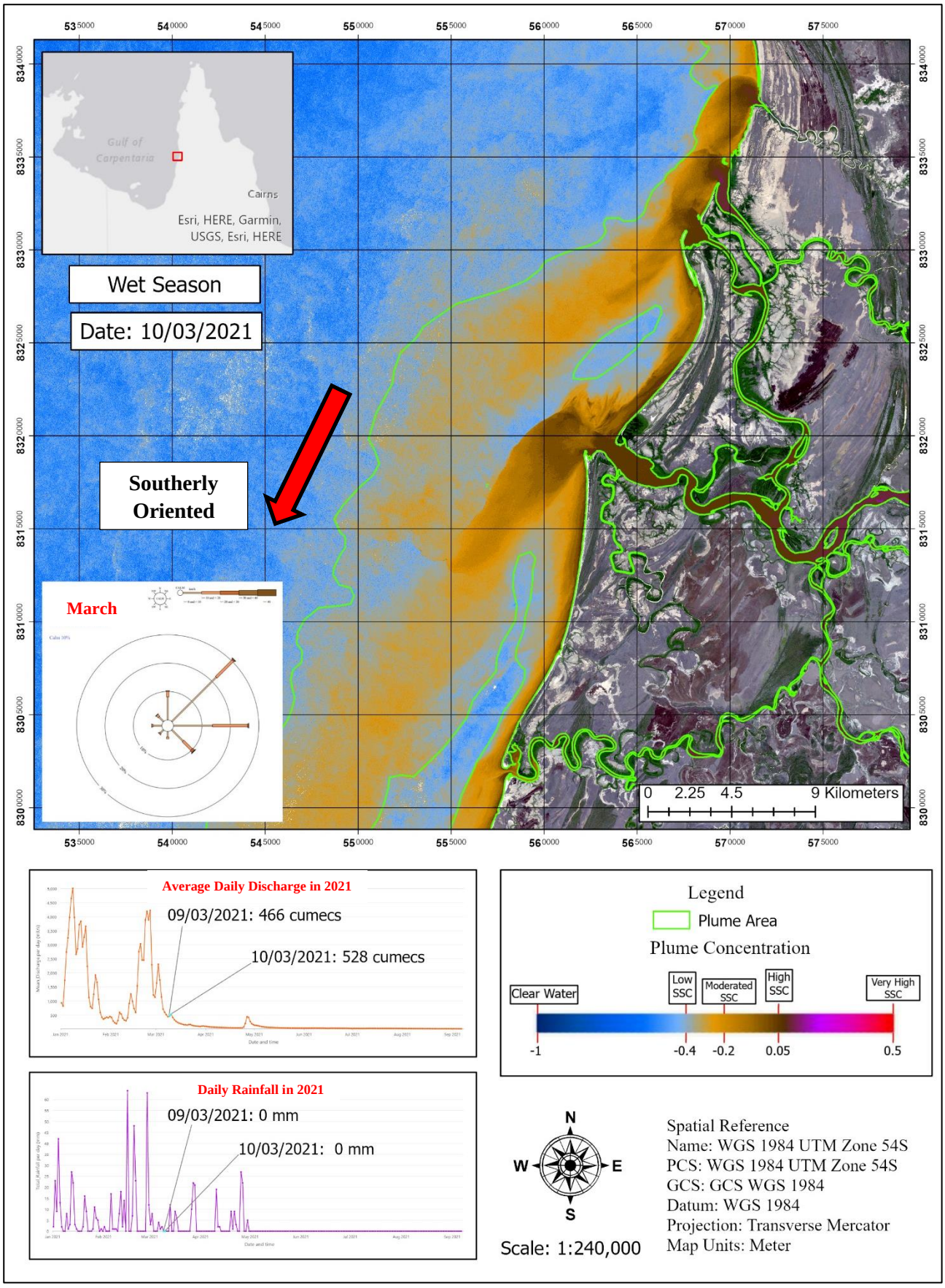

Figure 4.9 Sediment Plume Orientation, Dimension and Concentration in Wet Season on 10 March 2021. Wind roses represented in maps and appendices are aggregated monthly at the Kowanyama station by the Bureau of Meteorology. (Note: cumec = m^3/s for discharge)

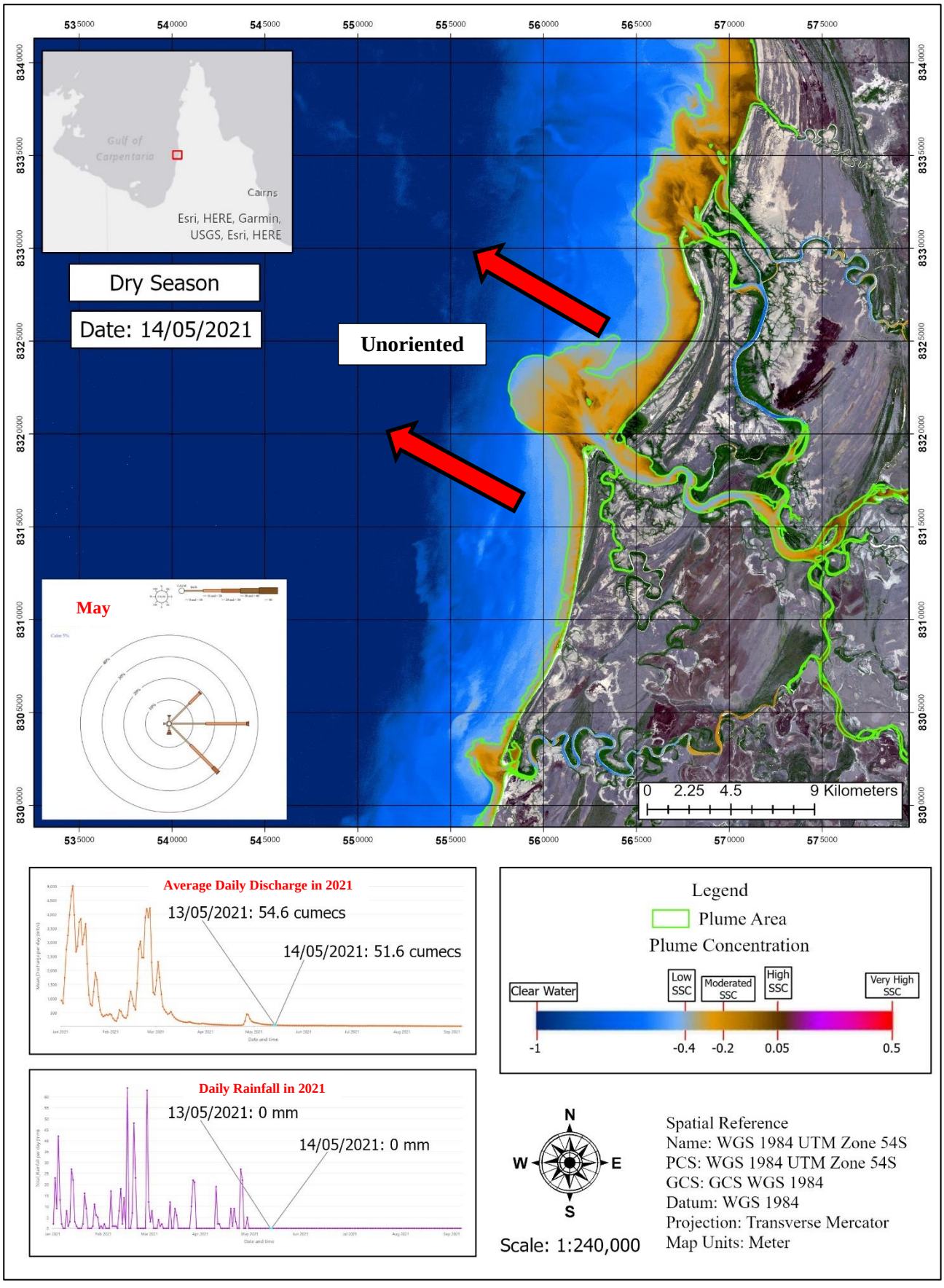

Figure 4.10 Sediment Plume Orientation, Dimension and Concentration in Dry Season on 14 May 2021. Wind roses represented in maps and appendices are aggregated monthly at the Kowanyama station by the Bureau of Meteorology. (Note: cumec = m^3/s for discharge)

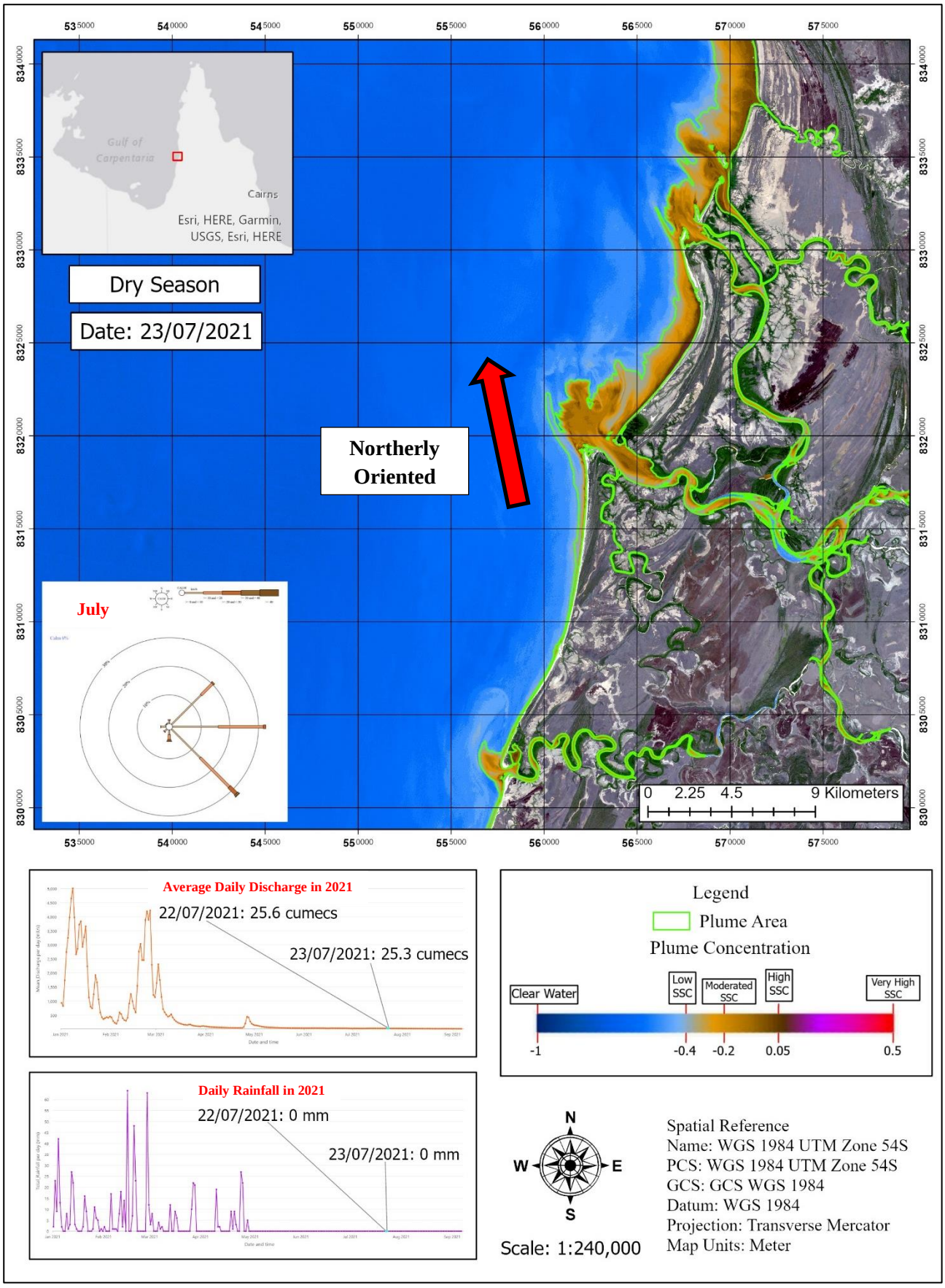

Figure 4.11 Sediment Plume Orientation, Dimension and Concentration in Dry Season on 14 July 2021. Wind roses represented in maps and appendices are aggregated monthly at the Kowanyama station by the Bureau of Meteorology. (Note: cumec = m^3/s for discharge)

4.2. Seasonal Variations of Mouth Bar Geometry

A total of 14 images over the study period were analysed to detect in mouth bar geometries and their subaqueous distributary channels deposited by the Main Mitchell River. Seven of the images were from 2020 (3 of wet season and 4 of dry season) and seven from 2021 (3 of wet season and 4 of dry season). The 2020 results are represented in **Appendix 4-01**, **Appendix 4-02**, **Appendix 4-03**, **Appendix 4-04**, **Appendix 4-05**, **Appendix 4-06** and **Appendix 4-07** for 15 January, 14 February, 20 March, 09 May, 03 June, 28 July and 11 September, respectively whilst the results in 2021 are signified in **Appendix 4-08**, **Appendix 4-09**, **Appendix 4-10**, **Appendix 4-11**, **Appendix 4-12**, **Appendix 4-13** and **Appendix 4-14** for 24 January, 10 March, 14 April, 14 May, 08 June, 23 July and 12 August, respectively. Furthermore, **Appendix 6-01** and **Appendix 6-02** show the overall evaluation of mouth bar geometries in 2020 and 2021, respectively.

Although 14 detected mouth bar patterns were mapped, only 5 distributary channels within the mouth bars could be optically identified for mapping, which specific dates summarised in **Table 4.7**. This table reveals that two time periods in 2020 (15 January and 11 September) and three dates in 2021 (14 May, 08 June and 12 August) are the phases in which the distributary channels within the mouth bars could be optically detected. Accordingly, these 5 results are considered significant and thoroughly analysed and interpreted correlating to the statistics of fluvial discharge, precipitation, tides, waves, and wind conditions as summarily exhibited in **Table 4.8** and **Table 4.9** for daily and hourly observations, respectively.

On 15 January 2020, **Figure 4.12** revealed the pattern of wet seasonal mouth bar (about 4.1 km into offshore) containing some optical structure of distributary channels, in particularly at the adjacent region of the main outlet of the Mitchell River mouth. However, the distributary channels could not be detected at the edge portions of the mouth bar. No rainfall condition was reported on the day, and the fluvial discharge coming out from the Mitchell River was 8 m^3/s. The wind direction and speed on that day could not be observed while the significant wave height was 0.217 m at the direction of 298-degree angle; the tide was reported to be 0.96 m. On 11 September 2020, the boundary of dry seasonal mouth bar (roughly 3.5 km from the main river mouth) was identified as demonstrated in **Figure 4.13** with more revealable proportions of the distributary channels within this asymmetrical delta. The reported statistics on the occurrence day are 0 mm for precipitation, 0.37 m^3/s for fluvial discharge, 9.4 km/h for the wind speed with north-east direction, 1.33 m for tide level, 0.302 m for significant wave height and 99-degree for wave direction.

On 14 May 2021, poorly defined sections of distributary channels along the dry seasonal mouth bar margin (approximately 3.8 km seaward) were mapped (**Figure 4.14**). It was difficult to identify the pattern of these channels due to some optical missing parts. The fluvial discharge of 51.6 m^3/s and 0 mm of precipitation with 13 km/h of wind speed and north-north-east of wind direction are informed on that day while 3.02 m of tide level are likewise notified in the hour of this occurrence, yet the

significant wave height and direction could not be accessible. On 08 June 2021, an architecture of dry seasonal mouth bar (approximately 3.6 km into offshore) was detected alongside the roughly completed structures of the distributary channels as displayed in **Figure 4.15**. With 0 mm of the precipitation rate and 35.6 m^3/s of the fluvial discharge are reported, the wind speed is informed to be 13 km/h while the wind direction is oriented to the east-south-east direction. The tide level is reported to be 2.26 m, yet the significant wave height and direction could not be obtainable on that day. On 12 August 2021, another dry seasonal mouth bar geometry (roughly 3.7 km from the river mouth) was discovered with the ideal pattern of distributary channels containing useful information (**Figure 4.16**). The statistics on the occurrence day are reported to be 0 mm for precipitation, 18.1 m^3/s for fluvial discharge, 3.20 m for tide level, 4.8 km/h for wind speed and eastward directed for wind direction while the significant wave height and wave direction are unavailable.

Table 4.7: Summary table of the specified mouth bar geometries with their distributary channels and lengths from the shoreline into the offshore at the main Mitchell River mouth on 5 specific dates during wet and dry seasons in 2020 to 2021.

	Dates	Seasons	Detected Channels	Mouth Bar Length (km)
1	15 / 01 / 2020	Wet	Yes	4.1
2	11 / 09 / 2020	Dry	Yes	3.5
3	14 / 05 / 2021	Dry	Yes	3.8
4	08 / 06 / 2021	Dry	Yes	3.6
5	12 / 08 / 2021	Dry	Yes	3.7

Table 4.8: Summary table of daily rainfall, discharge, wind direction and wind speed statistics related to 5 dates of specified mouth bar in 2020 and 2021. Daily wind direction and speed data are observed on 9 am at the Kowanyama station by the Bureau of Meteorology.

	Dates	Rainfall (mm)	Discharge (m^3/s)	Wind Direction	Wind Speed (km/h)
1	15 / 01 / 2020	0	8	NE	9.4
2	11 / 09 / 2020	0	0.37	ESE	19
3	14 / 05 / 2021	0	51.6	NNE	13
4	08 / 06 / 2021	0	35.6	ESE	13
5	12 / 08 / 2021	0	18.1	E	14.8

Table 4.9: Summary table of hourly tide, wave height and wave direction statistics related to 5 dates of specified mouth bar in 2020 and 2021.

	Dates	Time	Tide (m)	Wave Height (m)	Wave Direction (degree)
1	15 / 01 / 2020	10:50 am	0.96	0.217	298
2	11 / 09 / 2020	10:50 am	1.33	0.302	99
3	14 / 05 / 2021	10:50 am	3.02	N/A	N/A
4	08 / 06 / 2021	10:50 am	2.26	N/A	N/A
5	12 / 08 / 2021	10:50 am	3.20	N/A	N/A

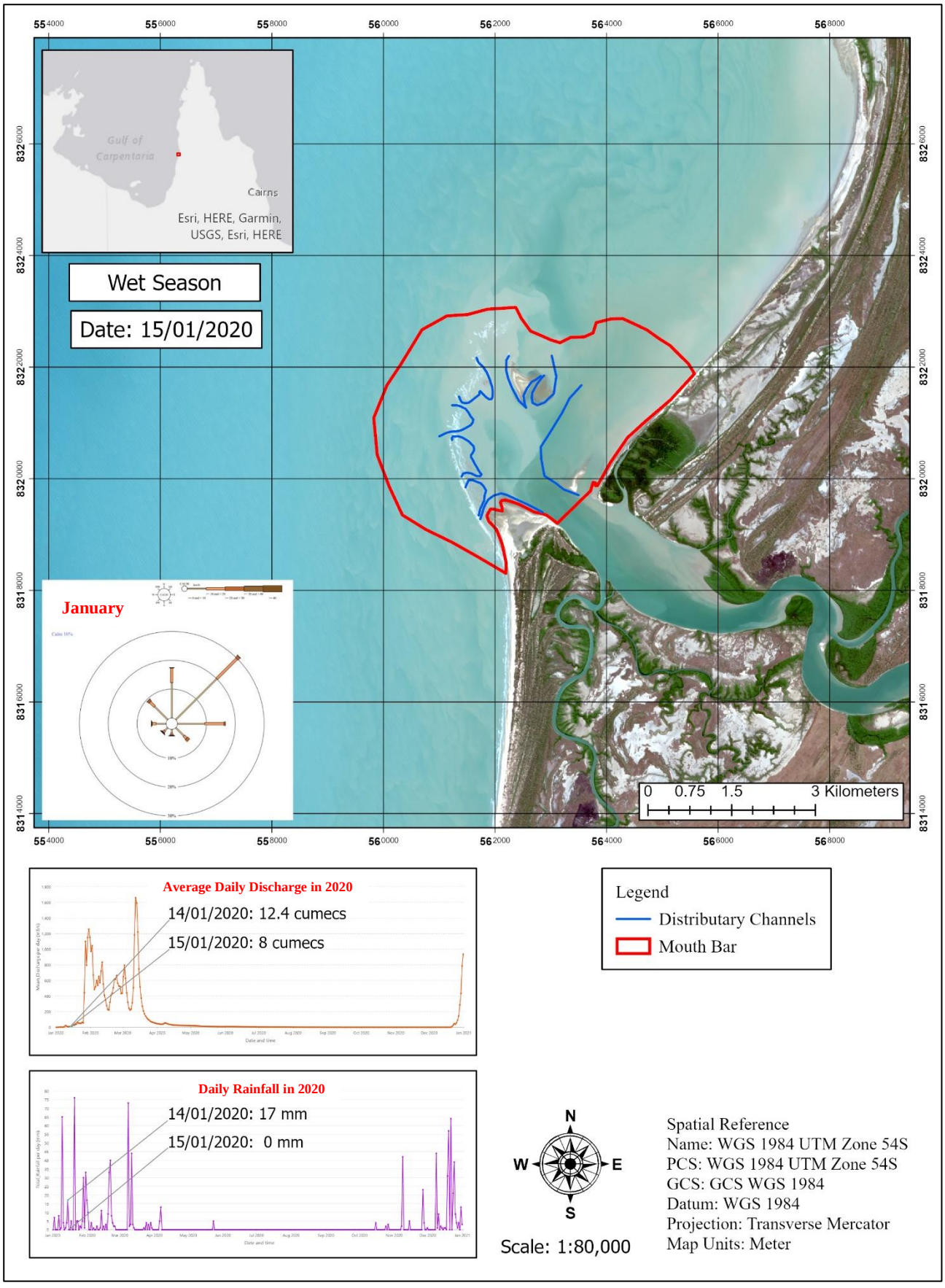

Figure 4.12 Mouth bar Geometry included its Boundary and Distributaty Channel in Wet Season on 15 January 2020. Wind roses represented in maps and appendices are aggregated monthly at the Kowanyama station by the Bureau of Meteorology. (Note: cumec = m^3/s for discharge)

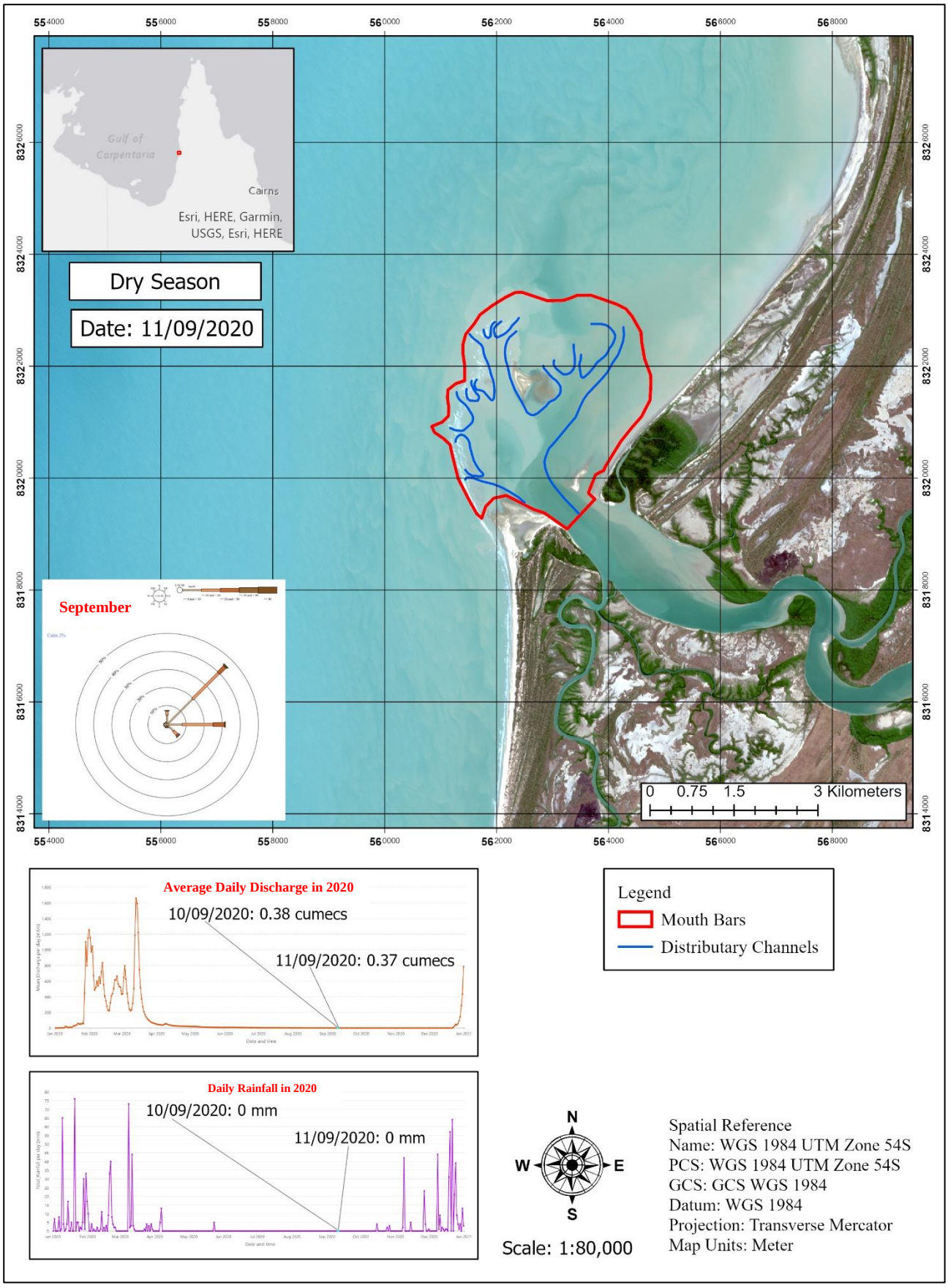

Figure 4.13 Mouth bar Geometry included its Boundary and Distributaty Channel in Dry Season on 11 September 2020. Wind roses represented in maps and appendices are aggregated monthly at the Kowanyama station by the Bureau of Meteorology. (Note: cumec = m^3/s for discharge)

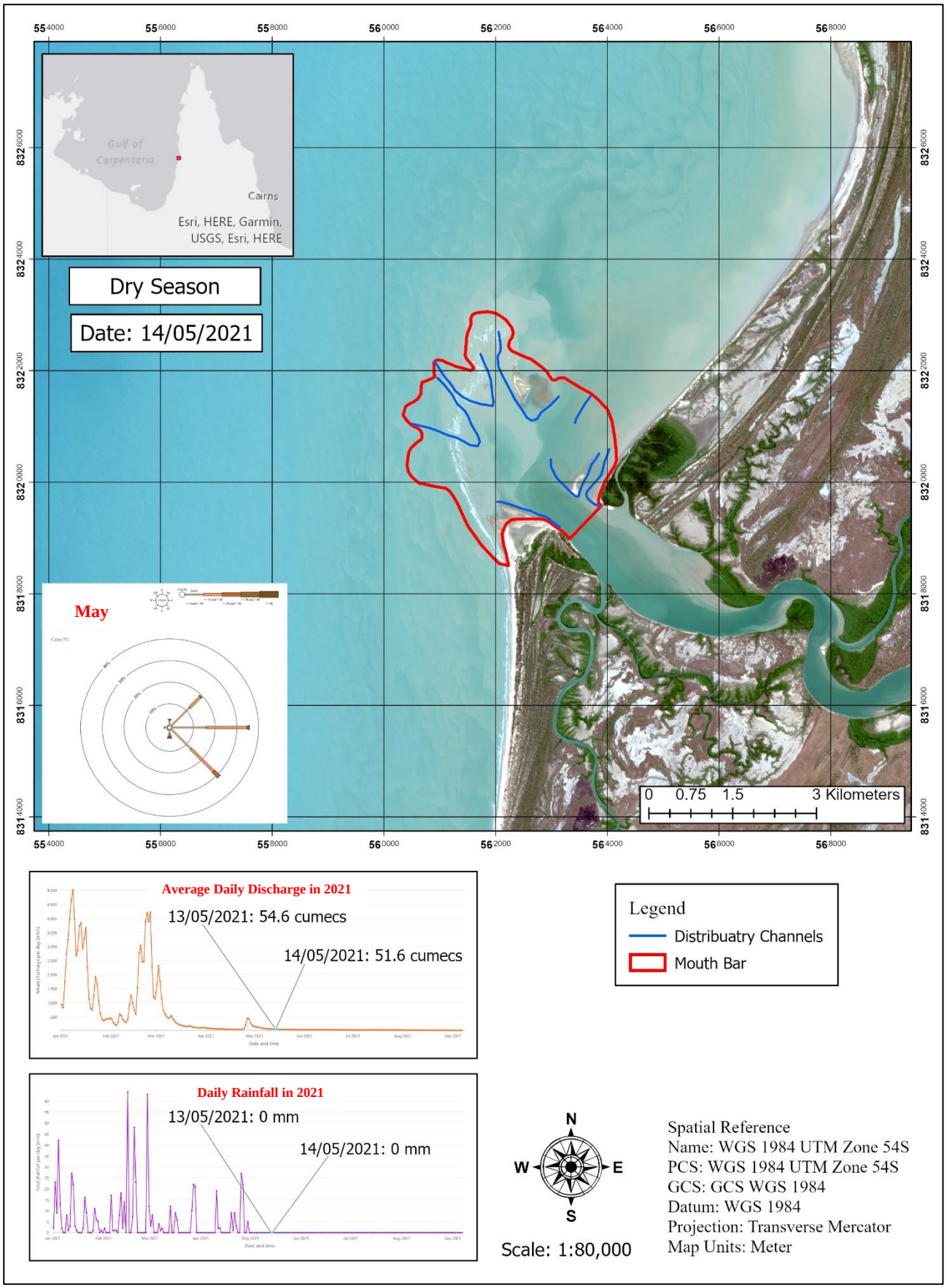

Figure 4.14 Mouth bar Geometry included its Boundary and Distributaty Channel in Dry Season on 14 May 2021. Wind roses represented in maps and appendices are aggregated monthly at the Kowanyama station by the Bureau of Meteorology. (Note: cumec = m^3/s for discharge)

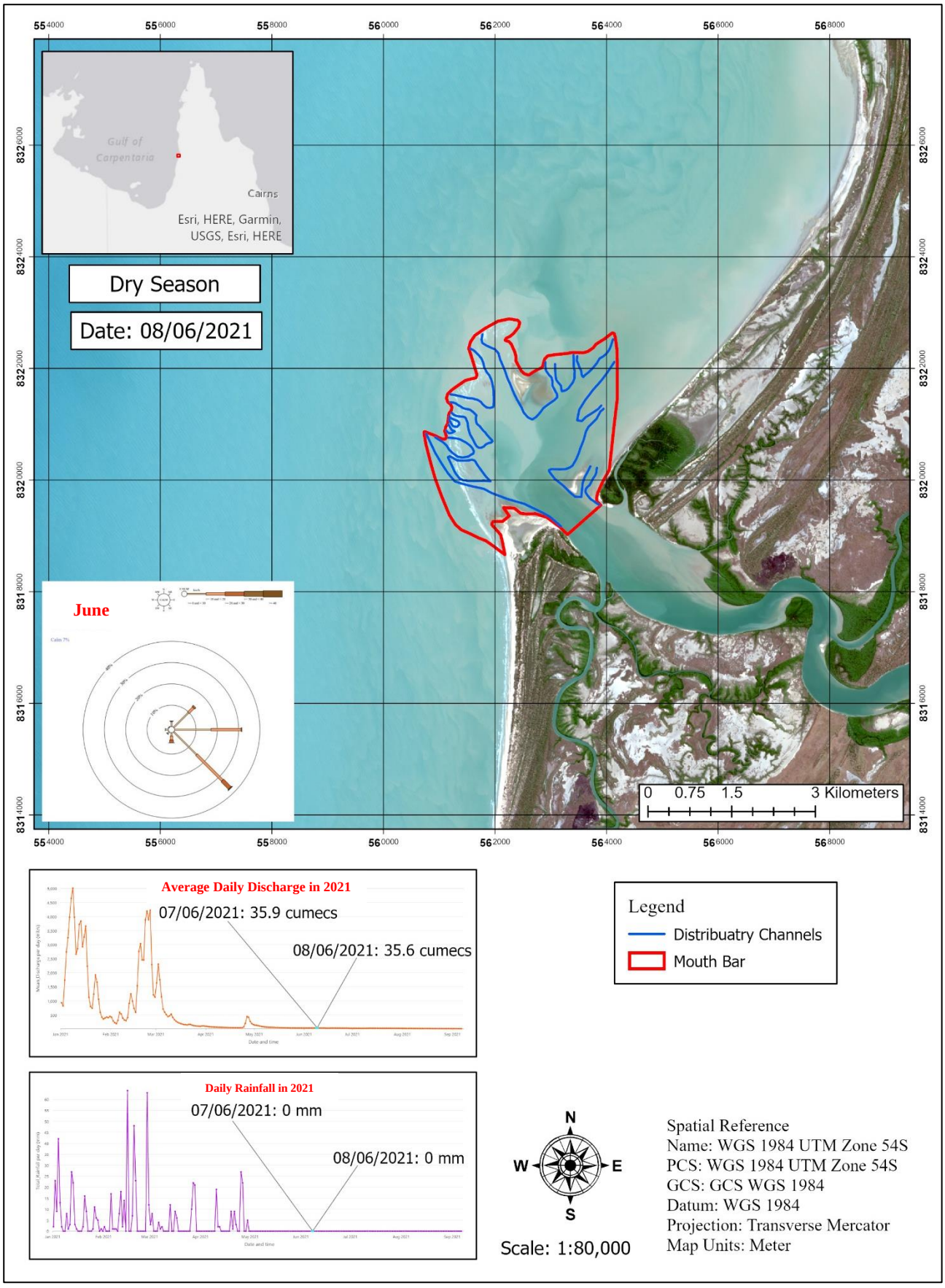

Figure 4.15 Mouth bar Geometry included its Boundary and Distributaty Channel in Dry Season on 08 June 2021. Wind roses represented in maps and appendices are aggregated monthly at the Kowanyama station by the Bureau of Meteorology. (Note: cumec = m^3/s for discharge)

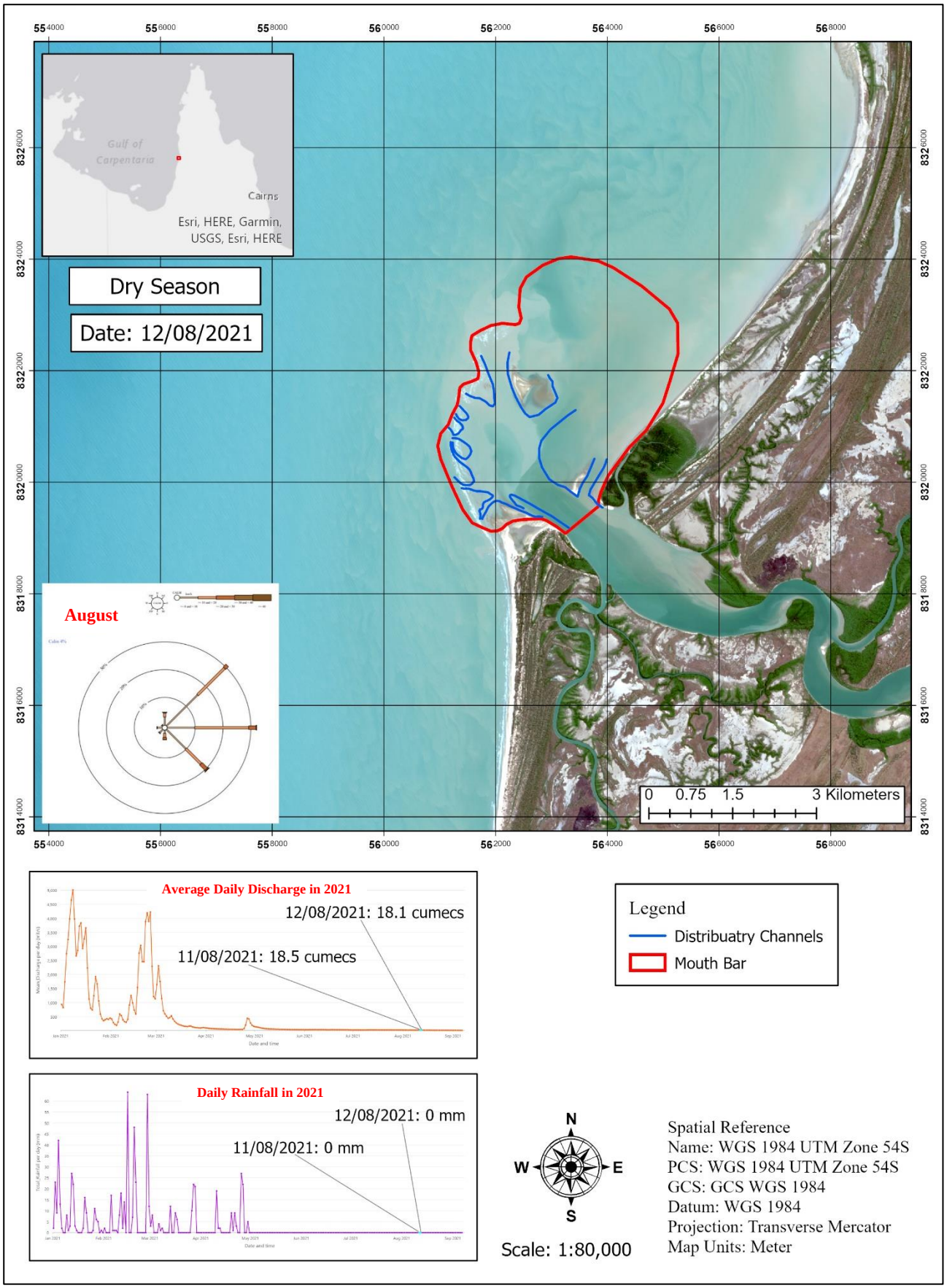

Figure 4.16 Mouth bar Geometry included its Boundary and Distributaty Channel in Dry Season on 12 August 2021. Wind roses represented in maps and appendices are aggregated monthly at the Kowanyama station by the Bureau of Meteorology. (Note: cumec = m^3/s for discharge)

4.3. Seasonal Variability of Turbidity Concentration associated to the Rates of Shoreline Changes

Four analysed images (2 in 2020 and 2 in 2021) were investigated a correlation to the rates of shoreline changes that has been detected by Digital Earth Australia from 1988 to 2019 as demonstrated in **Figure 4.17**, **Figure 4.18**, **Figure 4.19** and **Figure 4.20**.

For the wet season in 2020, **Figure 4.17** illustrates the turbidity that was identified on 15 January 2020. It is noted that the moderate turbidity concentration was found in the main river mouth, and the high turbidity concentration was revealed around the nearshore regions at the north side of the main river mouth. The nearshore regions at the south side, however, noticeably experienced a large scale of low turbidity concentration. **Figure 4.18** demonstrates the detected dry seasonal turbidity occurred in the 03 June 2020. It revealed the considerable extend of high turbidity concentration arose from the main river mouth to the north side in particular the nearshore regions. In contrary to that, the nearshore at the south side is discovered with an extremely minimal magnitude of the low turbidity concentration.

In the wet season of 2021, a high turbidity on 10 March 2021 was detected as represented in **Figure 4.19**. The result indicates the enormous high turbidity concentration amount occurred at the south side of the Mitchell River mouth from the nearshore to offshore regions while the north side of the nearshore region similarly experienced the high turbidity concentration but with lesser amount. It is additionally noticed that an intense minor ratio of very high turbidity concentration was exposed on that territory. In the dry season in 2021, **Figure 4.20** shows the occurrence of water turbidity in the 23 July 2021. This result exhibits the minimal magnitude of very high turbidity concentration scenario on the north nearshore zone while an intermediate high turbidity concentration ratio was suspended in the vicinity of the main river mouth. Nonetheless, the south nearshore territory experienced the insignificant turbidity phenomenon where extreme minimal magnitude wad detected around this area on that day.

These four results additionally imply the occurrence of the erosional coastline at the north nearshore zone where the high and very high turbidity concentration frequently occurred on both wet and dry seasons. At the same time, the coastline progradation is revealed at the south nearshore zone where experienced only the low turbidity phenomenon either on wet or dry season. The rates of shoreline changes from 1988 to 2019 provided from specified hot spots illustrate the erosional rates at the north nearshore zone from – 37 m near the north river mouth to the maximum of -190.86 m and later decreasing to – 20.86 m before it begins to prograde from 159.27 m until 241.91 m at the further north side. The progradation rates at the south nearshore are likewise indicated from the highest of 490.94 m near the south river mouth to 10.1 m and later to 7.1 at the further south spot.

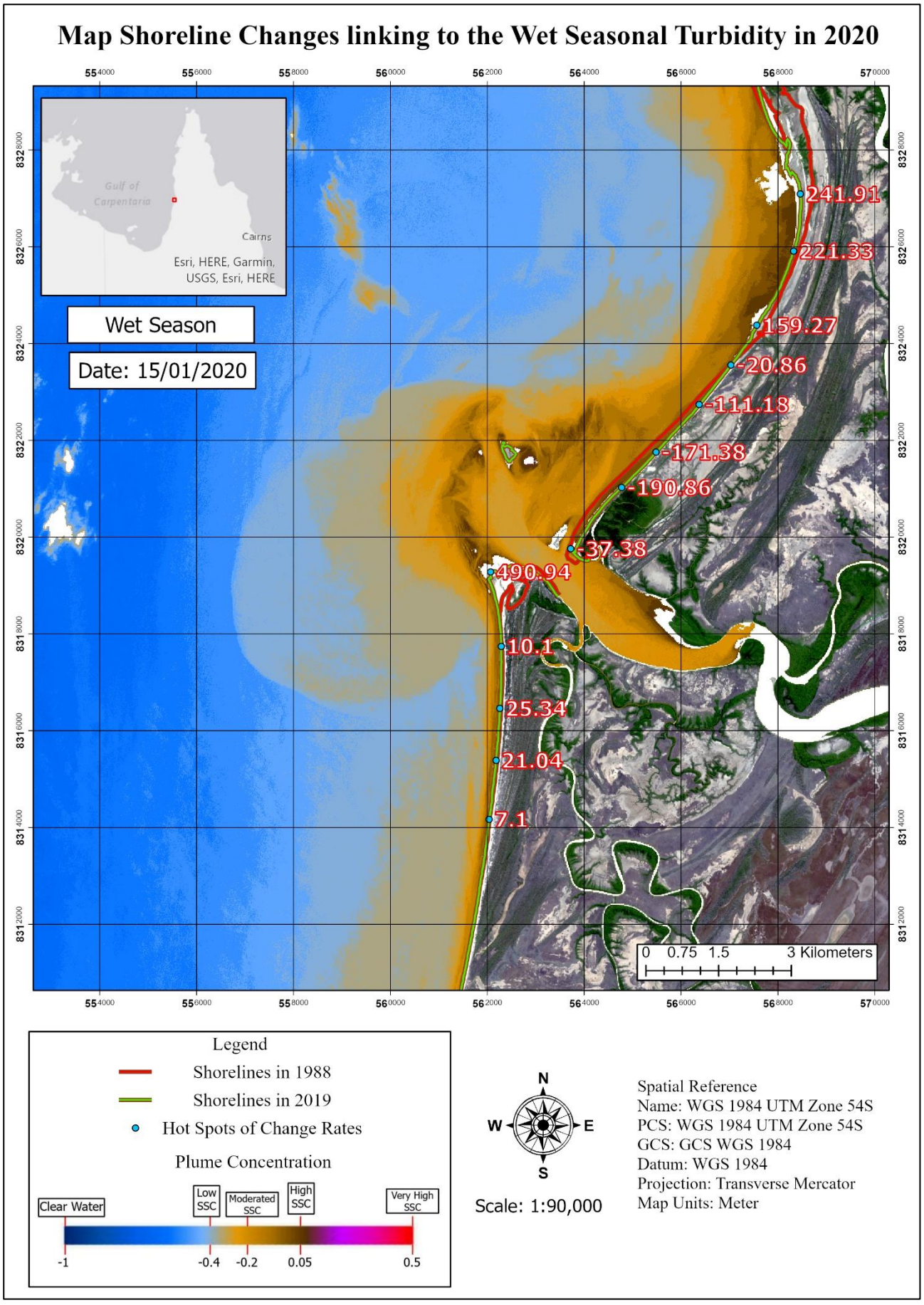

Figure 4.17 Sediment Plume Concentration relative to the rates of shoreline changes (1988 to 2019) in Wet Season on 15 January 2020.

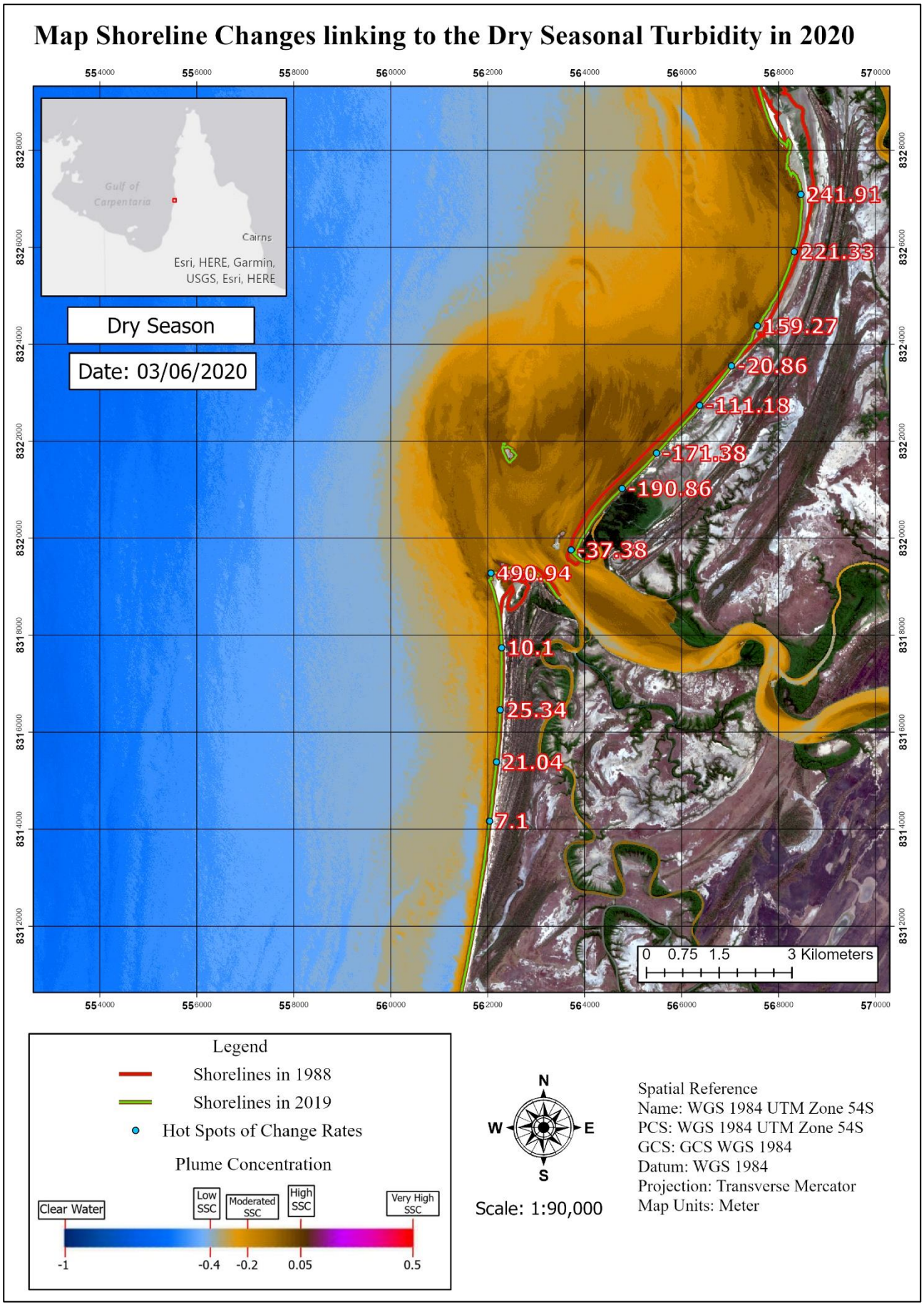

Figure 4.18 Sediment Plume Concentration relative to the rates of shoreline changes (1988 to 2019) in Dry Season on 03 June 2020.

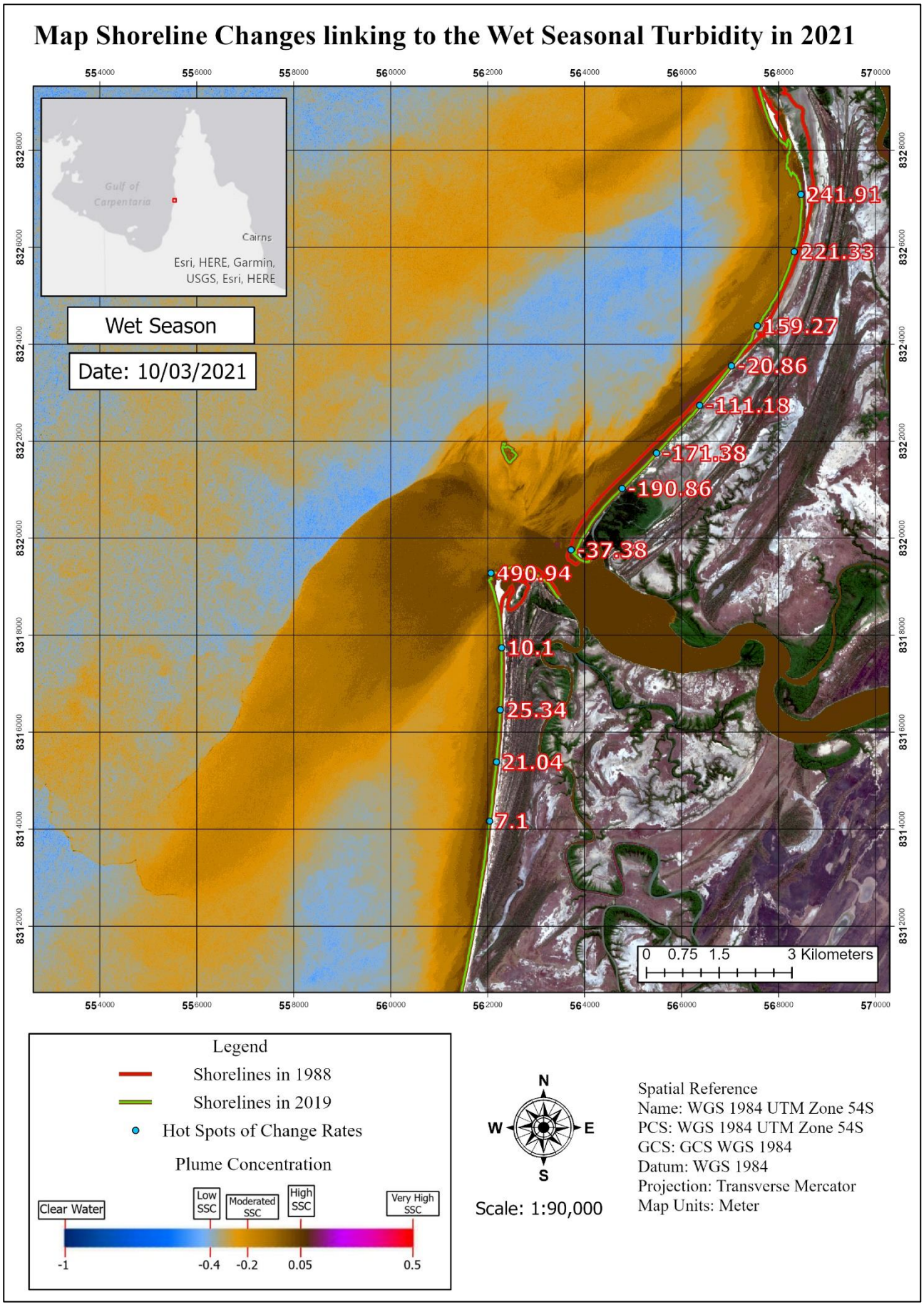

Figure 4.19 Sediment Plume Concentration relative to the rates of shoreline changes (1988 to 2019) in Wet Season on 10 March 2021.

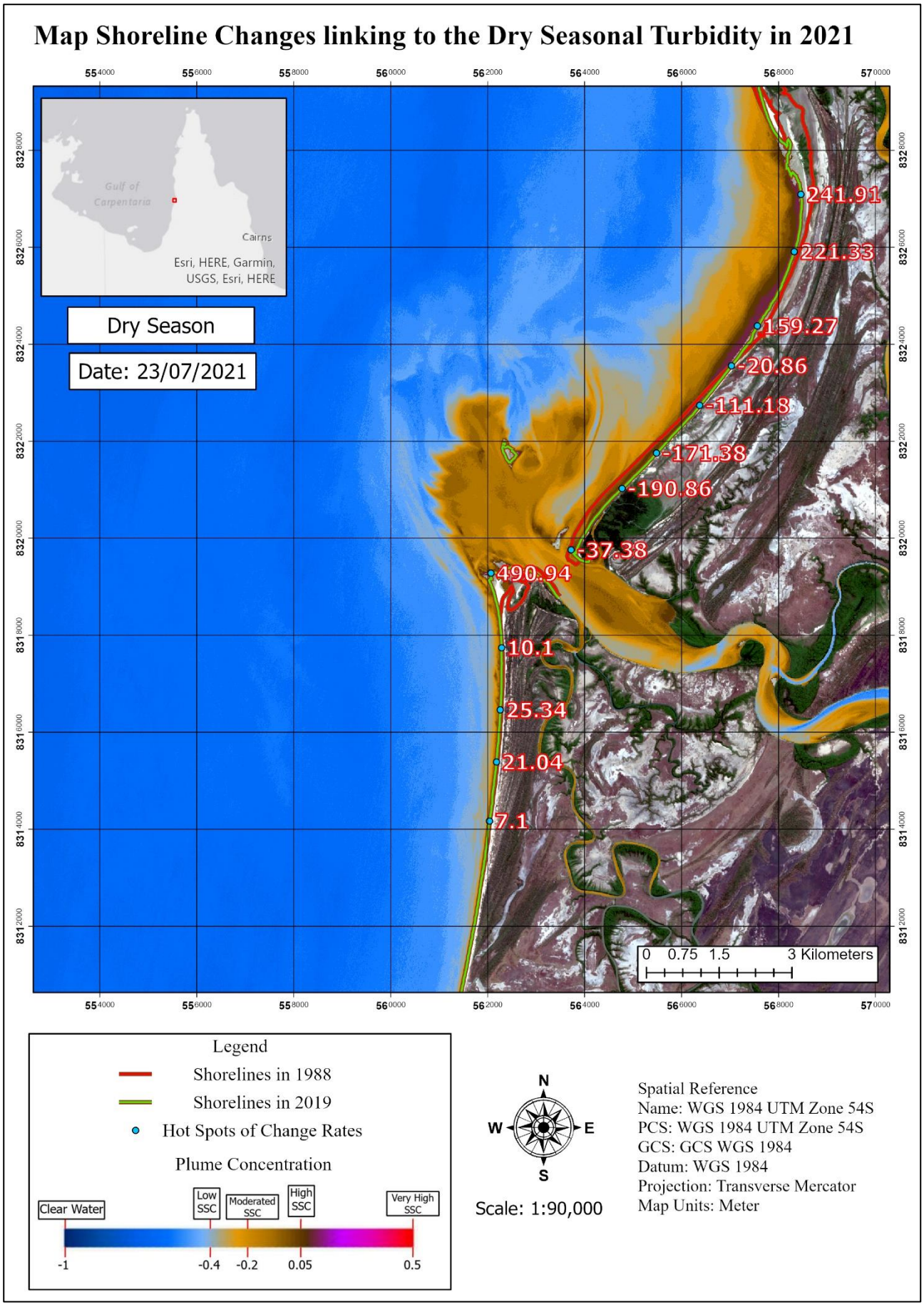

Figure 4.20 Sediment Plume Concentration relative to the rates of shoreline changes (1988 to 2019) in Wet Season on 23 July 2021.

CHAPTER 5. DISCUSSION

5.1. Sediment Plume Dimension and Orientation

Spatial and temporal variations in fluvial flow, wave and tide energies and longshore drift direction deliver the dynamic conditions in arranging the sedimentary deposition in the Mitchell River delta (Massey et al. 2014). Accordingly, the variability of sediment plumes including their magnitude and orientation are investigated in relation to these fundamental influences for three significant perspectives, the wet seasonal variability, dry seasonal variability, and the inter-annual variability.

5.1.1. Wet Seasonal Variability

Results from wet seasonal detected plume demonstrate huge plume dimensions are both orientated to the south direction (**Figure 4.3** and **Figure 4.9**). It is interpreted that the high fluvial discharge in wet season results in fluvial process dominance dominated over the basinal processes despite higher wind speeds (in **Figure 4.9**). The fluvial flow in the Mitchell River Delta is extremely seasonal where the peak discharge arises during the summer monsoon (December to April) (Rustomji 2010). However, there is a possibility of peak wave movement phenomenon throughout storm surges if the cyclones pass by (Massey et al. 2014). The correlation between this high monsoonal fluvial flow with this minimal wave amplitude during the wet season generate extreme turbid plumes with superior suspended sediment loads coming out from the Mitchell River into the shallow basin of GoC (Massey et al. 2014). While the high fluvial discharge during the monsoonal summer period generates large dimensions of high turbid plumes, there is evidence of the palaeo-flow influences on the plume orientation to the south in this period driven by longshore currents. Ainsworth et al. (2016) explained that the palaeo-flow orientation is directed alongshore from north to south opposed to the predominant longshore current direction, which is south to the north. However, the direction of the dry seasonal wind or a storm event might affect this paleo-flow direction which could cause breaking waves in southerly direction (Ainsworth et al. 2016). Suppiah (1992) mentioned that the direction of the wind in the dry season (May to November) is linked to the trade winds traveling from east to northwest path while opposite direction of winds is notified in the wet season (December to April). The clockwise trend of summer circulation is additionally reported in this shallow basin of GoC (Forbes & Church 1983; Wolanski 1993).

However, a strange phenomenon occurred on 15 January 2020 (as shown in **Figure 4.3**) where the fluvial discharge was revealed to be exceptionally minimal (8 m^3/s). This unusual circumstance creates an uncertainty about how this marginal fluvial flow could dominate over the process and create a huge scale of sediment plume. This could be due to the sediment in which was deposited at the earlier time has just been reworked on 15 January 2020. On the other hand, there is no doubt that this uncertainty might be due to the station where discharge data was gathered is not exactly on the main outlet of the Mitchell River. The Dunbar gauge station is situated at the upstream of the

Mitchell River and about 250 km from the river mouth. This means that the flow requires additional duration in reaching the river mouth while mysterious variables could arise during that traveling period, for instance the event of rainfall. In this case, the precipitation could possibly explain this circumstance. The precipitation data, which is likewise obtained from Dunbar station, shows that no rainfall event occurred on the 15 January 2020. However, about 17 mm of rainfall was recorded on 14 January 2020 at the Dunbar station. This event could enhance the discharge amount and sediment load from run off, which possibly implies the occurrence of big plume on 15 January 2020, if the flow duration from the Dunbar station to the river mouth was one day. However, further sediment transport modelling should be performed in analysing to demonstrate this inexplicable phenomenon.

5.1.2. Dry Seasonal Variability

In contrast to the wet season, results of dry seasonal sediment plumes reveal the occurrences of smaller dimensions orientating to the north direction as exhibited in **Figure 4.6** and **Figure 4.11**. These reduced plume dimensions are interpreted to be related to the low fluvial discharge during the dry season as revealed to be approximately 8 m^3/s and 25 m^3/s in **Figure 4.6** and **Figure 4.11**, respectively. Low fluvial discharge is associated with reduced sediment loads (including suspended) and reduced turbulence (Bhattacharya 2006). According to Petheram et al. (2018), the fluvial discharge in the dry season significantly declines compared to the wet season due to monsoonal wet-dry rainfall patterns. Since approximately 95 % of runoff occurs in the wet season, the Mitchell River has occasionally experienced periods of no fluvial flow. It is reported that the groundwater discharge from the Tertiary sediments and Great Artesian Basin aquifers is the major source of the Mitchell River flow during the dry season (Petheram et al. 2018). Downstream at the river mouth, flow in the dry season is dominated by tidal currents (Nanson et al. 2013). During this period of low fluvial flow, basinal processes (waves, tides, and longshore currents) dominate. This is evident in imagery where we can see. Furthermore, the longshore current switches direction and is oriented towards the north (see in **Figure 4.6** and **Figure 4.11**). This northerly directed longshore drift current occurring in the dry season is what we see preserved in the upper delta plain (see in **Figure 5.1**). For example, it is seen that palaoe-channels to the north of the Main Mitchell are oriented north of orthogonal to the palaeo-shoreline. This trend is also observed in the near offshore subaqueous distributary channels. This suggests that in spite of the temporary southerly orientated longshore drift current that occurs in the wet season, it is the northerly directed longshore current operating through the dry season that is influential what is ultimately preserved in the delta. It also supports interpretation that this northerly directed longshore current leading to delta has been operating for at least 2ka years based on dating and sedimentology of upper delta plain (Lane 2016; Massey et al. 2014; Nanson et al. 2013). The reversal of longshore correlates to the reversal of north-westerly trade wides in the April to November dry season to the south-easterly directed winds in the wet season.

On the other hand, noticeable scenarios arise during the dry season as displayed in the **Figure 4.5** and **Figure 4.10**. In the early dry season period of May, the directions of the plumes on both 2020 and 2021 seem like to be unoriented to either southward or northward. These two phenomena are not likely to be a coincidence since they were identically discovered in dry season, specifically in May, on not only 2020 but also 2021. It is hypothetically interpreted that these occurrences could possibly be due to the fluvial flow energy conflicting with the waves and tides energies were comparable or reach an impartial condition where neither energies of fluvial flow nor basinal processes could dominated over one another. Another possible explanation is that these scenarios occurred in a neutral period of the year where fluvial discharge, basinal processes and the winds were in a serene condition which could generate extremely insignificant influences on the plume directions and also the Mitchell River deltaic system. However, not any consistent evidence has been reported to emphasise this theory, and the further investigation with extended temporal scale should be performed in strengthening this hypothesis.

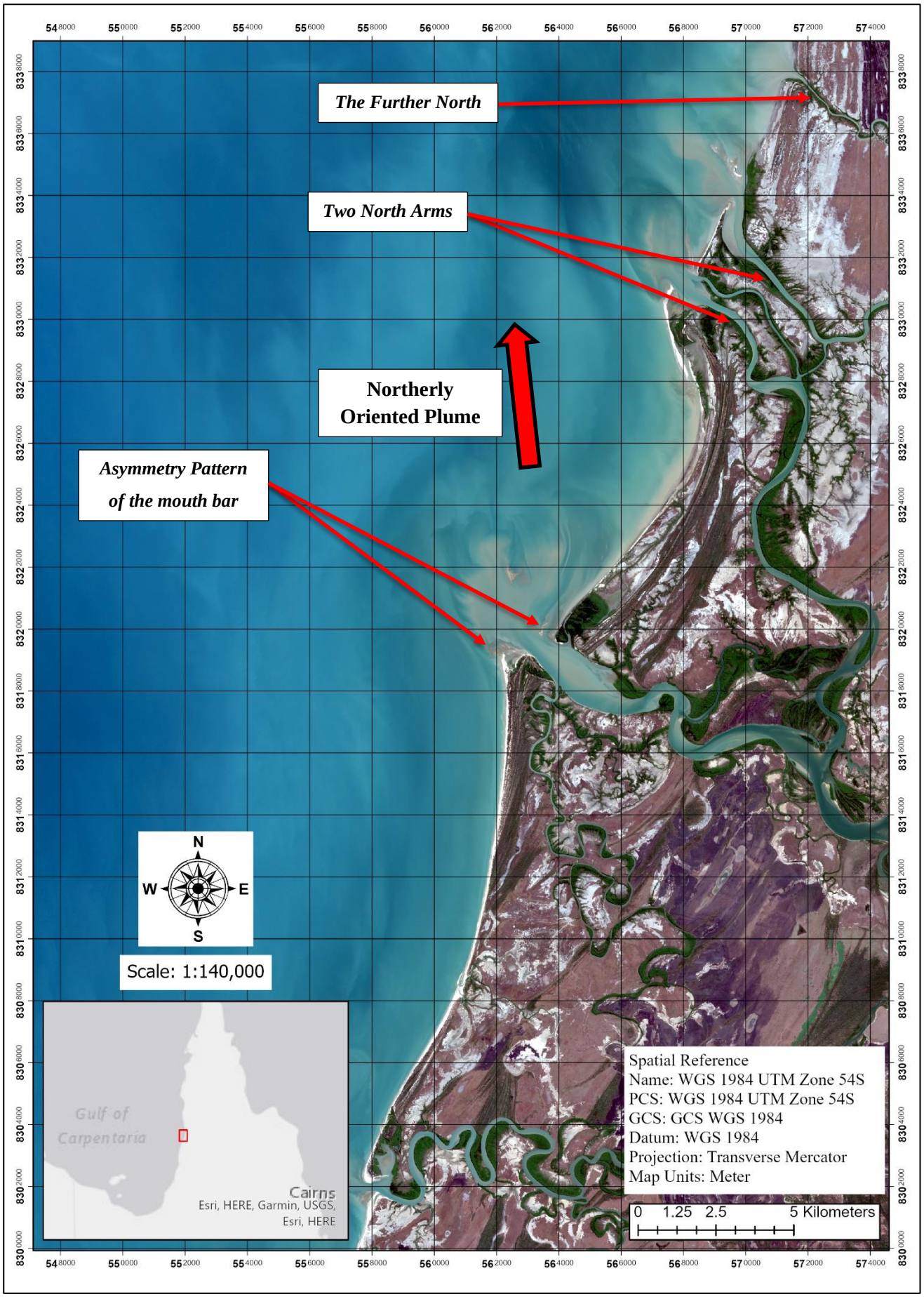

Figure 5.1 Example of Asymmetry Pattern and Distributary Arms Relative to the Northerly Sediment Plume Orientated in Dry Season on 03 June 2020.

5.2. The Variability of Mouth bar Geometry

The identification of mouth bar edges is mainly centred on the hypothesis that the mouth bar boundary is the submerged section of deltaic system. This identification was interpreted based on the Mitchell River delta morphology and other indicators included the wave breaking mostly occurring in the dry season at the edge of exposed mouth bar and the differences between high SSC and low SSC boundary in colour interpreted to be sand line of the mouth bar. Additionally, the mouth bar mapping is relative to the tides arising in those days of the images. This means that results of mouth bar geometries that we see in the images vary based on the tides. Due to the different of tidal range, results of the mouth bar mapping could contain some errors. Results reveal the expanded length of mouth bars vary from 3.5 km to 4.1 km into the offshore from the coastline. Nanson et al. (2013) stated that the width of modern Mitchell mouth bar was estimated to be 5 km seaward. This extend includes both sandy and muddy portions of the mouth bar. The sand line is approximately 3 km whilst mud line is considered to be over 3 km. By interpreting these results with sand-mud lines (**Figure 5.2**) generated from the sediment grab data in 2014 by Nanson et al. (2013), it is verified that the identified mouth bars are comparable to sand-mud lines in 2014. This also illustrates that the sand mouth bar could possibly prograde approximately 0.5 km to 1 km between 2014 and 2021.

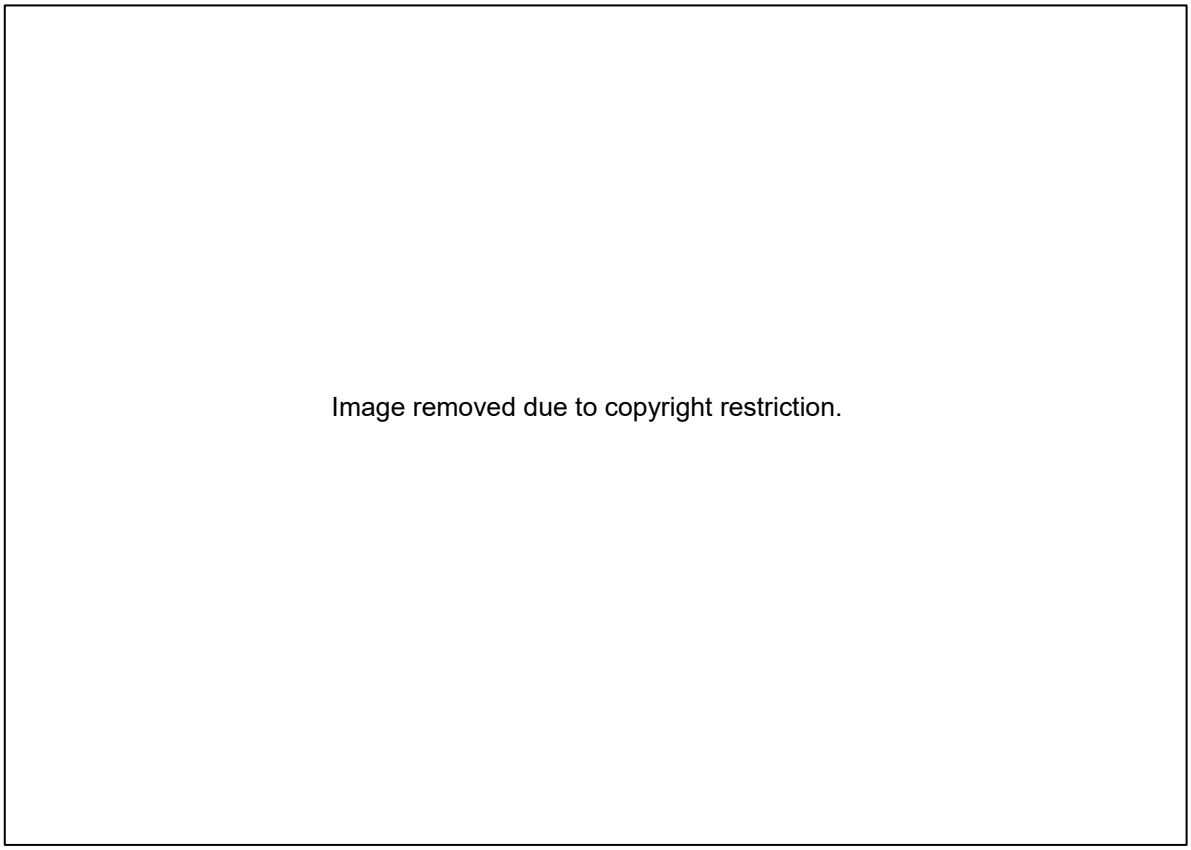

Figure 5.2 Sand Line (yellow dash line) shows the sand mouth bar boundary (Nanson et al. 2013).

In **Figure 4.12**, the wet seasonal mouth bar on 15 January 2020 was accumulated with a bulbous morphology. This pattern is similar to the fluvial-mouth bar element complex (F-Mouth Bar EC as displayed in **Figure 5.3**), which its architectural style was classified in a study by Vakarelov and

Ainsworth (2013). This accumulation pattern seems likely to be mainly affected by the fluvial discharge correlated to the sediment loads with the marginal influences from the basinal processes (waves, tides and longshore current) and the wind energy. Ainsworth et al. (2016) explained the prediction of a fluvial dominated mouth bar at the Mitchell River delta could possibly be due to the conflicting in directions between the palaeo-flow orientated alongshore and the paleo-current orientated offshore.

However, it was shown to be slightly distinct in the dry season. The architecture of dry seasonal mouth bar on the 11 September 2020 (in **Figure 4.13**) was commenced to disclose a wave-dominated, tide-influenced and fluvial-affected mouth bar element complex (Wft-Mouth Bar EC as displayed in **Figure 5.3**). It is assumed that the basinal processes might be dominated over the fluvial discharge in reworking the deposited high sediment plume with the assistance of the wind energy. Furthermore, this unusual circumstance was likewise discovered on another time period of the dry season on 12 August 2021 as exhibited in **Figure 4.16**. A previous study about the evolution of the Mitchell River Delta identically showed the reworking of mouth bar depositional sediments by basinal processes after the fluvial sedimentation (Lane 2016). The transported sediment from fluvial procedures for the duration of the wet season is altered by both wave and tide throughout the dry season. This study additionally stated that the modern mouth bar of the Mitchell River delta has resulted from this consequence to be the wave-dominated, tide-influenced and fluvial-affected (Wft).This series of phenomena is considered as the verification of this hypothesis that the high fluvial discharge mainly controls the mouth bar formation over the basinal processes in the wet season whereas wave energy, tidal level and longshore current assisted by the wind energy are dominated over the insignificant fluvial flow in mouth bar formation on the dry season.

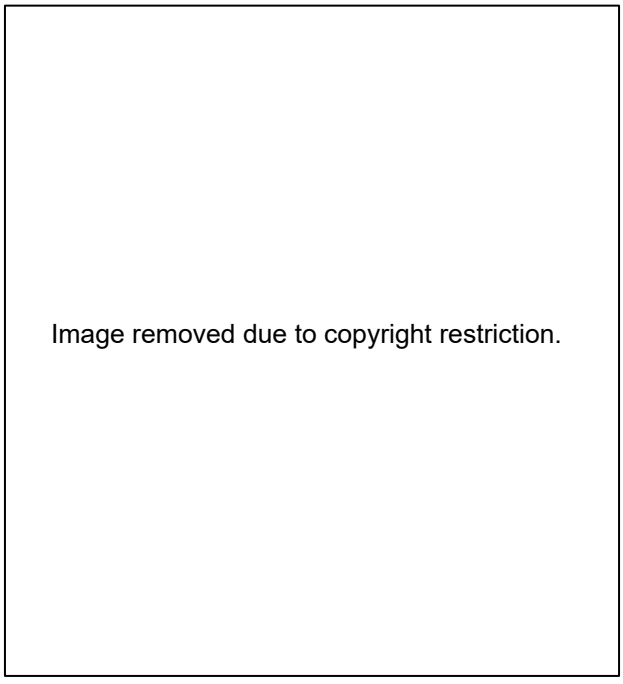

Figure 5.3 The Mouth Bar Element Complex Categories originally classified by Vakarelov and Ainsworth (2013).

5.3. Erosional and Accretional Rate of Shoreline Changes

The results from **Figure 4.17**, **Figure 4.18**, **Figure 4.19** and **Figure 4.20** illustrate the relationship between the shoreline alteration (erosion or progradation) rates and the turbidity conditions. It is revealed that the high and very high turbidity constantly dominate in the vicinity of the north nearshore spot in both wet and dry seasons where the coastline is extremely eroding. At the same time, the south nearshore territory of the Mitchell River mouth bar has differently experienced low turbidity concentration in the dry season and moderate turbidity circumstance in the wet season. The rates of shoreline changes from 1988 to 2019 show that the north shoreline near the mouth bar has retreated approximately 190 m (in total from 1988 to 2019) while the south coastline has prograded roughly between 7 m to 25 m in total from 1988 to 2019 (only the south spot adjacent to the river mouth with almost 490 m growth).

5.3.1. Erosional Coastline at North of the Main Mitchell River Outlet

In this research, the turbidity was implemented as a proxy for erosional activities along the Mitchell River delta shorelines. This relationship between turbidity and erosion exemplifies the high turbidity phenomena constantly arising in the vicinity of the north erosional coastline of the mouth bar. Since the erosional process can pollute the clarity of the water column, the turbidity will likewise increase as the extremely high turbidity might represented the severely erosional coastline condition. The coastal erosion is believed to be affected from both anthropogenic and naturogenic. While most of Australia's main erosion issues have occurred due to the development or construction from humans' activities, the variation of the Mitchell River delta coastline is reported to be moderately insignificant anthropogenic adjustment (Nanson et al. 2013). This means that there has not been infrastructure and disruptive irrigation (or purposeful channel diversion) as seen in other deltas. In the term of naturogenic influences, the interaction of increased sea level and the intense wave energy predominantly erode the coastline. Associating to the high wave energy, the storm surge event during the high tide related to the storm event could likewise wash out the sediment along the shore (Smith 2010).

It is known that the increase of local sea level commonly causes the erosion leading the coastline to retreat landward (Smith 2010). The raised sea level could likewise adjust the wave direction striking at the coast and allow the wave to expand its effect further up and wider along the coastline (Smith 2010). The sea level at the Mitchell River delta is estimated to have increased from modern baseline levels predicted (in 2014) approximately 0.5 m in 2020, 0.11 m in 2030, 0.83 m in 2100 and 1.43 m in 2150, according to the sea level projection tool from NASA (https://sealevel.nasa.gov/ipcc-ar6-sea-level-projection-tool). This sea level rise projection is relative to a baseline scenario in between 1994 to 2014. Additionally, it is believed that the intense wave energy plays an important role in causing the severe shoreline erosion in the north nearshore of the Mitchell River mouth bar. The accumulations of the coast along the Mitchell River delta principally comprise sand materials which

could be certainly damaged by waves (Nanson et al. 2013). Generally, the Australia's severe erosional coastlines similar to the shoreline the Mitchell River Delta has been experienced with temporary coastal erosion due to storm events relating to high wave energy and peculiarly the extreme water level as the occurrence of storm surges during spring tides (Smith 2010). Massey et al. (2014) stated that the tidal current could potentially disperse the sediment out of the coast into the ocean although it is occasionally considered as a sedimentary redistribution procedure from the offshore into the inland zone. The tidal range in the Mitchell River delta can vary between 0.3 m to 4 m during the neap tide and spring tide, respectively (Munro 1984). Nanson et al. (2013) additionally mentioned that the depositional alteration along the Mitchell River delta is a variability of climate conditions relating to the sediment flux. Because of either allogenic or autogenic aspects, the beach ridge along the shoreline of the Mitchell River Delta might erode when the sediment supply is marginal. Despite coastal erosion, the gradual and insignificant progradation could occasionally occur whilst the ridge vertically develops at the stalled coastline (Taylor & Stone 1996). Under comparable circumstance, the chenier plain could suffer the mudflat winnowing experience throughout multiple events of storms (Nanson et al. 2013).

5.3.2. Accretional Coastline at South of the Main Mitchell River Outlet

Results of turbidity concentration and accretion rates demonstrates the inter-annual occurrences of insignificant turbidity continuously arise in the vicinity of the south accretional shoreline of the mouth bar. Based on the relationship of turbidity and erosion, the less turbid water represents the minor erosional activities that could possibly allow the progradation to expand from depositional sediment from the Mitchell River mouth. Nanson et al. (2013) showed that the direction of longshore sediment transport is towards the south in the vicinity of the Mitchell River mouth, which causes asymmetric distribution of beach and barrier bar ridge to these visible at the modern shoreline, similar to the models of Bhattacharya and Giosan (2003). The bias is raised on this accretion hypothesis that this progradation should be due to the older erosional sediment from the Mitchell River Delta lobes as mentioned in a study by Lane (2016). This study mentioned about the autogenic evidence of obvious sediment rate increase in the central Mitchell depocentre during the modern shoreline evolution period. This sediment was sourced from the local supply in the main Mitchell depocentre including the Alice River (Lane 2016).

Under comparably extreme rates of finer sediment supply, tidal flats (or chenier plains) along the Mitchell River delta could be further prevalent (Rhodes 1980). It is assumed that most of the modern sediment contributed to the gully every year migrates from predominant vertical scarp retreat from the gully head (Brooks et al. 2008). However, it is not to imply that secondary erosion of partially eroded failed blocks, reworking of gully outwash deposits, or gully sidewall erosion do not contribute significant amounts of modern sediment (Brooks et al. 2008). If the deposited substance is not revised from the gully surface, scarp retreat will be decelerated (Shellberg et al. 2016). Additionally, land use changes have increased the magnitude and distribution of alluvial gully erosion substantially

(Shellberg et al. 2016). Limited evidence, however, suggests the increased sediment supply in the modern shoreline period might be related to the anthropogenic catchment disturbance. It is presumed that intensive post-European settlement agricultural procedures in particular cattle grazing and related disturbance concentrated in riparian regions during dry season exacerbated gully erosion in the monsoon season along steep banks, adjoining floodplain hollows, and precursor gullies (Shellberg et al. 2016).

5.4. Key Limitations

5.4.1. Errors and Limitations of the Algorithm

Although this implemented algorithm was successfully performed in detecting the water turbidity for this research, some technical issues were encountered causing some inaccuracies. These discovered errors play an important role in decreasing the precision of the outcomes, in this case the turbidity indices identification, so that the improvement should be considered in resolving these issues to obtain further accurate results. Various key sources of these inaccuracies can be varied from the MNDWI algorithm for water extraction, the NDTI algorithm for turbidity detection and the pixel-based classification methods in mapping the geometry of both sediment plume and mouth bar.

The inaccuracies of water extraction using the MNDWI algorithm were found from two distinct sources included the overclassified turbidity as land region and clouds properties as water region. Due to the complexity of the water turbidity along the coastline, it becomes extremely problematic for the MNDWI algorithm to differentiate between turbid water regions and land area leading to the over classification them as land region. This confusion results in masking out some rational turbid water regions along the coastline. However, these inaccuracies aspects and confusion have been reported to be ordinary concerns for water extraction procedure (Munasinghe, Cohen & Gadiraju 2021). It is stated that the identification of the coastline in deltaic regions is extremely challenging due to the shallowness and turbidity of water, vegetative gradients, and dynamical variable waterline. It was likewise reported that waters in the highly turbid coastal regions could frequently be categorised as land class in countless typical algorithms since they are integrated with a variety of substances including suspended particles, sediments, and phytoplankton (Munasinghe, Cohen & Gadiraju 2021). Another error of the MNDWI was the inability to identify the thin clouds and cloud shadows although this algorithm provided the most effective approach in clouds masking for this research. This inaccuracy would potentially cause further confusion as plume identification using the NDTI algorithm. The adjustment of the MNDWI indices could possibly be beneficial in lessen or completely mask out the thin clouds and cloud shadows, yet another inaccuracy was addressed since some high concentration turbidity portions could be overclassified resulting in missing plume areas. These inaccuracies are demonstrated in **Figure 5.4**.

The inaccuracies produced from the NDTI algorithm in turbidity detection were identified. It was revealed that the low turbidity concentration regions were partially misclassified. This NDTI algorithm

found those pixels extremely complicated to recognise due to undistinguished low concentration plume reflectance with water pixels as explained in **Figure 5.5**.

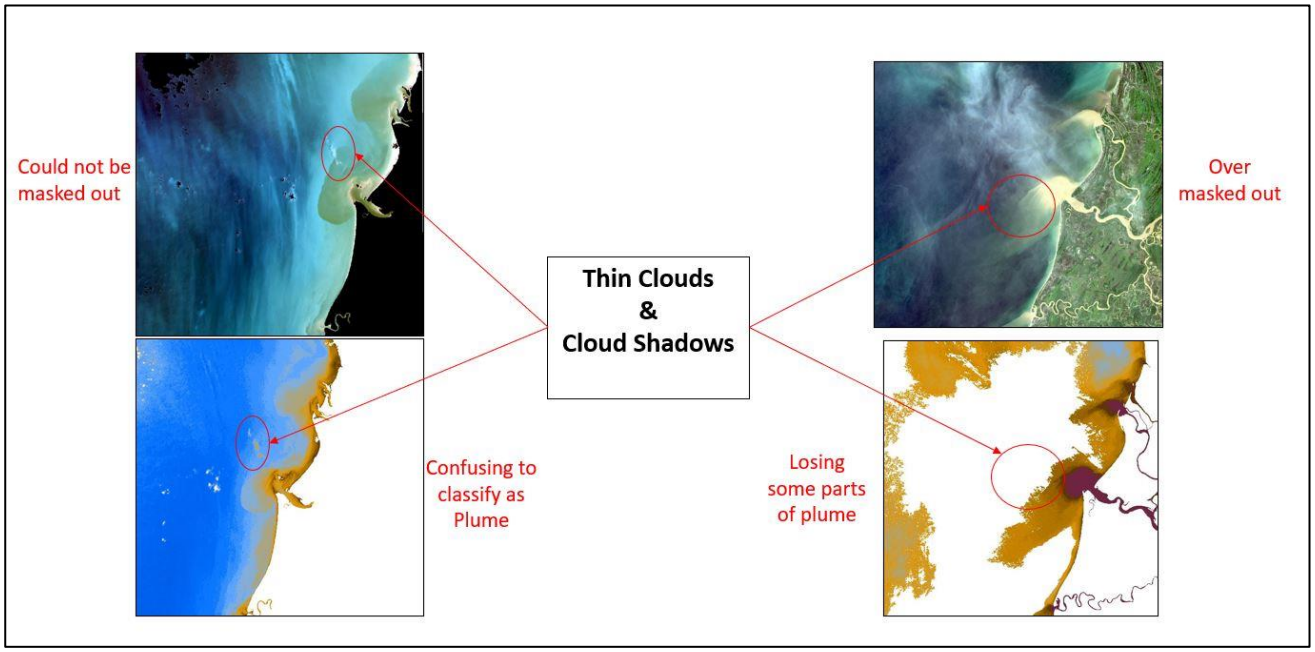

Figure 5.4 Inaccuracy of the NDTI algorithm in turbidity detection resulting from MNDWI errors.

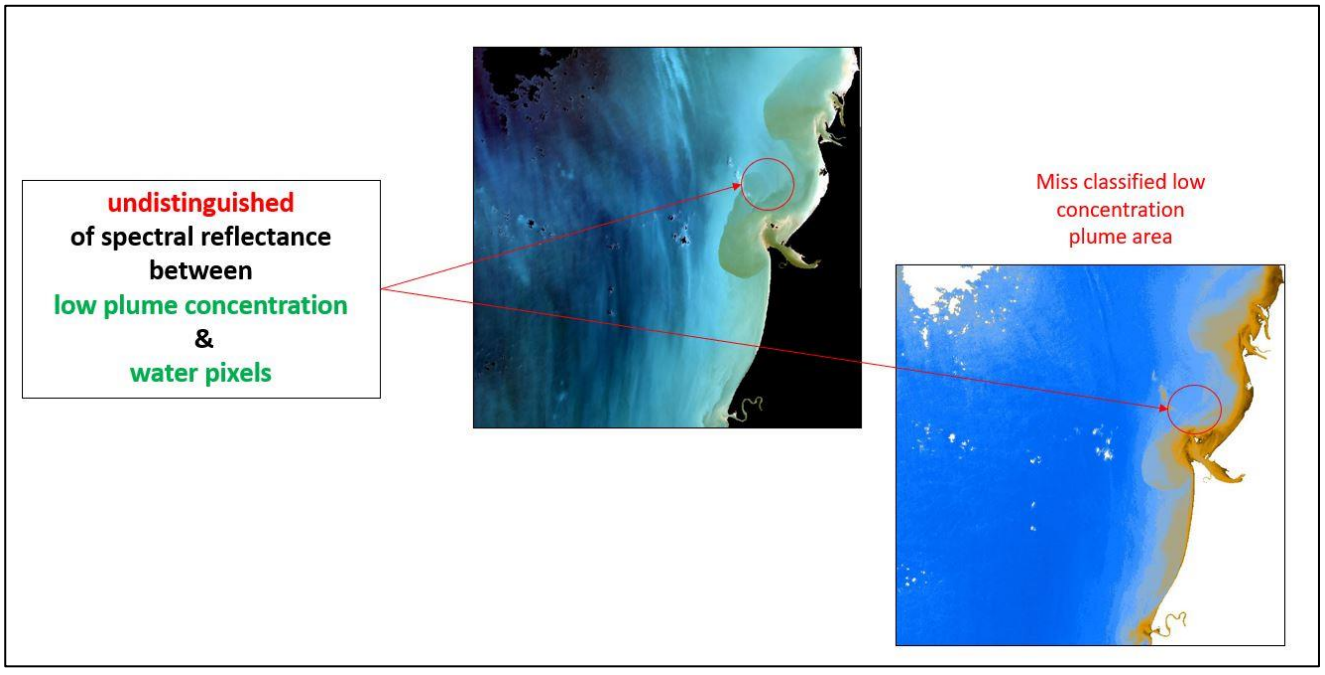

Figure 5.5 Inaccuracy of the NDTI algorithm in turbidity detection.

The classification for identifying the sediment plume boundary likewise provide some inaccuracies at the edge of the plume regions, especially the low concentration plume areas. Since this classification is mainly pixel-based method, the low concentration plume and water regions are frequently confused in characterising as either plume or water classes. Moreover, the assistance of manual digitisation would be an ideal solution in modifying the inappropriate edge of the plume in order to obtain the enhancement results. Although this integration is reported to be an effective

approach in mapping, mistakes still can be created during delineation in this study due to the repetitive operation linking to the interpretation of human eyes. Nath and Deb (2010) likewise mentioned these two issues in their study that it could be challenging for the human eyes to interpret the boundary since colour shades may gradually decay, especially with low-resolution images.

Despite these four issues, another difficulty within the ArcGIS Pro software environment was found. Although the algorithm generated in the Model Builder in the ArcGIS Pro (in **Appendix 1**) was successfully executed in detecting the turbidity, the python script converted from this Model Builder environment was not completely operational when it was applied in the ArcPy environment. Two errors were found in while this script was operating in the Arcpy environment as mentioned in red circles in **Appendix 2**. The first main error is due to the data selection tool while the iterator tool is realised to be the second major error as displayed in red boxes in **Figure 5.6**. In this case, the data selection tool in the Model Builder is performed to select sensitive bands for the MNDWI and NDTI calculations. Iterator tool is the Model Builder's function that could provide the capability in repeatedly process and analyse the entire available satellite images in a folder after one another. Instead of generating into a proper python format as they supposed to be, these two tools are converting into a string format (normal text in coding setting) resulting in incomprehensible coding language due to missing significant portions of variables and loop function. This ordinarily issue could be highly caused by the operating environments of the Model Builder and the ArcPy. The operation of ArcPy setting is the integration between python libraries with the geoprocessing toolbox whilst the Model Builder environment is operating within the geoprocessing toolbox associating to its distinct tool package, in this case the data selection and iterator tools. Consequently, these two distinct tools seem to not exist in the setting of ArcPy resulting in inappropriate conversion due to unrecognised language.

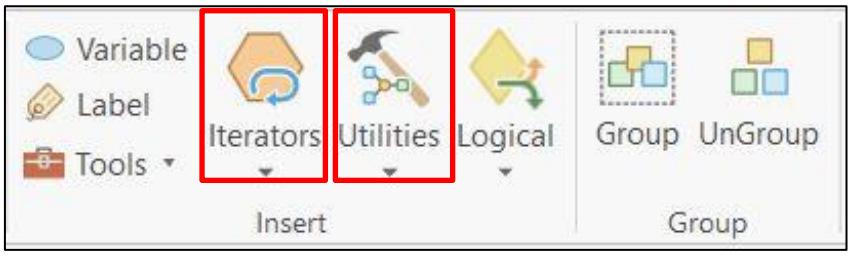

Figure 5.6 Iterators and Select Data (Utilities) tools in the Model Builder Enviroment.

It is strongly believed that the further correction of this ArcPy script would be an ideal solution in resolving this issue by applying two uncomplicated coding techniques. By replacing the useless string line of data selection tool with the variable creating to select the sensitive bands and applying these variables into the MNDWI and NDTI raster calculations. Similarly, substituting the ineffective string line of iterator tool with the loop function (could possibly a "For" loop) from python library would probably resolve this error and generate a proper functional script for detecting the turbidity. However, this hypothesis solution has not been implemented yet due to limited time period of this

research, and it is believed that this script correction procedure is not a priority circumstance in this research since the processing within the Model Builder was a successful operation to detect the turbidity.

However, this band ratioing of NDTI is considered as a sufficient and effective method in detecting turbidity especially with a massive amount of imagery. It can not only accelerate the detection performance but also provide satisfactory turbidity results. Munasinghe, Cohen and Gadiraju (2021) the method of band ratioing is the most instantaneously efficient process comparing to other techniques in the purpose to instantly extract the coastline and deltaic boundary lines with satisfactory results yet not extremely precise. Results of turbidity from this NDTI algorithm can provide very comprehensive information about the turbidity, especially the concentration range due to its normalised indices ratios comparing to other accurate sub-pixel methods like spectral unmixing.

5.4.2. Research Limitations

The fundamental limitations of this research are the accuracy and accessibility of the implemented data included interpretation statistics (meteorology and hydrology data) and analysed image (Sentinel 2 imagery).

In terms of accuracy, satellite imagery and meteorology and hydrology gathered may possibly be incompatible when evaluated to one another because of the data collection environments for this research where meteorology and hydrology data is acquired from secondary sources. There is a study reporting the limitation of secondary meteorology and hydrology data in the Mitchell catchment area are astonishingly marginal causing difficulty in investigation and analysis the findings (Petheram et al. 2018). On the other hand, due to the fact that the field observation data for validation is extremely complicated to be measured in this study region, the validation of applied method with field observation data could not be performed whilst the detection and investigation are primarily based on turbidity indices estimation of spectral surface reflectance from satellite imagery addressed in previous literature reviews about water turbidity detection.

In terms of data availabilities, implemented interpretation data will be inadequate to meteorological and hydrological site statistics available in the Mitchell catchment area and Gulf of Carpentaria through publicly Australia government data and other explicitly available sources since this research does not gather new primary data. According to a recent report about the study site, the availability of data in the Mitchell catchment area and the Gulf of Carpentaria are tremendously limited due to the lack of meteorological and hydrological stations with countless deficiency statistics while many gauge stations were closed (Petheram et al. 2018). Beside the interpretation data, designated satellite imagery accessibility will be restricted to the Sentinel 2 surface reflectance specifications of spectral, spatial and temporal resolutions related to the frequency of revisit time and the meteorological conditions.

CHAPTER 6. CONCLUSION

6.1. Summary

This research aimed to apply remote sensing technique to detect the relative suspended sediment concentration (SSC) for as a proxy for turbidity and erosional processes mapping the plume and mouth bar geometry for investigating two specific purposes: 1) to determine how fluvial (rainfall and river discharge) and basinal processes (waves, tides and longshore currents) affect sediment plume and mouth bar formation, and 2) to determine how the sea level change, sediment supply and erosional activities affect the localised erosion and progradation rates along the asymmetrical delta, Mitchell River delta, in the GoC.

The Sentinel 2 L2A products with spatial resolution of 10 m and temporal resolution of 5 days acquired between 15 January 2020 and 12 August 2021 were applied for this analysis and investigation. The MNDWI algorithm was employed to extract the water area before implementing the NDTI algorithm to detect the turbidity. This detected turbidity was utilised to map the plume and mouth bar geometries by classifying the NDTI indices with the assistance of manual digitising to enhance the results' accuracy.

The results showed that the huge magnitude of wet seasonal plume occurred and orientated to the southerly direction that is analogue to the southward monsoonal palaeo-flow direction. This occurrence was interpreted to be relative to the dominance of high fluvial discharge over the basinal processes during summer monsoonal period. In contrary, the sediment plume reduced its scale and altered its orientation to the northerly direction during the dry season that is analogue to the northerly directed longshore drift current. This plume orientation was noticed to be parallel to the palaeo-channels direction within the Mitchell River delta plain. It was interpreted that this phenomenon was related to the dominance of waves, tides and northerly directed longshore drift currents over low fluvial discharge during the dry season. Another discovery in this research illustrated that the high and very high turbidity constantly dominate in the vicinity of the north nearshore zone in both wet and dry seasons where severe coastline erosion has occurred. At the same time, the south nearshore zone of the Mitchell mouth bar, where the progradation coastline has prograded, experienced low turbidity in the dry season and moderate turbidity in the wet season. It was interpreted that localised shoreline changes (either side of the asymmetrical delta) were affected from the increased sea level relative to erosional activities (waves and tides) and amount of deposited sediment load. Due to the raised sea level during this modern shoreline period, the severe erosional coastline becomes noticeable at the north side of the Mitchell mouth bar whereas the south side of this asymmetrical mouth bar has prograded relative to the amount of sediment load from gully erosions triggered by humans' disturbance in agricultural sector, particularly the cattle grazing.

6.2. Future Research

For the future research, the temporal and spatial scale of the research should be extended. In the term of temporal extended, more annual periods should be considered for further analysis in order to investigate the inter-annual variability of the sediment plume and mouth bar formations. In this case, the Landsat series are recommended due to their extremely high temporal resolution (since 1960s until present). Additionally, the investigation of monthly variation with extended temporal scale should be performed to enhance the understanding on exact months for huge scale of southerly orientated plume and marginal northward plume magnitude while it is assumed that the plume direction is unoriented either southward or northward in May. The further investigation of monthly variation with extended annual periods could strengthen this hypothesis. In the term of spatial extended, the study area should be expanded further to the south region of the Mitchell River delta to enhance the understanding about delta morphology along the GoC. About 200 km southward of this asymmetrical delta, there is another delta (the Gilbert River delta) that should be considered for further study since the research about the Gilbert River delta is extremely constrained as well as the Mitchell River delta.

Due to the limitation of interpretation data from Australian government sources in the Mitchell catchment (Petheram et al. 2018), there are some data gaps and missing that could affect to the investigation. For instance, the relationship of the main Mitchell River with the distributary streams is mysterious since there is no discharge data measured at the downstream of the Dunbar gauge. This leads to error in analysis (the phenomenon occurred on 15 January 2020 as explained in the **Section 5.1.1**). Because of that, the flied measurement (if possibly) should be considered in linking with the satellite remote sensing to improve the accuracy of the analysis. In the case of flied measurement could be performed, however, various modellings for streamflow, tides and waves should be considered to obtain the data at the Mitchell River mouth.

With climate change, it is assumed that the storm activity might be increased. This increased storm activity could adjust the wave energy. Hence, the investigation of storm activity due to climate change should be considered for the further research.

Finally, the script correction for the automation process should be considered. The future research should revise the python script in order to operate the turbidity detection. The revised python script will be very beneficial since it can be operated in online environments (ArcGIS Python for API) such Google Colab or Jupyter Notebook, which can allow other researcher to perform automation process for turbidity detection.

BIBLIOGRAPHY

Ahn, Y, Shanmugam, P, Moon, J & Ryu, J-H 2008, 'Satellite remote sensing of a low-salinity water plume in the East China Sea', in *Annales Geophysicae*, vol. 26, pp. 2019-35.

Ainsworth, RB, Vakarelov, BK, MacEachern, JA, Nanson, RA, Lane, TI, Rarity, F & Dashtgard, SE 2016, 'Process-driven architectural variability in mouth-bar deposits: a case study from a mixed-process mouth-bar complex, Drumheller, Alberta, Canada', *Journal of Sedimentary Research*, vol. 86, no. 5, pp. 512-41.

Ainsworth, RB, Vakarelov, BK & Nanson, RA 2011, 'Dynamic spatial and temporal prediction of changes in depositional processes on clastic shorelines: toward improved subsurface uncertainty reduction and management', *Aapg Bulletin*, vol. 95, no. 2, pp. 267-97.

Alesheikh, AA, Ghorbanali, A & Nouri, N 2007, 'Coastline change detection using remote sensing', *International Journal of Environmental Science & Technology*, vol. 4, no. 1, pp. 61-6.

Anthony, EJ 2015, 'Wave influence in the construction, shaping and destruction of river deltas: A review', *Marine Geology*, vol. 361, pp. 53-78.

Bates, CC 1953, 'Rational theory of delta formation', *Aapg Bulletin*, vol. 37, no. 9, pp. 2119-62.

Bhattacharya, JP 2006, 'Deltas', in pp. 237-92, DOI 10.2110/pec.06.84.0237.

Bhattacharya, JP & Giosan, L 2003, 'Wave-influenced deltas: Geomorphological implications for facies reconstruction', *Sedimentology*, vol. 50, no. 1, pp. 187-210.

Bhattacharya, JP & MacEachern, JA 2009, 'Hyperpycnal rivers and prodeltaic shelves in the Cretaceous seaway of North America', *Journal of Sedimentary Research*, vol. 79, no. 4, pp. 184-209.

Bian, J, Li, A, Liu, Q & Huang, C 2016, 'Cloud and snow discrimination for CCD images of HJ-1A/B constellation based on spectral signature and spatio-temporal context', *Remote Sensing*, vol. 8, no. 1, p. 31.

Bishop-Taylor, R, Sagar, S, Lymburner, L, Alam, I & Sixsmith, J 2019, 'Sub-pixel waterline extraction: Characterising accuracy and sensitivity to indices and spectra', *Remote Sensing*, vol. 11, no. 24, p. 2984.

Braud, D & Feng, W 1998, 'Semi-automated construction of the Louisiana coastline digital land/water boundary using Landsat Thematic Mapper satellite imagery', *Louisiana Applied Oil Spill Research and Development Program, OS2 RAPD Technical Report Series*, vol. 97, no. 002.

Brezonik, P, Menken, KD & Bauer, M 2005, 'Landsat-based remote sensing of lake water quality characteristics, including chlorophyll and colored dissolved organic matter (CDOM)', *Lake and Reservoir Management*, vol. 21, no. 4, pp. 373-82.

Brooks, A, Spencer, J, Shellberg, J, Knight, J & Lymburner, L 2008, 'Using remote sensing to quantify sediment budget components in a large tropical river-Mitchell River, Gulf of Carpentaria', *Sediment dynamics in changing environments*, pp. 225-36.

Burpee, AP, Slingerland, RL, Edmonds, DA, Parsons, D, Best, J, Cederberg, J, McGuffin, A, Caldwell, R, Nijhuis, A & Royce, J 2015, 'Grain-size controls on the morphology and internal geometry of river-dominated deltas', *Journal of Sedimentary Research*, vol. 85, no. 6, pp. 699-714.

Caballero, I, Navarro, G & Ruiz, J 2018, 'Multi-platform assessment of turbidity plumes during dredging operations in a major estuarine system', *International journal of applied earth observation and geoinformation*, vol. 68, pp. 31-41.

Caballero, I, Stumpf, RP & Meredith, A 2019, 'Preliminary assessment of turbidity and chlorophyll impact on bathymetry derived from Sentinel-2A and Sentinel-3A satellites in South Florida', *Remote Sensing*, vol. 11, no. 6, p. 645.

Chander, S, Gujrati, A, Hakeem, KA, Garg, V, Issac, AM, Dhote, PR, Kumar, V & Sahay, A 2019, 'Water quality assessment of River Ganga and Chilika lagoon using AVIRIS-NG hyperspectral data', *Current Science*, vol. 116, no. 7, pp. 1172-81.

2016, *Climate data and their characterisation for hydrological and agricultural scenario modelling across the Fitzroy, Darwin and Mitchell catchments*, by Charles, S, Petheram, C, Berthet, A, Browning, G, Hodgson, G, Wheeler, M, Yang, A, Gallant, S, Vaze, J, Wang, B, Marshall, A, Hendon, H, Kuleshov, Y, Dowdy, A, Reid, P, Read, A, Feikema, P, Hapuarachchi, P, Smith, T, Gregory, P & Shi, L, CSIRO, DOI https://doi.org/10.25919/5jqw-y808.

Chen, X, Chen, W, Bai, Y & Wen, X 2021, 'Changes in turbidity and human activities along Haihe River Basin during lockdown of COVID-19 using satellite data', *Environmental Science and Pollution Research*, pp. 1-16.

Chu, V, Smith, LC, Rennermalm, AK, Forster, R & Box, J 2012, 'Hydrologic controls on coastal suspended sediment plumes around the Greenland Ice Sheet', *The Cryosphere*, vol. 6, no. 1, pp. 1-19.

Chu, VW, Smith, LC, Rennermalm, AK, Forster, RR, Box, JE & Reeh, N 2009, 'Sediment plume response to surface melting and supraglacial lake drainages on the Greenland ice sheet', *Journal of Glaciology*, vol. 55, no. 194, pp. 1072-82.

Coleman, JM 1976, 'Deltas-Processes of Deposition and Models for Exploration: Continuing Education Publicat ion Company', *Champaign, IL*, vol. 102.

Coleman, JM & Wright, L 1975, 'Modern river deltas: variability of processes and sand bodies'.

Dominguez, J 1996, 'The Sao Francisco strandplain: a paradigm for wave-dominated deltas?', *Geological Society, London, Special Publications*, vol. 117, no. 1, pp. 217-31.

Dona, C, Chang, N-B, Caselles, V, Sánchez, JM, Camacho, A, Delegido, J & Vannah, BW 2015, 'Integrated satellite data fusion and mining for monitoring lake water quality status of the Albufera de Valencia in Spain', *Journal of environmental management*, vol. 151, pp. 416-26.

Dörnhöfer, K & Oppelt, N 2016, 'Remote sensing for lake research and monitoring–Recent advances', *Ecological Indicators*, vol. 64, pp. 105-22.

Doxaran, D, Froidefond, J-M, Lavender, S & Castaing, P 2002, 'Spectral signature of highly turbid waters: Application with SPOT data to quantify suspended particulate matter concentrations', *Remote Sensing of Environment*, vol. 81, no. 1, pp. 149-61.

Edmonds, DA & Slingerland, RL 2007, 'Mechanics of river mouth bar formation: Implications for the morphodynamics of delta distributary networks', *Journal of Geophysical Research: Earth Surface*, vol. 112, no. F2.

Enderle, DI & Weih Jr, RC 2005, 'Integrating supervised and unsupervised classification methods to develop a more accurate land cover classification', *Journal of the Arkansas Academy of Science*, vol. 59, no. 1, pp. 65-73.

Forbes, A & Church, J 1983, 'Circulation in the Gulf of Carpentaria. II. Residual currents and mean sea level', *Marine and freshwater research*, vol. 34, no. 1, pp. 11-22.

Frohn, RC, D'Amico, E, Lane, C, Autrey, B, Rhodus, J & Liu, H 2012, 'Multi-temporal sub-pixel Landsat ETM+ classification of isolated wetlands in Cuyahoga County, Ohio, USA', *Wetlands*, vol. 32, no. 2, pp. 289-99.

Galloway, WE 1975, 'Process framework for describing the morphologic and stratigraphic evolution of deltaic depositional systems'.

Galloway, WE & Hobday, DK 2012, *Terrigenous clastic depositional systems: applications to fossil fuel and groundwater resources*, Springer Science & Business Media.

Garg, V, Aggarwal, SP & Chauhan, P 2020, 'Changes in turbidity along Ganga River using Sentinel-2 satellite data during lockdown associated with COVID-19', *Geomatics, Natural Hazards and Risk*, vol. 11, no. 1, pp. 1175-95.

Garg, V, Kumar, AS, Aggarwal, S, Kumar, V, Dhote, PR, Thakur, PK, Nikam, BR, Sambare, RS, Siddiqui, A & Muduli, PR 2017, 'Spectral similarity approach for mapping turbidity of an inland waterbody', *Journal of hydrology*, vol. 550, pp. 527-37.

Gernez, P, Lafon, V, Lerouxel, A, Curti, C, Lubac, B, Cerisier, S & Barillé, L 2015, 'Toward Sentinel-2 high resolution remote sensing of suspended particulate matter in very turbid waters: SPOT4 (Take5) Experiment in the Loire and Gironde Estuaries', *Remote Sensing*, vol. 7, no. 8, pp. 9507-28.

Gholizadeh, MH, Melesse, AM & Reddi, L 2016, 'A comprehensive review on water quality parameters estimation using remote sensing techniques', *Sensors*, vol. 16, no. 8, p. 1298.

Guariglia, A, Buonamassa, A, Losurdo, A, Saladino, R, Trivigno, ML, Zaccagnino, A & Colangelo, A 2006, 'A multisource approach for coastline mapping and identification of shoreline changes', *Annals of geophysics*, vol. 49, no. 1.

Guo, K, Zou, T, Jiang, D, Tang, C & Zhang, H 2017, 'Variability of Yellow River turbid plume detected with satellite remote sensing during water-sediment regulation', *Continental Shelf Research*, vol. 135, pp. 74-85.

Güttler, FN, Niculescu, S & Gohin, F 2013, 'Turbidity retrieval and monitoring of Danube Delta waters using multi-sensor optical remote sensing data: An integrated view from the delta plain lakes to the western–northwestern Black Sea coastal zone', *Remote Sensing of Environment*, vol. 132, pp. 86-101.

Heap, A, Bryce, S, Ryan, D, Radke, L, Smith, C, Smith, R, Harris, P & Heggie, D 2001, 'Australian estuaries and coastal waterways. A geoscience perspective for improved integrated management. A report to the National Land and Resources Audit. Theme 7', *Ecosystem Health. AGSO, Geoscience Australia*.

Hopkins, J, Lucas, M, Dufau, C, Sutton, M, Stum, J, Lauret, O & Channelliere, C 2013, 'Detection and variability of the Congo River plume from satellite derived sea surface temperature, salinity, ocean colour and sea level', *Remote Sensing of Environment*, vol. 139, pp. 365-85.

Hu, C, Chen, Z, Clayton, TD, Swarzenski, P, Brock, JC & Muller–Karger, FE 2004, 'Assessment of estuarine water-quality indicators using MODIS medium-resolution bands: Initial results from Tampa Bay, FL', *Remote Sensing of Environment*, vol. 93, no. 3, pp. 423-41.

Jones, BG, Martin, GR & Senapati, N 1993, 'Riverine—tidal interactions in the monsoonal Gilbert River fandelta, northern Australia', *Sedimentary Geology*, vol. 83, no. 3-4, pp. 319-37.

Kamal, M & Phinn, S 2011, 'Hyperspectral data for mangrove species mapping: A comparison of pixel-based and object-based approach', *Remote Sensing*, vol. 3, no. 10, pp. 2222-42.

Khatami, R, Mountrakis, G & Stehman, SV 2016, 'A meta-analysis of remote sensing research on supervised pixel-based land-cover image classification processes: General guidelines for practitioners and future research', *Remote Sensing of Environment*, vol. 177, pp. 89-100.

Kong, D, Miao, C, Borthwick, AG, Duan, Q, Liu, H, Sun, Q, Ye, A, Di, Z & Gong, W 2015, 'Evolution of the Yellow River Delta and its relationship with runoff and sediment load from 1983 to 2011', *Journal of hydrology*, vol. 520, pp. 157-67.

Kuhn, C, de Matos Valerio, A, Ward, N, Loken, L, Sawakuchi, HO, Kampel, M, Richey, J, Stadler, P, Crawford, J & Striegl, R 2019, 'Performance of Landsat-8 and Sentinel-2 surface reflectance products for river remote sensing retrievals of chlorophyll-a and turbidity', *Remote Sensing of Environment*, vol. 224, pp. 104-18.

Lacaux, J, Tourre, Y, Vignolles, C, Ndione, J & Lafaye, M 2007, 'Classification of ponds from high-spatial resolution remote sensing: Application to Rift Valley Fever epidemics in Senegal', *Remote Sensing of Environment*, vol. 106, no. 1, pp. 66-74.

Lahet, F & Stramski, D 2010, 'MODIS imagery of turbid plumes in San Diego coastal waters during rainstorm events', *Remote Sensing of Environment*, vol. 114, no. 2, pp. 332-44.

Lane, TI 2016, 'Evolution and architecture of the Holocene Mitchell River megafan and delta, Gulf of Carpentaria, Australia'.

Lane, TI, Nanson, RA, Vakarelov, BK, Ainsworth, RB & Dashtgard, SE 2017, 'Evolution and architectural styles of a forced-regressive Holocene delta and megafan, Mitchell River, Gulf of Carpentaria, Australia', *Geological Society, London, Special Publications*, vol. 444, no. 1, pp. 305-34.

Le Moigne, J & Tilton, JC 1995, 'Refining image segmentation by integration of edge and region data', *IEEE transactions on geoscience and remote sensing*, vol. 33, no. 3, pp. 605-15.

Lee, Z 2006, 'Reports of the International Ocean-Colour Coordinating Group'.

Liedtke, J, Roberts, A & Luternauer, J 1995, 'Practical remote sensing of suspended sediment concentration', *Photogrammetric engineering and remote sensing*, vol. 61, no. 2, pp. 167-75.

Lim, J & Choi, M 2015, 'Assessment of water quality based on Landsat 8 operational land imager associated with human activities in Korea', *Environmental monitoring and assessment*, vol. 187, no. 6, pp. 1-17.

Lohani, B 1999, 'Construction of a digital elevation model of the Holderness coast using the waterline method and airborne thematic mapper data', *International Journal of Remote Sensing*, vol. 20, no. 3, pp. 593-607.

Loos, EA & Niemann, KO 2002, 'Shoreline feature extraction from remotely-sensed imagery', in *IEEE International Geoscience and Remote Sensing Symposium*, vol. 6, pp. 3417-9.

Lu, D, Moran, E & Batistella, M 2003, 'Linear mixture model applied to Amazonian vegetation classification', *Remote Sensing of Environment*, vol. 87, no. 4, pp. 456-69.

Luis, KM, Rheuban, JE, Kavanaugh, MT, Glover, DM, Wei, J, Lee, Z & Doney, SC 2019, 'Capturing coastal water clarity variability with Landsat 8', *Marine pollution bulletin*, vol. 145, pp. 96-104.

Malthus, TJ & Mumby, PJ 2003, 'Remote sensing of the coastal zone: an overview and priorities for future research'.

Marghany, M, Sabu, Z & Hashim, M 2010, 'Mapping coastal geomorphology changes using synthetic aperture radar data', *International Journal of Physical Sciences*, vol. 5, no. 12, pp. 1890-6.

Massey, T, Fernie, A, Ainsworth, R, Nanson, R & Vakarelov, B 2014, 'Detailed mapping, three-dimensional modelling and upscaling of a mixed-influence delta system, Mitchell River delta, Gulf of Carpentaria, Australia', *Geological Society, London, Special Publications*, vol. 387, no. 1, pp. 135-51.

Moore, GK 1980, 'Satellite remote sensing of water turbidity/Sonde de télémesure par satellite de la turbidité de l'eau', *Hydrological Sciences Journal*, vol. 25, no. 4, pp. 407-21.

Mouhoupt, J, Cunningham, V, Hart, G, Shortell, J, Conwell, D, Newport, C, Hanis, D, Hansen, M, Waldron, J & Christoffeis, E 2004, 'Wave Data Recording Program: Weipa Region, 1978–2004', *Queensland Government Environmental Protection Agency, Coastal Sciences Data Report W*, vol. 2004.

Mulder, T, Syvitski, JP, Migeon, S, Faugères, J-C & Savoye, B 2003, 'Marine hyperpycnal flows: initiation, behavior and related deposits. A review', *Marine and Petroleum Geology*, vol. 20, no. 6-8, pp. 861-82.

Munasinghe, D, Cohen, S & Gadiraju, K 2021, 'A Review of Satellite Remote Sensing Techniques of River Delta Morphology Change', *Remote Sensing in Earth Systems Sciences*, pp. 1-32.

Munro, ISR 1984, *Atlas of operational, environmental, and biological data from the Gulf of Carpentaria prawn survey, 1963-65. Part 3. Physical and chemical environment*, Commonwealth Scientific and Industrial Research Organization, Marine ….

Nanson, R, Vakarelov, B, Ainsworth, R, Williams, F & Price, D 2013, 'Evolution of a Holocene, mixed-process, forced regressive shoreline: the Mitchell River delta, Queensland, Australia', *Marine Geology*, vol. 339, pp. 22-43.

Nath, RK & Deb, S 2010, 'Water-body area extraction from high resolution satellite images-an introduction, review, and comparison', *International Journal of Image Processing (IJIP)*, vol. 3, no. 6, pp. 265-384.

Neukermans, G, Ruddick, K, Bernard, E, Ramon, D, Nechad, B & Deschamps, P-Y 2009, 'Mapping total suspended matter from geostationary satellites: a feasibility study with SEVIRI in the Southern North Sea', *Optics Express*, vol. 17, no. 16, pp. 14029-52.

Nichols, G 2009, *Sedimentology and stratigraphy*, John Wiley & Sons.

Ody, A, Doxaran, D, Vanhellemont, Q, Nechad, B, Novoa, S, Many, G, Bourrin, F, Verney, R, Pairaud, I & Gentili, B 2016, 'Potential of high spatial and temporal ocean color satellite data to study the dynamics of suspended particles in a micro-tidal river plume', *Remote Sensing*, vol. 8, no. 3, p. 245.

Ogashawara, I, Mishra, DR & Gitelson, AA 2017, 'Remote sensing of inland waters: background and current state-of-the-art', in *Bio-optical modeling and remote sensing of inland waters*, Elsevier, pp. 1-24.

Orton, G & Reading, H 1993, 'Variability of deltaic processes in terms of sediment supply, with particular emphasis on grain size', *Sedimentology*, vol. 40, no. 3, pp. 475-512.

Ozesmi, SL & Bauer, ME 2002, 'Satellite remote sensing of wetlands', *Wetlands ecology and management*, vol. 10, no. 5, pp. 381-402.

Pahlevan, N, Chittimalli, SK, Balasubramanian, SV & Vellucci, V 2019, 'Sentinel-2/Landsat-8 product consistency and implications for monitoring aquatic systems', *Remote Sensing of Environment*, vol. 220, pp. 19-29.

Palacios, SL, Peterson, TD & Kudela, RM 2009, 'Development of synthetic salinity from remote sensing for the Columbia River plume', *Journal of Geophysical Research: Oceans*, vol. 114, no. C2.

Pavelsky, TM & Smith, LC 2009, 'Remote sensing of suspended sediment concentration, flow velocity, and lake recharge in the Peace-Athabasca Delta, Canada', *Water Resources Research*, vol. 45, no. 11.

Petheram, C, Watson, I, Bruce, C & Chilcott, C 2018, *Water Resource Assessment for the Mitchell Catchment; A Report to the Australian Government from the CSIRO Northern Australia Water Resource Assessment, Part of the National Water Infrastructure Development Fund: Water Resource Assessments*, CSIRO: Canberra, Australia.

Posamentier, H, Jervey, MT & Vail, P 1988, 'Eustatic controls on clastic deposition I—conceptual framework'.

Potes, M, Costa, MJ & Salgado, R 2012, 'Satellite remote sensing of water turbidity in Alqueva reservoir and implications on lake modelling', *Hydrology and Earth System Sciences*, vol. 16, no. 6, pp. 1623-33.

Potes, M, Rodrigues, G, Penha, AM, Novais, MH, Costa, MJ, Salgado, R & Morais, MM 2018, 'Use of Sentinel 2–MSI for water quality monitoring at Alqueva reservoir, Portugal', *Proceedings of the International Association of Hydrological Sciences*, vol. 380, pp. 73-9.

Preda, M & Cox, ME 2005, 'Chemical and mineralogical composition of marine sediments, and relation to their source and transport, Gulf of Carpentaria, Northern Australia', *Journal of Marine Systems*, vol. 53, no. 1-4, pp. 169-86.

Quang, NH, Sasaki, J, Higa, H & Huan, NH 2017, 'Spatiotemporal variation of turbidity based on landsat 8 oli in cam ranh bay and thuy trieu lagoon, vietnam', *Water*, vol. 9, no. 8, p. 570.

Reading, HG 2009, *Sedimentary environments: processes, facies and stratigraphy*, John Wiley & Sons.

Renosh, PR, Doxaran, D, Keukelaere, LD & Gossn, JI 2020, 'Evaluation of atmospheric correction algorithms for sentinel-2-msi and sentinel-3-olci in highly turbid estuarine waters', *Remote Sensing*, vol. 12, no. 8, p. 1285.

Rhodes, EG 1980, 'Modes of Holocene coastal progradation: Gulf of Carpentaria'.

Ridd, P, Sandstrom, MW & Wolanski, E 1988, 'Outwelling from tropical tidal salt flats', *Estuarine, Coastal and Shelf Science*, vol. 26, no. 3, pp. 243-53.

Ritchie, JC, Zimba, PV & Everitt, JH 2003, 'Remote sensing techniques to assess water quality', *Photogrammetric Engineering & Remote Sensing*, vol. 69, no. 6, pp. 695-704.

Roy, DP, Kovalskyy, V, Zhang, H, Vermote, EF, Yan, L, Kumar, S & Egorov, A 2016, 'Characterization of Landsat-7 to Landsat-8 reflective wavelength and normalized difference vegetation index continuity', *Remote Sensing of Environment*, vol. 185, pp. 57-70.

Rustomji, P 2010, 'A statistical analysis of flood hydrology and bankfull discharge for the Mitchell River catchment, Queensland, Australia'.

Ryu, J-H, Won, J-S & Min, KD 2002, 'Waterline extraction from Landsat TM data in a tidal flat: a case study in Gomso Bay, Korea', *Remote Sensing of Environment*, vol. 83, no. 3, pp. 442-56.

Schild, KM, Hawley, RL, Chipman, JW & Benn, DI 2017, 'Quantifying suspended sediment concentration in subglacial sediment plumes discharging from two Svalbard tidewater glaciers using Landsat-8 and in situ measurements', *International Journal of Remote Sensing*, vol. 38, no. 23, pp. 6865-81.

Sebastiá-Frasquet, M-T, Aguilar-Maldonado, JA, Santamaría-Del-Ángel, E & Estornell, J 2019, 'Sentinel 2 analysis of turbidity patterns in a coastal lagoon', *Remote Sensing*, vol. 11, no. 24, p. 2926.

Seybold, H, Andrade, JS & Herrmann, HJ 2007, 'Modeling river delta formation', *Proceedings of the National Academy of Sciences*, vol. 104, no. 43, pp. 16804-9.

Shalaby, A & Tateishi, R 2007, 'Remote sensing and GIS for mapping and monitoring land cover and land-use changes in the Northwestern coastal zone of Egypt', *Applied geography*, vol. 27, no. 1, pp. 28-41.

Shellberg, J, Spencer, J, Brooks, A & Pietsch, T 2016, 'Degradation of the Mitchell River fluvial megafan by alluvial gully erosion increased by post-European land use change, Queensland, Australia', *Geomorphology*, vol. 266, pp. 105-20.

Shi, W & Wang, M 2009, 'Satellite observations of flood-driven Mississippi River plume in the spring of 2008', *Geophysical Research Letters*, vol. 36, no. 7.

Shulmeister, J 1999, 'Australasian evidence for mid-Holocene climate change implies precessional control of Walker Circulation in the Pacific', *Quaternary International*, vol. 57, pp. 81-91.

Sloss, CR, Nothdurft, L, Hua, Q, O'Connor, SG, Moss, PT, Rosendahl, D, Petherick, LM, Nanson, RA, Mackenzie, LL & Sternes, A 2018, 'Holocene sea-level change and coastal landscape evolution in the southern Gulf of Carpentaria, Australia', *The Holocene*, vol. 28, no. 9, pp. 1411-30.

Small, C 2004, 'The Landsat ETM+ spectral mixing space', *Remote Sensing of Environment*, vol. 93, no. 1-2, pp. 1-17.

Smith, S 2010, *Coastal Erosion & Sea Level Rise*, NSW Parliamentary Library.

Soomets, T, Uudeberg, K, Jakovels, D, Brauns, A, Zagars, M & Kutser, T 2020, 'Validation and comparison of water quality products in baltic lakes using sentinel-2 msi and sentinel-3 OLCI data', *Sensors*, vol. 20, no. 3, p. 742.

Suppiah, R 1992, 'The Australian summer monsoon: A review', *Progress in Physical Geography*, vol. 16, no. 3, pp. 283-318.

Taylor, M & Stone, GW 1996, 'Beach-ridges: a review', *Journal of Coastal Research*, pp. 612-21.

Theseira, M, Thomas, G, Taylor, J, Gemmell, F & Varjo, J 2003, 'Sensitivity of mixture modelling to end-member selection', *International Journal of Remote Sensing*, vol. 24, no. 7, pp. 1559-75.

Toming, K, Kutser, T, Laas, A, Sepp, M, Paavel, B & Nõges, T 2016, 'First experiences in mapping lake water quality parameters with Sentinel-2 MSI imagery', *Remote Sensing*, vol. 8, no. 8, p. 640.

Vakarelov, BK & Ainsworth, RB 2013, 'A hierarchical approach to architectural classification in marginal-marine systems: bridging the gap between sedimentology and sequence stratigraphy', *Aapg Bulletin*, vol. 97, no. 7, pp. 1121-61.

Vanhellemont, Q, Neukermans, G & Ruddick, K 2014, 'Synergy between polar-orbiting and geostationary sensors: Remote sensing of the ocean at high spatial and high temporal resolution', *Remote Sensing of Environment*, vol. 146, pp. 49-62.

Vanhellemont, Q & Ruddick, K 2014, 'Turbid wakes associated with offshore wind turbines observed with Landsat 8', *Remote Sensing of Environment*, vol. 145, pp. 105-15.

—— 2015, 'Advantages of high quality SWIR bands for ocean colour processing: Examples from Landsat-8', *Remote Sensing of Environment*, vol. 161, pp. 89-106.

—— 2016, 'Acolite for Sentinel-2: Aquatic applications of MSI imagery', in *Proceedings of the 2016 ESA Living Planet Symposium, Prague, Czech Republic*, pp. 9-13.

Wang, M & Shi, W 2007, 'The NIR-SWIR combined atmospheric correction approach for MODIS ocean color data processing', *Optics Express*, vol. 15, no. 24, pp. 15722-33.

Wei, W, Zhang, X, Chen, X, Tang, J & Jiang, M 2008, 'Wetland mapping using subpixel analysis and decision tree classification in the Yellow River delta area', *ISPRS Archives*, vol. 38, no. B7, pp. 667-70.

Wolanski, E 1993, 'Water circulation in the Gulf of Carpentaria', *Journal of Marine Systems*, vol. 4, no. 5, pp. 401-20.

Wright, L 1977, 'Sediment transport and deposition at river mouths: a synthesis', *Geological Society of America Bulletin*, vol. 88, no. 6, pp. 857-68.

—— 1978, 'River deltas', in *Coastal sedimentary environments*, Springer, pp. 5-68.

Xiao-ge, Z 2002, 'Remote sensing monitoring of coastline changes in Pearl River Estuary [J]', *Marine Environmental Science*, vol. 2.

Yoshino, K, Kawaguchi, S, Kanda, F, Kushida, K & Tsai, F 2014, 'Very high resolution plant community mapping at High Moor, Kushiro Wetland', *Photogrammetric Engineering & Remote Sensing*, vol. 80, no. 9, pp. 895-905.

Zhang, B 2009, 'A CART based sub-pixel method to map spatial and temporal patterns of prairie Pothole Lakes with climatic variability', *Unpublished manuscript, Ohio State University, Columbus, Ohio*.

APPENDICES

Appendix 1:

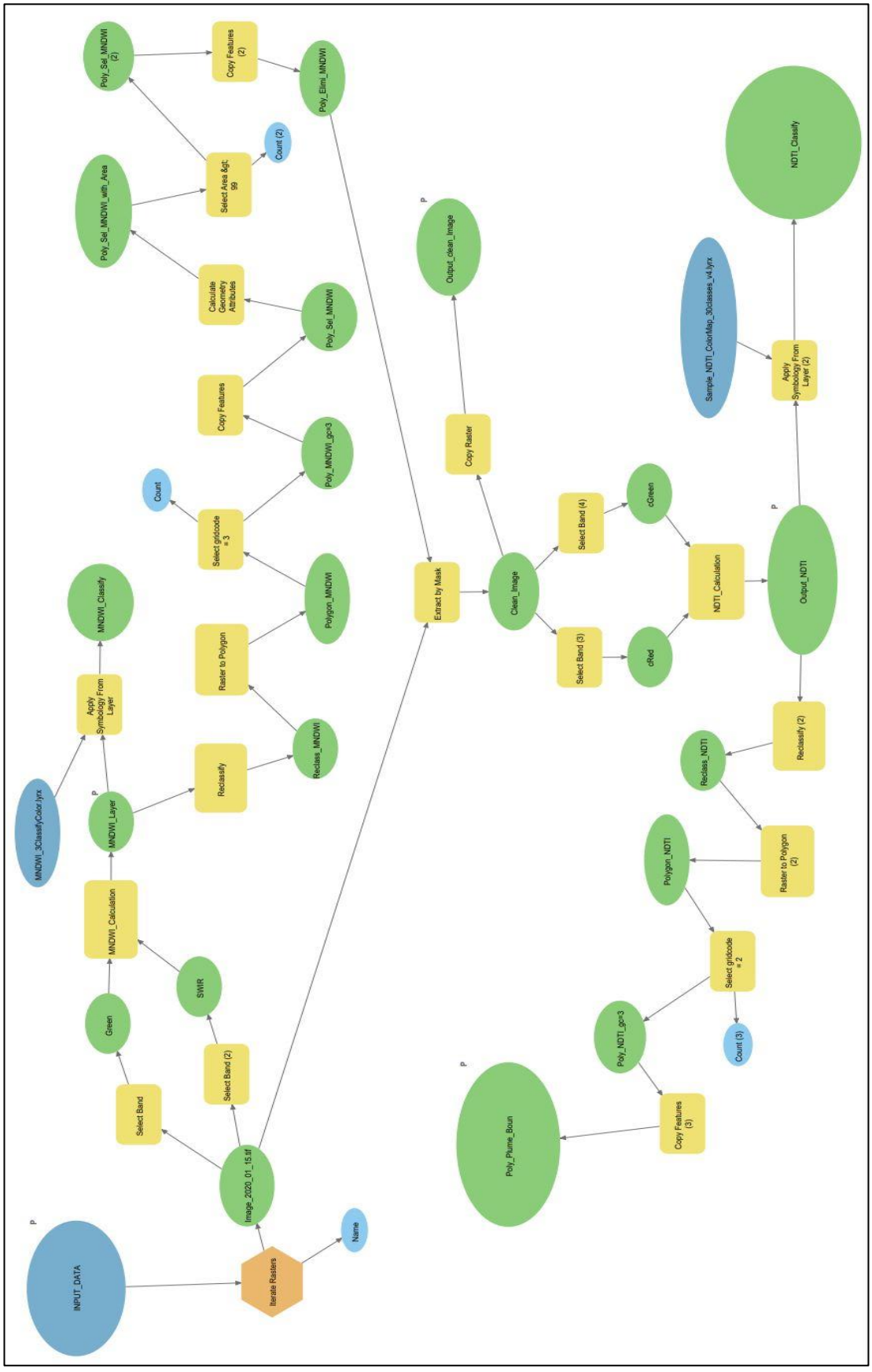

Appendix 2: Python Scripts in ArcPy Environment.

Part 1: Script of Setting Up the Working Folders.

```
# -*- coding: utf-8 -*-
"""Generated by ArcGIS ModelBuilder on : 2021-10-19 01:18:08"""
import arcpy
from sys import argv
def
CreateWorkingFolder(OUTPUT="C:\\Kevin\\MGISc2020\\Thesis\\Methodology\\ImageProcessing\\PlumeDect
ionUsingNDTI(2020)\\OUTPUT"):
# CreateWorkingFolder
# To allow overwriting outputs change overwriteOutput option to True.
arcpy.env.overwriteOutput = False
# Model Environment settings
with
arcpy.EnvManager(scratchWorkspace=r"C:\Kevin\MGISc2020\Thesis\Methodology\ImageProcessing\PlumeDe
ctionUsingNDTI(2020)",
workspace=r"C:\Kevin\MGISc2020\Thesis\Methodology\ImageProcessing\PlumeDectionUsingNDTI(2020)"):
# Process: Create Folder (Create Folder) (management)
MNDWI = arcpy.management.CreateFolder(out_folder_path=OUTPUT, out_name="MNDWI")[0]
# Process: Create Folder (2) (Create Folder) (management)
MNDWI_Reclass = arcpy.management.CreateFolder(out_folder_path=OUTPUT,
out_name="MNDWI_Reclass")[0]
# Process: Create Folder (3) (Create Folder) (management)
MNDWI_Poly = arcpy.management.CreateFolder(out_folder_path=OUTPUT, out_name="MNDWI_Poly")[0]
# Process: Create Folder (4) (Create Folder) (management)
MNDWI_Poly_Selected = arcpy.management.CreateFolder(out_folder_path=OUTPUT,
out_name="MNDWI_Poly_Selected")[0]
# Process: Create Folder (5) (Create Folder) (management)
MNDWI_Poly_Elimin = arcpy.management.CreateFolder(out_folder_path=OUTPUT,
out_name="MNDWI_Poly_Elimin")[0]
# Process: Create Folder (6) (Create Folder) (management)
Cleaned_Images = arcpy.management.CreateFolder(out_folder_path=OUTPUT,
out_name="Cleaned_Images")[0]
# Process: Create Folder (7) (Create Folder) (management)
NDTI = arcpy.management.CreateFolder(out_folder_path=OUTPUT, out_name="NDTI")[0]
# Process: Create Folder (8) (Create Folder) (management)
Processing_Folder = arcpy.management.CreateFolder(out_folder_path=OUTPUT,
out_name="Processing_Folder")[0]
# Process: Create Folder (9) (Create Folder) (management)
Output_Plume_Boundary = arcpy.management.CreateFolder(out_folder_path=OUTPUT,
out_name="Output_Plume_Area")[0]if __name__ == '__main__':
```

```
# Global Environment settings
with
arcpy.EnvManager(outputCoordinateSystem="PROJCS["WGS_1984_UTM_Zone_54S",GEOGCS["GCS_WGS_1984",DAT
UM["D_WGS_1984",SPHEROID["WGS_1984",6378137.0,298.257223563]],PRIMEM["Greenwich",0.0],UNIT["Degre
e",0.0174532925199433]],PROJECTION["Transverse_Mercator"],PARAMETER["False_Easting",500000.0],PAR
AMETER["False_Northing",10000000.0],PARAMETER["Central_Meridian",141.0],PARAMETER["Scale_Factor",
0.9996],PARAMETER["Latitude_Of_Origin",0.0],UNIT["Meter",1.0]]"):
CreateWorkingFolder(*argv[1:])
```

Part 2: Script of Creating a Replica Dataset for Analysis.

```
# -*- coding: utf-8 -*-
"""Generated by ArcGIS ModelBuilder on : 2021-10-19 01:16:55"""
import arcpy
def #  NOT  IMPLEMENTED# Function Body not implemented
def CreateDataset():
# CreateDataset
# To allow overwriting outputs change overwriteOutput option to True.
arcpy.env.overwriteOutput = False
DATA =
"C:\\Kevin\\MGISc2020\\Thesis\\Methodology\\ImageProcessing\\PlumeDectionUsingNDTI(2020)\\DATA"
for Raster, Name in #  NOT  IMPLEMENTED(DATA, "", "", "RECURSIVE"):
# Process: Copy Raster (Copy Raster) (management)
_name_ =
"C:\\Kevin\\MGISc2020\\Thesis\\Methodology\\ImageProcessing\\PlumeDectionUsingNDTI(2020)\\INPUT_D
ATA\\%name%"
arcpy.management.CopyRaster(in_raster=Raster, out_rasterdataset=_name_,
config_keyword="Image_2020_01_15", background_value=None, nodata_value="65536",
onebit_to_eightbit="NONE", colormap_to_RGB="NONE", pixel_type="16_BIT_UNSIGNED",
scale_pixel_value="NONE", RGB_to_Colormap="NONE", format="TIFF", transform="NONE",
process_as_multidimensional="CURRENT_SLICE", build_multidimensional_transpose="NO_TRANSPOSE")
if __name__ == '__main__':
# Global Environment settings
with
arcpy.EnvManager(outputCoordinateSystem="PROJCS["WGS_1984_UTM_Zone_54S",GEOGCS["GCS_WGS_1984",DAT
UM["D_WGS_1984",SPHEROID["WGS_1984",6378137.0,298.257223563]],PRIMEM["Greenwich",0.0],UNIT["Degre
e",0.0174532925199433]],PROJECTION["Transverse_Mercator"],PARAMETER["False_Easting",500000.0],PAR
AMETER["False_Northing",10000000.0],PARAMETER["Central_Meridian",141.0],PARAMETER["Scale_Factor",
0.9996],PARAMETER["Latitude_Of_Origin",0.0],UNIT["Meter",1.0]]",
scratchWorkspace=r"C:\Kevin\MGISc2020\Thesis\Methodology\ImageProcessing\PlumeDectionUsingNDTI(20
20)",
workspace=r"C:\Kevin\MGISc2020\Thesis\Methodology\ImageProcessing\PlumeDectionUsingNDTI(2020)"):
CreateDataset()
```

Part 3: Script of Automation Analysis for Turbidity Detection.

```
# -*- coding: utf-8 -*-
"""Generated by ArcGIS ModelBuilder on : 2021-10-19 01:13:50"""
import arcpy
from arcpy.ia import *
from arcpy.ia import *
from sys import argv
def #  NOT  IMPLEMENTED# Function Body not implemented
def
PlumeDectectionUsingNDTI(INPUT_DATA="C:\\Kevin\\MGISc2020\\Thesis\\Methodology\\ImageProcessing\\
PlumeDectionUsingNDTI(2020)\\INPUT_DATA",
MNDWI_Layer="C:\\Kevin\\MGISc2020\\Thesis\\Methodology\\ImageProcessing\\PlumeDectionUsingNDTI(20
20)\\OUTPUT\\MNDWI\\MNDWI_%name%",
Output_clean_Image="C:\\Kevin\\MGISc2020\\Thesis\\Methodology\\ImageProcessing\\PlumeDectionUsing
NDTI(2020)\\OUTPUT\\Cleaned_Images\\c_%name%",
Output_NDTI="C:\\Kevin\\MGISc2020\\Thesis\\Methodology\\ImageProcessing\\PlumeDectionUsingNDTI(20
20)\\OUTPUT\\NDTI\\NDTI_%name%",
Poly_Plume_Boun="C:\\Kevin\\MGISc2020\\Thesis\\Methodology\\ImageProcessing\\PlumeDectionUsingNDT
I(2020)\\OUTPUT\\Output_Plume_Area\\Poly_Boun_Plume_%name%.shp"):
# PlumeDectectionUsingNDTI
# To allow overwriting outputs change overwriteOutput option to True.
arcpy.env.overwriteOutput = False
# Check out any necessary licenses.
arcpy.CheckOutExtension("3D")
arcpy.CheckOutExtension("spatial")
arcpy.CheckOutExtension("ImageAnalyst")
arcpy.ImportToolbox(r"c:\program files\arcgis\pro\Resources\ArcToolbox\toolboxes\Data Management
Tools.tbx")
MNDWI_3ClassifyColor_lyrx =
"C:\\Kevin\\MGISc2020\\Thesis\\Methodology\\ImageProcessing\\PlumeDectionUsingNDTI(2020)\\Symbolo
gy_Samples\\MNDWI_3ClassifyColor.lyrx"
Sample_NDTI_ColorMap_30classes_v4_lyrx =
"C:\\Kevin\\MGISc2020\\Thesis\\Methodology\\ImageProcessing\\PlumeDectionUsingNDTI(2020)\\Symbolo
gy_Samples\\Sample_NDTI_ColorMap_30classes_v4.lyrx"
for Image_2020_01_15_tif, Name in #  NOT  IMPLEMENTED(INPUT_DATA, "", "", "NOT_RECURSIVE"):
# Process: Select_Band (Select Data)         # Select Data Utility is not implemented
# Process: Select_Band_2_ (Select Data)         # Select Data Utility is not implemented
# Process: MNDWI_Calculation (Raster Calculator) (ia)
MNDWI_Calculation = MNDWI_Layer
MNDWI_Layer = (Green - SWIR)  / (Green + SWIR)
MNDWI_Layer.save(MNDWI_Calculation)
# Process: Reclassify (Reclassify) (sa)
```

```
Reclass_MNDWI =
"C:\\Kevin\\MGISc2020\\Thesis\\Methodology\\ImageProcessing\\PlumeDectionUsingNDTI(2020)\\OUTPUT\
\Processing_Folder\\Reclass_MNDWI"
Reclassify = Reclass_MNDWI
Reclass_MNDWI = arcpy.sa.Reclassify(in_raster=MNDWI_Layer, reclass_field="VALUE", remap="-
0.982405 -0.267951 1;-0.267951 0.361079 2;0.361079 1 3", missing_values="DATA")
Reclass_MNDWI.save(Reclassify)
# Process: Raster to Polygon (Raster to Polygon) (conversion)
Polygon_MNDWI =
"C:\\Kevin\\MGISc2020\\Thesis\\Methodology\\ImageProcessing\\PlumeDectionUsingNDTI(2020)\\OUTPUT\
\Processing_Folder\\Polygon_MNDWI.shp"
with arcpy.EnvManager(outputMFlag="Disabled", outputZFlag="Disabled"):
arcpy.conversion.RasterToPolygon(in_raster=Reclass_MNDWI, out_polygon_features=Polygon_MNDWI,
simplify="SIMPLIFY", raster_field="VALUE", create_multipart_features="SINGLE_OUTER_PART",
max_vertices_per_feature=None)
# Process: Select gridcode = 3 (Select Layer By Attribute) (management)
Poly_MNDWI_gc_3, Count = arcpy.management.SelectLayerByAttribute(in_layer_or_view=Polygon_MNDWI,
selection_type="NEW_SELECTION", where_clause="gridcode = 3", invert_where_clause="")
# Process: Copy Features (Copy Features) (management)
Poly_Sel_MNDWI =
"C:\\Kevin\\MGISc2020\\Thesis\\Methodology\\ImageProcessing\\PlumeDectionUsingNDTI(2020)\\OUTPUT\
\Processing_Folder\\Poly_sele_MNDWI.shp"
arcpy.management.CopyFeatures(in_features=Poly_MNDWI_gc_3, out_feature_class=Poly_Sel_MNDWI,
config_keyword="Image_20200911.tif", spatial_grid_1=None, spatial_grid_2=None,
spatial_grid_3=None)
# Process: Calculate Geometry Attributes (Calculate Geometry Attributes) (management)
Poly_Sel_MNDWI_with_Area =
arcpy.management.CalculateGeometryAttributes(in_features=Poly_Sel_MNDWI,
geometry_property=[["Area", "AREA"]], length_unit="", area_unit="SQUARE_KILOMETERS",
coordinate_system="PROJCS[\"WGS_1984_UTM_Zone_54S\",GEOGCS[\"GCS_WGS_1984\",DATUM[\"D_WGS_1984\",
SPHEROID[\"WGS_1984\",6378137.0,298.257223563]],PRIMEM[\"Greenwich\",0.0],UNIT[\"Degree\",0.01745
32925199433]],PROJECTION[\"Transverse_Mercator\"],PARAMETER[\"False_Easting\",500000.0],PARAMETER
[\"False_Northing\",10000000.0],PARAMETER[\"Central_Meridian\",141.0],PARAMETER[\"Scale_Factor\",
0.9996],PARAMETER[\"Latitude_Of_Origin\",0.0],UNIT[\"Meter\",1.0]]",
coordinate_format="SAME_AS_INPUT")[0]
# Process: Select Area &gt; 99 (Select Layer By Attribute) (management)
Poly_Sel_MNDWI_2_, Count_2_ =
arcpy.management.SelectLayerByAttribute(in_layer_or_view=Poly_Sel_MNDWI_with_Area,
selection_type="NEW_SELECTION", where_clause="Area > 99", invert_where_clause="")
# Process: Copy Features (2) (Copy Features) (management)
Poly_Elimi_MNDWI =
"C:\\Kevin\\MGISc2020\\Thesis\\Methodology\\ImageProcessing\\PlumeDectionUsingNDTI(2020)\\OUTPUT\
\Processing_Folder\\Poly_Elimi_MNDWI.shp"
arcpy.management.CopyFeatures(in_features=Poly_Sel_MNDWI_2_, out_feature_class=Poly_Elimi_MNDWI,
config_keyword="Image_20200911.tif", spatial_grid_1=None, spatial_grid_2=None,
spatial_grid_3=None)
```

```
# Process: Extract by Mask (Extract by Mask) (sa)
Clean_Image =
"C:\\Kevin\\MGISc2020\\Thesis\\Methodology\\ImageProcessing\\PlumeDectionUsingNDTI(2020)\\OUTPUT\
\Processing_Folder\\c_image"        Extract_by_Mask = Clean_Image        Clean_Image =
arcpy.sa.ExtractByMask(in_raster=Image_2020_01_15_tif, in_mask_data=Poly_Elimi_MNDWI)
Clean_Image.save(Extract_by_Mask)
# Process: Copy Raster (Copy Raster) (management)
arcpy.management.CopyRaster(in_raster=Clean_Image, out_rasterdataset=Output_clean_Image,
config_keyword="", background_value=None, nodata_value="-32768", onebit_to_eightbit="NONE",
colormap_to_RGB="NONE", pixel_type="16_BIT_UNSIGNED", scale_pixel_value="NONE",
RGB_to_Colormap="NONE", format="TIFF", transform="NONE",
process_as_multidimensional="CURRENT_SLICE", build_multidimensional_transpose="NO_TRANSPOSE")
# Process: Apply Symbology From Layer (Apply Symbology From Layer) (management)
MNDWI_Classify = arcpy.management.ApplySymbologyFromLayer(in_layer=MNDWI_Layer,
in_symbology_layer=MNDWI_3ClassifyColor_lyrx, symbology_fields=[["COLOR_EXPRESSION_FIELD", "",
""]], update_symbology="DEFAULT")[0]
# Process: Select_Band_3_ (Select Data)         # Select Data Utility is not implemented
# Process: Select_Band_4_ (Select Data)         # Select Data Utility is not implemented
# Process: NDTI_Calculation (Raster Calculator) (ia)
NDTI_Calculation = Output_NDTI
Output_NDTI = ( cRed  - cGreen ) / ( cRed  + cGreen )
Output_NDTI.save(NDTI_Calculation)
# Process: Apply Symbology From Layer (2) (Apply Symbology From Layer) (management)
NDTI_Classify = arcpy.management.ApplySymbologyFromLayer(in_layer=Output_NDTI,
in_symbology_layer=Sample_NDTI_ColorMap_30classes_v4_lyrx, symbology_fields=[["VALUE_FIELD", "",
""]], update_symbology="DEFAULT")[0]
# Process: Reclassify (2) (Reclassify) (sa)
Reclass_NDTI =
"C:\\Kevin\\MGISc2020\\Thesis\\Methodology\\ImageProcessing\\PlumeDectionUsingNDTI(2020)\\OUTPUT\
\Processing_Folder\\Reclass_NDTI"
Reclassify_2_ = Reclass_NDTI
Reclass_NDTI = arcpy.sa.Reclassify(in_raster=Output_NDTI, reclass_field="VALUE", remap="-1 -
0.400000 1;-0.400000 0.500000 2;0.500000 1 3", missing_values="DATA")
Reclass_NDTI.save(Reclassify_2_)
# Process: Raster to Polygon (2) (Raster to Polygon) (conversion)
Polygon_NDTI =
"C:\\Kevin\\MGISc2020\\Thesis\\Methodology\\ImageProcessing\\PlumeDectionUsingNDTI(2020)\\OUTPUT\
\Processing_Folder\\Polygon_NDTI.shp"
with arcpy.EnvManager(outputMFlag="Disabled", outputZFlag="Disabled"):
arcpy.conversion.RasterToPolygon(in_raster=Reclass_NDTI, out_polygon_features=Polygon_NDTI,
simplify="SIMPLIFY", raster_field="VALUE", create_multipart_features="SINGLE_OUTER_PART",
max_vertices_per_feature=None)
# Process: Select gridcode = 2 (Select Layer By Attribute) (management)
Poly_NDTI_gc_3, Count_3_ = arcpy.management.SelectLayerByAttribute(in_layer_or_view=Polygon_NDTI,
selection_type="NEW_SELECTION", where_clause="gridcode = 2", invert_where_clause="")
```

```
# Process: Copy Features (3) (Copy Features) (management)
arcpy.management.CopyFeatures(in_features=Poly_NDTI_gc_3, out_feature_class=Poly_Plume_Boun,
config_keyword="Image_20200911.tif", spatial_grid_1=None, spatial_grid_2=None,
spatial_grid_3=None)
if __name__ == '__main__':
# Global Environment settings
with
arcpy.EnvManager(outputCoordinateSystem="PROJCS["WGS_1984_UTM_Zone_54S",GEOGCS["GCS_WGS_1984",DAT
UM["D_WGS_1984",SPHEROID["WGS_1984",6378137.0,298.257223563]],PRIMEM["Greenwich",0.0],UNIT["Degre
e",0.0174532925199433]],PROJECTION["Transverse_Mercator"],PARAMETER["False_Easting",500000.0],PAR
AMETER["False_Northing",10000000.0],PARAMETER["Central_Meridian",141.0],PARAMETER["Scale_Factor",
0.9996],PARAMETER["Latitude_Of_Origin",0.0],UNIT["Meter",1.0]]",
scratchWorkspace=r"C:\Kevin\MGISc2020\Thesis\Methodology\ImageProcessing\PlumeDectionUsingNDTI(20
20)",
workspace=r"C:\Kevin\MGISc2020\Thesis\Methodology\ImageProcessing\PlumeDectionUsingNDTI(2020)"):
PlumeDectectionUsingNDTI(*argv[1:])
```

Appendix 3-01: Sediment Plume Geometry Map in 2020.

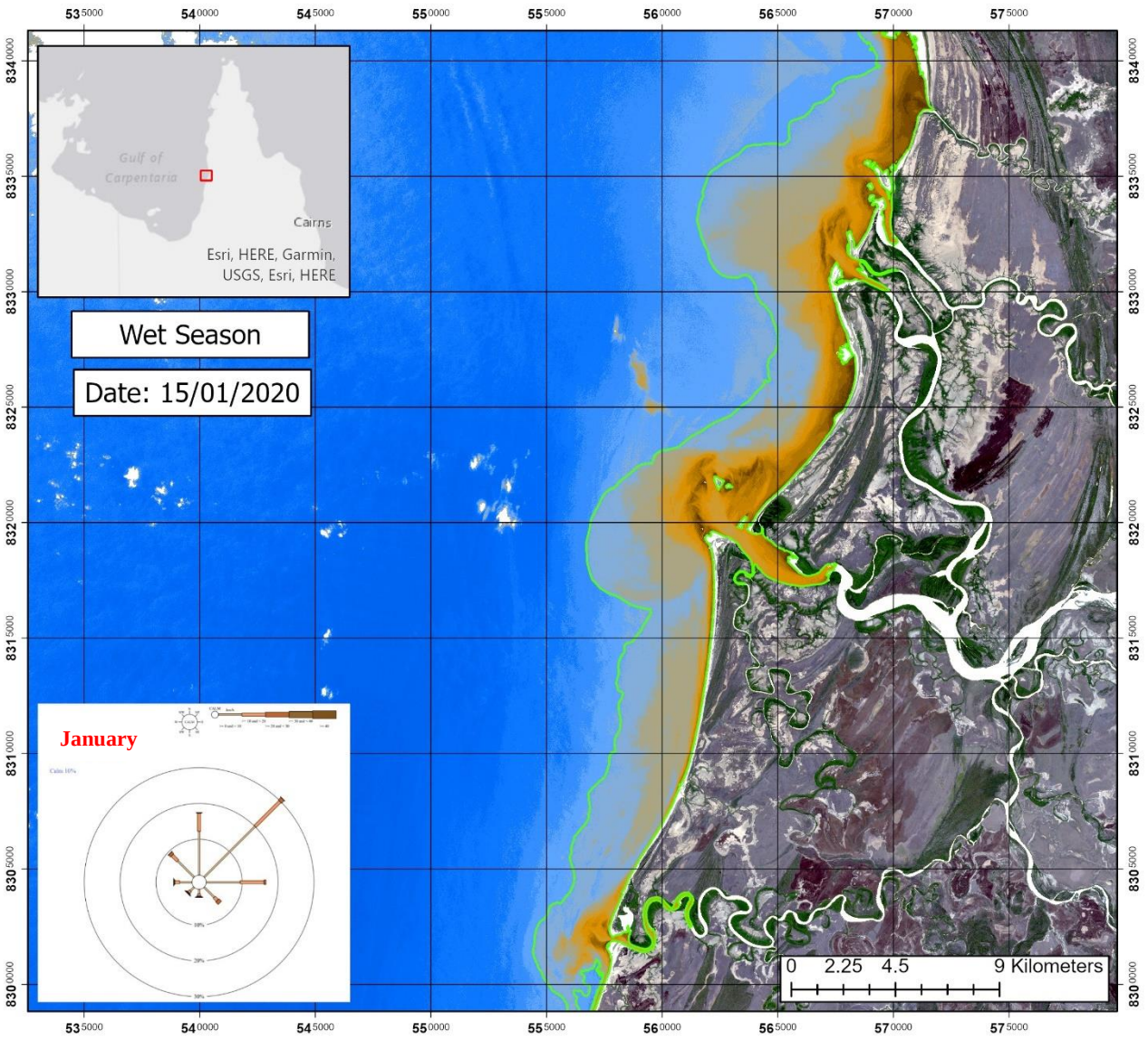

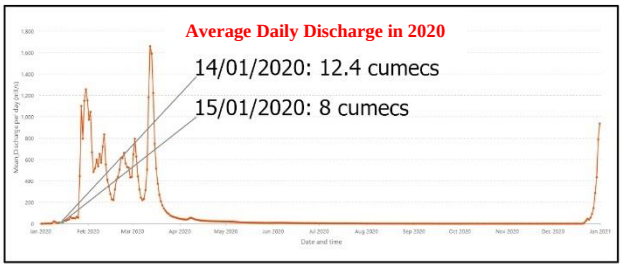

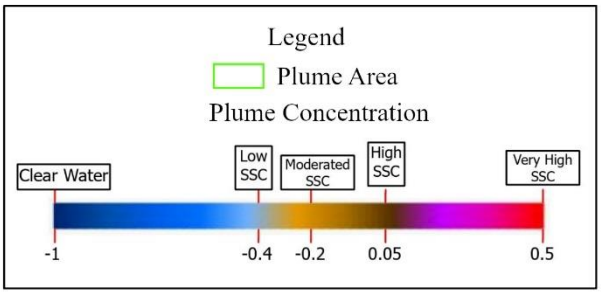

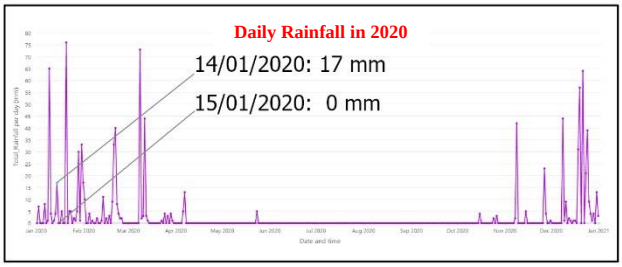

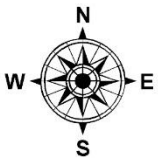

Scale: 1:240,000

Spatial Reference
Name: WGS 1984 UTM Zone 54S
PCS: WGS 1984 UTM Zone 54S
GCS: GCS WGS 1984
Datum: WGS 1984
Projection: Transverse Mercator
Map Units: Meter

Appendix 3-02: Sediment Plume Geometry Map in 2020.

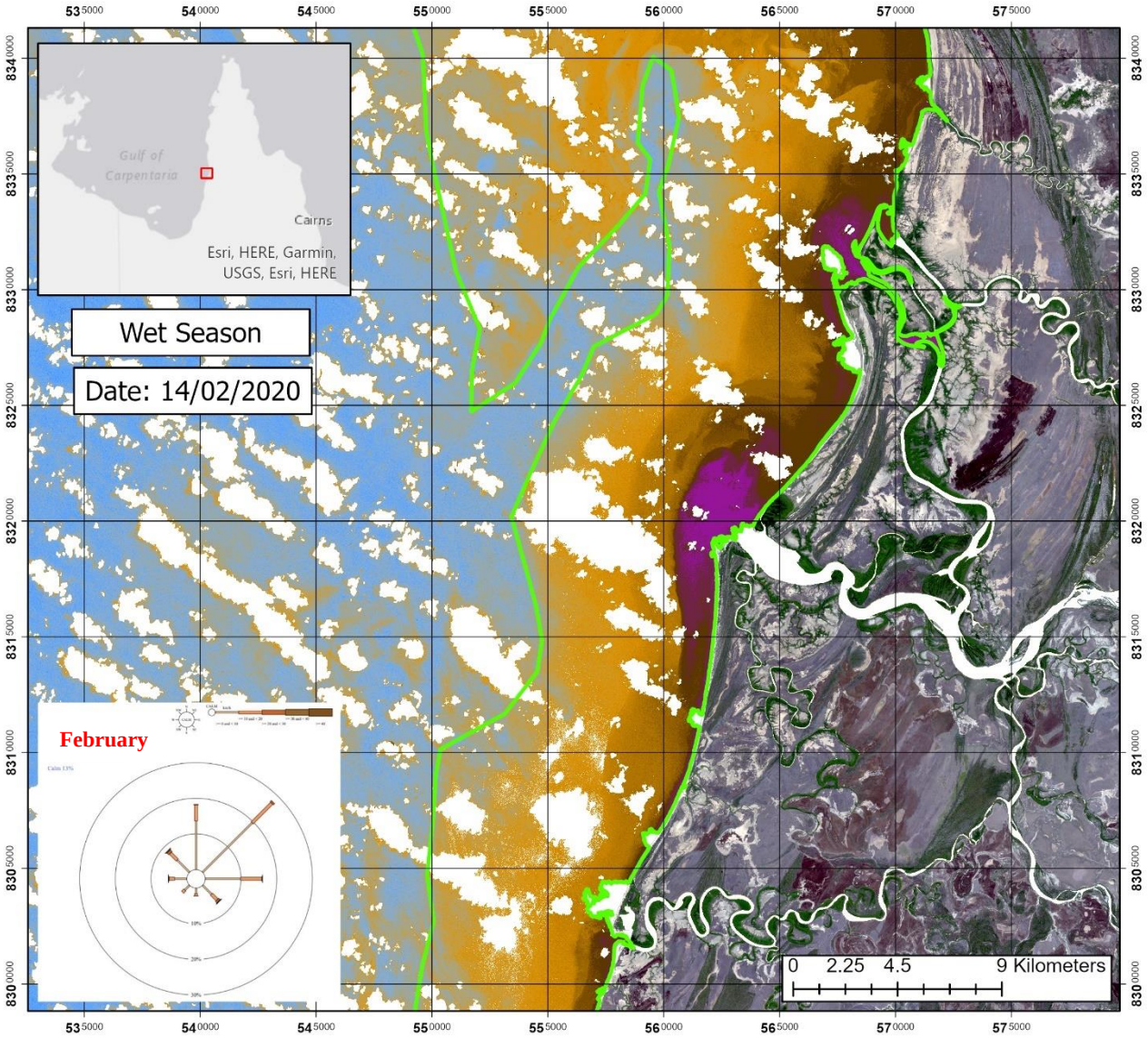

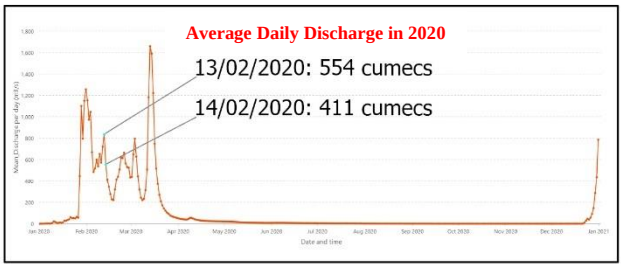

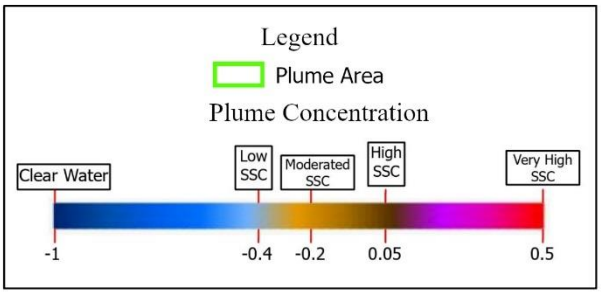

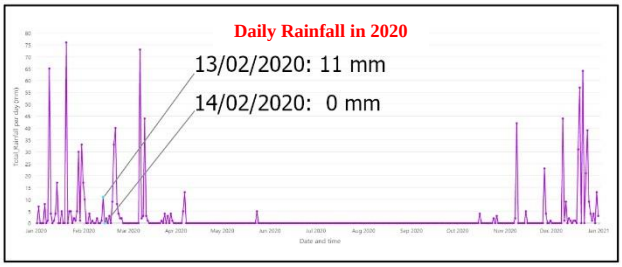

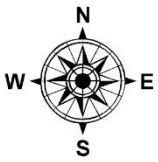

Scale: 1:240,000

Spatial Reference
Name: WGS 1984 UTM Zone 54S
PCS: WGS 1984 UTM Zone 54S
GCS: GCS WGS 1984
Datum: WGS 1984
Projection: Transverse Mercator
Map Units: Meter

Appendix 3-03: Sediment Plume Geometry Map in 2020.

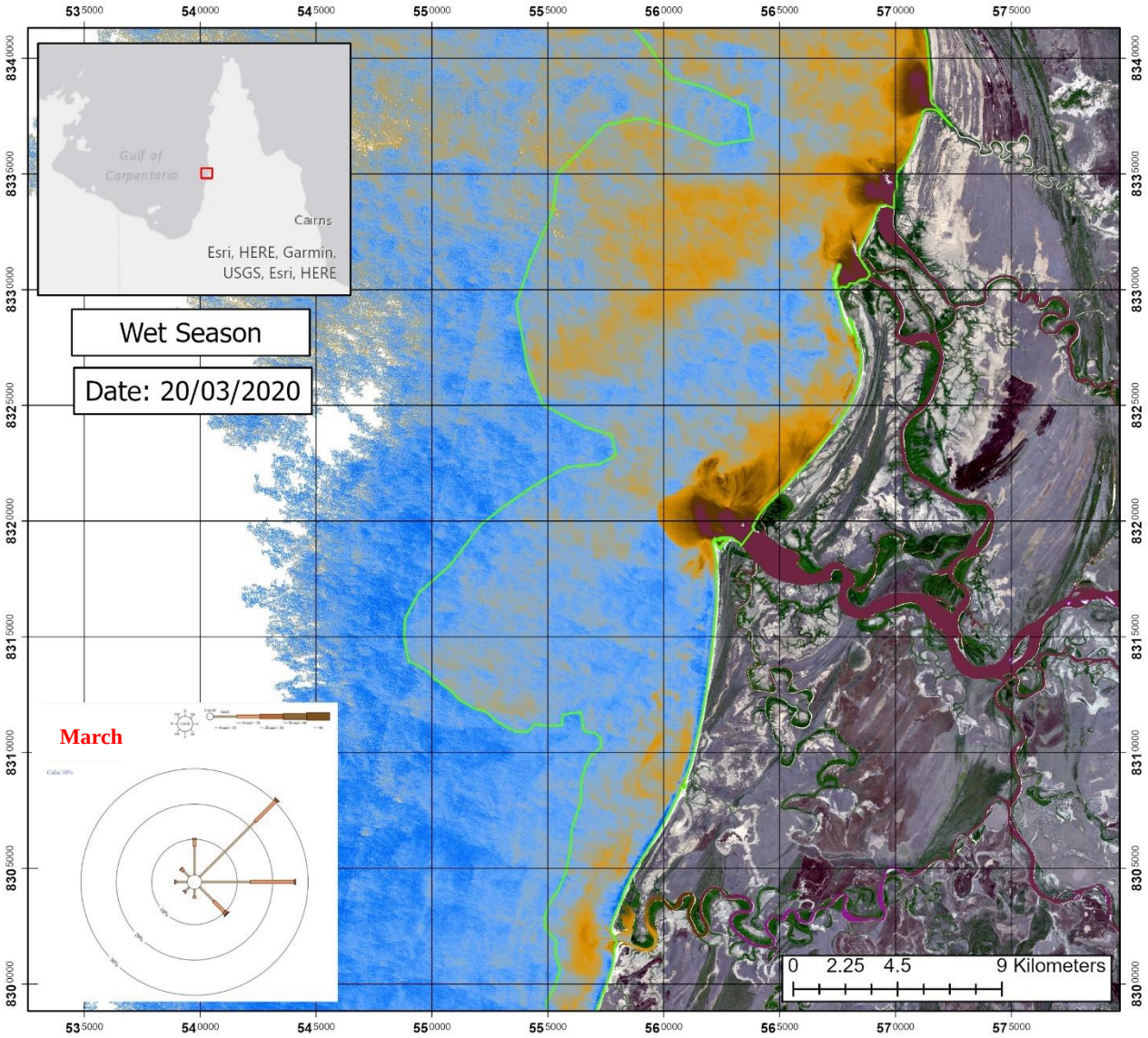

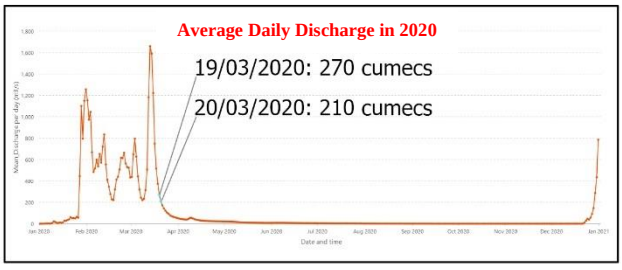

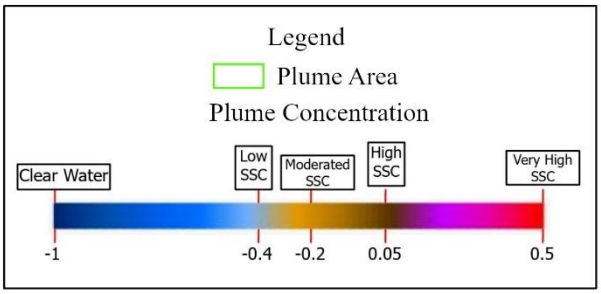

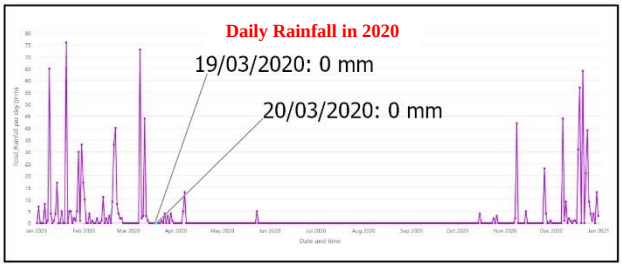

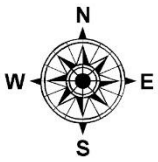

Scale: 1:240,000

Spatial Reference
Name: WGS 1984 UTM Zone 54S
PCS: WGS 1984 UTM Zone 54S
GCS: GCS WGS 1984
Datum: WGS 1984
Projection: Transverse Mercator
Map Units: Meter

Appendix 3-04: Sediment Plume Geometry Map in 2020.

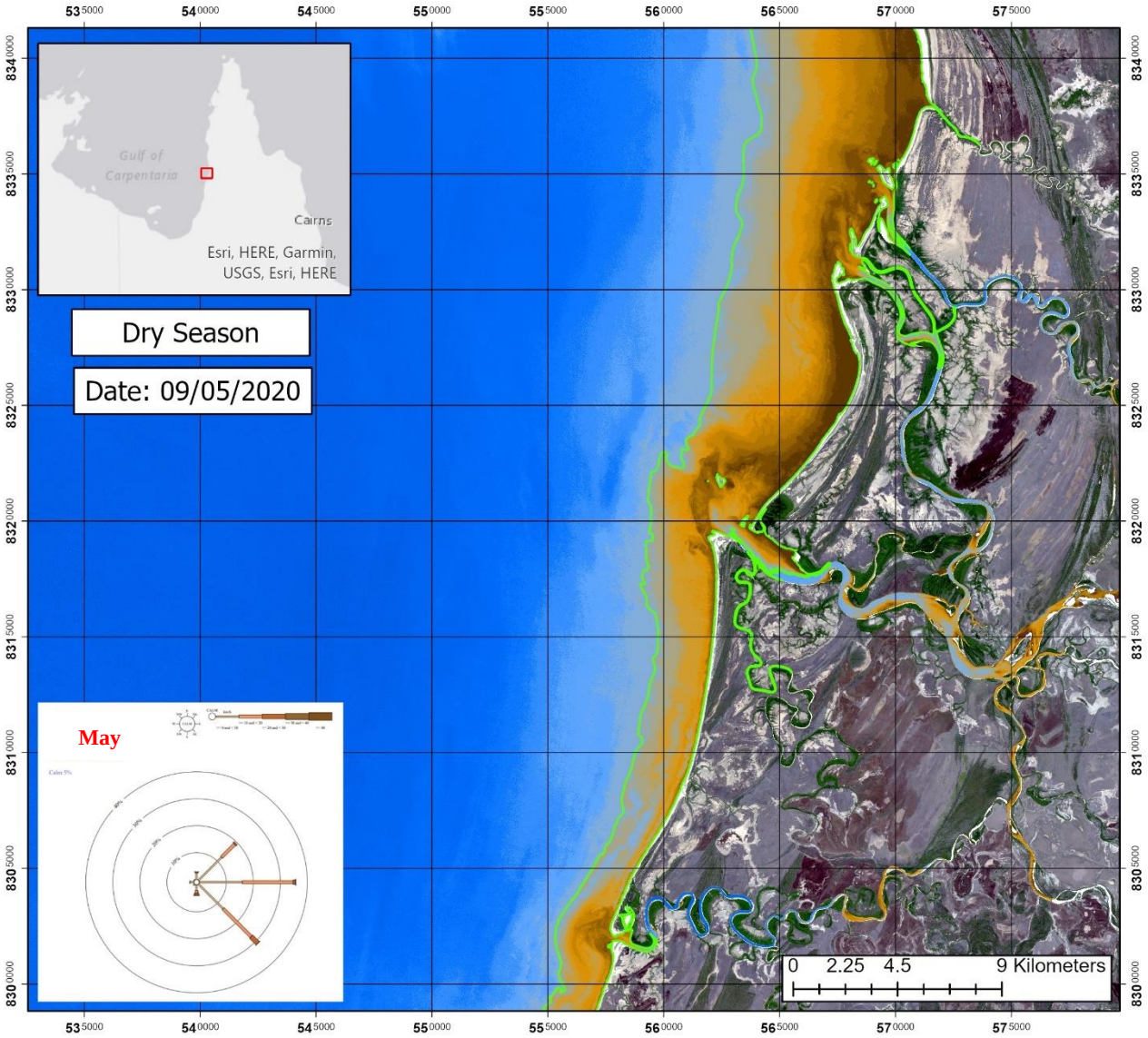

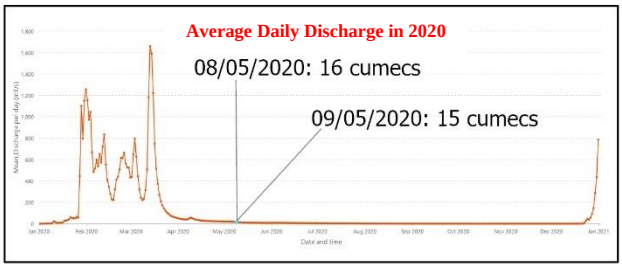

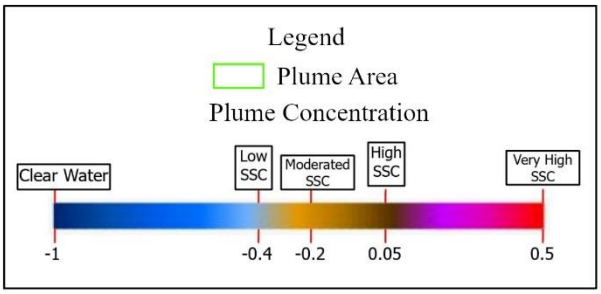

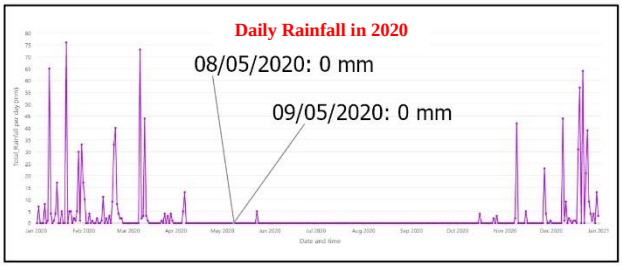

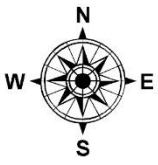

Scale: 1:240,000

Spatial Reference
Name: WGS 1984 UTM Zone 54S
PCS: WGS 1984 UTM Zone 54S
GCS: GCS WGS 1984
Datum: WGS 1984
Projection: Transverse Mercator
Map Units: Meter

Appendix 3-05: Sediment Plume Geometry Map in 2020.

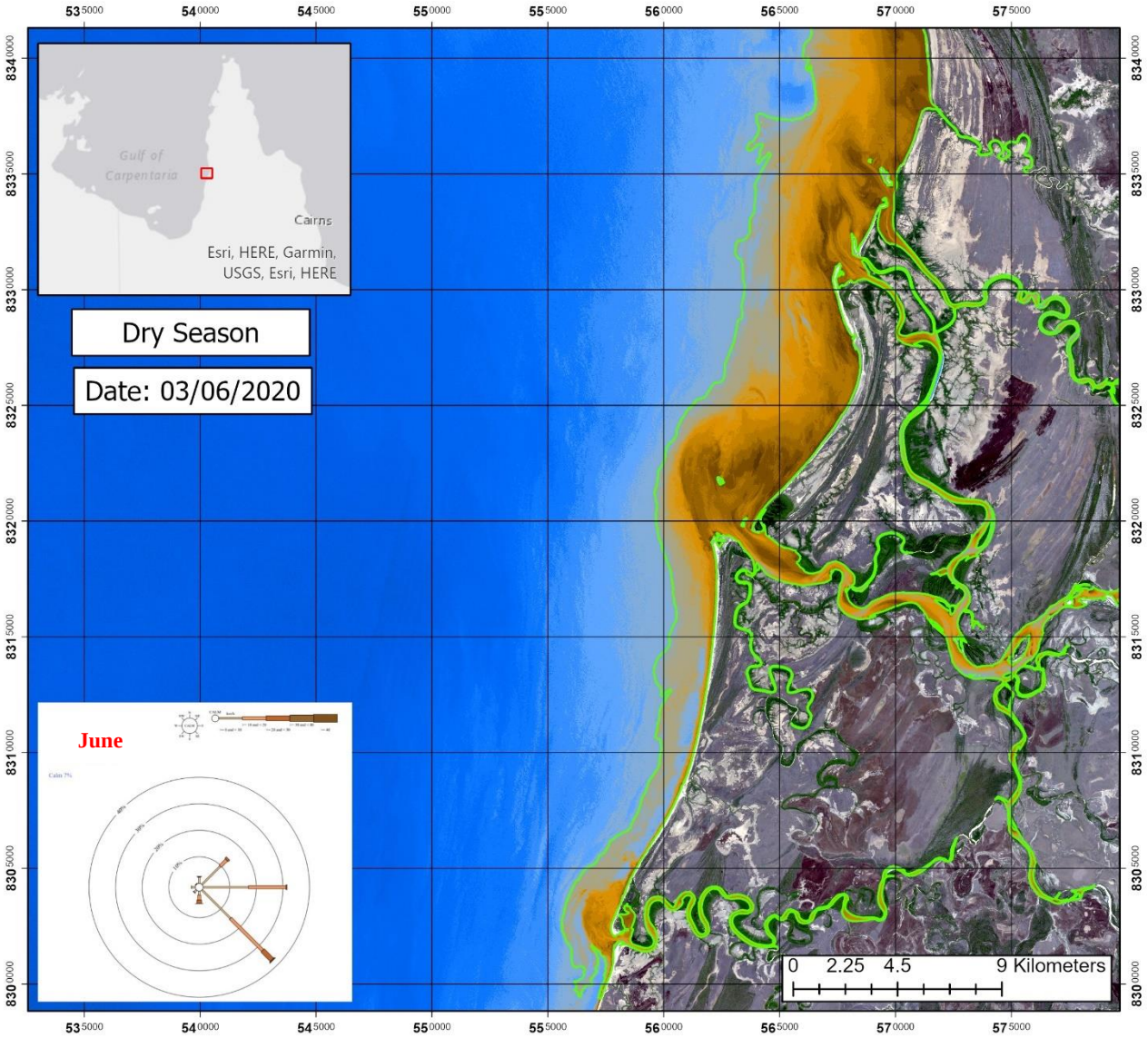

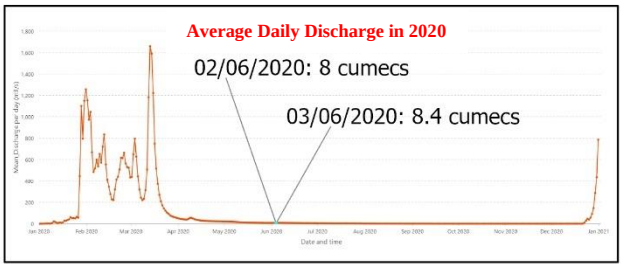

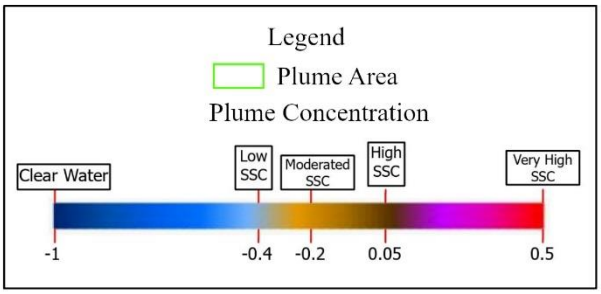

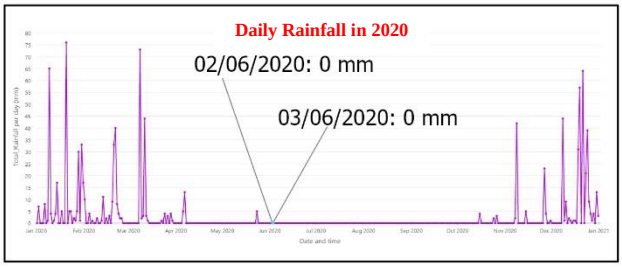

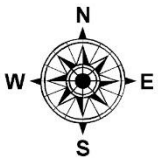

Scale: 1:240,000

Spatial Reference
Name: WGS 1984 UTM Zone 54S
PCS: WGS 1984 UTM Zone 54S
GCS: GCS WGS 1984
Datum: WGS 1984
Projection: Transverse Mercator
Map Units: Meter

Appendix 3-06: Sediment Plume Geometry Map in 2020.

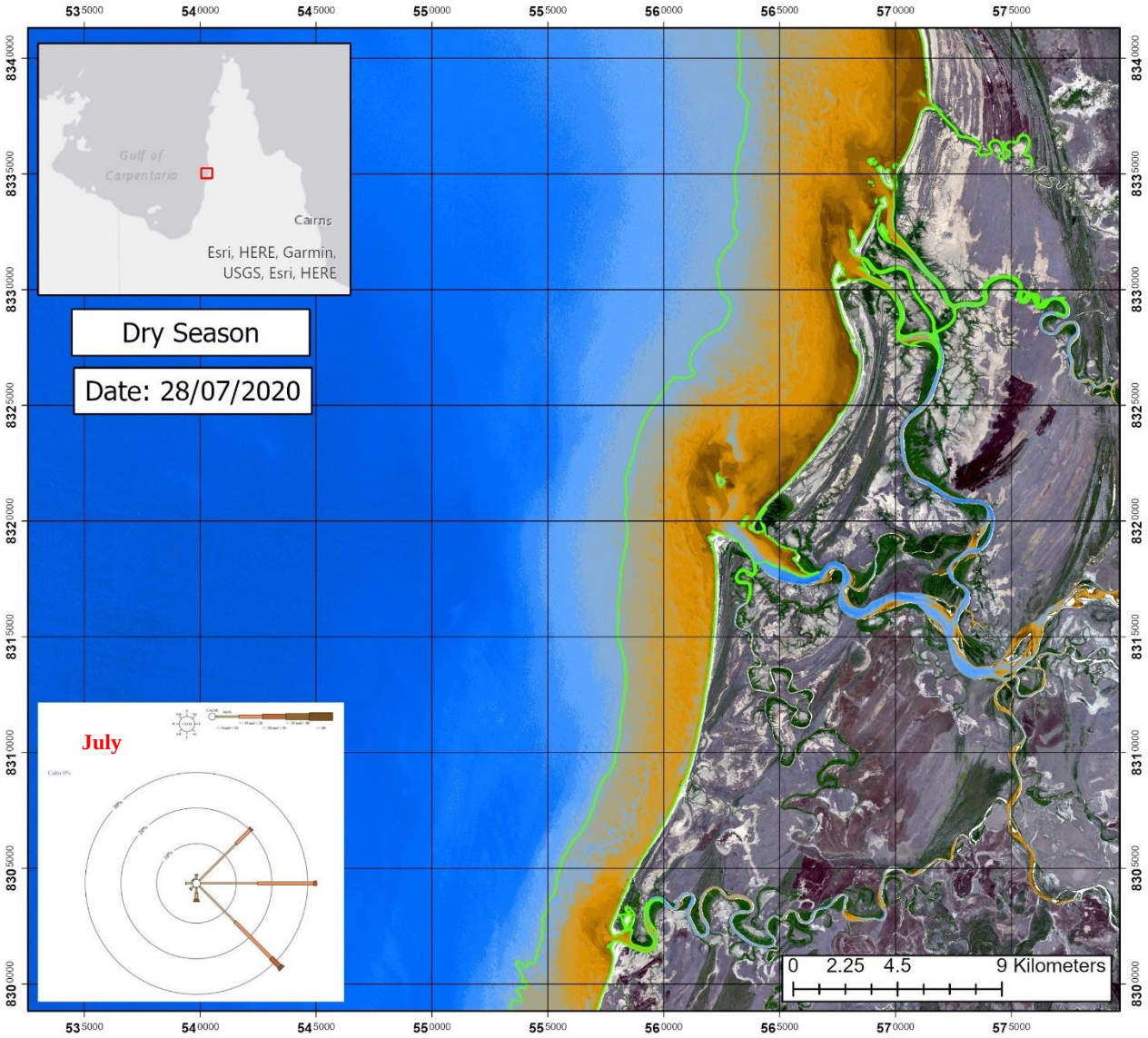

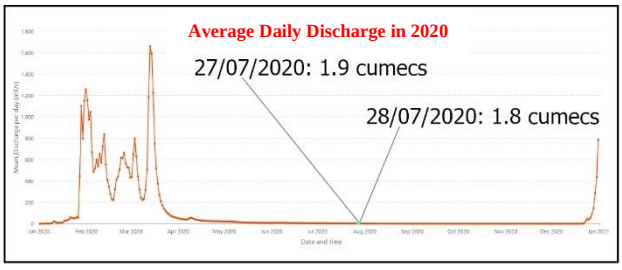

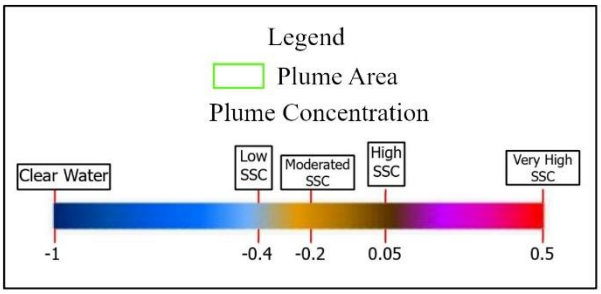

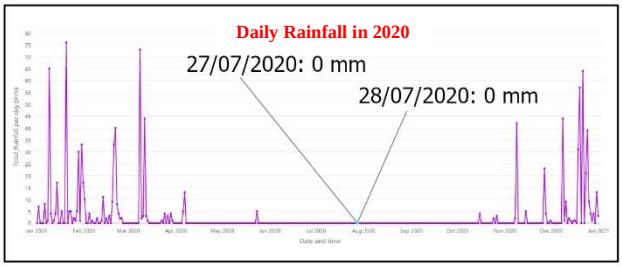

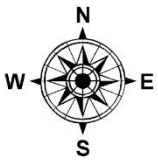

Scale: 1:240,000

Spatial Reference
Name: WGS 1984 UTM Zone 54S
PCS: WGS 1984 UTM Zone 54S
GCS: GCS WGS 1984
Datum: WGS 1984
Projection: Transverse Mercator
Map Units: Meter

Appendix 3-07: Sediment Plume Geometry Map in 2020.

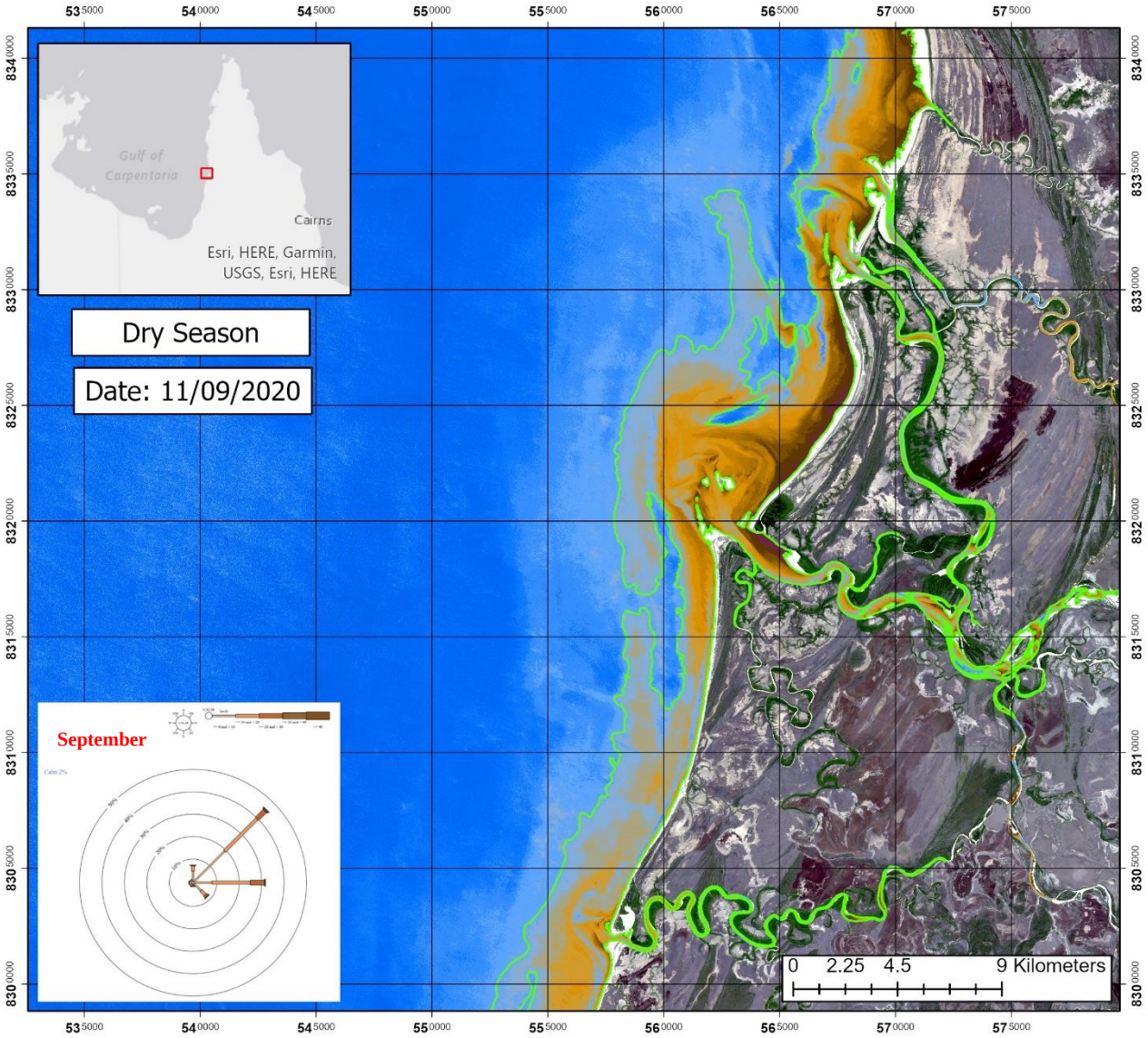

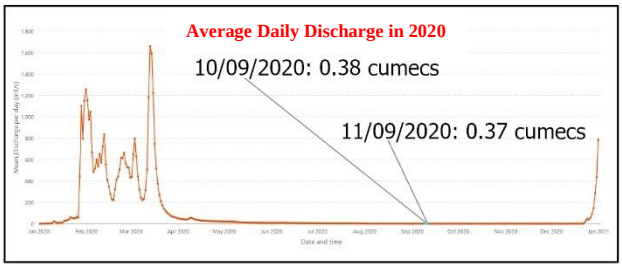

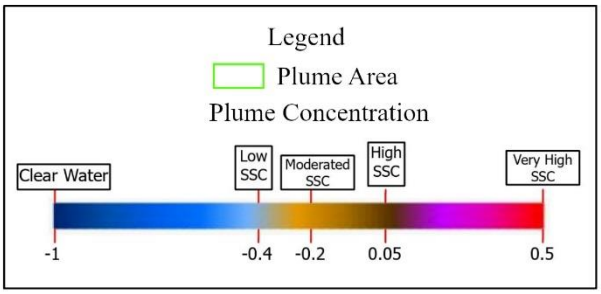

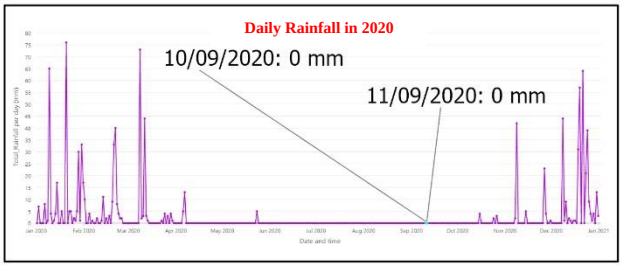

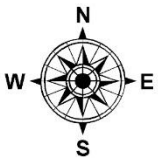

Scale: 1:240,000

Spatial Reference
Name: WGS 1984 UTM Zone 54S
PCS: WGS 1984 UTM Zone 54S
GCS: GCS WGS 1984
Datum: WGS 1984
Projection: Transverse Mercator
Map Units: Meter

Appendix 3-08: Sediment Plume Geometry Map in 2021.

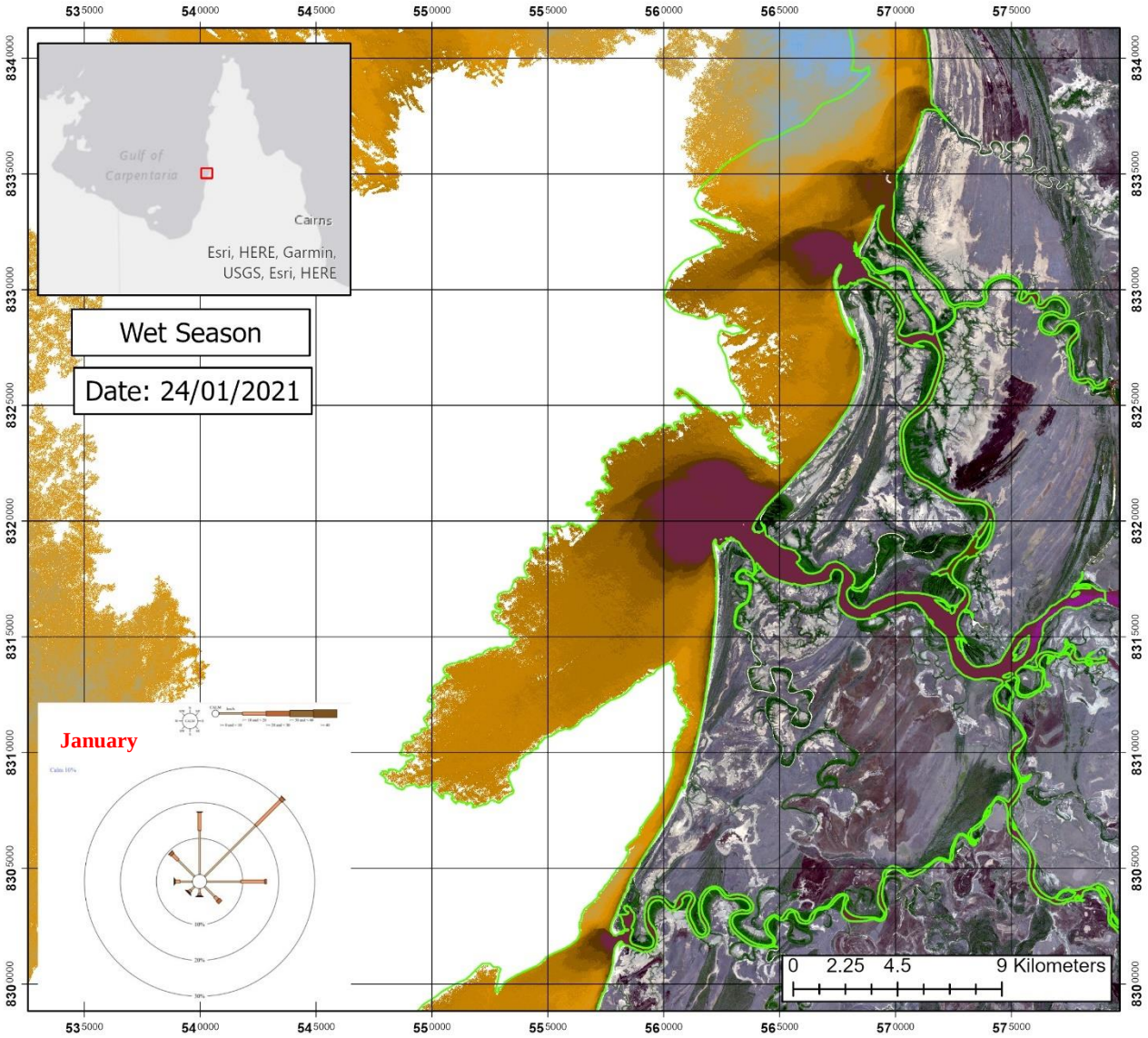

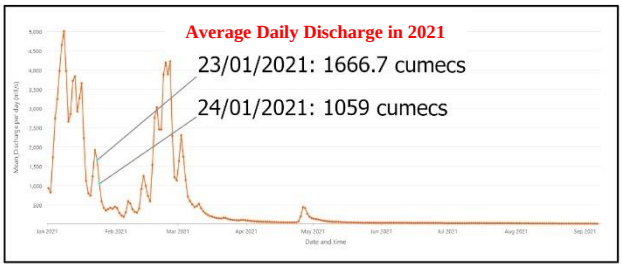

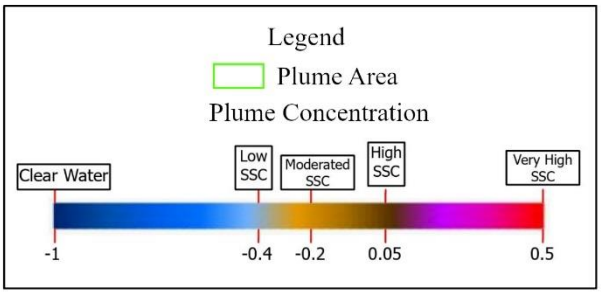

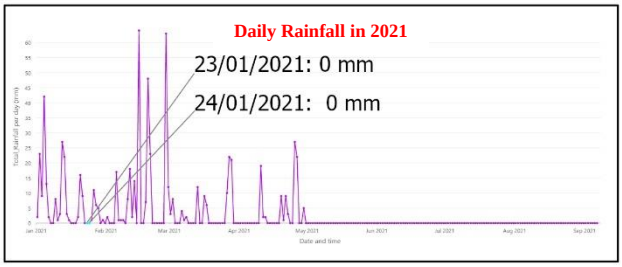

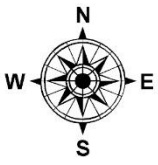

Scale: 1:240,000

Spatial Reference
Name: WGS 1984 UTM Zone 54S
PCS: WGS 1984 UTM Zone 54S
GCS: GCS WGS 1984
Datum: WGS 1984
Projection: Transverse Mercator
Map Units: Meter

Appendix 3-09: Sediment Plume Geometry Map in 2021.

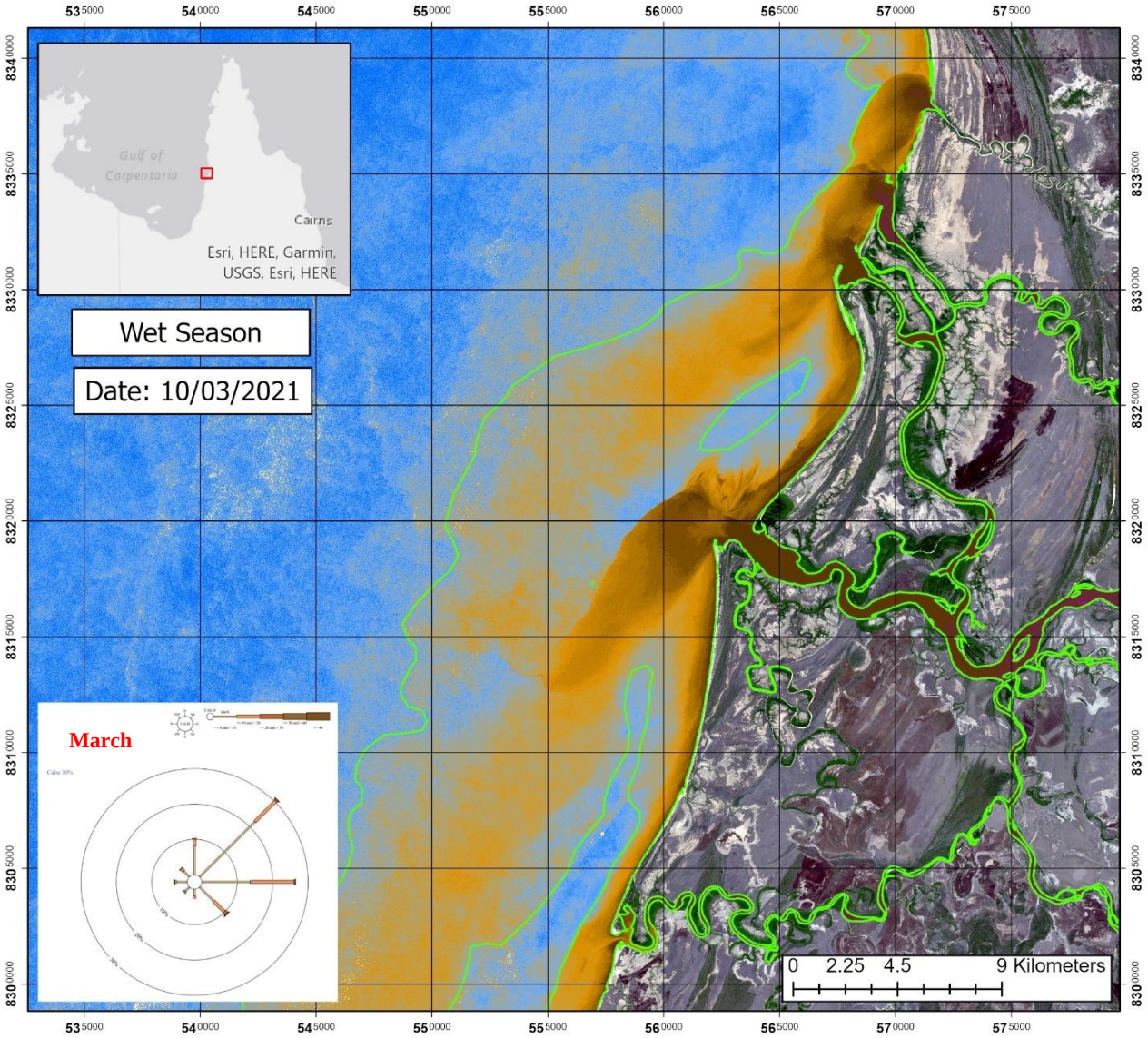

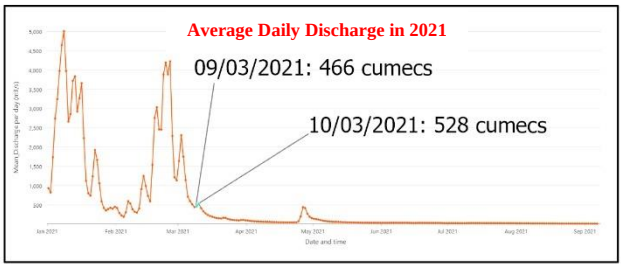

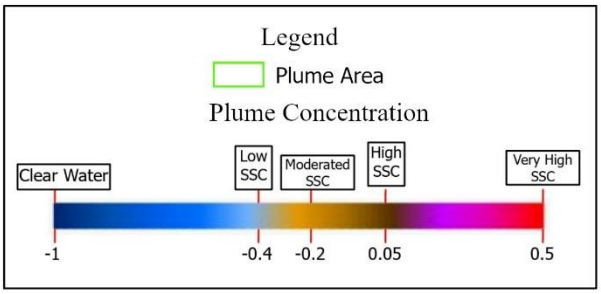

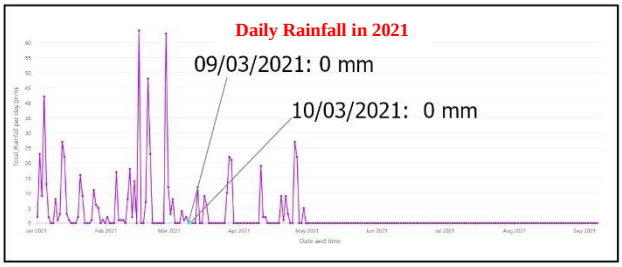

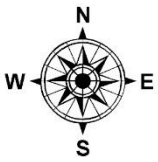

Scale: 1:240,000

Spatial Reference
Name: WGS 1984 UTM Zone 54S
PCS: WGS 1984 UTM Zone 54S
GCS: GCS WGS 1984
Datum: WGS 1984
Projection: Transverse Mercator
Map Units: Meter

Appendix 3-10: Sediment Plume Geometry Map in 2021.

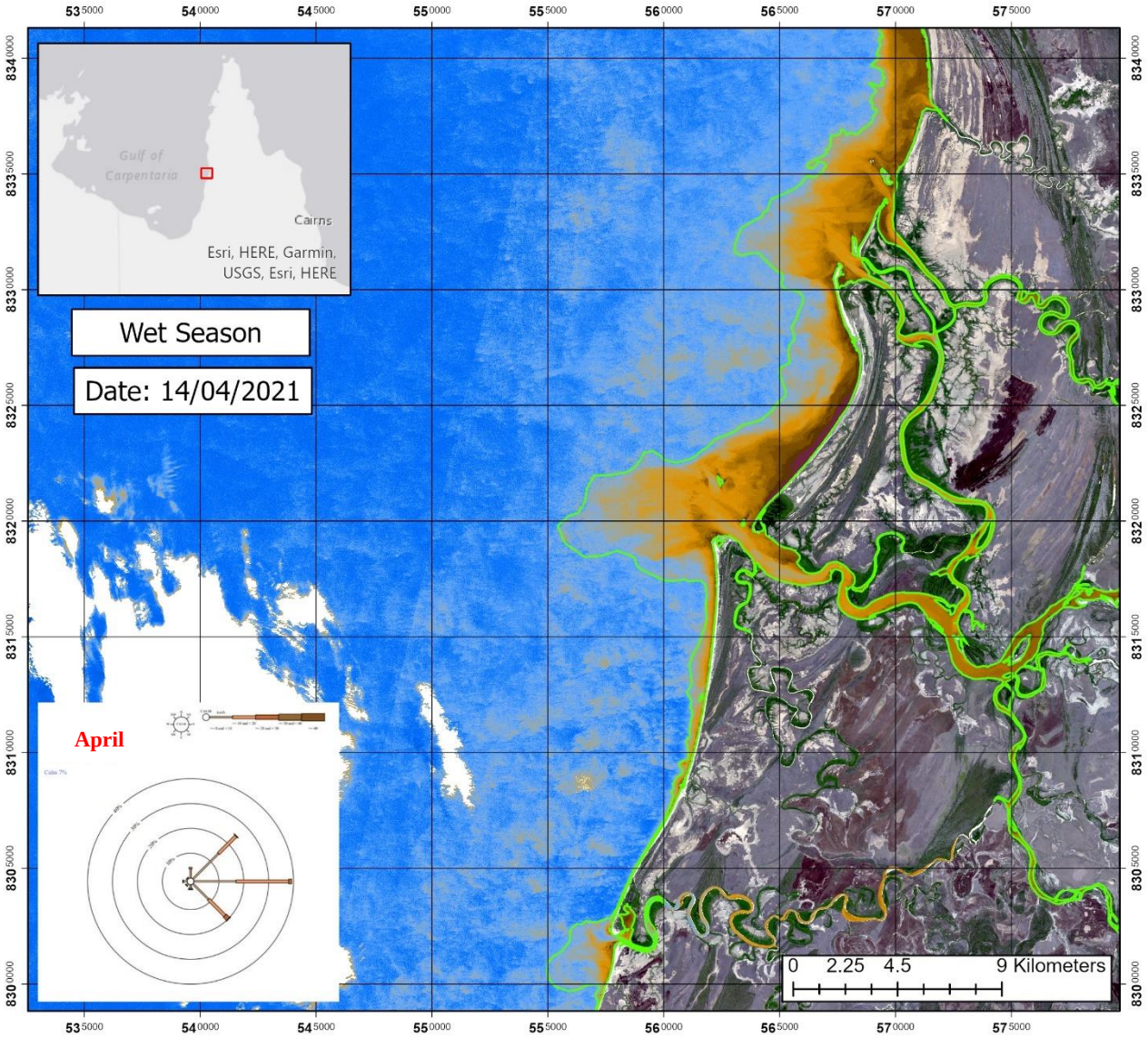

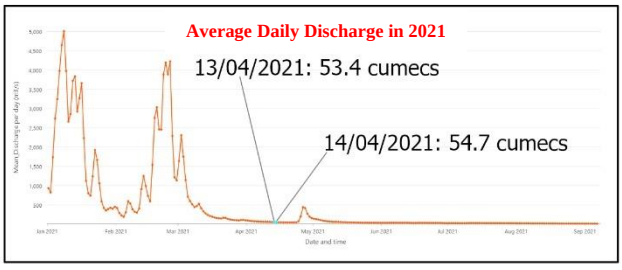

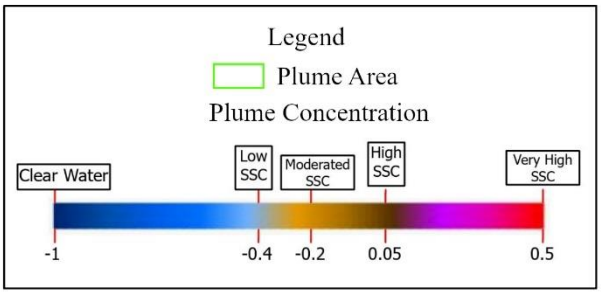

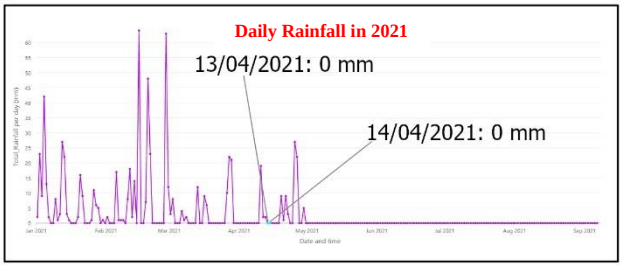

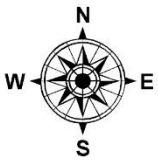

Scale: 1:240,000

Spatial Reference
Name: WGS 1984 UTM Zone 54S
PCS: WGS 1984 UTM Zone 54S
GCS: GCS WGS 1984
Datum: WGS 1984
Projection: Transverse Mercator
Map Units: Meter

Appendix 3-11: Sediment Plume Geometry Map in 2021.

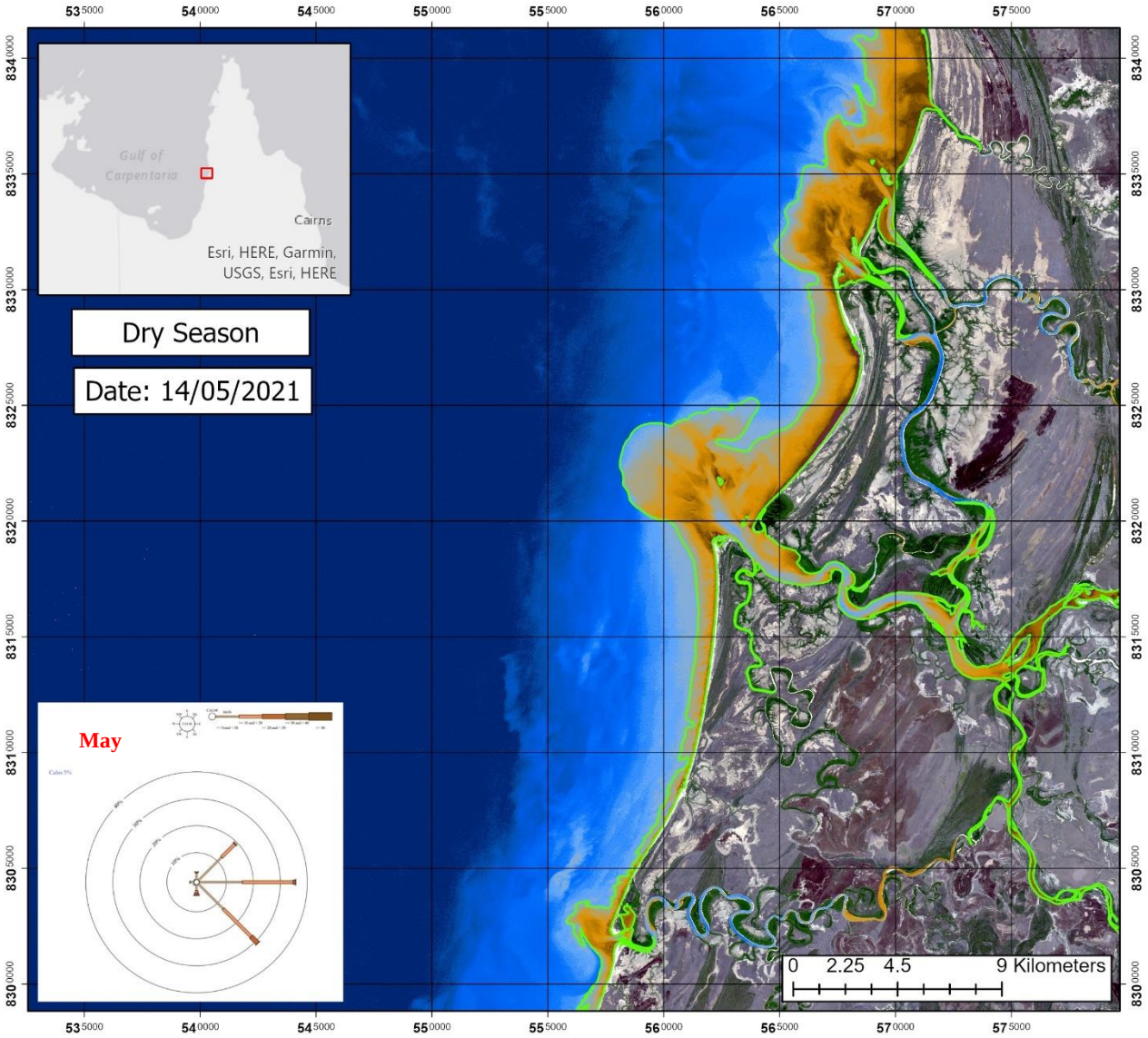

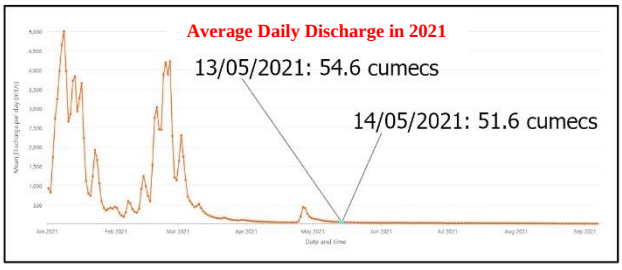

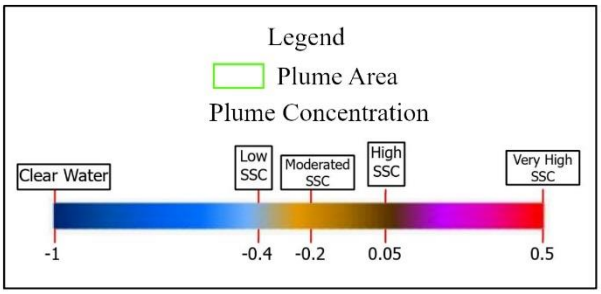

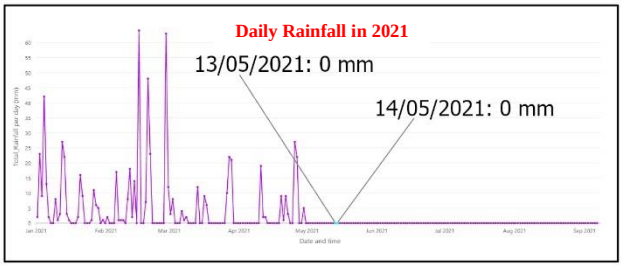

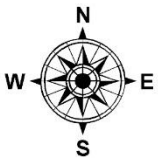

Scale: 1:240,000

Spatial Reference
Name: WGS 1984 UTM Zone 54S
PCS: WGS 1984 UTM Zone 54S
GCS: GCS WGS 1984
Datum: WGS 1984
Projection: Transverse Mercator
Map Units: Meter

Appendix 3-12: Sediment Plume Geometry Map in 2021.

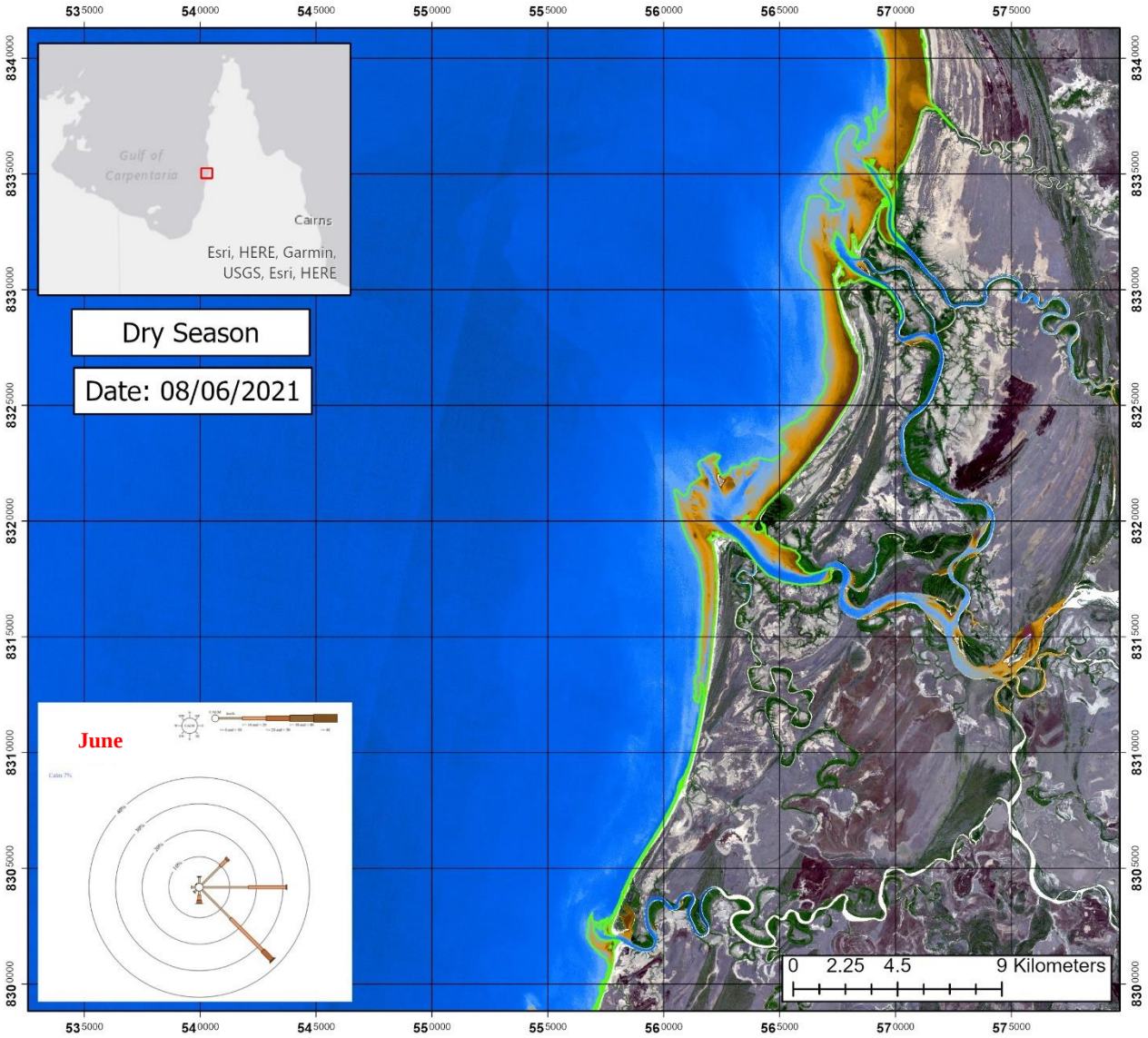

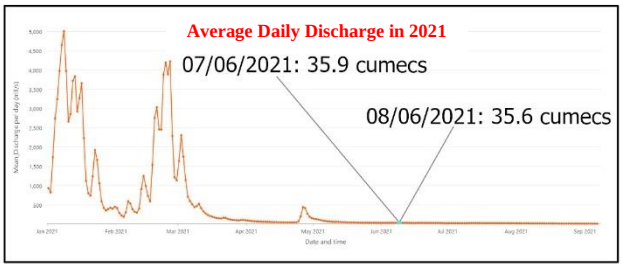

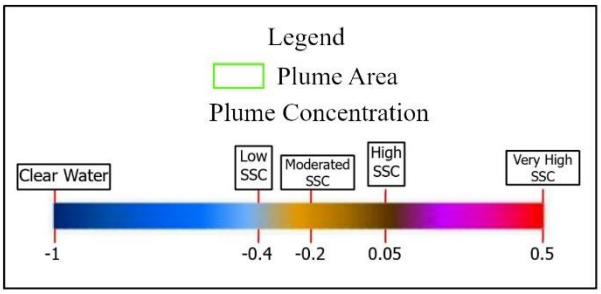

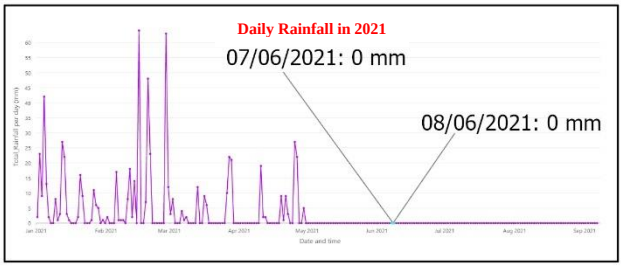

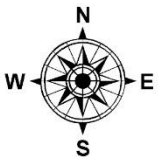

Scale: 1:240,000

Spatial Reference
Name: WGS 1984 UTM Zone 54S
PCS: WGS 1984 UTM Zone 54S
GCS: GCS WGS 1984
Datum: WGS 1984
Projection: Transverse Mercator
Map Units: Meter

Appendix 3-13: Sediment Plume Geometry Map in 2021.

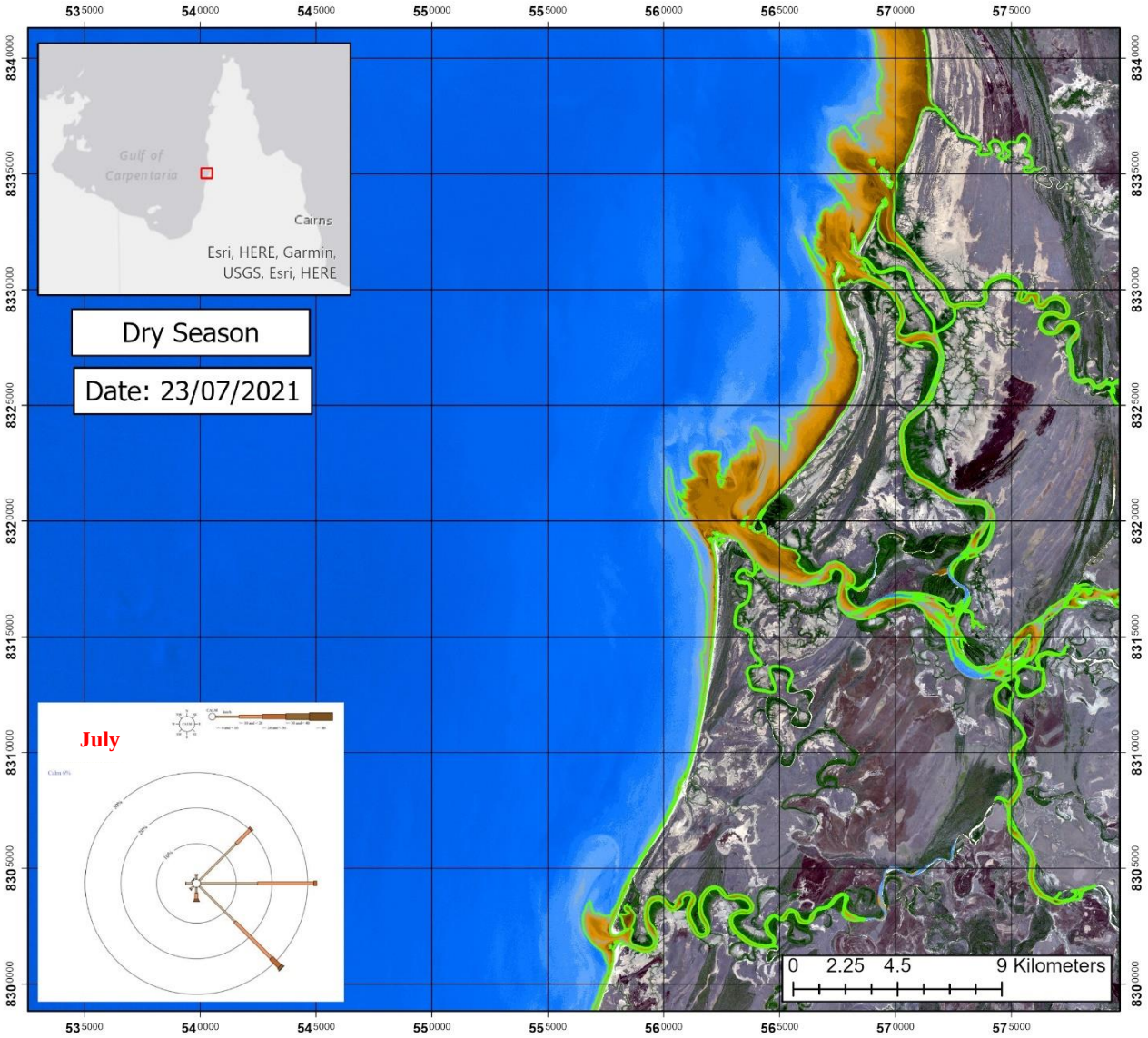

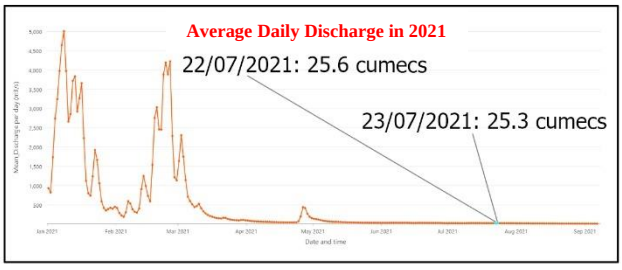

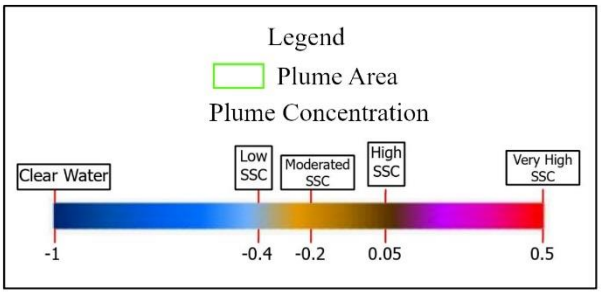

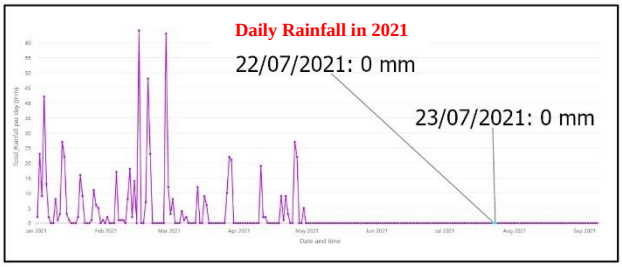

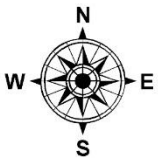

Scale: 1:240,000

Spatial Reference
Name: WGS 1984 UTM Zone 54S
PCS: WGS 1984 UTM Zone 54S
GCS: GCS WGS 1984
Datum: WGS 1984
Projection: Transverse Mercator
Map Units: Meter

Appendix 3-14: Sediment Plume Geometry Map in 2021.

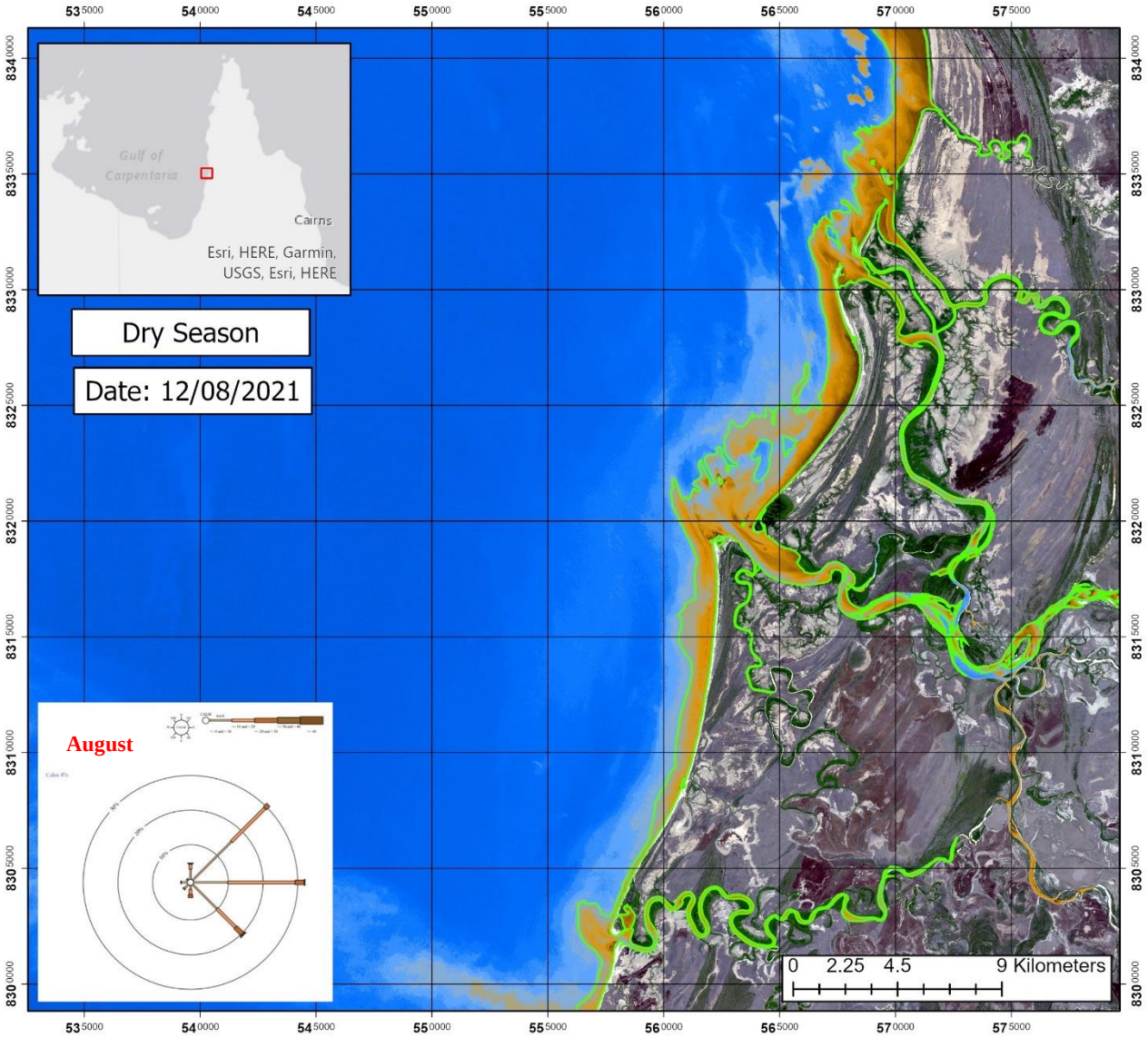

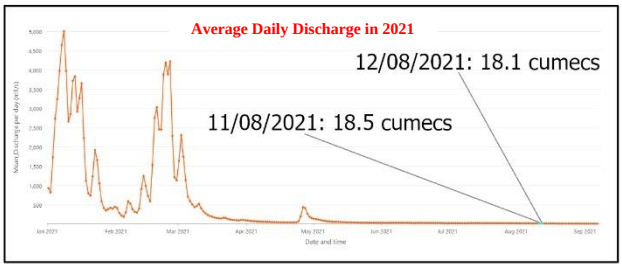

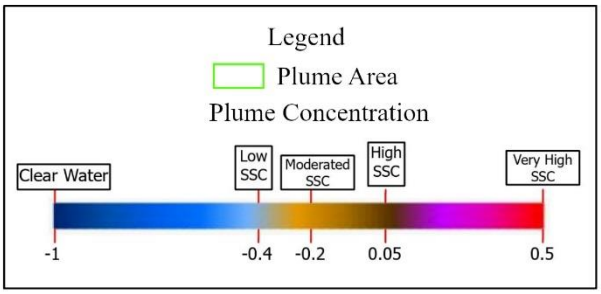

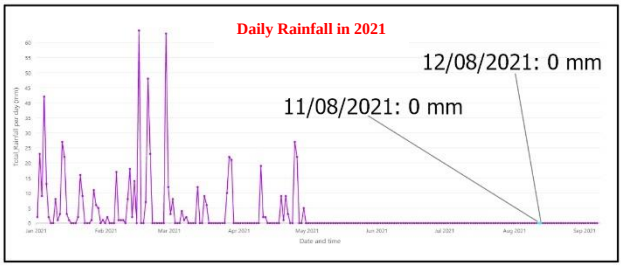

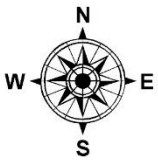

Scale: 1:240,000

Spatial Reference
Name: WGS 1984 UTM Zone 54S
PCS: WGS 1984 UTM Zone 54S
GCS: GCS WGS 1984
Datum: WGS 1984
Projection: Transverse Mercator
Map Units: Meter

Appendix 4-01: Mouth Bar Geometry Map in 2020.

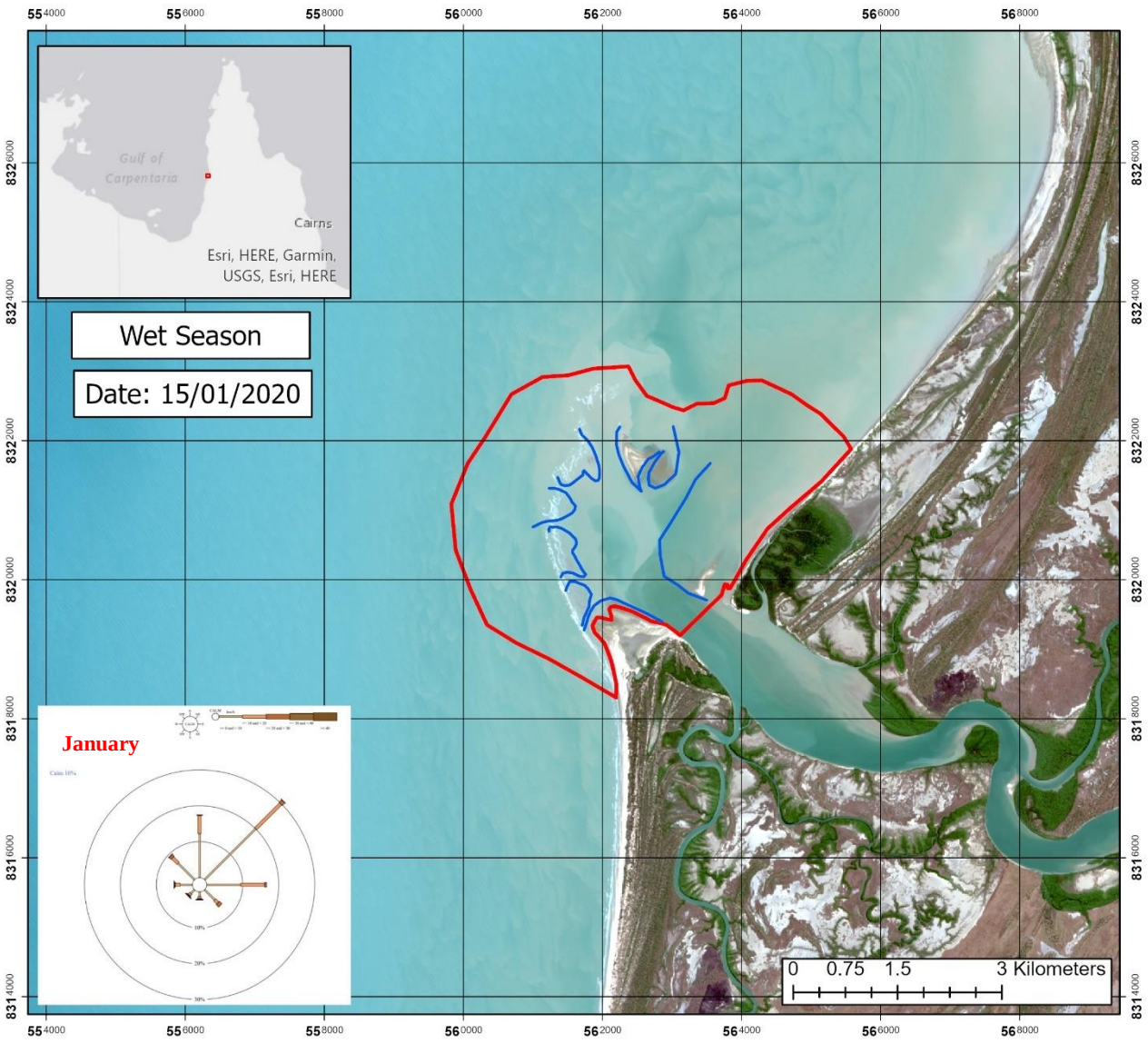

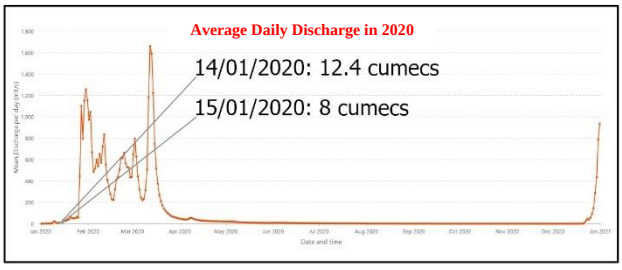

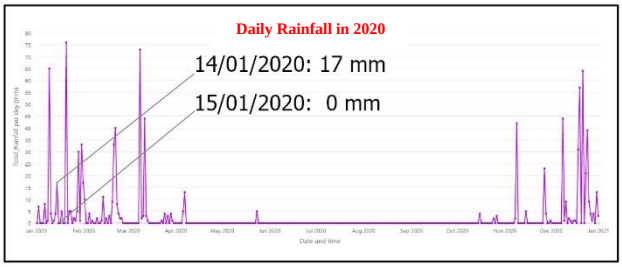

Legend
- Distributary Channels
- Mouth Bar

N
W E
S

Scale: 1:80,000

Spatial Reference
Name: WGS 1984 UTM Zone 54S
PCS: WGS 1984 UTM Zone 54S
GCS: GCS WGS 1984
Datum: WGS 1984
Projection: Transverse Mercator
Map Units: Meter

Appendix 4-02: Mouth Bar Geometry Map in 2020.

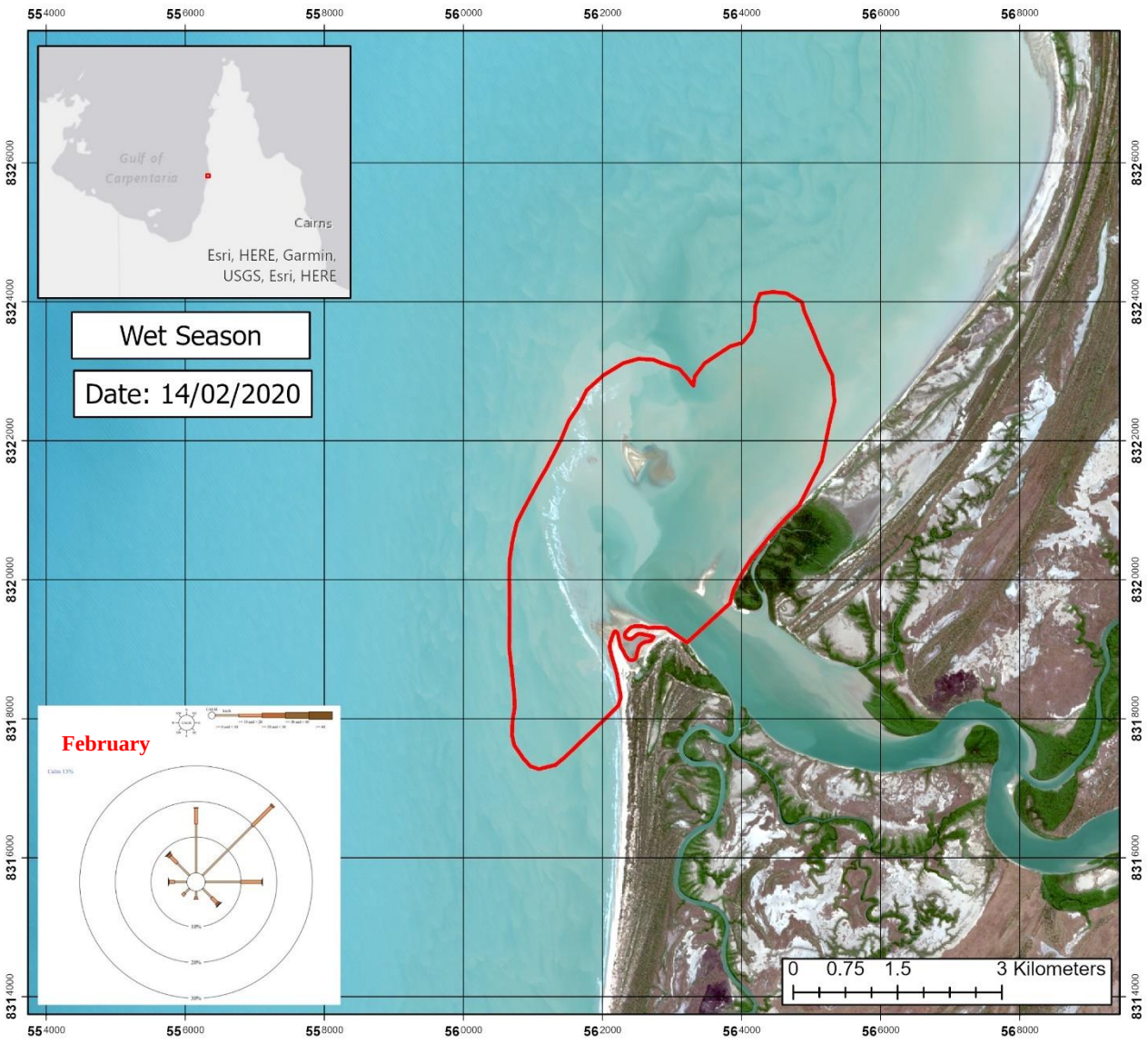

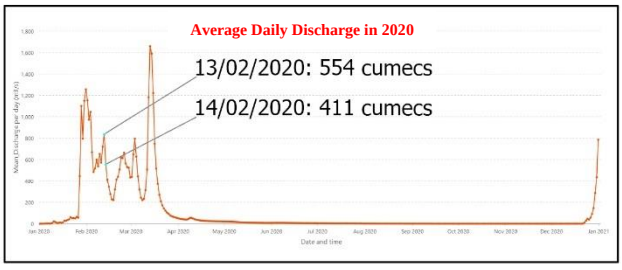

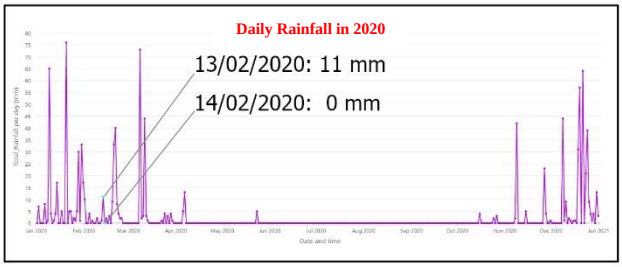

Legend
Mouth Bar

N
W E
S

Scale: 1:80,000

Spatial Reference
Name: WGS 1984 UTM Zone 54S
PCS: WGS 1984 UTM Zone 54S
GCS: GCS WGS 1984
Datum: WGS 1984
Projection: Transverse Mercator
Map Units: Meter

Appendix 4-03: Mouth Bar Geometry Map in 2020.

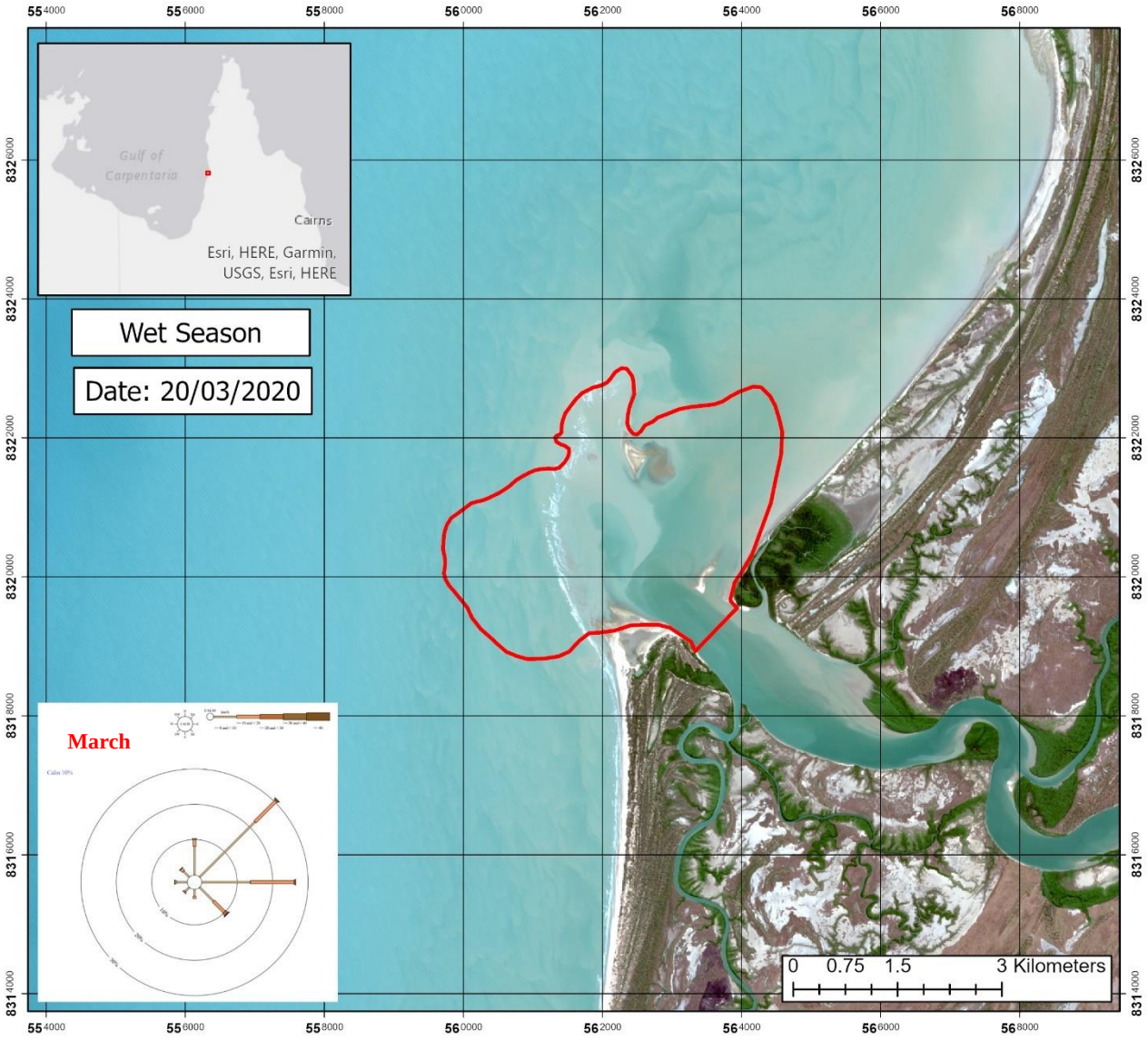

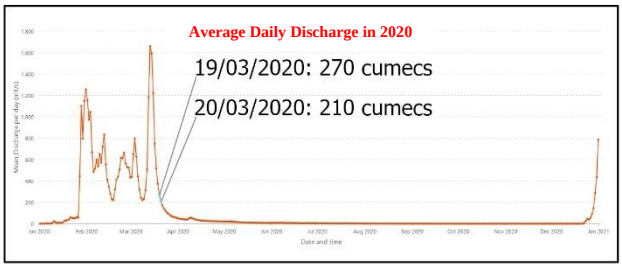

Legend
Mouth Bar

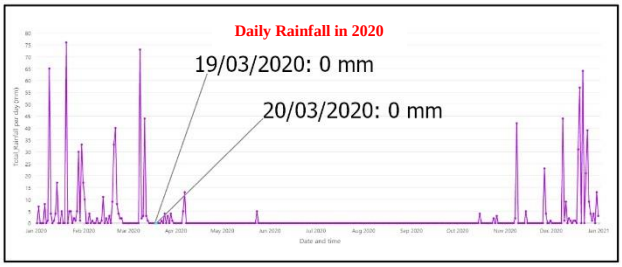

N
W E
S

Scale: 1:80,000

Spatial Reference
Name: WGS 1984 UTM Zone 54S
PCS: WGS 1984 UTM Zone 54S
GCS: GCS WGS 1984
Datum: WGS 1984
Projection: Transverse Mercator
Map Units: Meter

Appendix 4-04: Mouth Bar Geometry Map in 2020.

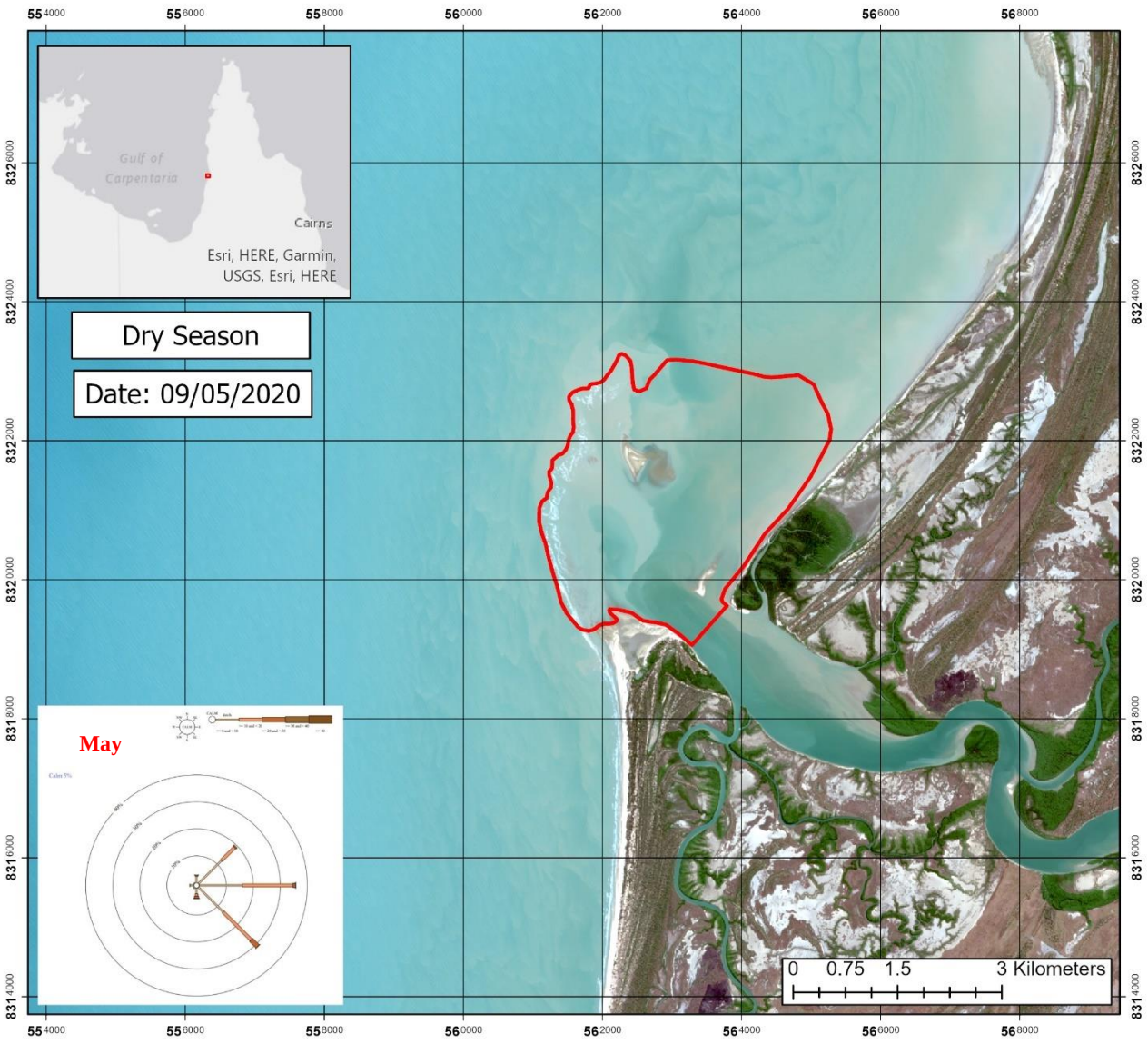

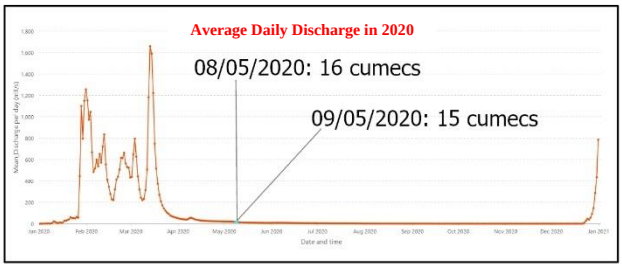

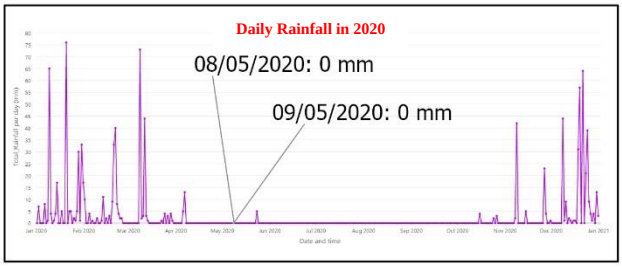

Legend
Mouth Bar

N
W E
S

Scale: 1:80,000

Spatial Reference
Name: WGS 1984 UTM Zone 54S
PCS: WGS 1984 UTM Zone 54S
GCS: GCS WGS 1984
Datum: WGS 1984
Projection: Transverse Mercator
Map Units: Meter

Appendix 4-05: Mouth Bar Geometry Map in 2020.

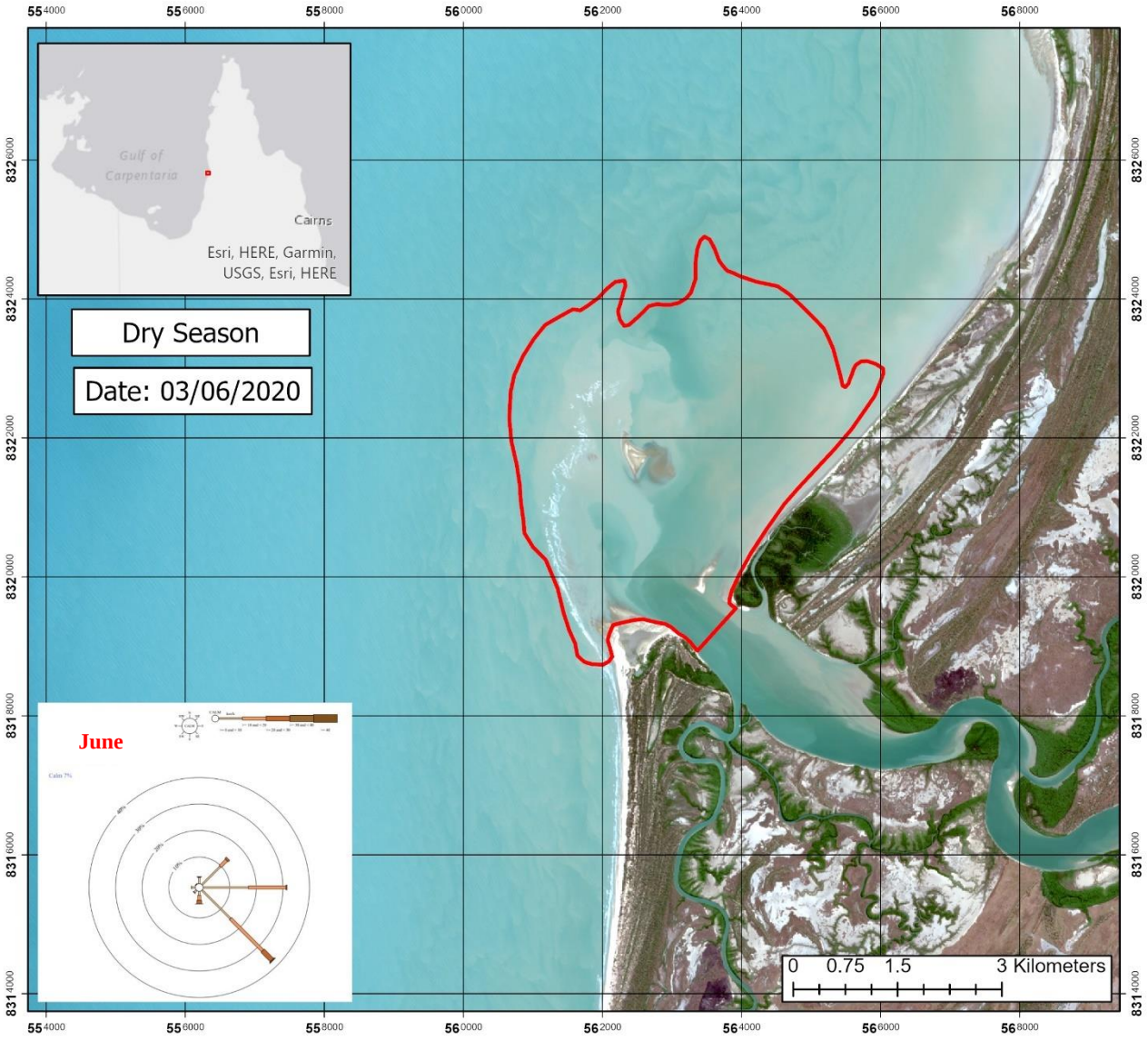

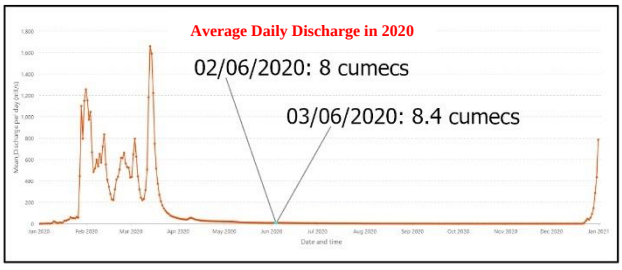

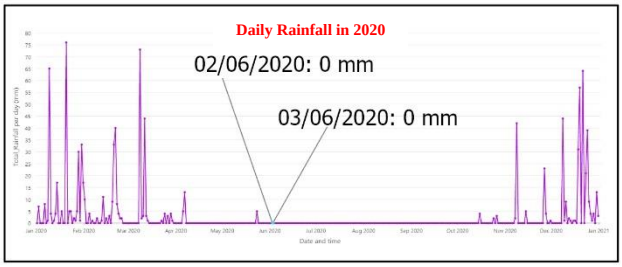

Legend
Mouth Bar

N
W E
S

Scale: 1:80,000

Spatial Reference
Name: WGS 1984 UTM Zone 54S
PCS: WGS 1984 UTM Zone 54S
GCS: GCS WGS 1984
Datum: WGS 1984
Projection: Transverse Mercator
Map Units: Meter

Appendix 4-06: Mouth Bar Geometry Map in 2020.

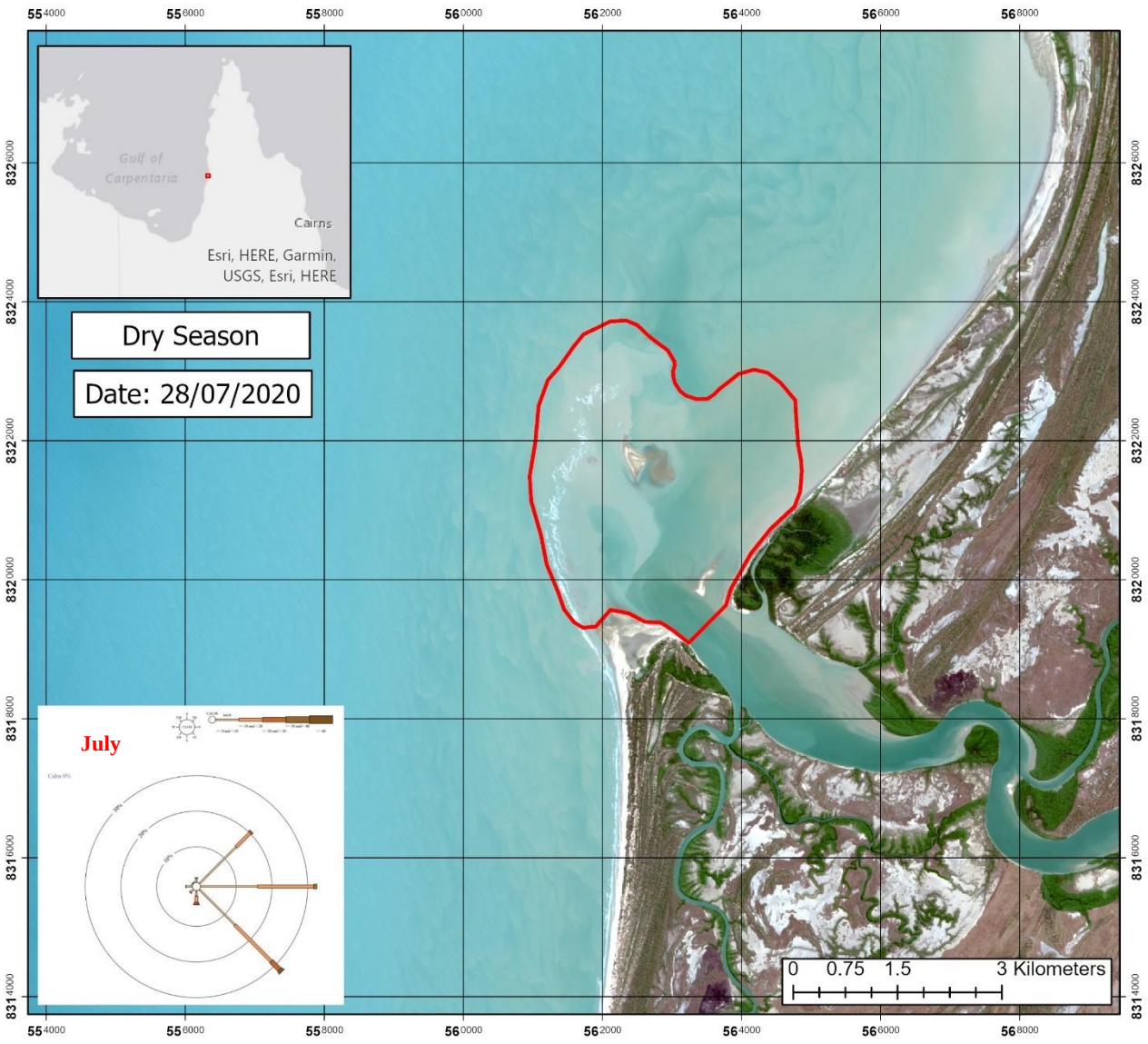

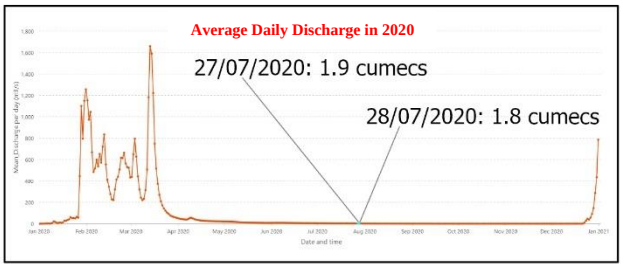

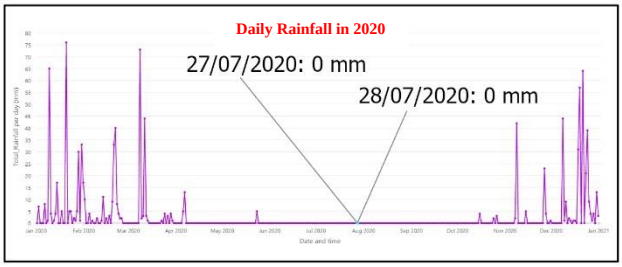

Legend
Mouth Bar

N
W E
S

Scale: 1:80,000

Spatial Reference
Name: WGS 1984 UTM Zone 54S
PCS: WGS 1984 UTM Zone 54S
GCS: GCS WGS 1984
Datum: WGS 1984
Projection: Transverse Mercator
Map Units: Meter

Appendix 4-07: Mouth Bar Geometry Map in 2020.

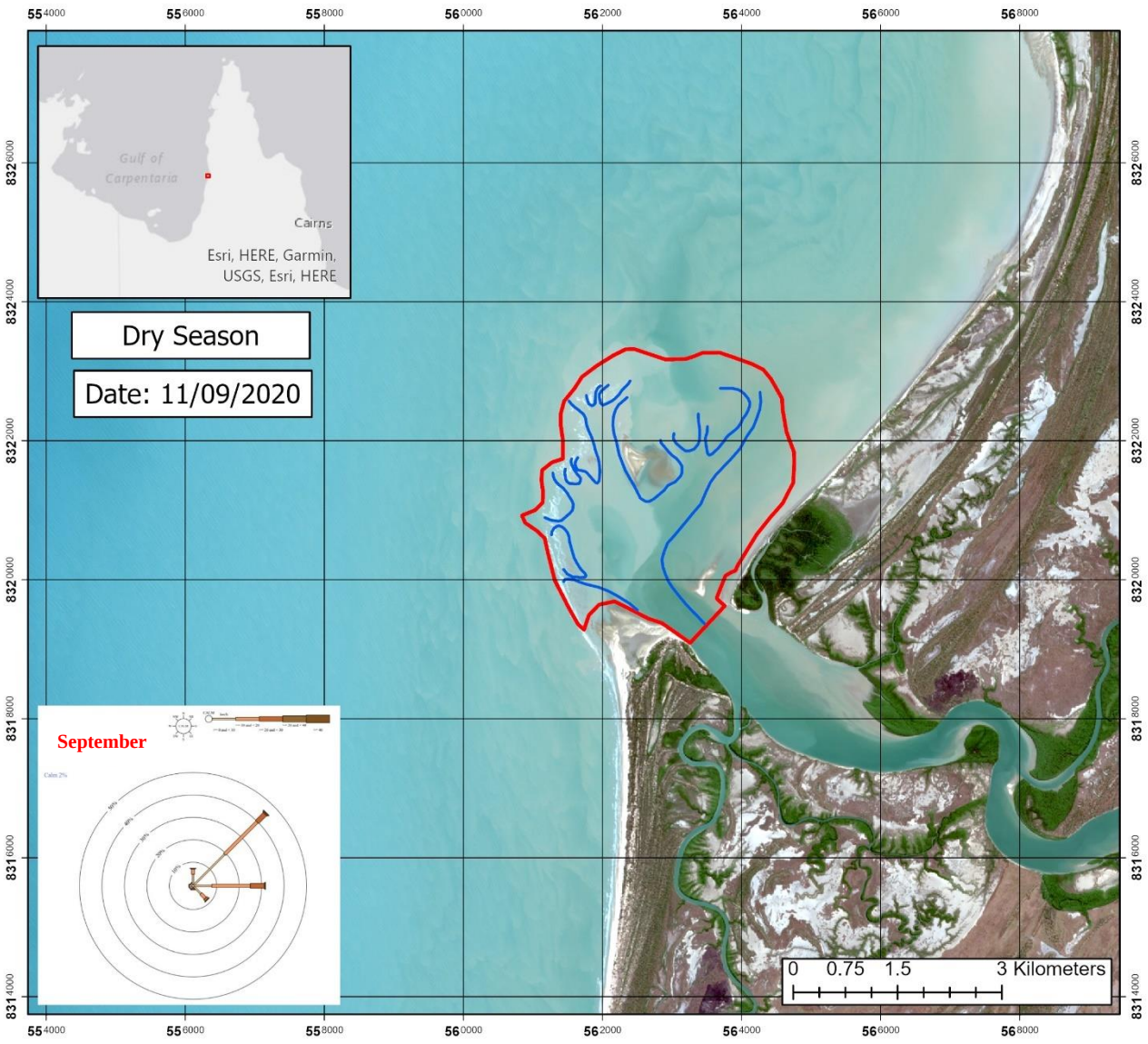

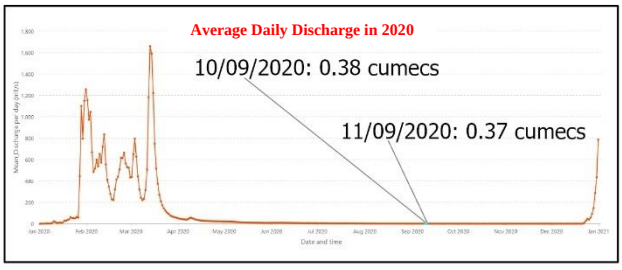

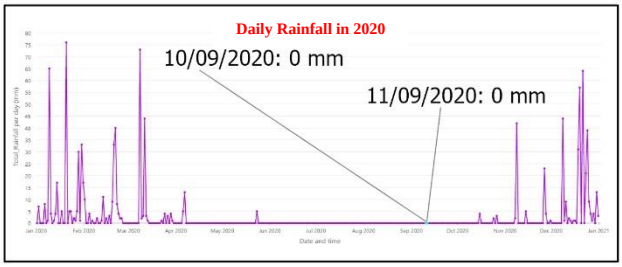

Legend
- Mouth Bars
- Distributary Channels

N
W E
S

Scale: 1:80,000

Spatial Reference
Name: WGS 1984 UTM Zone 54S
PCS: WGS 1984 UTM Zone 54S
GCS: GCS WGS 1984
Datum: WGS 1984
Projection: Transverse Mercator
Map Units: Meter

Appendix 4-08: Mouth Bar Geometry Map in 2021.

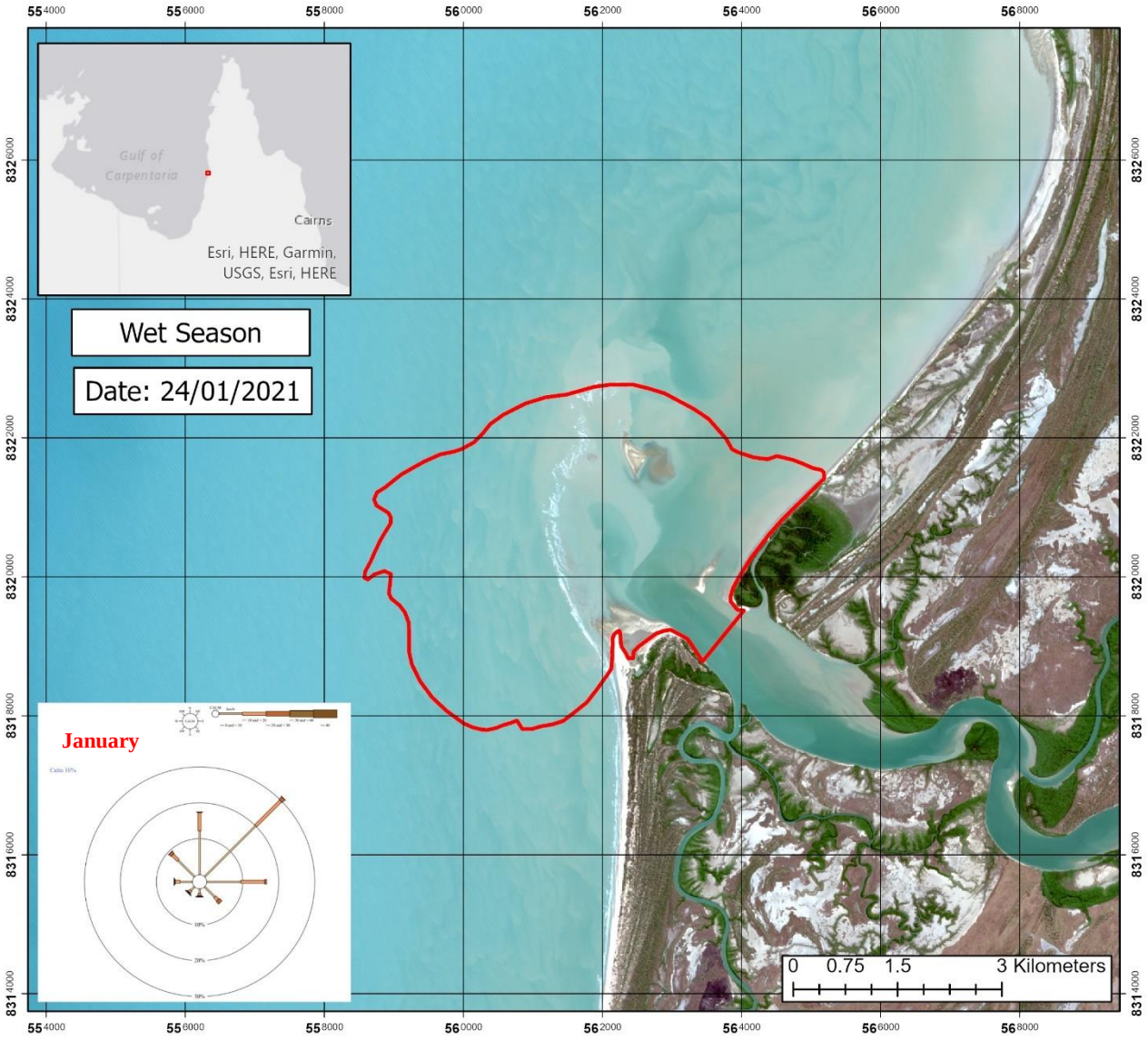

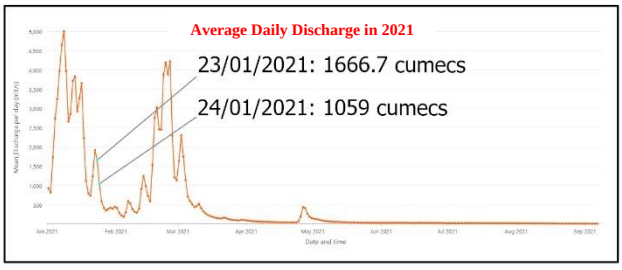

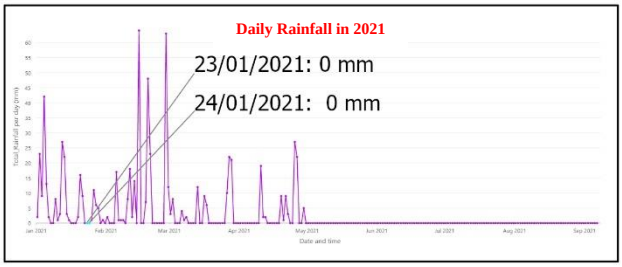

Legend
Mouth Bar

N
W E
S

Scale: 1:80,000

Spatial Reference
Name: WGS 1984 UTM Zone 54S
PCS: WGS 1984 UTM Zone 54S
GCS: GCS WGS 1984
Datum: WGS 1984
Projection: Transverse Mercator
Map Units: Meter

Appendix 4-09: Mouth Bar Geometry Map in 2021.

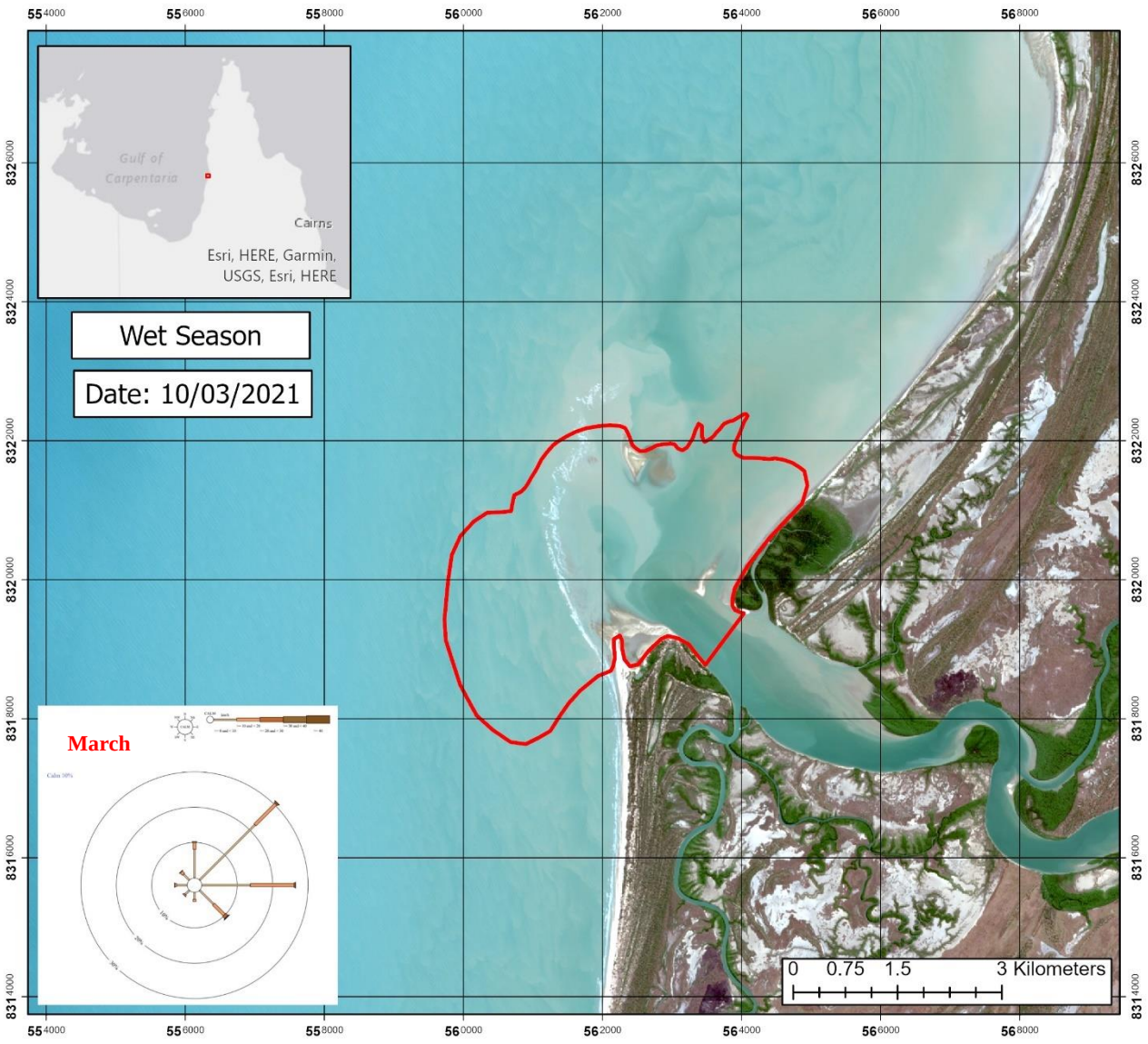

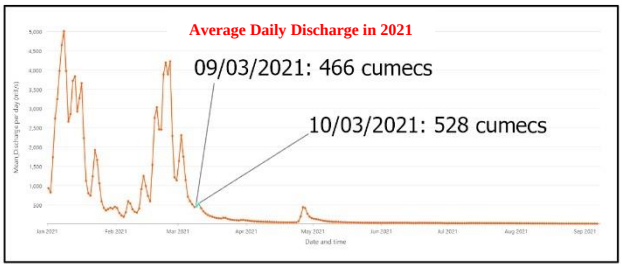

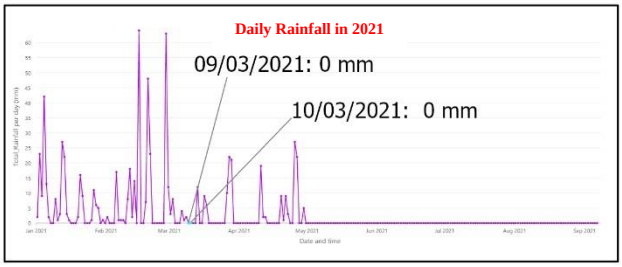

Legend
Mouth Bar

N
W E
S

Scale: 1:80,000

Spatial Reference
Name: WGS 1984 UTM Zone 54S
PCS: WGS 1984 UTM Zone 54S
GCS: GCS WGS 1984
Datum: WGS 1984
Projection: Transverse Mercator
Map Units: Meter

Appendix 4-10: Mouth Bar Geometry Map in 2021.

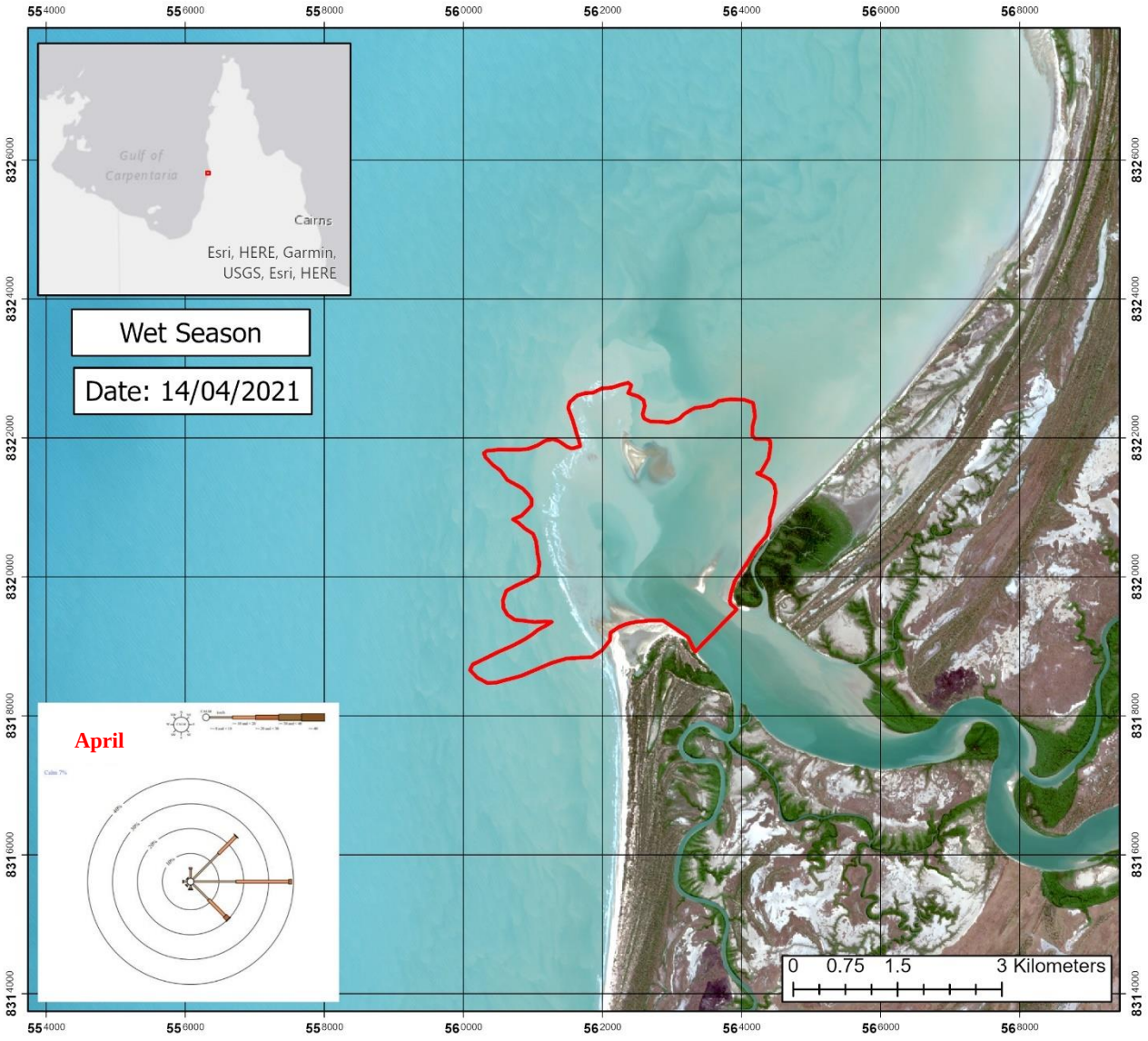

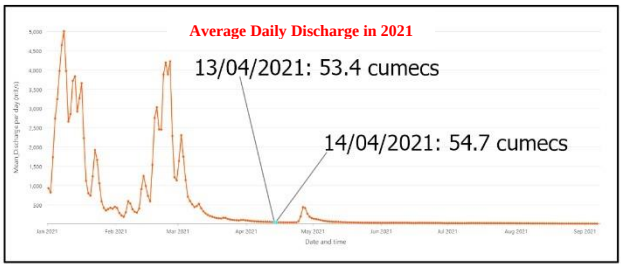

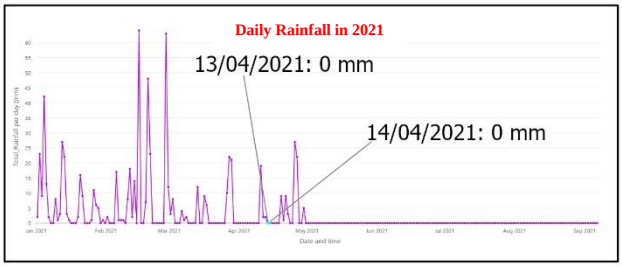

Legend
Mouth Bar

N
W E
S

Scale: 1:80,000

Spatial Reference
Name: WGS 1984 UTM Zone 54S
PCS: WGS 1984 UTM Zone 54S
GCS: GCS WGS 1984
Datum: WGS 1984
Projection: Transverse Mercator
Map Units: Meter

Appendix 4-11: Mouth Bar Geometry Map in 2021.

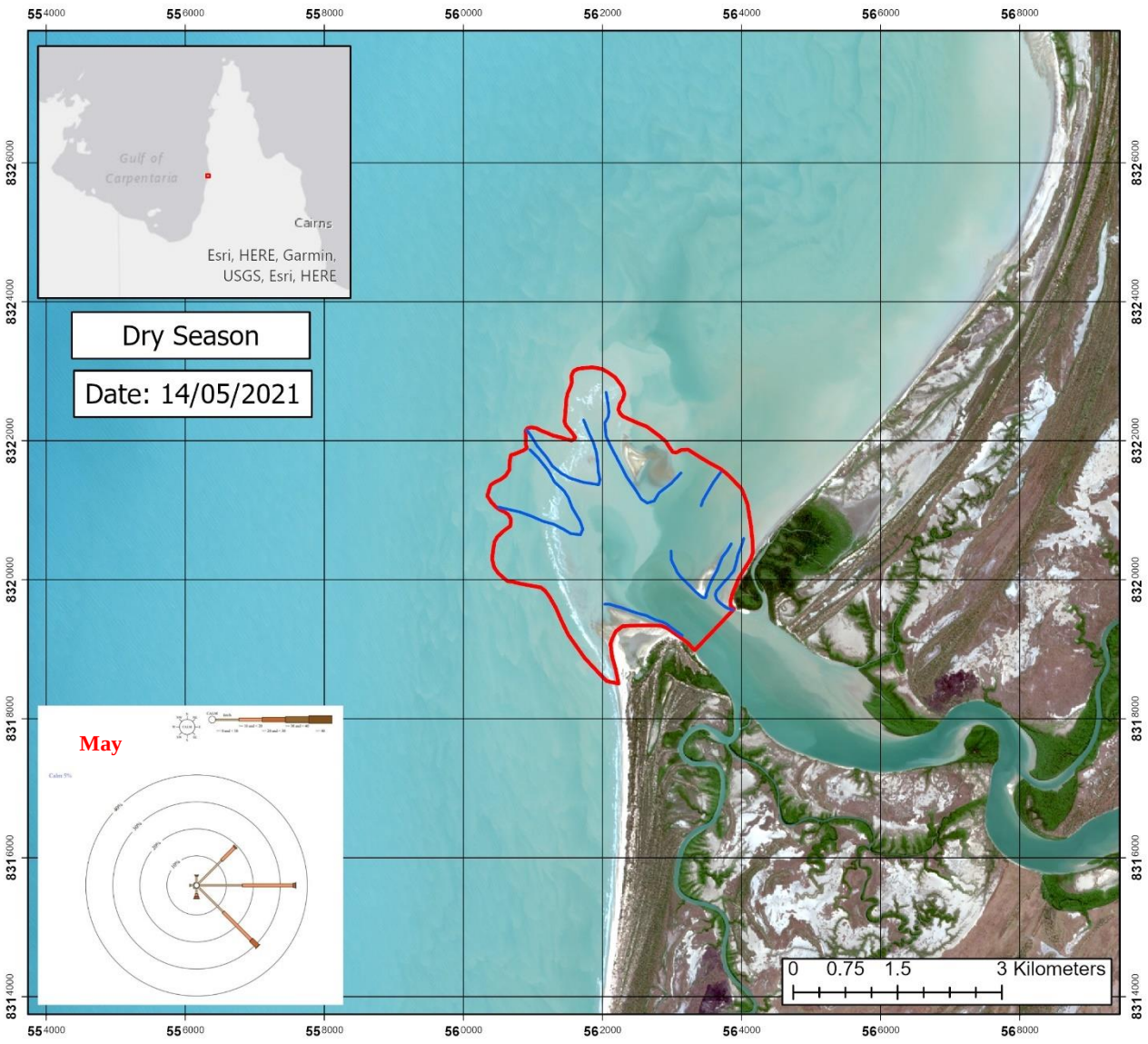

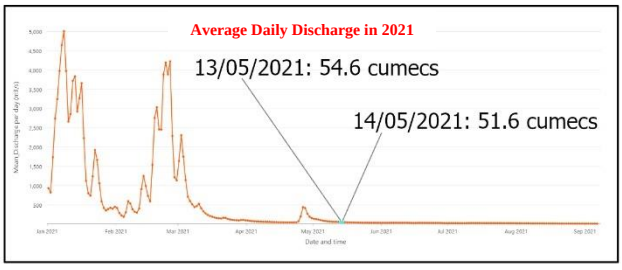

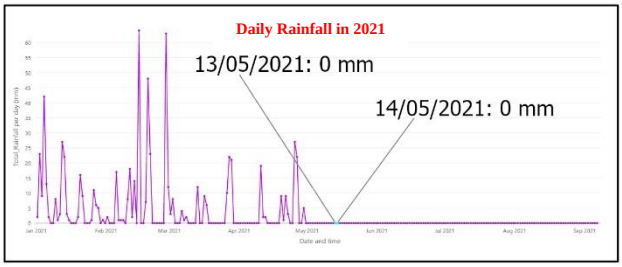

Legend
- Distributary Channels
- Mouth Bar

N
W E
S

Scale: 1:80,000

Spatial Reference
Name: WGS 1984 UTM Zone 54S
PCS: WGS 1984 UTM Zone 54S
GCS: GCS WGS 1984
Datum: WGS 1984
Projection: Transverse Mercator
Map Units: Meter

Appendix 4-12: Mouth Bar Geometry Map in 2021.

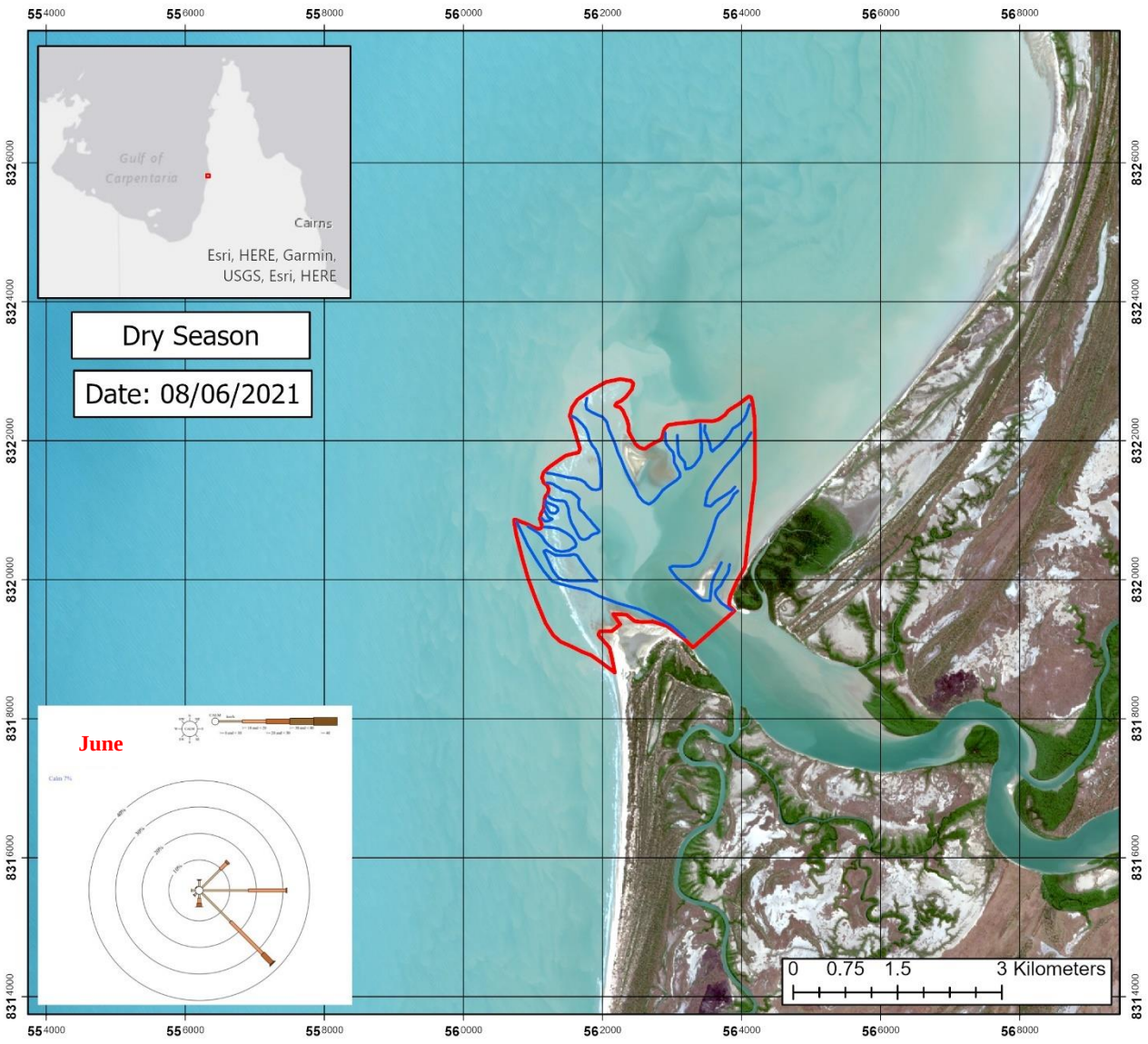

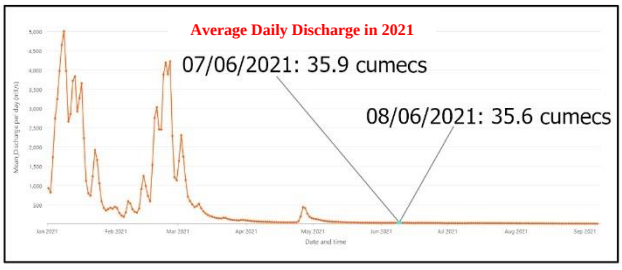

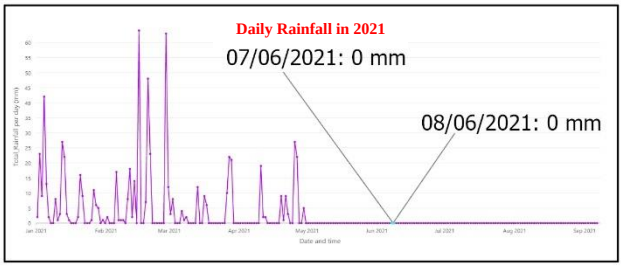

Legend
- Distributary Channels
- Mouth Bar

N
W E
S

Scale: 1:80,000

Spatial Reference
Name: WGS 1984 UTM Zone 54S
PCS: WGS 1984 UTM Zone 54S
GCS: GCS WGS 1984
Datum: WGS 1984
Projection: Transverse Mercator
Map Units: Meter

Appendix 4-13: Mouth Bar Geometry Map in 2021.

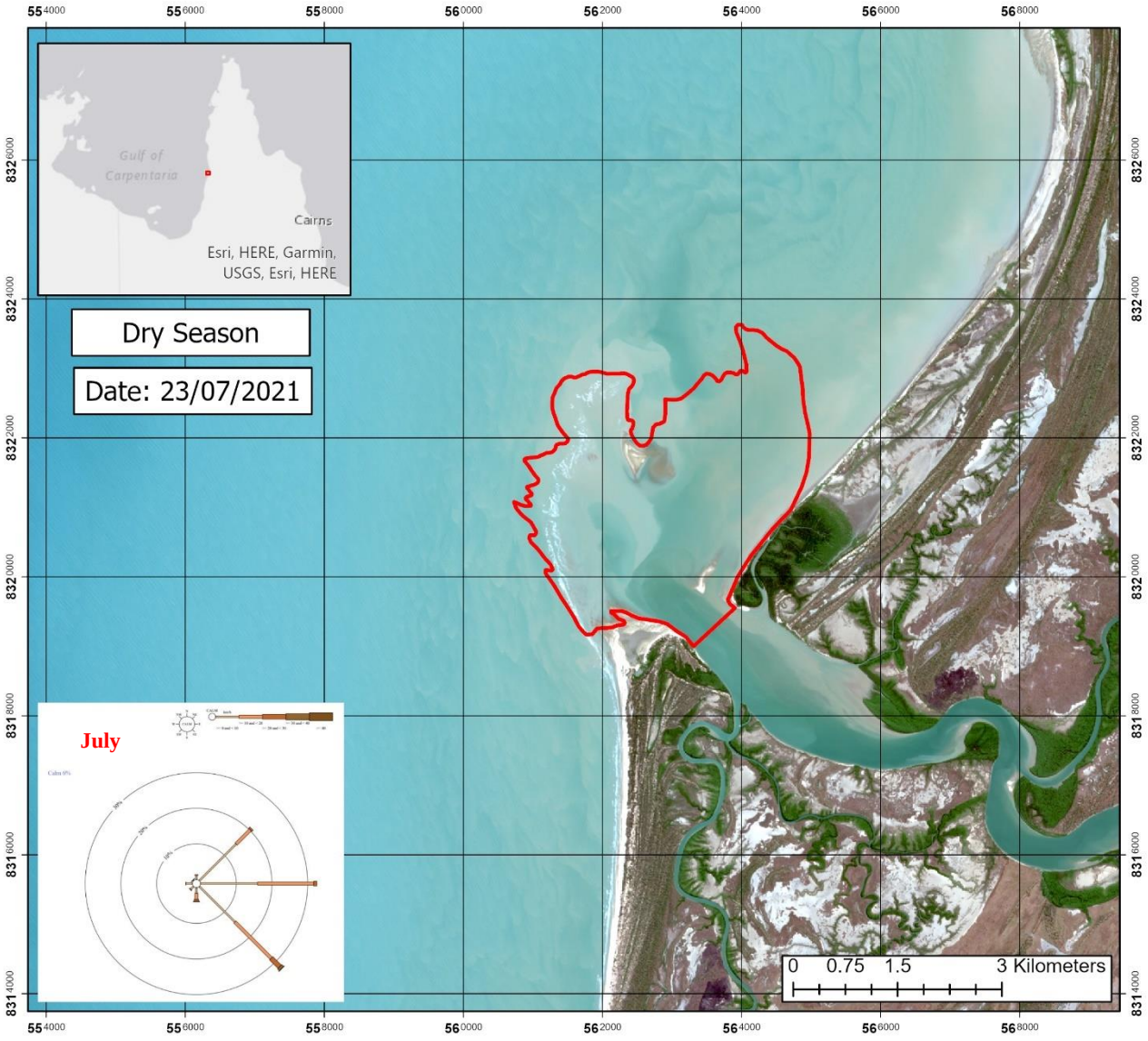

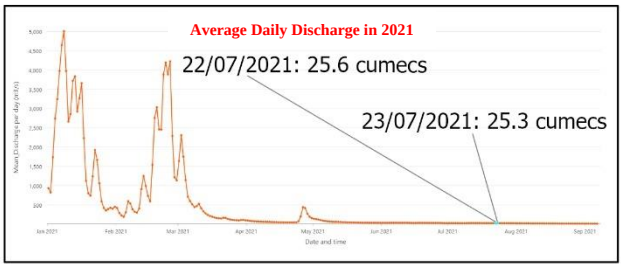

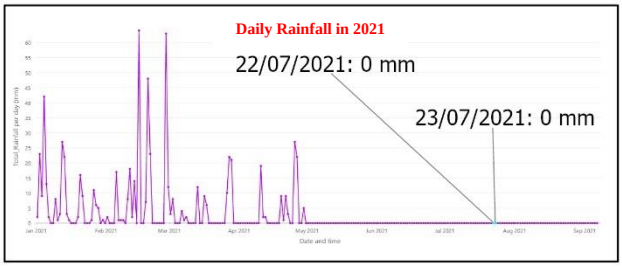

Legend
Mouth Bar

N
W E
S

Scale: 1:80,000

Spatial Reference
Name: WGS 1984 UTM Zone 54S
PCS: WGS 1984 UTM Zone 54S
GCS: GCS WGS 1984
Datum: WGS 1984
Projection: Transverse Mercator
Map Units: Meter

Appendix 4-14: Mouth Bar Geometry Map in 2021.

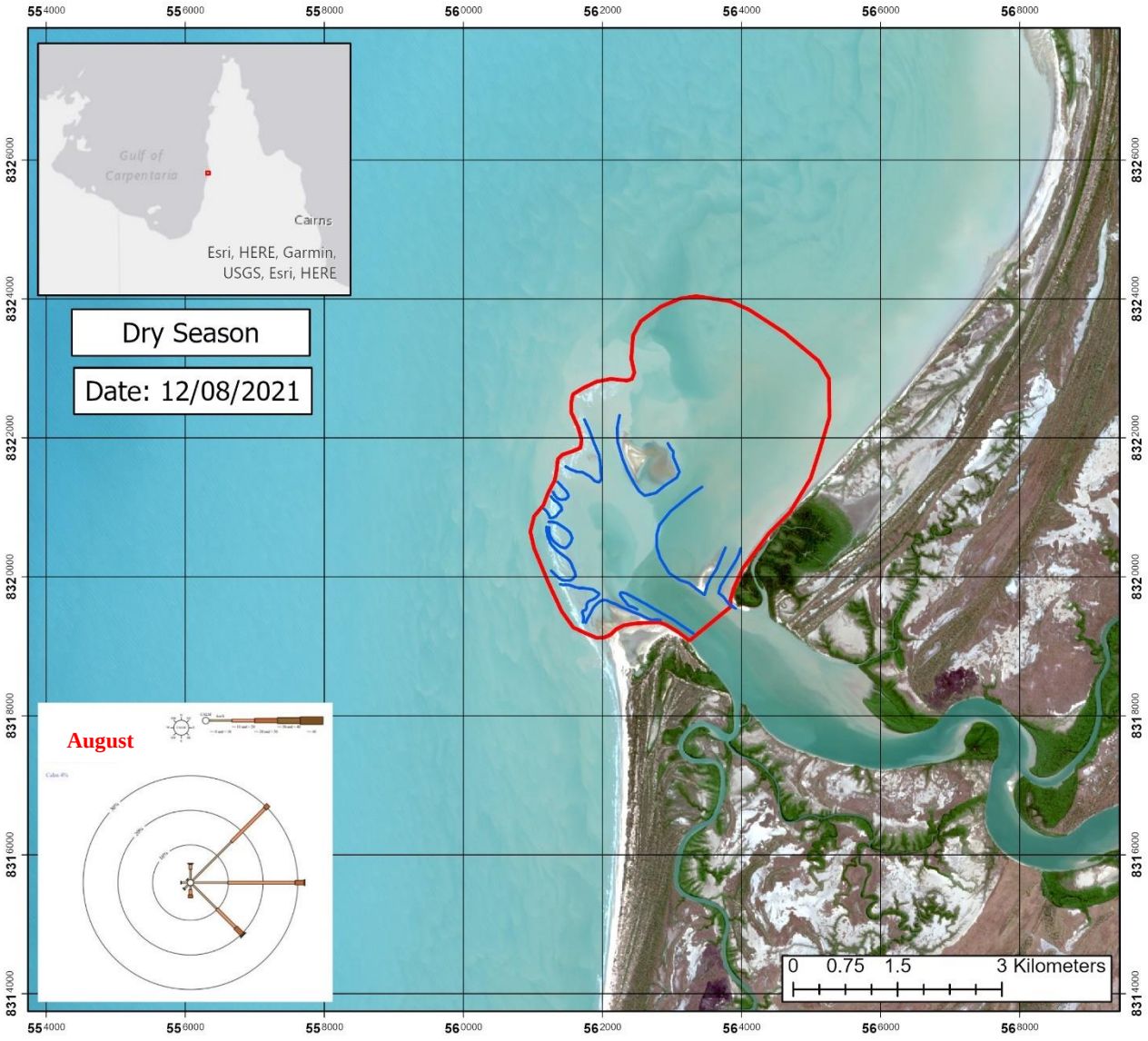

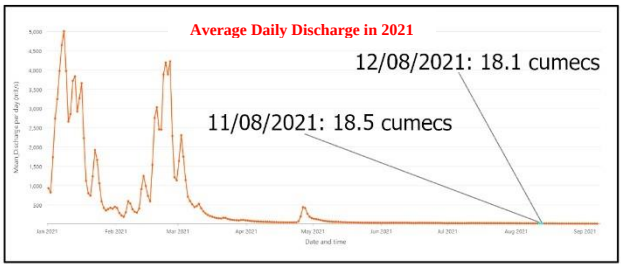

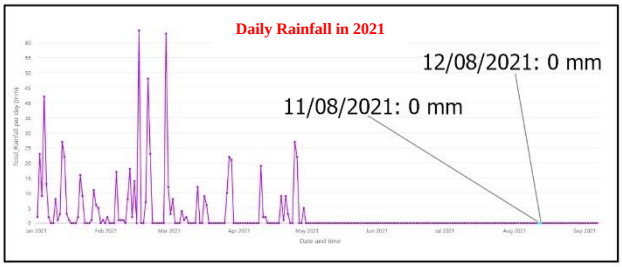

Legend
- Distributary Channels
- Mouth Bar

N
W E
S

Scale: 1:80,000

Spatial Reference
Name: WGS 1984 UTM Zone 54S
PCS: WGS 1984 UTM Zone 54S
GCS: GCS WGS 1984
Datum: WGS 1984
Projection: Transverse Mercator
Map Units: Meter

APPENDIX 5-01: Overall Seasonal Variations Map of Sediment Plume Geometry in 2020

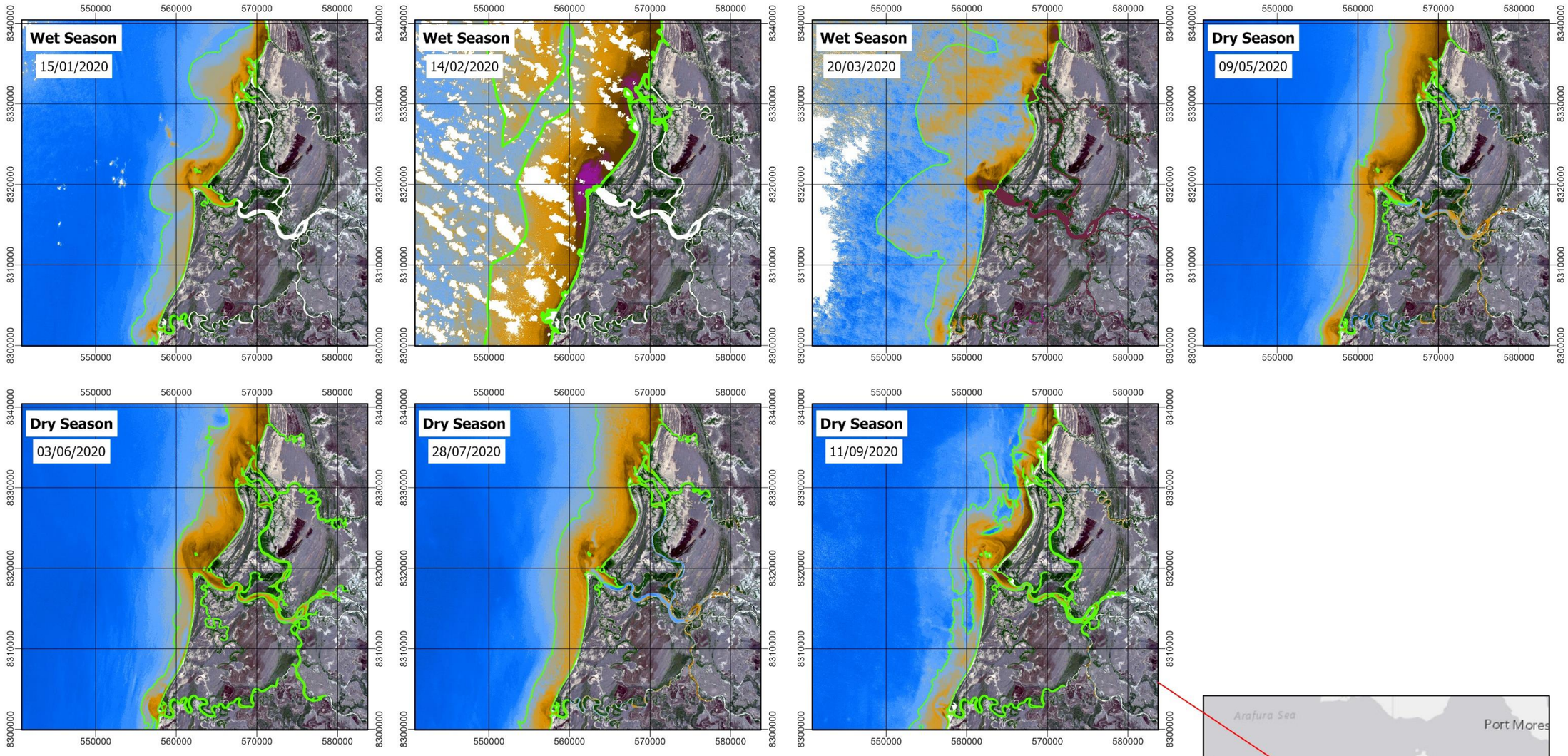

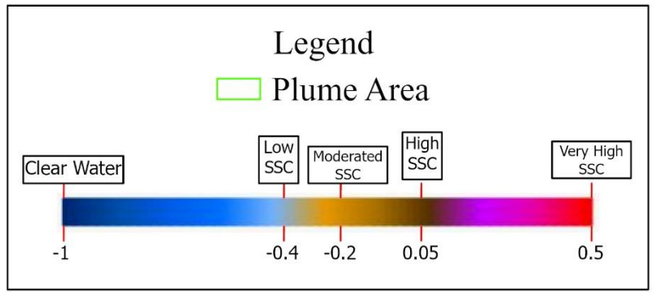

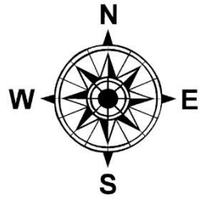

Scale: 1:470,000

0 5 10 20 30 40 Kilometers

Spatial Reference
Name: WGS 1984 UTM Zone 54S
PCS: WGS 1984 UTM Zone 54S
GCS: GCS WGS 1984
Datum: WGS 1984
Projection: Transverse Mercator
Map Units: Meter

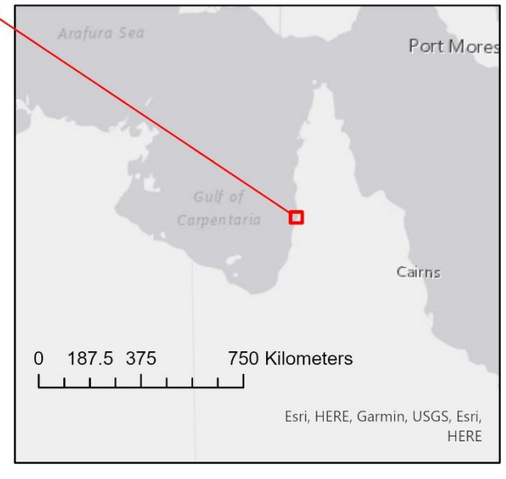

APPENDIX 5-02: Overall Seasonal Variations Map of Sediment Plume Geometry in 2021

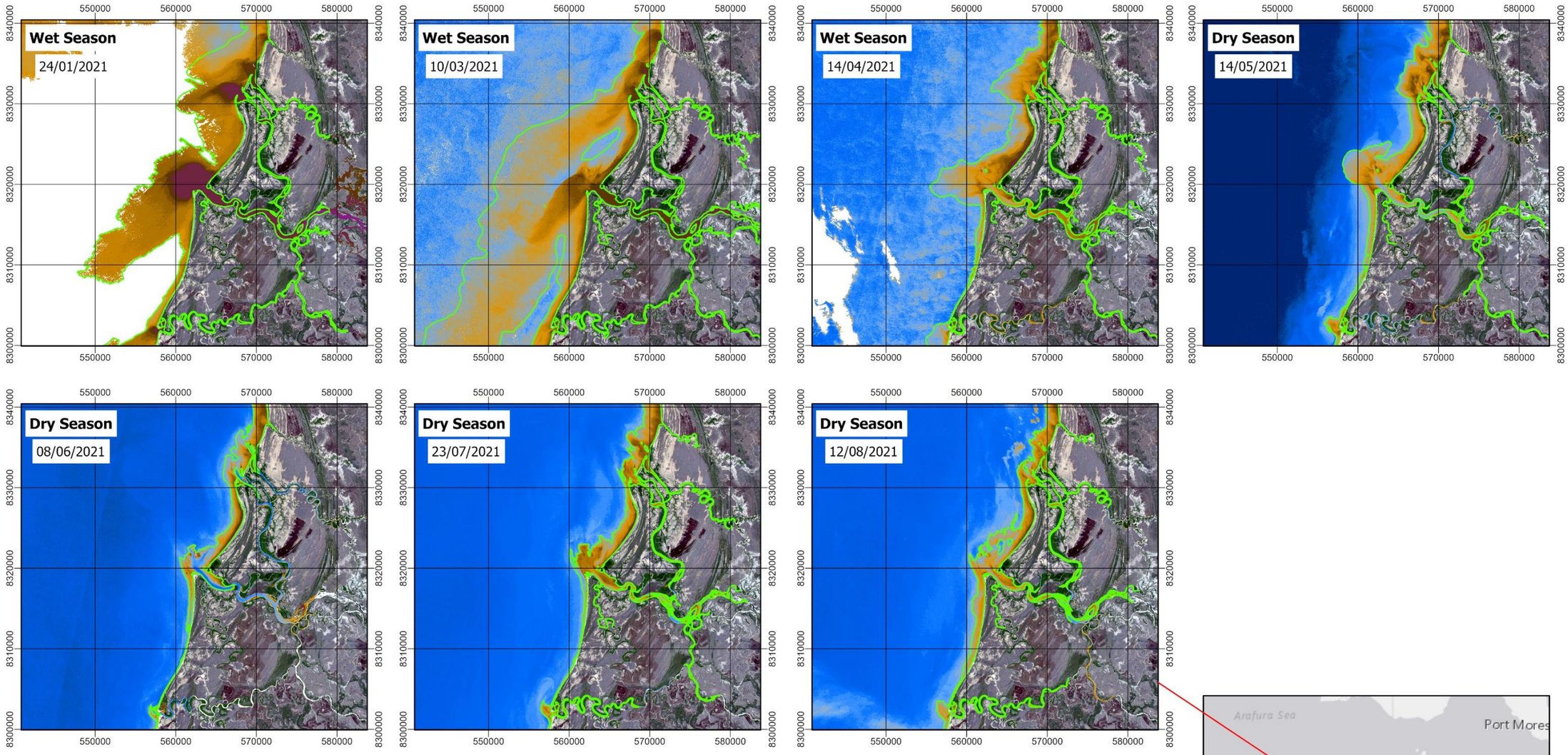

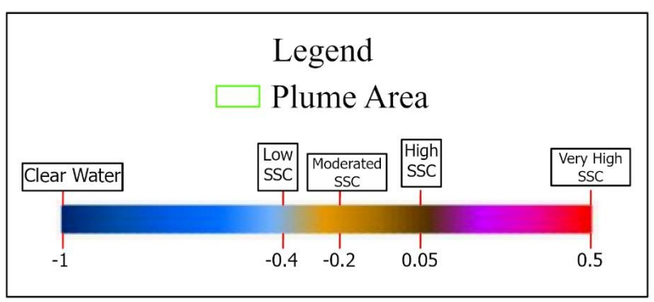

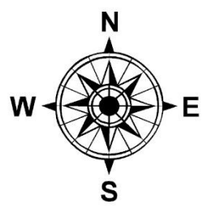

Scale: 1:470,000

0 5 10 20 30 40 Kilometers

Spatial Reference
Name: WGS 1984 UTM Zone 54S
PCS: WGS 1984 UTM Zone 54S
GCS: GCS WGS 1984
Datum: WGS 1984
Projection: Transverse Mercator
Map Units: Meter

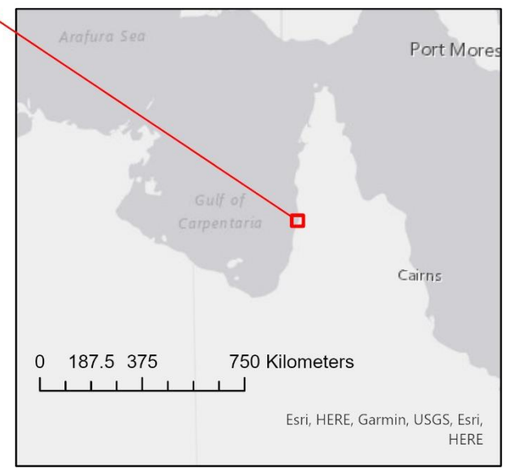

APPENDIX 6-1: Overall Seasonal Variations Map of Mouth Bar Geometry in 2020

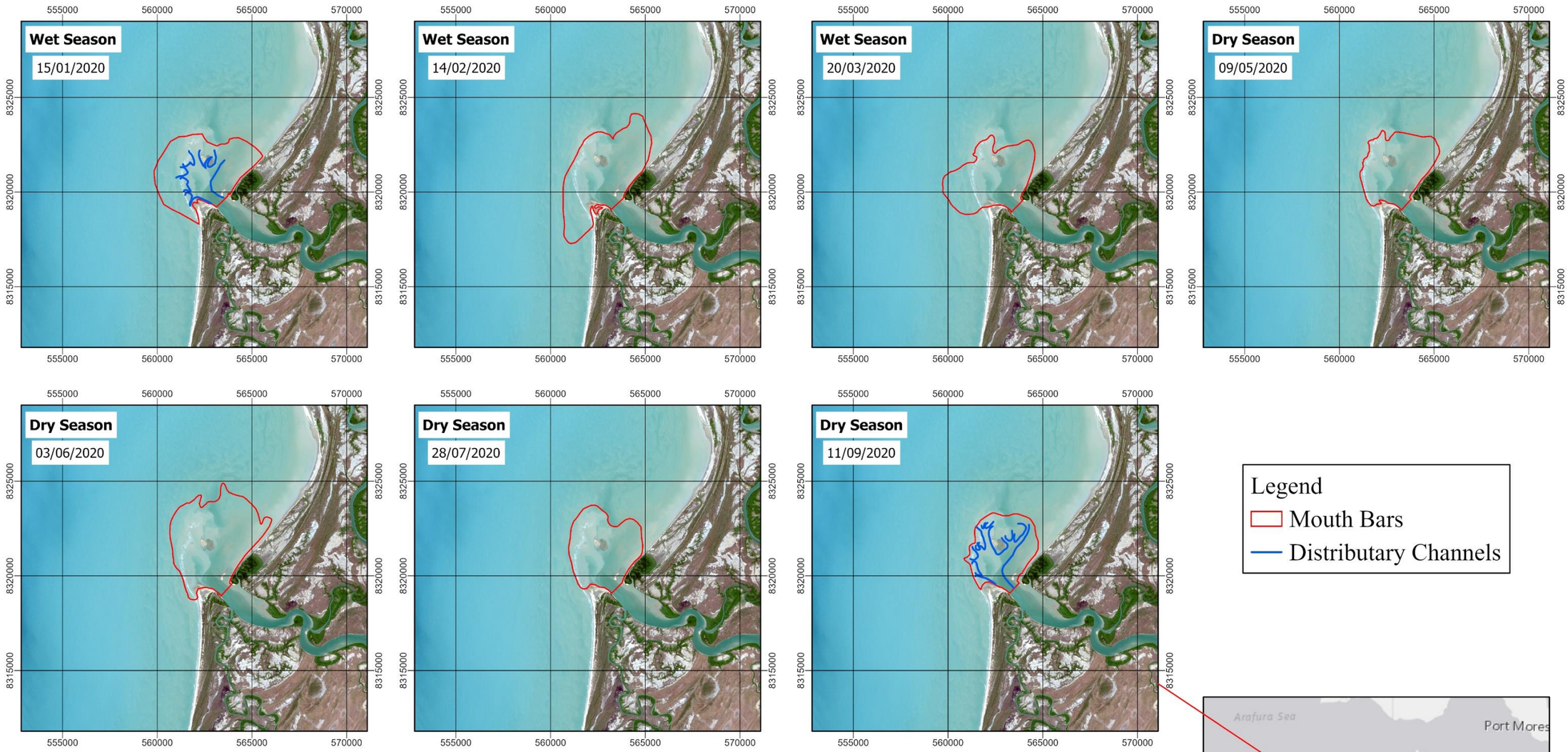

Scale: 1:200,000

N
W E
S

0 2 4 8 12 16 Kilometers

Spatial Reference
Name: WGS 1984 UTM Zone 54S
PCS: WGS 1984 UTM Zone 54S
GCS: GCS WGS 1984
Datum: WGS 1984
Projection: Transverse Mercator
Map Units: Meter

APPENDIX 6-2: Overall Seasonal Variations Map of Mouth Bar Geometry in 2021

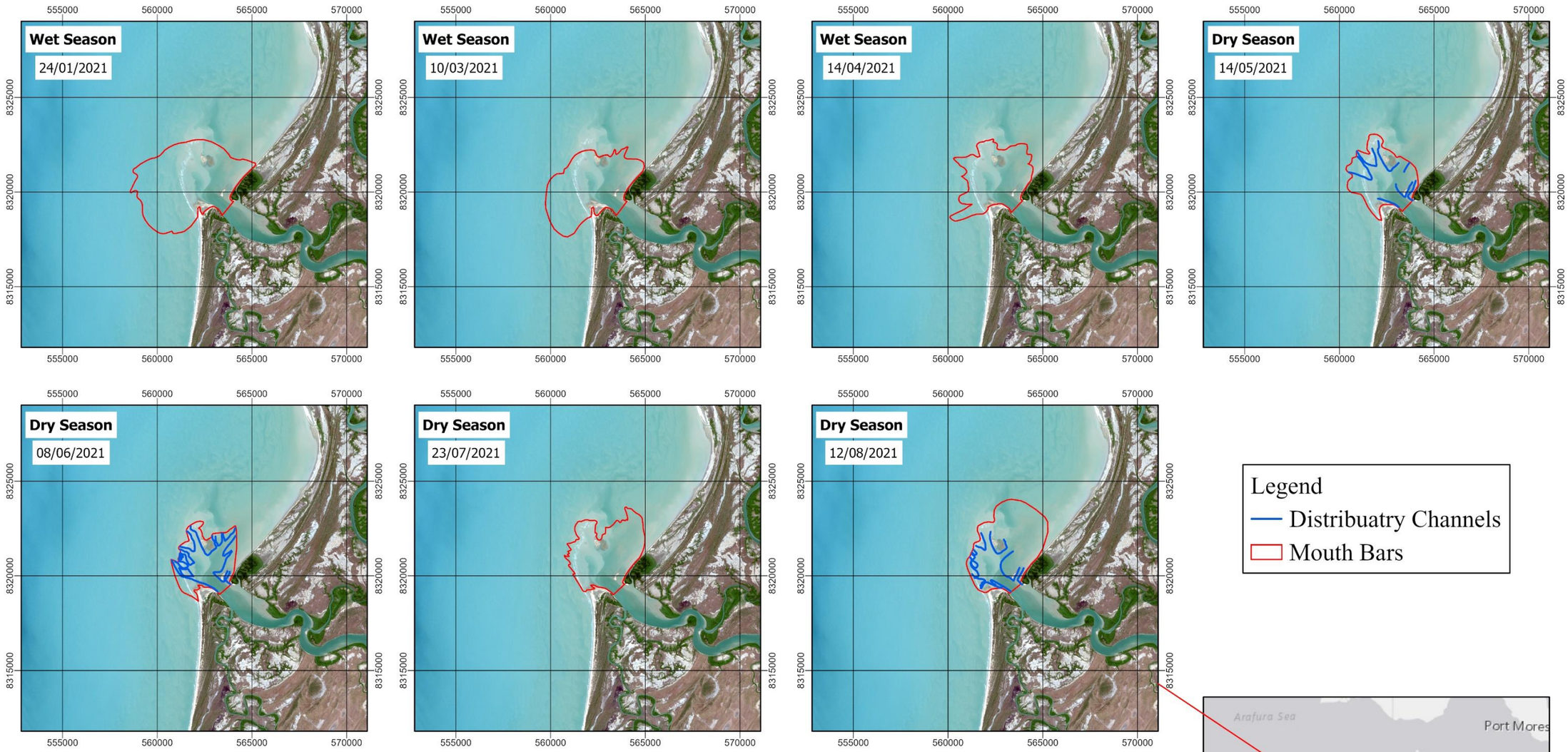

Spatial Reference
Name: WGS 1984 UTM Zone 54S
PCS: WGS 1984 UTM Zone 54S
GCS: GCS WGS 1984
Datum: WGS 1984
Projection: Transverse Mercator
Map Units: Meter